Skeletons in the labyrinth

Medial Representations and packing properties of bicontinuous space partitions

by Gerd Elmar Schröder

A thesis submitted for the degree of
Doctor of Philosophy at
The Australian National University

Canberra, 18 February 2005 (submission date)

Typeset in Palatino by TeX and LaTeX 2_ε.

Except where otherwise indicated, this thesis is my own original work.

Gerd Elmar Schröder

18 February 2005

Acknowledgments

Abstract

This thesis discusses medial skeleton representations of labyrinthine domains. These generalised channel-graph representations succinctly characterise both topology *and* geometry of bicontinuous space partitions and provide quantitative measures of extrinsic packing properties beyond volume-to-surface ratios. Analyses are presented of infinite periodic minimal surfaces as model structures for bicontinuous liquid crystalline mesophases and of electron-tomography data of a novel triblock copolymer network phase.

We describe the construction of both a geometrically-centered 1D line graph and a 2D medial surface skeleton of 3D labyrinthine domains. The medial surface is a branched surface structure centered within the domain, resulting from collapse of parallel surfaces of the domain's bounding surface S. Together with an associated distance function it affords a complete geometric description, that means the domain can be reconstructed from it as a union of balls centered on the MS. The radius of these balls provides a concise definition of local channel thickness.

We use the variations of the ball radii l to quantify *packing homogeneity* (as opposed to curvature homogeneity) of labyrinthine domains in $\mathbb{E}^3$. We define the degree of packing homogeneity as the width of the distribution of l over S, with perfect homogeneity corresponding to constant l. The average $\langle l \rangle$ can be interpreted as the average channel diameter, allowing for the definition of an average shape parameter $\langle l \rangle / (V/A)$. These concepts are applicable to self-assembly processes of liquid crystalline mesophases from nearly mono-disperse building blocks of typical molecular dimensions.

Analyses are presented for families of infinite periodic minimal surfaces. Among the cubic Primitive, Diamond and Gyroid surfaces and their tetragonal and rhombohedral distortions, the cubic Gyroid is shown to be the most homogeneous, for various physically motivated normalisations of the length scale.

We describe Voronoi-based algorithms for MS computations of triangulated surface data, including a novel adaption particularly suitable for exact data from mathematical parameterisations. An algorithm to obtain evenly triangulated representations of surfaces is also described.

The medial surface construction is also successfully applied to the interpretation of electron-tomography data of a novel symmetric but non-cubic network phase (or-

thorhombic symmetry $Fddd$) in a linear triblock copolymer melt. This analysis demonstrates that the medial surface is a useful tool for spatial structure recognition of space-filling hyperbolic structures as it combines complete geometric and topological description with the spatial sparsity of its representation (as compared to the bounding surface). This holds true despite its sensitivity to noise.

The network phase identified in a PS-block-PI-block-PDMS copolymer blend consists of two identical intertwined networks of eight-rings with three- and four-coordinated nodes ("tfa" in O'Keeffe's notation) with likely symmetry Fddd and c/a ratio of about 4. It is different from another Fddd phase (based on a single three-coordinated network) recently proposed for a similar system [54].

Date of this version: 19 September 2006, with small changes compared to the accepted version of this thesis

Contents

List of Figures

List of Abbreviations and Symbols

EDM	D	Euclidean Distance map
MA		Medial Axis
MS		Medial Surface
IPMS		Infinite Periodic Minimal Surface
	K	Gaussian curvature
	H	mean curvature
DF	d	MS distance function
PDMS		Polydimethylsilocane
PS		Polystyrene
PI		Polyisoprene
SEM		Scanning Electron Microscopy
TEM		Transmission Electron Microscopy

Introduction

Mazes or labyrinths in three-dimensional space at small length scales, regular or disordered, are ubiquitous as the spatial structure in physical systems. Examples include bicontinuous liquid crystalline mesophases in mixtures of water and lipids or surfactants [140, 141, 69, 124, 14, 125], self-assembled copolymer blends [86, 209], late stage spinodal decomposition in polymer blends [105], biomineralisation in sea urchin skeletons [159], periodic chitin structures with photonic bandgaps in butterfly wings [6], synthetic photonic crystals [147] and the alveolar surface of the lung [126]. In these processes, the system adopts a labyrinthine structure because it represents the minimal energy configuration. The emergence of these apparently complex structures is often called self-assembly.

Other interesting physical processes take place inside a labyrinth and are crucially influenced by the labyrinthine geometry, but do not alter the shape of the labyrinth. These include many phenomena in and properties of porous materials, such as permeability [104], two-phase flow [118] or capillary condensation.

While there are irregular and disordered labyrinths where the channels vary greatly in size, shape and channel connectivity, there are also highly regular, periodic and symmetric labyrinth structures. This thesis is mostly concerned with this second type. An important class of regular labyrinths is given by the family of *infinite periodic minimal surfaces* (IPMS): These are surfaces that partition space into two intertwined labyrinths, one on either side of the surface. They are periodic in three linearly independent directions in Euclidean space and have minimal surface area (in a variational sense). Because of the fact that IPMS divide space into two labyrinths, each of which is a continuous subset of $\mathbb{E}^3$, they are called *bicontinuous*. Fig. 1.1 shows their most prominent member, the so-called *Gyroid* surface.

A succinct, and physically relevant, geometric and topological description of these mazes is surprisingly difficult. Commonly labyrinths are represented as the sub-
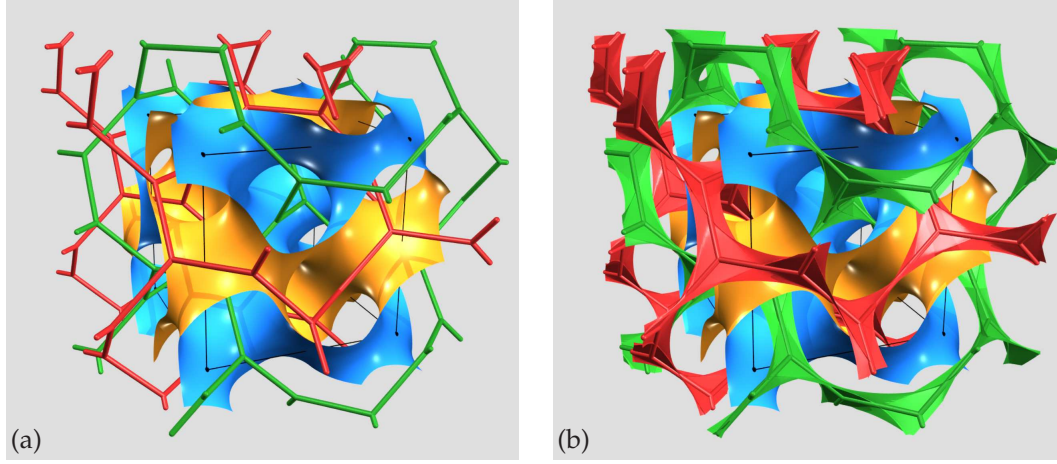
Figure 1.1: The Gyroid surface as an example for a member of the class of infinite periodic minimal surfaces. One side of the surface is coloured blue, the other orange. It divides space into two intertwined labyrinths, one on either side of the surface. The thin black lines represent the translational unit cell of the cubic space group. (a) Also shown are the line graphs in either of the two mazes, that are often used as primary descriptor of the labyrinth. While correctly representing the connectivity of the channel system, they do not capture its geometry completely. (b) Also shown are the medial surfaces in either of the two mazes. These are skeletons made up of surface patches rather than lines. They correctly represent both the topology and geometry, but are obviously not graphs.

volume of space that represents the labyrinth, as the interface that is bounding the labyrinth channel, or as graphs (or networks or skeletons) that are in some sense centered in the labyrinths and correctly represent the connectivity of the channels. Among these, networks of 1D line graphs (Fig. 1.1, a) that only partially capture the geometry, are distinguished from so-called medial surfaces (Fig. 1.1, b) that fully retain the geometric shape of the channels but are composed of surface patches rather than 1D curves.

A channel line graph is often the primary description of a labyrinth capturing the essential characteristics, in particular the connectivity. For a labyrinth that is made up of channels with circular cross-section (with possibly varying radius) that meet in well-defined pores, this description is well-suited and even a good representation of the geometry. Then, the labyrinth itself is an inflated version of the line graph, to be more precise, the union of spheres of size given by the channel radius along the line graph. It is however often overlooked that this is a very particular geometry; for a general labyrinth a line graph is much less well-defined.

In order to capture the geometry of a general labyrinth, a skeletal representation by *medial surfaces* (MS) is more appropriate. This structure is the main focus of this thesis, and defined in detail in section 1.2 and chapter 2. As the line graph, the MS is centered within the labyrinthine domain, yet it is made up of surface patches. Every point on the MS has a radius d assigned to it, which gives the maximal radius of the sphere that, placed on that MS point, is still fully contained within the domain. Again as the line graph, the labyrinth domain itself is the union of all those spheres, hence an inflated version of the MS. By virtue of the definition of the radius, the MS also allows a meaningful point-wise definition of a local channel diameter, see Fig. 1.2.
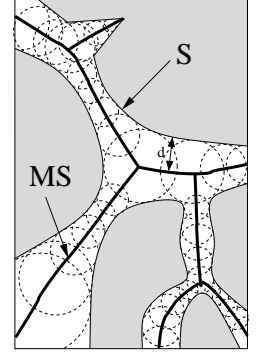
Figure 1.2: A 2D labyrinth and its medial surface.

Especially for IPMS, much research has addressed questions relating to the curvature properties of labyrinthine surfaces, in particular the Gaussian curvature. Gaussian and mean curvature are point-wise properties of surfaces S embedded in $\mathbb{E}^3$, derived from the principal curvatures κ_1 and κ_2. For every point p on S, the *principal curvatures* κ_1 and κ_2 are the maximum and minimum of the normal curvature at the point p. Gaussian curvature K and mean curvature H are then defined as

$$K = \kappa_1 \cdot \kappa_2 \qquad H = \frac{1}{2}\left(\kappa_1 + \kappa_2\right). \tag{1.1}$$

Minimal surfaces, including IPMS, have vanishing mean curvature $H = 0$. Both are properties of the surface, and not of specific parametrisation of the surface (although the mean curvature changes sign when the orientation changes). See textbooks on differential geometry for proper definitions of curvature properties [48, 83].

Much of the interest in curvature properties of labyrinthine structures is motivated by the fact that the "perfect labyrinth", that is one with constant curvature throughout, does not exist. The equivalent of the sphere, as the perfect convex body where all points have the same curvatures, cannot be embedded in euclidean three-space. This is a consequence of the very general result that a surface of constant negative Gaussian curvature cannot be embedded in $\mathbb{E}^3$ [90, 202]. The lack of the perfect labyrinth implies that any labyrinthine system striving for curvature homogeneity is necessarily frustrated, see section 1.1 below.

The curvature properties and the channel diameter as defined by the MS construction are not completely independent of each other (A trivial example is that of a cylinder where the constant curvature immediately imposes a constant radius on the MS, being the rotational axis). Curvature variations always imply variations of the local channel

diameter, but their degrees may be different. This motivates our suggestion to analyse the variations of the channel diameter as an additional homogeneity measure, as explained below.

1.1 Frustration in Self-assembled mesophases

Self-assembly of lipids and surfactants into labyrinthine surface forms is an example for a process where the phase diagram can be understood to a large degree by consideration of shape properties of the labyrinthine structure candidates. This section briefly reviews the origin of frustration in these systems, and outlines the novel approach taken in this thesis to quantify that frustration.

Self-assembly of liquid crystalline phases of mixtures of amphilic molecules, water and possibly oil has been widely described using energy functionals that are expansions in the curvature of the interface, due to Canham [25] and Helfrich [87]. The hydrophobic hydrocarbon chains and the polar hydrophilic headgroups tend to arrange in space such that the heads are shielded from the hydrophobic phase, and the tails shielded from the water. This drives microphase separation which results in oil-water interfaces lined with amphiphilic molecules.

Among such interfaces are bicontinuous space partitions based on IPMS. So-called type 2 phases consist of two intertwined water channels that are separated by a bilayer of lipid molecules, the polar headgroups towards the channels, the hydrophobic tails towards the interface surface. A geometric interpretation is that the molecules (that are assumed to be relatively monodisperse of typical size given by the area A of the polar headgroup, their individual volume V and the average length of the liquid hydrocarbon chains l) assemble onto surface forms that best fits with their typical shape. Hence the preference for surface forms with a particular average curvature and little variations around this average.

As explained above, a unique geometric feature of the bicontinuous geometries is that they are inherently frustrated because a labyrinthine structure without fluctuations of curvatures and channel thickness does not exist. As a consequence, a system with preferred curvature and preferred chain length is necessarily frustrated: two approximately parallel surfaces (the $H = 0$ interface and the polar headgroup surface in Type II systems) either have variations in the curvature and constant distance (real parallel surfaces), or constant mean curvature at the expense of variations in the thickness [5]. Another early account of the competition of bilayer thickness and curvature is given

in [176].

Helfrich ascertained that fluctuations of the Gaussian curvature of the IPMS correspond to frustration in Helfrich-Canham systems [88]. Similar results have been obtained more recently that include data for the variations of the Gaussian curvature [187, 186].

Hyde *et al.* introduced and analysed a *homogeneity index* $\mathcal{H}$, a scale-invariant parameter relating global properties V, A and integrated Gaussian curvature (topology) [95, 99, 66]. It combined scale-invariance with independence of the extent of the surface patch on which it is evaluated (e.g. which unit-cell and how many translational unit-cells) where the latter was a problem of earlier scale-invariant surface to volume ratios of the form $A/V^{2/3}$ [183]. This definition was motivated by the fact that a fictional hyperbolic partition of constant curvature (and hence MS distance function or channel diameter) has the value of 3/4, and on the belief that the absolute value

Figure 1.3: Hypothetical ideal surface with negative constant K (from [99].)

of deviations from 3/4 corresponded to curvature inhomogeneities. However, since then it has been found that, for some value of the free parameter, Schwarz' Hexagonal surface has large curvature fluctuations and nevertheless the "ideal" value of 3/4. Large variations in curvature are balanced by variations of the channel width in a subtle way to give the ideal $\mathcal{H} = 3/4$.

The fictional perfectly homogeneous minimal surface of *constant* negative Gaussian curvature has the property that its focal surfaces (composed of the set of points $p + 1/\sqrt{K}\,N(p)$ where K is the Gaussian curvature, $p \in S$ and N the surface normal field) degenerate to a surface of vanishing area, see Fig. 1.1. For infinite periodic minimal surfaces, the picture is that of parallel surfaces at distance r to the surface collapsing onto the channel graph for all points on the surface *at once*, i.e. for a constant value of r. Space is foliated by identical bricks, bounded by a small patch of a minimal saddle surface and a corresponding small line segment onto which it collapses ...wishful thinking in a flat three-dimensional Euclidean space!

In this thesis we keep the notion of a space tiling partition of the labyrinthine domain based on small surface patches and their corresponding volume, but relieve the constraint that the length of the space tiles is given by $\sqrt{-1/K}$. Instead, it is the maximal length by which the surface patch can be moved along the surface normal field, before it encounters the parallel surface of a different patch of the surface. That is exactly the distance between a point of the surface and its counter-part on the medial surface.

In this way one obtains a tiling of space into small volume elements. Analysis of the variations of the shape of these infinitesimally narrow but macroscopically long volume elements gives two measures for the homogeneity: variations of the wedge angle corresponding to curvature, and variations of their length (i.e. the MS distance) providing a measure of global *packing homogeneity.*

1.2 MS concept to characterise channel geometries

The concepts used in this thesis to characterise the shape of a labyrinthine domain are those of medial surfaces (MS) and geometrically centered lines. The former is a centered skeleton of the domain that retains the complete geometric description of the domain. For 3D domains, it consists of an assembly of 2D surface patches, with a point-wise defined *distance function* indicating the distance to original domain boundary. The union of balls on it with radius equal to the distance function provide a complete reconstruction of the labyrinthine domain.

The latter is a centered line skeleton consisting in 1D curves through the labyrinth. The geometric information about the domain shape it retains is equivalent to representing the domain as a channel system of tunnels with circular cross-section (of varying radius).

Medial Surface Transform

The MS construction is illustrated in Figure 1.4 using the analogy of a grassfire transform, from the first description of (2D) medial surfaces [18]. The figure shows a piece of the Gyroid infinite periodic minimal surface with the outside colored green and its inside colored orange. The sequence of images (a-f) shows the Gyroid surface with its interior non-overlapping parallel surfaces (in yellow). These *reduced parallel surfaces* are obtained from the Gyroid surface by transport along its surface normal direction by a distance corresponding to $\min\{r, d(p)\}$, thus $p + \min\{r, d(p)\} N(p)$. The number r is the evolution parameter and $d(p)$ indicates the maximal distance by which a point can be transported along its normals without colliding with another point $p_2 + r N(p_2)$ (which is when the parallel surfaces first overlap). For large r, where every point has reached its maximal distance, the structure is the medial surface of the Gyroid domain.

Imagine the domain to be solid and flammable, and its boundary set on fire. A simplified fire burns the material in layers parallel to the boundary. Areas where two fire fronts collide (or one fire front develops a cusp) mark the end points of the burning

process. This explains the name "grassfire transform", created for the 2D analog of burning a grass field.

The reduced parallel surface is colored yellow wherever $r < d(p)$, and colored according to d where points have collapsed. Blue corresponds to the largest values, then green and yellow, and then red to the smallest (where the only red areas, located on the fringes of the MS, are hardly visible). In (a-c) no collapse has occured, the reduced parallel surfaces remain real parallel surfaces. In (d) collapse is starting to occur, yet the domain inside the reduced parallel surface is still a connected net with the same topology as the original Gyroid surface. In (e) the collapse is almost complete, the inside domain is no longer continuous but split into small volumes near the regions of largest distance. In (f) the collapse is complete. In this case (but not in general), the MS is almost a ribbon following the three-coordinated Gyroid line graph. The collapse points with the smallest distance function are on the boundary of the MS.

It is clear from this process that the MS is indeed centered, in the sense of being maximally distant from the domain walls. It is also clear that all points of MS have two or more corresponding surface points. These are tangentially touched by spheres around the MS points of radius given by the distance function.

The details of the MS definition and its computation for numerical manifold representations of domain boundaries is described in Chapter 2. The medial surfaces of the four cubic IPMS are described in detail in Chapter 5, those of non-cubic IPMS in Chapter 6, and finally those of a labyrinth in an experimental electron-tomography data set of a block-copolymer phase in Chapter 7.

Geometrically centered line graphs

Upon a first glance, the Gyroid is best described by a network of straight edges meeting in 3-nodes. This is the concept of a line graph. It captures the topology, and a little of the geometry, but not the cross-sectional shape of the channels. Despite the apparent simplicity of the concept, it is difficult to define unambiguously.

We analyse a line graph that is required to be geometrically centered. That means that it has to lie on the MS, but its precise path *within* the MS is still to be determined. We keep to the idea of maximising the distance to the original bounding Gyroid surface and analyse the distance topography on the MS. This distance function profile is indicated by the color scheme on the MS. The obvious analogy to a topography of a mountain range is helpful, although not quite correct as the MS has in general , in contrast to the globe, branchlines.

Nevertheless, paths on the MS that maximise the distance to the bounding surfaces are analogons to ridges of mountain ranges (where height corresponds to distance function). Points of minimal distance function along those lines are saddle points of the distance function on MS. From there, following lines of steepest ascent will lead necessarily to a maximum.

Thus, determining geometrically centered line graphs reduces to finding saddle points of the distance function (or distance map) on the MS and following lines of steepest ascent from those points. This is illustrated in Figure 1.4 (g,h) where the maxima correspond to blue spheres and the saddles (in this case monkey saddles) to the yellow spheres.

This definition bears problems in that the line graph may have a homotopy different to that of the domain itself. A deformation of the Gyroid can be imagined (although we believe it to be a non-minimal one, see Chapter 3) where these geometrically centered lines connect maxima to maxima in straight lines forming a triangle around the central point (of course the saddles must move onto the edges of this triangle). Then the graph forms a loop that has no counterpart in the actual labyrinthine domain.

The construction of geometrically centered line graphs and a discussion of its subtleties and ambivalences are given in Chapter 3. The line graphs of IPMS are discussed in Chapters 5 and 6. For the experimental data, an automated computation of the so defined line graph turned out to be impossible due to noisy data, yet we kept to the spirit of the definition in manually determining a model of the line graph.

Unusual features of the line graph

These line graphs show a number of noteworthy features even for the fairly generic labyrinthine domains based on IPMS. The Gyroid example already demonstrates the falsehood of the notion occasionally adopted in the literature (e.g. [198]) that nodes of the line graph correspond to widest points of the labyrinth. In the case of the Gyroid the maximal width of the channel system is indeed reached at the center of the graph edges. This feature is also observed in one of the two channel domains of the I-WP space partition, see Section 5.5.

Furthermore, those IPMS families that are in general non-cubic but contain one or more cubic members provide good models for transitions of generic line graphs involving changes to the coordination number. Analysis of their line graphs shows that the transition between for example the 3-coordinated graph of the Gyroid surface and the 4-coordinated graph of the tD surface family (via the tG surfaces) is not

one that merges two symmetric trigonal three-nodes to form a symmetric tetrahedral four-node. The transition is rather the split of a symmetric three-node into two edge midpoints, leading to the formation of a strongly deformed 4-node (with two pairs of tangential incident edges) followed by the relaxation of the shape to that of a symmetric 4-node. This illustrates that the ostensibly abrupt topological transition is overlayed by a geometric shape deformation (see Figure 6.5, d+e, on page 146)

Variations of the MS distance as a measure for chain stretching homogeneity in mesophase formation

The MS distance function allows for a simple geometric definition of packing homogeneity. The simplistic picture is that of Type 1 self-assembly of surfactant/lipid molecules in binary mixtures with water, see Figure 5.4 on page 108. The picture is that of a film of water separating two intertwined channels containing the hydrophobic chains (but no additional oil). The interface between oil and water is assumed as a parallel surface to the IPMS that represents the middle of the water film. The molecules are assumed to be pointing normally away from the surface towards the MS of the hydrophobic microdomain.

The tail ends then have to lie on the MS of the hydrophobic phase in order to be space-filling which necessarily involves stretching or squashing as hyperbolic surfaces with constant distance function do not exist (for the same reason as constant Gaussian curvature surface do not exist). Approximating the penalty for stretching of the hydrophobic hydrocarbon chains from their preferred length as $(d - l_0)^2$ gives a measure for the packing homogeneity, namely the mean square deviation of d from l_0.

It is important to note though that these measures are (in the same way as curvature measures) not scale-invariant. They depend on the length scale of the system, that may be well approximated by the strongest contribution to the free-energy or may need to be determined by a combination of all contributions. We do not dwell on the details of an actual system, but stick to an analysis of the geometric properties and present them in a variety of normalisations. This approach does justice to the large number of different systems in which these generic structures are observed.

An analysis of this kind is presented in Chapter 5.4 for the cubic IPMS and in Chapter 6.2 for non-cubic IPMS families. This analysis clearly demonstrates the packing homogeneity of IPMS families to be greatly enhanced "in the vicinty" of the cubics compared their family members with axes ratios distinctly different from 1.

The MS as a clear identifier of channel topology *and* geometry

Finally, the MS is a useful tool for the visual inspection of labyrinth structures as it combines the complete geometric and topological information of the labyrinth with the advantage of a fairly sparse representation. In Chapter 7 we present an analysis of electron-tomography data of a novel triblock copolymer phase of distinctly non-cubic symmetry.

The novel copolymer phase found is intriguing in that it is distinctly non-cubic. Our analysis shows it to be of the same symmetry as a phase recently found in another triblock-copolymer system [12, 54], but the topology is completely different. We find a system of two intertwined graphs of 4- and 3-coordinated nodes with $Fddd$ symmetry, whereas their claim (based on SAXS measurements and TEM images) is a single network of $Fddd$ symmetry.

The MS construction is useful in this context despite its sensitivity to noise in the representation of the bounding surface (clearly, any small convex angle generates a MS branch that extends all the way to the bounding surface; a sharp convex cusp can only be reconstructed by a union of spheres with at least some of vanishing radii and hence close to the surface). In this particular data set, we have benefitted from the relatively small channel diameters of the imaged phase and of the fact that the MS is not branched.

1.3   MS-like structures and line skeletons in physics

Physical analysis of labyrinth-forming structures based on skeletons of their channels is ubiquitous. The typical representation is as that of a line graph, which is assumed to correctly represent the topology of the labyrinth, yet also capture some of the geometry.

Network models for fluid flow and transport through random porous media are widely used [13, 200]. Upon increasing pressure, the water-vapour interface advances along the network edges (representing the thin capillaries, *throats*, between pores) overcoming the Laplace pressure given by the point of narrowest cross-section along the edge. Graph edges have geometric significance, in that they are associated with a diameter of the throats. Some of the algorithms applied to network generation of random porous material make implicit use of the MS concept, by associating pores with maxima of the distance function [198].

The notion that the bicontinuous mesophase structures adopted in self-assembled lipid, surfactant or copolymer blends are described by their line graphs is widespread.

More explicitly, Luzatti *et al.* have suggested the concept of *chaotic zones* as the regions deep inside labyrinths where the flexible hydrophobic hydrocarbon chains (or the orientation of the polar dipoles) are the least ordered [139, 142]. This construction is clearly reminiscent of the MS construction and the reduced parallel surfaces described above.

In a different approach, distances from the $H = 0$ interface to the line graph, and fluctuations of it, have been suggested to quantify packing frustration [50]. In this thesis, we analyse infinite periodic minimal surfaces using a very similar idea, yet with the MS distance function rather than the distance to the line graph.

A bite through an icy-pole reveals another physical phenomenon where interface evolution terminates on a structure reminiscent of the MS. The sugar solution is rapidly frozen starting at the cold metal mould, leading to the formation of linear ice crystals that are oriented perpendicular to the mold surface, and extend into the frozen block to a structure that is reminiscent of the MS (the Y-shape in Figure 1.5).
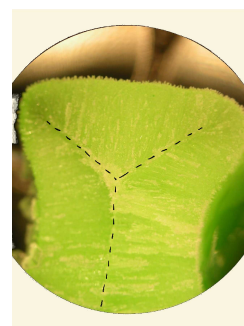
Figure 1.5: Icy-Pole

This is somewhat reminiscent of the Avrami-Johnson-Mehl model of grain nucleation and growth where growth occurs in circles around nucleation sites at the expense of a liquid matrix. In 2D, growth stops stops where two growing interfaces meet [175, 210]. If growth starts from a more general interface, the interface where it stops is similar to the MS construction.

It has been shown that analysis of (reduced) parallel surfaces of interfaces in terms of their Minkowski integrals (foliated volume, area, integrated mean curvature and Euler index) is a robust and physically relevant tool for spatial structure characterisation [152]. Examples include descriptions of pore space morphologies in porous media [7] and reaction-diffusion systems [151]. At least implicitly, this analysis assumes that the parallel surfaces do not pass through each other but terminate on the MS. Mecke notes that these measures are robust with respect to small variations of the domain shape [152]. This property does not hold true for the MS construction, which is sensitive to small changes of the domain shape if these changes represent strong changes to the normal field (note that curvature analyses are affected by it in the same way as the MS).

A structural model for the construction of achiral smectic blue phases, that fill space by layers parallel to infinite periodic minimal surfaces, has been suggested and analysed for the Primitive and I-WP surfaces [44, 43]. Line defects of these liquid crystals are located on the boundary of the MS, representing lines of highest intrinsic curvature.

Generalised Voronoi-constructions of the complement of sets of convex particles have been suggested as models in which fluid-flow and diffusion through porous materials can be simulated [153, 138]. Their *navigational map* consists of the branch-lines of the MS, which in that case gives a continuous network centered in the domain and can be computed exactly for simple particle shapes.

Organisation of this thesis

In the second chapter, the concept of a Medial Surface is introduced. Its main properties are explained and the literature reviewed. An algorithm to compute the medial surface is discussed that is based on triangulated representations of the bounding surface. These are most appropriate for the mathematical models of infinite minimal surfaces that are discussed here. The algorithm computes a Voronoi diagram of the sample points of the surface, that is then reduced to the medial surface.
A novel adaptation of the algorithm is presented that is particularly suited for computation of medial surfaces of exact surface data, such as from mathematical parameterisations.

The third chapter discusses the reduction of the medial surface to a line graph. The definition of line-graph that we use emphasises the geometric centeredness of the line graph within the labyrinth, at the expense of topological equivalence to the labyrinthine domain. The difficulties with line graph definitions in general are explained in detail.

The fourth chapter describes the parametrisation of infinite periodic minimal surface using the Weierstrass equations. The literature on these space partitions is reviewed and parametrisations for all IPMS analysed in the subsequent chapters are given. We present a new algorithm to obtain triangulations of IPMS asymmetric unit-patches with even triangle edge lengths, as this is a requirement for the MS computations.

The fifth and sixth chapters present analyses of the MS and properties derived from the MS for domains bounded by infinite periodic minimal surfaces, first of the cubic Primitive, Diamond, Gyroid and I-WP surfaces and then of the surface families tD, tG, rPD and rG of non-cubic symmetry. The notion of packing homogeneity is described and analysed for these space partitions. The properties of the channel graphs, in particular their transitions during the evolution of the surface families, is analysed.

The seventh chapter describes an analysis of an experimental electron-tomography data set of a novel, non-cubic ABC triblock copolymer phase. The domain shape is described in terms of its symmetry and shape – both derived from the MS representation.

(a)

(b)

(c)

(d)

(e)

(f)

(g)

(h)
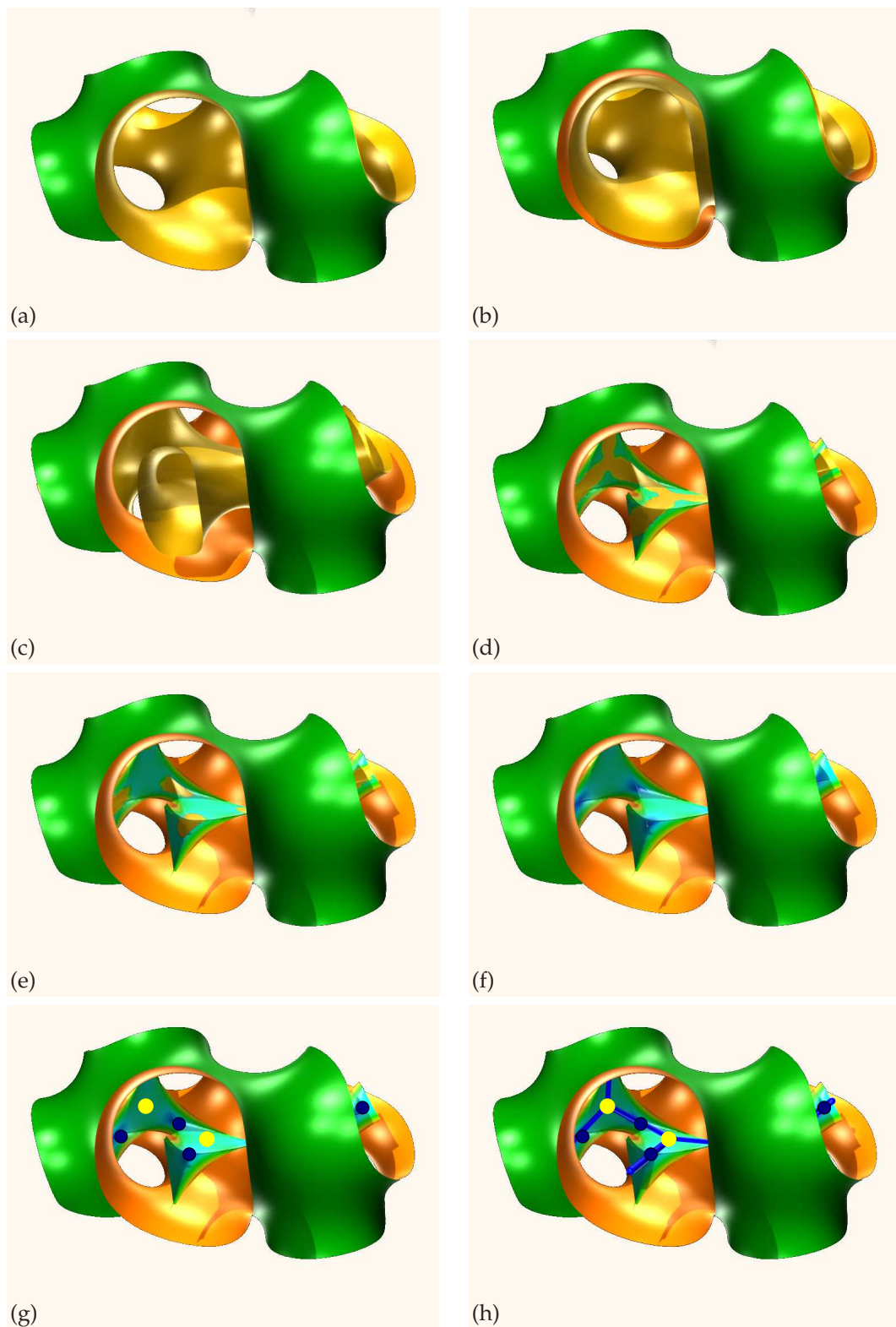
Figure 1.4: Illustration for the MS construction as the end point of the grassfire transform and the idea behind a geometrically centered graph.

Medial Surfaces

This chapter provides a definition of the medial surface, gives an overview of some of the main properties of this structure, and describes algorithms to compute it. A bibliography of literature on both theoretical and computational aspects of the MS is given.

Algorithms are presented that compute approximations to medial surfaces of 3D domains that take a triangulation of the bounding surface of the domain as input data. They then approximate the MS as a subset of the Voronoi diagram of the sample points of the bounding surface. In particular, a novel adaption that provides better MS approximations if the bounding surfaces stems from mathematical parametrisations is described.

A word on the terminology is in order. The naming of the "Medial Surface" is not uniform in the literature, and we here adopt the name "Medial Surface" even though it is much less common than "Medial Axis". However, we find the former term more descriptive for the 3D MS – and it distinguishes the MS nicely from line graph representations that, in the physics literature, have sometimes been called "Medial Axes". Occasionally, the MS is also called "skeleton".

The bibliography includes the most important contributions to research into the MS for the 3D case. The body of literature on the 2D case, both conceptual and algorithmic, is so vast that even a review is beyond the scope of this chapter. Therefore, apart from a few exceptions, we refrain from providing references for the equivalent 2D results.

2.1 Definition and basic properties of the MS

We define the MS for a domain C in Euclidean 3D space. A domain C is an open, connected subset of $\mathbb{E}^3$ whose boundary, or *skin*, is an oriented piece-wise smooth
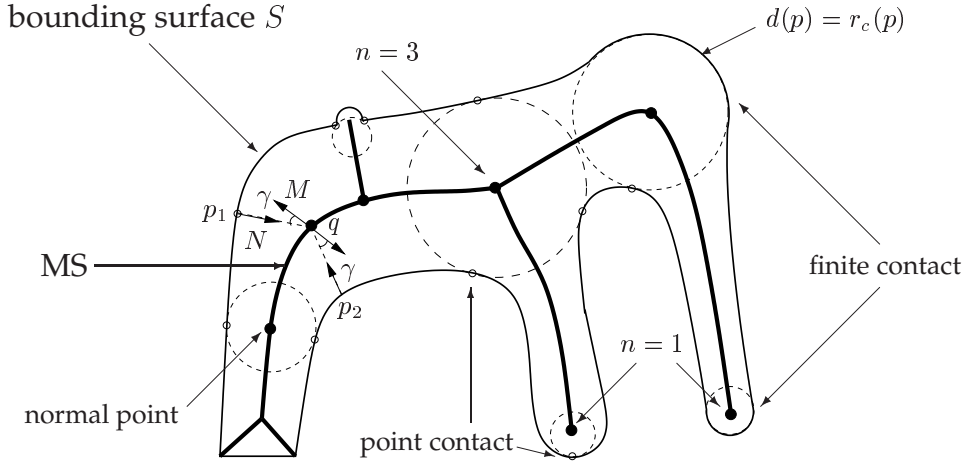
Figure 2.1: Sketch of an elephant and its medial axis in the plane. Some features of the MS are illustrated in this figure: Points on the MS, and their counterparts on the polygon can be classified according to the number of contact points of the corresponding maximal spheres. Normal points have contact order $n = 2$; end points of the medial axis correspond to osculating maximal circles. For a point p on the skin the corresponding medial axis point is in normal direction from p: $ms(p) = p + d(p)\,N(p)$. The medial axis normal M at $q = ms(p)$ and the surface normal $N(p)$ of corresponding points subtend an angle $\gamma \in [0, \pi/2]$ with each other. Two points p_1 and p_2 corresponding to a normal MS point q are MS mirror images of each other in the sense that the angles $\angle N(p_1), M(p_1)$ and $\angle N(p_2), M(p_2)$ are identical and, by definition, $d(p_1) = d(p_2)$. Small features of the skin, such as the pimple on the elephant's back, can induce dominant features on the medial axis, if they drastically change the normal field $N(p)$.

manifold, or a set of piece-wise smooth manifolds in $\mathbb{E}^3$.

For example, a domain might be one of the two subvolumes bounded by an infinite periodic minimal surface, the void or the solid phase of a porous medium, a three-dimensional solid, or the complement of a set of disjoint solid objects.

As said above, the boundary surface is always orientable, and has a piecewise smooth normal field N defined everywhere on S. The normal field along edges and vertices is defined by replacing edges by a cylindrical surface element and vertices by a spherical cap, both of vanishingly small radius. We assume the surface normals are of unit length and oriented to point into the domain C.

The MS is, in a loose sense, the geometrically centered skeleton or backbone of the domain C. The medial surface MS of the domain C is the locus of centers of all *maximal spheres* in C. A *maximal sphere* is a sphere contained in C which is not contained in any other sphere contained in C.

These spheres are necessarily tangential to S. It is immediately obvious that the medial surface is the set of points inside C with two or more nearest points on S, together
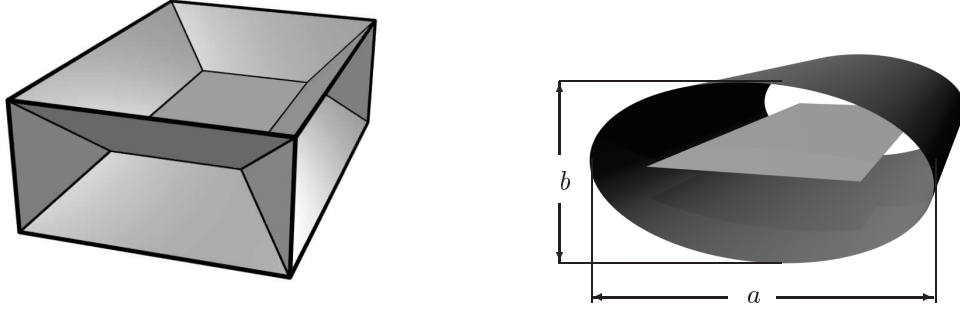
Figure 2.2: Examples of medial surfaces in 3D. (Left) The MS of a rectangular box (Right) A cylinder with elliptic cross-section together with its MS.

with limit points of this set. These limit points are points where these two nearest surface points converge to a single point (see for example the elephant's front foot in Fig. 2.1).

The medial surface of a domain generally consists of surface patches meeting along one-dimensional curves. In particular cases, the patches may extend to infinity, or degenerate to curves or even points. If S has a convex edge (or vertex), i.e. a line (point) where the normal field is discontinuous and the corner is pointing out of the domain, then there is a MS patch extending up into the corners of the surface, see the rectangular box in Fig. 2.2 (left).

Some examples clarify the features of the MS construction. The medial surface of an infinite slab of thickness d (bounded by two parallel planes) is a parallel plane at distance $d/2$ between the two original planes. The medial surface of a sphere is its center point, and the medial surface of a cylinder with circular cross section is its rotational symmetry axis. The MS of a straight cylinder along the z-axis whose cross section is the ellipse given by $(x/a)^2 + (y/b)^2 = 1$ with $a > b$ is a flat ribbon $\{(x, 0, z)| -\infty \leq z \leq \infty, |x| \leq a - b^2/a\}$ in the $y = 0$ plane, see Fig. 2.2 (right).

Any point $p \in S$ on the boundary S of the domain C has exactly one corresponding point $q := ms(p)$ on the MS of C. The converse is, evidently, not true. The point p is located at the shortest distance from q compared with all other points on S. Therefore, the map ms from a point on S to the corresponding MS point can be written as

$$ms : S \to \mathbb{E}^3, \qquad p \mapsto ms(p) := p + d(p)\, N(p) \tag{2.1}$$

where N is the normal field of S and $d : S \to \mathbb{R}^+$ is called the distance or radius

function.

The MS accurately represents the topology of the original domain, in the sense that the MS is a strong deformation retract (see [201] for a definition) of the original domain C in 2D [29] and in 3D [219, 195][1]. This means that, although the dimension of C is in general different to that of its MS, they have the same tunnels, holes and connected components.

An alternative description of the MS construction, that makes the topological equivalence between the skin and the MS very obvious, has given the name *grassfire transform* to the MS. In Blum's own words [19]: "Imagine an object whose border is set on fire. The subsequent internal quency (*sic*) points of the fire represent the symmetric axis, the time of quench for unit velocity propagation being the radius function."

Furthermore, the medial surface together with the distance function d allows for the reconstruction of the domain C as the union of maximal spheres of radius $d'\left(ms(p)\right) = d(p)$ centered at the MS points $ms(p)$ [219]. Explicit formulae for the reconstruction can be found in [78].

These two properties lend a robustness to the MS concept that all other skeletonisation techniques do not possess. The MS transform, i.e. the MS together with the radii of the maximal spheres, is topologically and geometrically a complete and accurate description of the structure.

A property that is for most, but not all, purposes a drawback is the sensitivity of the MS construction to small variations in the normal field N of the boundary $S = \partial C$. Perturbations under which the MS changes continuously must involve only small changes in the normal field of S. Addition of a small bump in S can create a big change in the MS, see Fig. 2.1.

Most importantly, the medial surfaces of a domain bounded by a smooth manifold S, or bounded by a faceted surface approximating S differ strongly from each other, regardless how good the surface approximation is: the MS of the faceted surface domain has MS patches extending into all facet edges and corners.

This sensitivity of the MS construction to surface normal variations is inherent to its definition and not due to the algorithmic details of its computation.

A second consequence is that the MS is sensitive to *roughness* of the bounding surface S. This causes difficulties for the determination of the MS of noisy data sets. The extraction of the MS of a smooth object that is given by noisy surface data of its bounding surface is a difficult issue, discussed later in this chapter.

---

[1]The first reference requires S to be smooth, rather than piecewise smooth. The second reference does not seem to impose this restriction.

The distance function $d : S \to \mathbb{R}^+$ is formally similar to the radius of curvature $r_c : S \to \mathbb{R}$ in the sense that both measure distances in normal direction from points on S. In general, at any given point $p \in S$ there exist two distinct radii of curvature $r_{c,1}$ and $r_{c,2}$ corresponding to the two principal directions in p. Only positive curvature (i.e. bending of the surface towards the normal N) can lead to curvature induced points of the MS in positive normal direction. We therefore define r_c as the minimum of the positive radii of curvature and infinity. Indeed, the maximal sphere K_m centered at $ms(p)$ with radius $d(p)$ and the sphere K_r centered at the center of curvature $p + r_c(p) N(p)$ with radius $r_c(p)$ are both tangential to S in p. By definition, K_m is contained in C (global). In contrast, K_r need not be contained in C but is osculating[2].

It is straightforward to see that the distance function is always smaller than the radius of curvature[3]

$$\forall p \in S : \qquad d(p) \leq r_c(p). \tag{2.2}$$

For all points on free boundaries of MS patches (i.e. the ones that are not intersections of more than two MS sheets) this inequality holds as an equality. However, in addition there can be isolated points that are not on free boundaries, or continuous subsets of S that are cylindrical segments or spherical caps for which $d(p) = r_c(p)$. Furthermore, there is the pathological case of convex corners and edges on S that have $r_c(p) = d(p) = 0$.

2.2 Some results and literature about the MS

This section provides a review of some theoretical results about concepts concerning the MS, together with literature references. In particular for the 2D case, the literature is abundant, and we do not claim to give a comprehensive account.

The geometric structure of the MS in 3D is mostly understood: Points q on the MS are

---

[2]The word osculating, usually used in planar curve theory, is here applied in the following sense: if r_c is infinite no osculating sphere exists. Otherwise, the principal direction through p that corresponds to r_c is denoted by T_c. Then, restricted to the plane P_n through p with directional vectors $N(p)$ and $T_c(p)$ (normal section) the circle $K_r \cup P_n$ is an osculating circle to the planar curve given by $S \cup P_n$.

[3]To see this assume it exists a sphere K whose radius exceeds r_c, which grazes S in p and lies in positive normal direction from p. The sphere K contains K_r. But K_r and S have identical curvature in a neighbourhood of p along at least one direction. Therefore, a finite part of S is contained in K. Thus, K cannot be a maximal sphere. This can be phrased more precisely: A unit speed space curve α coincident with the intersection of S with the plane containing the normal $N(p)$ and the principal direction $T_c(p)$ has curvature $1/r_c$ at the point p. Also the surface normal $N(p)$ is identical to the curve normal, see e.g. corollary 16.8 in [83]. A finite part of this curve is contained in the larger sphere K with $r > r_c$ because α curves more strongly towards $N(p)$ than does K, leading to the above conclusion.

classified according to their order n (i.e. the number of disjoint subsets of the set of points $p \in S$ with $ms(p) = q$) [18]. In particular, the MS consists in patches of $n = 2$ points, bounded by two types of lines: $n > 2$ curves where three or more sheets meet, and the open $n = 1$ boundaries of MS patches that in fact correspond to centers of curvatures and are hence identical to the cusp lines of the focal surface, as shown by Giblin and Kimia [78]. In 2D, the MS is a collection of $n = 2$ patches, $n = 1$ points corresponding to curvature extrema and $n \geq 3$ lines where where $n = 2$ patches meet [19, 29], see Fig. 2.1.

In addition, one distinguishes between *point contact* [156, 19] (or regular tangency [78]), where the touching subset is a single point, and *finite contact* where it is finite and therefore a spherical cap or a circular arc, see Fig. 2.1.

Blum and Nagel [19] and Nackman [156] have defined differential geometric properties of the MS, in 2D and 3D respectively. They introduce the notion of *radius curvature*, that is the distance function takes the role of the radius of curvature in the usual definition of the curvature tensor, and derive relations between the radius curvature and the standard curvature of the bounding surface (Nackman restricts himself to the $n = 2$ sheets). Both are concerned with a segmentation of objects for the purpose of shape description.

Wolter [219] provides proofs of a number of fundamental properties of the MS in n dimensions – both of topological and geometric nature. His article is phrased in the mathematical language of cut loci, from the French *ligne de partage*, which, for a closed set A in Euclidean space $\mathbb{E}$, is the closure of the set containing all points p which have a least two shortest paths to A. He provides rigorous proof for the equivalence of the homotopy type of a domain and its surface by explicit construction of the deformation retract: points inside C move, by virtue of a homotopy, onto the MS along the corresponding normal as a parameter t varies from 0 to 1. His article also includes a formal proof of the statement that the domain can be reconstructed from the union of maximal spheres centered at the medial surface.

In an equally fundamental paper, Choi *et al* [29] present many results for the 2D case: in particular, they give the same result for the homotopy relation between C and its MS. They also give requirements on the smoothness of the skin for the MS to be well-behaved. In particular, the skin must be piece-wise real analytic to avoid infinite numbers of bifurcations of the medial axis; $\mathcal{C}^\infty$ is not a sufficient condition.[4] For example, a highly oscillating function such as $e^{-1/t^2} \sin(1/t)$ is smooth but not real-analytic and

---

[4]The skin is $\mathcal{C}^\infty$ if, as a planar curve, it can be parametrised by coordinate functions $x_i(t)$ for which the derivatives of any order $x_i^{(j)}$ are continuous. It is real analytic if, in addition, the coordinate functions agrees with their Taylor series in a neighbourhood at every point.

produces infinitely many prongs on its medial axis. It medial axis is not a finite graph.

The *grassfire* interpretation of the MS construction makes clear links between the MS and wave propagation: The MS construction can be interpreted as the search for weak solutions of the Hamilton-Jacobi equation with constant propagation velocity 1. See for example the first chapters in Sethian's book [191].

Many papers address the issue of sensitivity of the MS to small changes of the skin S. Choi *et al.* [31, 30] quantify this instability in terms of Hausdorff distance measures. The Hausdorff distance is defined for two compact and non-empty sets D_1 and D_2 in $\mathbb{E}^n$. For any point in D_1 the distance to the nearest point in D_2 is determined, and vice versa. The Hausdorff distance between the two sets is the maximum of these distances over all points of D_1 and D_2. Small difference in Hausdorff distance between two domains does not guarantee small differences between the respective MS. In [31] they introduce the hyperbolic Hausdorff distance, i.e. the point to point distance for MS points is the Euclidean distance reduced by the difference in radius between the two maximal spheres. They show that the hyperbolic Hausdorff distance between two medial surfaces is small if the conventional Hausdorff distance between the two corresponding domains is small.

This instability is an obvious problem for pattern recognition and shape description applications of the MS, as small irrelevant features generate dominant MS features. Shaked and Bruckstein [192], among others, have suggested pruning schemes to eliminate non-essential parts of the MS. Giblin and Kimia [77] analyse the transition between medial surfaces under perturbation of the domain. In particular, they relate these transitions to the classification of *perestroikas* (transitions) of the viscosity solutions of the Hamilton-Jacobi equation by Bogaevsky [20].

The MS bears a noteworthy relation to the so-called Euclidean distance map. The Euclidean distance map assigns a distance D to every point q in a domain C that is the length of the shortest path from q to a point on $S = \partial C$. The gradient of the field D is $\nabla D(q) = N(p)$ (where p is the nearest contact point) everywhere apart from points q on the MS where D has a singularity.

2.3   **Voronoi diagrams and algorithms**

Some basic concepts from discrete geometry are essential to further discussion of the MS. This section gives a brief definition of the *Voronoi diagram* of a set of points, and of its dual structure, the *Delaunay triangulation*. The computational complexity of the Delaunay triangulation is described as it is the same as the complexity of the MS.
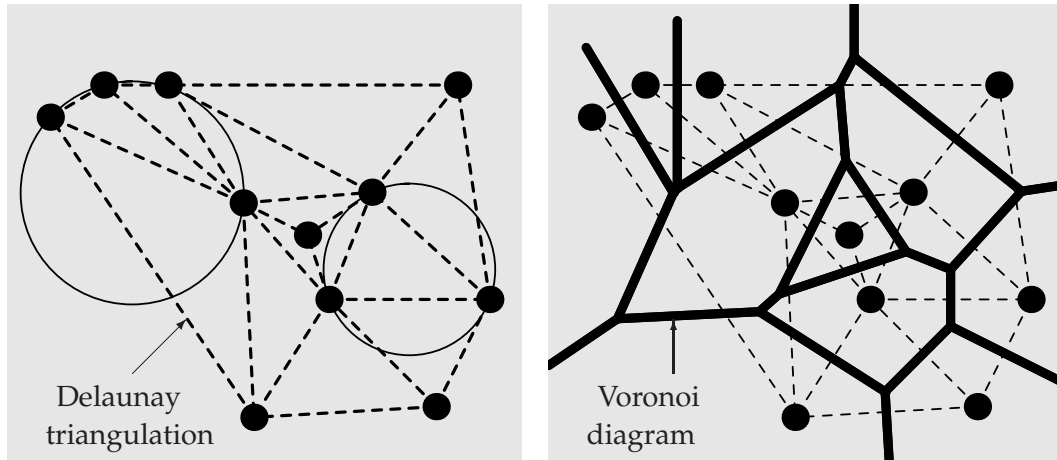
Figure 2.3: Delaunay triangulation and Voronoi diagram of a set of points V in the plane. The dashed lines are edges of the Delaunay triangulation of the set of points, and thick black lines are the boundaries of the Voronoi cells. The vertices of the Voronoi diagram are the centers of the circumscribing spheres of the Delaunay triangles (Delaunay circles). The Delaunay circles are devoid of other point of V. However, *geometric degeneracies* with four or more points on a single Delaunay circle may occur, e.g. the left circle. These lead to Voronoi vertices with four or more emanating edges.

Let $V = \{(x, y, z)\}$ be a set of points in $\mathbb{E}^3$. In keeping with the usual definition, we define the Voronoi diagram to be the division of space with respect to V into n convex cells $C_V(p) \subset \mathbb{E}^3$ such that for any point $p \in V$ any point $q \in C_V(p)$ is closer to p than to any other point $p' \in V$ where n is the number of vertices in V (see Fig. 2.3).

The first comprehensive account of the concept of Voronoi diagrams were given by Dirichlet [46] and Voronoï [214].[5] It has since been the subject of intense study and research in many branches of fundamental and applied sciences. A huge body of literature on Voronoi diagrams exist; comprehensive accounts are e.g. refs. [10, 162, 71, 49, 220].

From the Voronoi diagram of the points in V, a dual structure called the Delaunay triangulation (or tesselation) is obtained: any two points p_1 and p_2 in V are connected by an edge if their Voronoi cells $C_V(p_1)$ and $C_V(p_2)$ have a common face in the Voronoi diagram of V.

The Delaunay triangulation has several strong properties:
(1) It defines a tesselation of space[6] into convex polyhedra with respect to the point

---

[5]However, as early as 1644 Descartes published diagrams that ressemble Voronoi diagrams. He applied them in his analysis of the distribution of matter in the universe. For more details, see the chapter on the history of the Voronoi diagram in [162].

[6]More precisely, it tesselates the *convex hull* of the set of points V. The convex hull of a set of points

set V. We can even assume that these polyhedra are simplices [7]. These simplices are called Delaunay simplices.

(2) The circumspheres of all Delaunay simplices are empty (of points of V).

(3) By definition, the Voronoi diagram and the Delaunay triangulation are dual to each other.

Algorithms for the Delaunay triangulation and the Voronoi diagram

Many algorithms that compute the Voronoi diagram first determine the Delaunay triangulation and then use the duality between the two structures to compute the Voronoi diagram. Algorithms to compute Delaunay triangulations are numerous (see the bibliographies in the above mentioned surveys). One that is commonly used is the randomised incremental flip algorithm, developed in [129, 107, 108, 172, 51] and described e.g. in [154]:

This algorithm incrementally builds up a Delaunay triangulation, starting from the trivial triangulation $\mathcal{T}$ of four of the vertices in V that is trivially a Delaunay triangulation. Repeatedly, another point from the set V is added to $\mathcal{T}$, such that $\mathcal{T}$ remains a triangulation, though, in general not a Delaunay triangulation.[8] Through a number of flips (the 3D equivalent of flipping the diagonal in a convex planar four-gon) $\mathcal{T}$ is then transformed into a Delaunay triangulation. This is repeated until all points in V are added.

An inherent problem for Delaunay triangulation algorithms is robustness: In order to check if a triangulation $\mathcal{T}$ is (locally) Delaunay a so-called *insphere test (or predicate)* is invoked, to decide if a point p lies outside, on or inside the circumscribing sphere of a simplex S_1. This test is a crucial component of all Delaunay triangulation algorithms.

The insphere test is inherently numerically unstable if p is near the surface of the sphere, see e.g. [197]. A number of schemes have been suggested to circumvent this problem, among them the use of robust adaptive floating-point predicates [196], symbolic pertubation schemes [154] and exact integer arithmetic schemes [32].

Incorrect incircle and orientation predicates may not only produce a triangulation that is not a Delaunay triangulation, but can also generate a result that is not even combinatorially a triangulation (see [196, 197] for an illustrative example).

$\overline{V} \in \mathbb{E}^d$ is the smallest (inclusionwise) convex subset of $\mathbb{E}^d$ containing V, see for example [82].

[7]A simplex is a polyhedra with four vertices, a topological tetrahedra. The assumption that the polyhedra are simplices is violated if any of the Delaunay spheres has more than four of the points in V on its surface. However, even in this case the non-simplicial polyhedra can be split up into simplices, for details see e.g. [162].

[8]Note that this step requires a point-location scheme

Complexity of Delaunay triangulation, Voronoi diagram and Medial Surface

The computational complexity of the MS algorithms discussed in this thesis is given by the complexity of the Voronoi diagram. Once the Voronoi diagram is computed, all other steps are local operations and computationally inexpensive. We therefore now discuss the complexity of the Voronoi diagram and Delaunay triangulation, in particular the case where the point set is a set of sample points of a manifold in $\mathbb{E}^3$.

The worst-case time complexity of the Delaunay triangulation in 3D is $\mathcal{O}(n^2)$ where n is the number of points. The randomised incremental flip algorithm is optimal for the worst case. However, typical run-times are much faster, and the worst case is generally only reached for specific examples, for example for equidistant points on two skew lines. The expected time is often proportional to the final number of simplices in the Delaunay triangulation.

For point sets V that are sample points on a surface recent articles suggest improved worst-case bounds: In particular, imposing a mild sampling condition for a set of sample points on a generic[9] surface in $\mathbb{E}^3$, it can be shown that the complexity of the Delaunay triangulation is $\mathcal{O}(n \log n)$ [8]. If the points are randomly and uniformly distributed on a convex polytope the complexity is even $\mathcal{O}(n)$ [80]. For a cylinder, though, it has been shown that even a "nice point set" may have $\mathcal{O}(n \sqrt{n})$ complexity [55]. The bottle neck to further improvement beyond the logarithmic behaviour is the point location scheme; a biased randomised insertion order "which removes enough randomness to significantly improve performance, but leaves enough randomness so that the algorithm remains theoretically optimal" has been suggested [4].

Robust and efficient implementations of randomised incremental algorithms for Delaunay triangulations for $\mathbb{R}^3$ are available, including Clarkson's *hull*[10], the CGAL Delaunay hierarchy[11], Shewchuk's *pyramid*[12] and the α-shape software of Edelsbrunner et al.[13]

---

[9]A surface is generic if "roughly, the ridges, i.e. the points of the surface where one of the principal curvatures is locally maximal, is a finite set of curves whose total length is bounded. In particular, spheres and cylinders are excluded." [8]

[10]http://cm.bell-labs.com/netlib/voronoi/hull.html

[11]http://www.cgal.org

[12]as yet unpublished

[13]ftp://ftp.ncsa.uiuc.edu/Visualization/Alpha-shape/

2.4   Voronoi based medial surface algorithms

The representation of a domain most suitable for the problems addressed in this thesis is a *triangulation* of the boundary surface. A *triangulation*[14] of S consists in a set of points $V = \{(x, y, z) \in S\}$ and a set T of oriented triangles whose vertices are the points in V. The coordinates x, y and z are floating-point numbers.

This representation is natural for surface data derived from mathematical parametrisations (such as the Weierstrass form of chapter 4), or for data collected from e.g. laser range scanners.

This section describes the general idea common to all those MS algorithms for triangulated representations of a domain. Such algorithms are based on analyses of the 3D Voronoi diagram of the vertices of the triangulation.

The loose idea behind all Voronoi-based MS algorithms is that the Voronoi cells of a dense set of sample points on a surface are long, thin and roughly in direction of the surface normal, and reaching as far into the void as possible. Therefore, some parts of each Voronoi cell – either vertices, edges, faces or points on them – have to lie on the MS. See Fig. 2.4 for an illustration.

Early suggestions to use subsets of the Voronoi diagram were made by Attali and Montanvert [9] and Sheehy *et al.* [193]. Even earlier, but incorrectly, Goldack *et al.* [79] argued that the (complete) set of Voronoi vertices converges to the MS with increasing sampling density. Amenta *et al.* [2, 3] and Boissonnat and Cazal [21] eventually established that a certain subset of the Voronoi vertices, the maximally distant *poles*, converges to the MS in the dense sampling limit. Dey and Zhao [42] discern the faces, rather than the vertices, of the Voronoi diagram that converge to the MS.

The situation in 3D is fundamentally different from the planar case. In the planar case, all Delaunay circles converge to maximal circles with increasing sampling density on the domain boundary S, see Figs. 2.4 and 2.5. Hence, the complete set of Voronoi vertices (the centers of the Delaunay circles) converges to the MS. In 2D and in the limit of dense sampling, a Delaunay sphere is not an approximation of a maximal sphere only if S is not well sampled.

In 3D, Voronoi vertices may lie arbitrarily close to S – and thus far from MS – even in the limit of dense sampling. The reason is simple: The radius of a circle defined by three neighbouring points on a well-sampled 2D polygon is approximately the radius of curvature. i.e. the radius of the osculating circle. The radius of the sphere defined

---

[14]Note the differences between the use of the word in this context and in the context of Delaunay triangulations: A Delaunay triangulation tesselates $\mathbb{E}^3$ into tetrahedra (the 3D equivalent of triangles). Here a triangulation tesselates a two dimensional surface by triangles.

"triangulated" boundary

Delaunay sphere

badly sampled

Voronoi edge
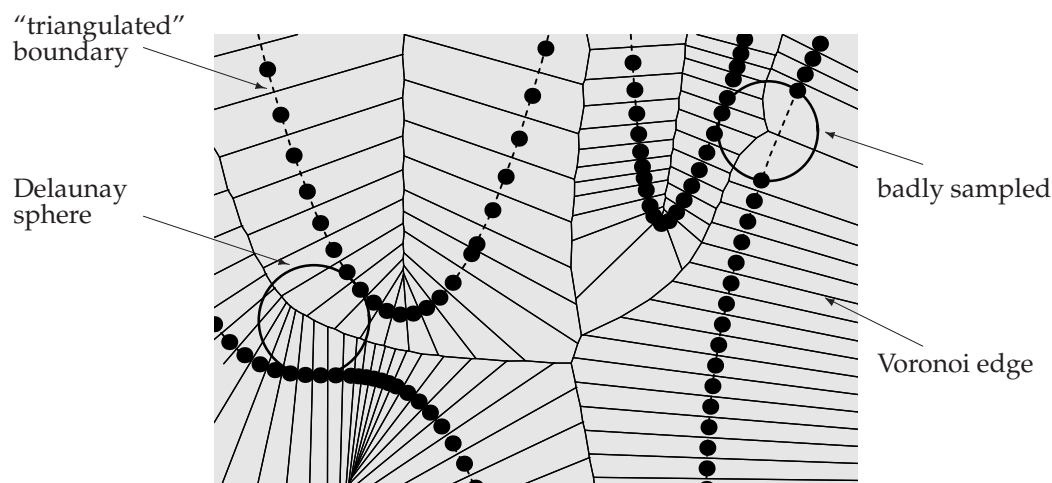
Figure 2.4: Voronoi diagram of a set of points in 2D that represent a (relatively good) sample of a curve S in the plane. The Voronoi cells are mostly thin and long and roughly in normal direction of S. Upon increase of the sampling density the cells narrow further. Delaunay circles are good approximations of maximal disks provided the sampling of S is sufficient.
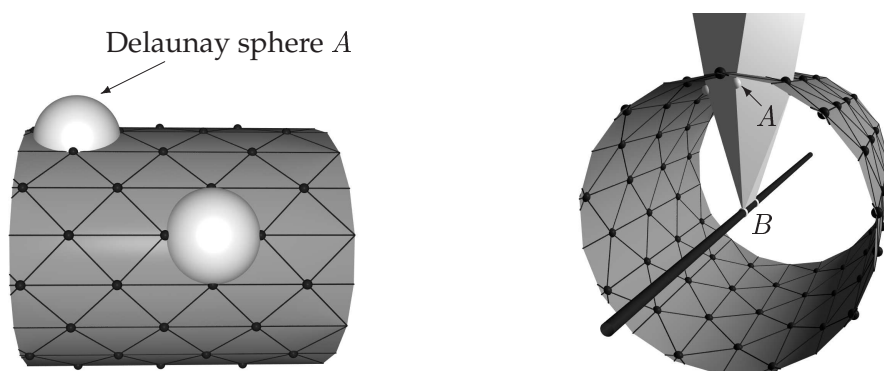
Delaunay sphere A

Figure 2.5: Failure of the Delaunay spheres to converge to maximal spheres in 3D: The centers of some Delaunay spheres (A) of the Delaunay triangulation of the vertices of this cylinder triangulation lie close to the cylinder surface itself. Even upon refinement of the triangulation their centers remain at the same distance from the cylinder surface. These spheres sit "in between four neighbouring vertices of the triangulation". However, for each surface vertex some of the Voronoi vertices (small white spheres in the right image) of its Voronoi cell – which are the centers of Delaunay spheres – are far from the surface and, in the dense sampling limit, good approximations to the MS point (B).

by four neighbouring[15] points on a well-sampled surface in 3D is not bounded from below by curvature properties of the surface. The sphere is not necessarily osculating[16] to the surface, its center can be closer to the surface than even the smaller one of the two radii of curvature. In fact, the sphere center can lie on the surface – for example when the four vertices form a nearly flat square within the triangulation.

However, Amenta *et al.* [2, 3] and Boissonnat and Cazal [21] established that, even in 3D, a subset of the Voronoi vertices lies near the MS. For every surface point $p \in S$ they define the *pole* as the Voronoi vertex q_p of the Voronoi cell $C_V(p)$ in normal hemisphere[17] from p that maximises the distance to p. They show that this subset converges to the MS if the sample is a good sample:

Amenta *et al.* introduce the notion of an r-sample. The vertices V of a triangulation of S are an r-sample if the distance from any point $p \in S$ to its closest sample in V is at most a constant fraction r times the MS distance function value $d(p)$. In this context they call $d(p)$ the local feature size (LFS).
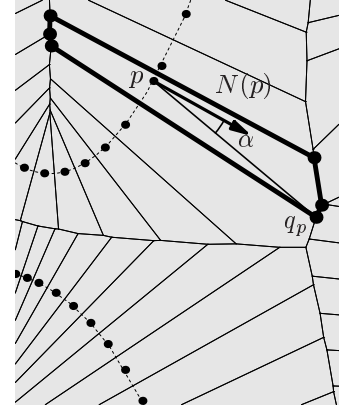
Figure 2.6: The *pole vertex*

With this notation they prove that the set of poles converges to the MS with decreasing value of r: They show that the polar balls, i.e. the Delaunay spheres of the poles, have shallow intersection with S. They also show that the direction of the vector from a vertex $p \in S$ to its pole approaches $N(p)$ in the limit of small r. In the subsequent sections we will refer to Amenta's analysis to guarantee the convergence of our construction of the MS.

2.5 MS of labyrinthine structures

This thesis is particularly concerned with the generation of skeletons of labyrinthine structures. These are, by definition, not closed in $\mathbb{E}^3$, but have open ends. This situation is in contrast to those commonly discussed in the computational geometry com-

---

[15]For two points on S to be neighbouring it is neither sufficient nor necessary that they are connected by an edge of the triangulation – as the topology of the triangulation may be uneven. Loosely, two points are neighbouring if they are connected by a Delaunay edge that is more or less perpendicular to the surface normal. See the definition of umbrella in [42] for details.

[16]For a point p on a surface in 3D, an osculating sphere is a sphere centered in positive (negative) normal direction at a distance equal to the smaller of the positive (negative) radii of curvature of the surface at p.

[17]I.e. $\langle (q_p - p), N(p) \rangle > 0$ where $\langle ., . \rangle$ denotes scalar product in $\mathbb{E}^3$.
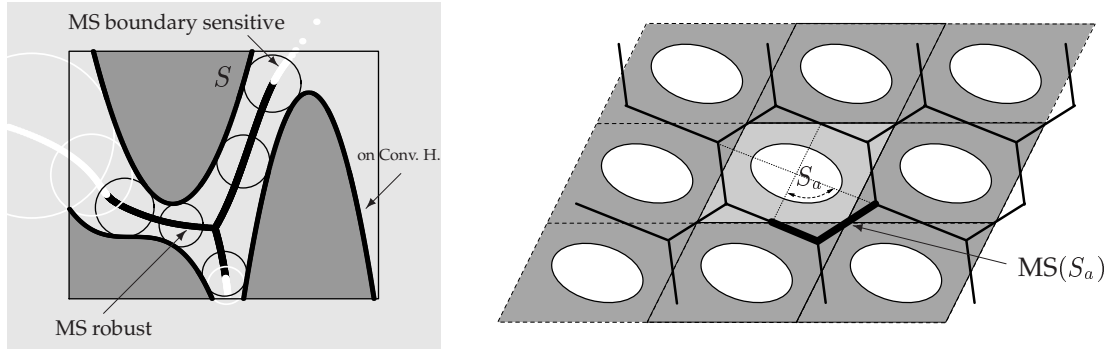
Figure 2.7: (Left) MS computation of a finite open portion of a labyrinthine structure. The skin S of a domain within a rectangular box is given (black interface between light and dark gray). The MS is computed as the complete set of Voronoi vertices. White maximal circles do overlap with the bounding box, and are hence subject to how S is continued beyond the bounding box, whereas black ones do not. Note that points of S on the convex hull of S have no corresponding Voronoi vertices. (Right) A periodic labyrinth: The domain, gray, is the complement of a periodic arrangement of ellipses. Its translational unit is marked by the slightly lighter color, and its asymmetric unit patch S_a by the curved arrow. For computation of the MS of S_a an array of 3^d translational unit cells is sufficient, albeit often too large.[19]

munity where the typical domain is a solid, and hence the boundary surface a closed manifold in $\mathbb{E}^3$.

In the case of a labyrinth structure D (with skin S) with open channel ends, a meaningful definition of the MS may be restricted to an interior subset D' of D. The reason is that the MS points of points on S near the open channel ends may be influenced by the boundary of S.

The typical situation is the following, illustrated in Fig. 2.7 (left): A domain D representing a labyrinth structure is assumed to be infinite throughout space, but only a subset S' of it is known. S' is contained in a rectangular bounding box B. We further assume that $S' = S \cup B$, i.e. it is the maximal subset of S contained in B.

Any MS computation on S' yields a MS with parts that are influenced by the boundary. These parts have the property that the corresponding maximal spheres (or disks) overlap with the bounding box B. If there is no overlap the continuation of S outside of B cannot make a difference to the maximal sphere. Those parts of the MS are hence *robust*.[20]

In the special case of periodic labyrinth structures one has – by virtue of the possibility

---

[19]The MS is hand-drawn in this illustration, not incorporating the slight bend of its edges. However, deviations from linearity are approximately of the size of the line thickness.

[20]This criterion is obviously the same as for the Delaunay triangulation of a subset S' of a larger point set S. It has been previously described in [41].

of translation – a choice of the size of the bounding box. The question then is what the smallest subset S' to yield the correct MS of the asymmetric unit patch[21] S_{asy} of S is. Fig. 2.7 (right) illustrates the situation.

The maximal size of S' to yield a correct MS of S_{asy} has been shown to be an array of $3 \times 3 \times 3$ (in 3D, or 3×3 in 2D) translational unit cells. This follows from a result in [149] about the corresponding situation for the Voronoi diagram.

However, it is often possible to restrict oneself to a smaller subset. In particular, if the maximal distance function value is known a sufficient subset S' are those sample points of S that are contained within the spheres of $2\,d(p)$ around all points p of S_{asy}. Application of this criterion reduces the size of the sample point set – crucial for densely sampled, large data sets with computationally expensive Voronoi tessellations.

2.6   Voronoi-based MS for exact surface data

This section describes our algorithm to compute the MS of an exact triangulated domain in 3D by analysis of the Voronoi diagram of the sample points V of the triangulation of S. It works well for exact surface data, i.e. that the points V of the triangulation are points of S without any noise and that exact surface normals can be computed for these points. It is based on previous ideas, in particular Amenta's work. The contribution of this thesis is an adaption that improves the algorithm for the case of exact representations of the surface, such as mathematical parametrisations. It is summarised by the following statement:

> Every point p of the triangulation of S has a corresponding MS point q that lies in normal direction from p. We demand that q is closer to p than to any other surface vertex, but also as distant from p as possible. Therefore, q must lie on the boundary of the Voronoi cell of p. We deduce that q has to be at the intersection of the straight line in normal direction through p with the Voronoi cell of p.

The process is illustrated in Fig. 2.8 (2D) and Fig. 2.9 (3D).

Let S' be a surface sampled by the set of points $V' = \{x, y, z) \in S'\}$ such that the subset S whose MS shall be computed is embedded in S'. S is sampled by a set of points $V = \{(x, y, z) \in S\}$ together with a set T of oriented triangles whose vertices are the points in V. Normal vectors $N(p)$ for all points $p \in V$ are known, and are assumed to point into the domain C.

---

[21]or the translational unit cell if there are not any additional symmetries
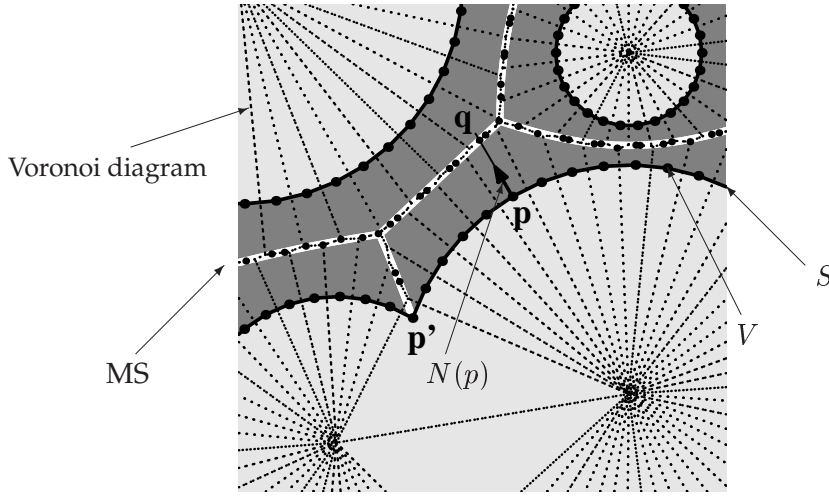
Figure 2.8: (Left) Illustration of our MS algorithm in 2D: The domain C (dark gray) is the complement of an assembly of overlapping disks (light gray). The boundary $S = \partial C$ of the domain is discretised into vertices V (black points) connected by edges. The interface normal vectors are pointing into C. The first step is the computation of the Voronoi diagram of the set of vertices V (dashed lines). For every point $p \in V$ there is a corresponding point q on the medial surface which is the intersection of the straight line in normal direction through p with the Voronoi cell of p (the black points on the white line), unless p is at a cusp of S. If p is at a concave cusp of S (as is the vertex p'), then $ms(p) = p$. The white line is the exact medial axis, for which an analytic form is known in the case of disk assemblies [138, 153].

The sampling of S' coincides with the sample points of S for all points on S. S' is assumed to be so large that the boundaries of S' have no influence on the MS of S. For the periodic surface discussed in the next chapter, S is typically an asymmetric unit patch or a translational unit cell and S' a $3 \times 3 \times 3$ array of translational unit cells surrounding S.

The points p and normals $N(p)$ are assumed to be accurate, e.g. from a mathematical parametrisation of S where any inaccuracy stems from rounding errors only. We assume that the sampling density is sufficiently high.

Fig. 2.10 (top) gives a pseudocode description of the algorithm.

In fact, computation of the actual Voronoi cells can be avoided. For any point $p \in S$, one may intersect the planes that are perpendicular bisector of all Delaunay edges emanating from p with the ray through p in surface normal direction $N(p)$. An intersection that is closest to p exists (because of the convex properties of the Voronoi cells) and is exactly the same point obtained by intersection of the normal with the Voronoi cell $C_V(p)$. The Voronoi facets of $C_V(p)$ are, of course, subsets of the bisector planes. Fig. 2.10 (bottom) gives a pseudocode description of this algorithm.
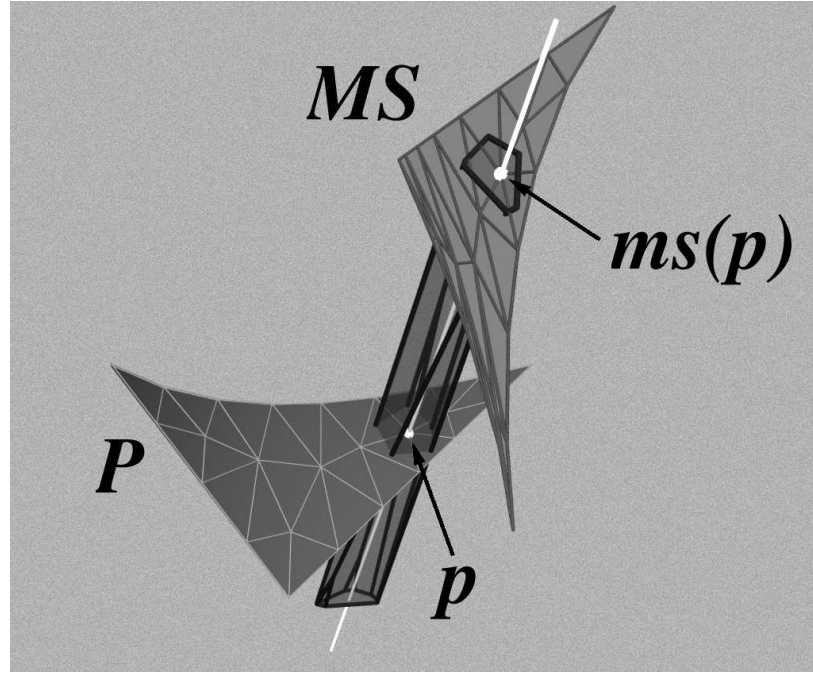
Figure 2.9: The $3D$ case: A small patch P of the boundary $S = \partial C$ of a domain C is shown (the lower surface patch) together with its triangulation. Also shown is the Voronoi cell of a vertex p (marked by a small white point on the surface inside the cell) of the triangulation which is an elongated, convex polyhedron oriented along the surface normal direction (bounded by thick black lines, joined by opaque faces). The white line is the straight line in normal direction through p, which intersects the Voronoi cell of p at $ms(p)$ (white point). The surface patch in the top part of the image is the MS patch corresponding to P and its triangulation is inherited from P. Note that for the computation of the Voronoi diagram as a global property of C, a much larger fraction of S is needed than the patch shown.

The MS points produced by this algorithm are approximations that in the limit of perfect sampling converge to the true MS of C. This is guaranteed by Amenta's proofs, as our algorithm yields the same points as her algorithm in the dense sampling limit ($r \to 0$ in her notation of r-samples).

Our algorithm yields a better triangulation of the MS (inherited from the triangulation of S) than that of $ms(p)$ approximated by the pole vertex, since quasi-degeneracy of pole distances can lead to overlapping MS triangles.[22] Consider, for an example, the hexagonal Voronoi cells of a set of parallel planes triangulated by congruent equilateral triangles (Fig. 2.11).

Our triangulation avoids this problem. However, on the free boundaries of the MS – where MS points correspond to centers of curvature – our approach may generate

---

[22] We note that Amenta *et al.* are not suggesting to use this trivial triangulation on the set of poles.

```
Algorithm MS Points of Exact Surfaces (Voronoi cells)
   Initialise large set of surface points V' ∈ S'
   Initialise small subset of surface points V
   Initialise normals of points in V

   Compute Delaunay triangulation of V'

   Forall points p ∈ V do
      Compute Voronoi cell C_V(p)
      NormalRay := ray from p in direction N(p)
      MSPoint := intersection NormalRay with C_V(p)
   Infer triangulation of MS from triangulation of S
```

```
Algorithm MS Points of Exact Surfaces (Voronoi planes)
   Initialise large set of surface points V' ∈ S'
   Initialise small subset of surface points V
   Initialise normals of points in V

   Compute Delaunay triangulation of V'

   Forall points p ∈ V do
      MinDist = ∞, MSPoint = ∅
      Forall Delaunay edges (p, p_1) with p_1 ∈ V' do
         VoronoiPlane := perpendicular bisector plane of (p, p_1)
         NormalRay := ray from p in direction N(p)
         q = Intersection of VoronoiPlane and NormalRay if exists
         if Intersection exists and d(p, q) < MinDist do
            MinDist = d(p, q)
            MSPoint = q
   Infer triangulation of MS from triangulation of S
```

Figure 2.10: Pseudocode for MS calculation of exact surface representations that avoids the actual computation of Voronoi cells

triangles that, nearly or completely, degenerate to a line. Errors in these areas are more likely, as the direction of the MS normals changes by π.

It is important to note that the MS as computed here is in fact a double cover of the MS. Every point on the MS corresponds strictly to one sample point on the surface. Turning this double cover into a single cover of the MS is not easy to do, but it also is not what this algorithm aims to do.

In summary, this section has described an MS algorithm that allows for accurate MS computations of surfaces for which mathematical parametrisations are available. In that case, without noise in position or normals of the surface points, this algorithm yields superior MS approximations to previously presented algorithms. It yields a one-to-one correspondence of points on the skin S and points on the MS, and the
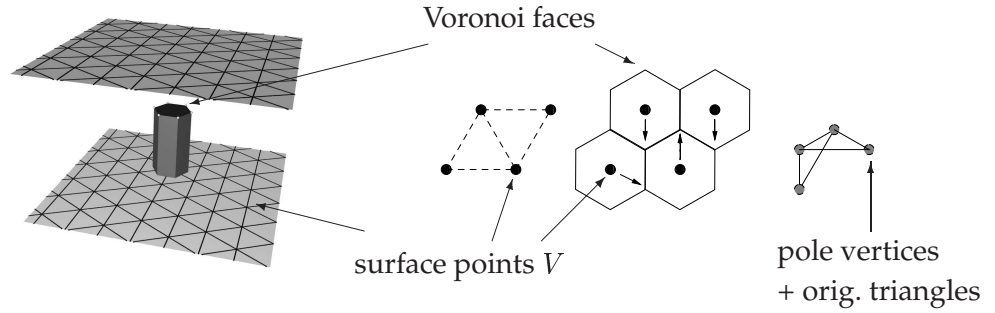
Figure 2.11: A problem when inferring the triangulation from the original surface to the set of poles: (Left) the Voronoi cells of the vertices of two parallel planes (triangulated by congruent equilateral triangles) are hexagonal cylinders. The distance from a surface vertex to all of the six Voronoi vertices – in each normal direction – is the same, i.e. the choice of the pole is arbitrary. (right) two non-overlapping triangles of the original surface (top) can induce two overlapping triangles on the medial surface (bottom) due to a bad mapping from the surface vertices to the poles. This scenario is not a pure artifact of the high degeneracy in this case. The algorithm presented here largely avoids this problem.

triangulation of S also provides a well-behaved triangulation of the MS. All results on issues relating to IPMS in this thesis are obtained with this algorithm.

2.6.1   Analysis of the numerical robustness

We conclude this section with a discussion of the numerical robustness of our algorithm. Note that this is a different issue from the geometric convergence problem dealt with by Amenta *et al.* and described earlier.

Here, we estimate for the two-dimensional situation: (1) the precision of the center of curvature approximation by intersecting local Voronoi cells with straight lines in normal direction, and (2) the influence of imprecision of the normal vector in this case. We then argue that the MS construction is most fragile in the situation where MS vertices correspond to centers of curvature. Therefore, the error analysis for the center of curvature approximation gives an upper bound on the error of the MS construction. Finally, an argument is presented mapping the $3D$ case onto $2D$, thus allowing an estimate of the robustness of the MS algorithm.

We first establish the precision of the approximation of the center of curvature by intersections of local Voronoi cells with straight lines in normal direction. Consider a cell $C \subset \mathbb{E}^2$ whose boundary is given by a unit-speed curve $\alpha : [-a, b] \to \mathbb{E}^2$, together with its normal field N $(a, b > 0)$. The real valued function $\kappa : [-a, b] \to \mathbb{R}$ measures

the curvature of α. Also given is a discretisation

$$\{\alpha(t_i) \mid -a = t_{-k} < \dots t_{-1} < 0 = t_0 < t_1 < \dots < t_{n-k} = b\}$$

of the boundary α, see Fig. 2.12.

The *local* Voronoi cell $V(0)$ of the three vertices $\alpha(t_{-1})$, $\alpha(0)$ and $\alpha(t_1)$ is bounded by the two perpendicular bisectors

$$b_i(s) = \alpha(0) + \frac{\alpha(t_i) - \alpha(0)}{2} + s\, J\left(\frac{\alpha(t_i) - \alpha(0)}{2}\right) \tag{2.3}$$

where J denotes the counter-clockwise rotation in $\mathbb{E}^2$, $i \in \{-1, 1\}$ and s is a real parameter defining the position on the bisector.

We now determine how well the intersection of the straight line through $\alpha(0)$ in normal direction $N(0)$ with the local Voronoi cell $V(0)$ approximates the center of curvature $\alpha(0) + 1/\kappa(0)\, N(0)$ in the case of positive curvature at $t_0 = 0$. To this end we expand α in curvature terms at $t_0 = 0$.

Assuming sufficient smoothness and applying the Frenet formulae, a curve α can be expanded in terms of its curvature at $t_0 = 0$:

$$
\begin{aligned}
\alpha(t) = \alpha(0) + \quad & T(0) \quad \left(t - \frac{\kappa(0))^2}{6}t^3 + \mathcal{O}(t^4)\right) \\
+ \quad & N(0) \quad \left(\frac{\kappa(0)}{2}t^2 + \frac{\kappa'(0)}{6}t^3 + \mathcal{O}(t^4)\right)
\end{aligned}
\tag{2.4}
$$

Substituting the curvature expansion, eq. 2.4, into the representation of the bisector, eq. 2.3, and determining the intersection q of the bisector with the straight line in normal direction through $\alpha(0)$ one obtains

$$r_i = \frac{1}{\kappa(0)}\left(1 - \frac{\kappa'(0)}{3\kappa(0)}t_i + \mathcal{O}(t_i^2)\right) \tag{2.5}$$

for the distance $r_i = \|q_i - \alpha(0)\|$ between $\alpha(0)$ and the intersection q of the straight line in normal direction through $\alpha(0)$ with b_i.

The smaller of the two values r_{-1} and r_1 defines the radius of curvature at t_0 by the Voronoi intersection method. No distinction between the two values can be made by general consideration. Equation 2.5 represents the general precision for the approximation of the radius of curvature by intersecting straight lines in normal direction with the local Voronoi cell.

We now analyse the effect of uncertainty in the normal $N(0)$ on the position of the
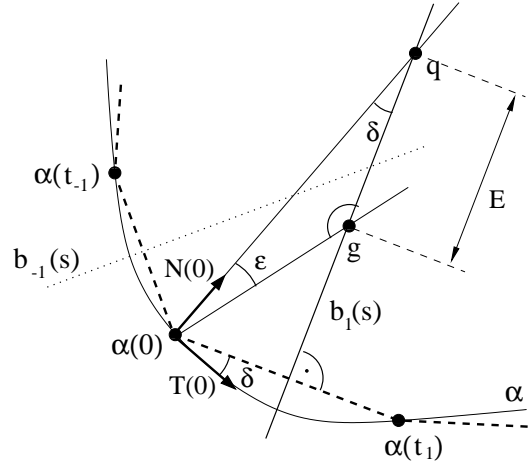
Figure 2.12: Sketch of the $2D$ precision analysis. See text for details. Note that the discretisation in this case is a particularly bad approximation of the center of curvature, as the curvature properties of the edges (t_0, t_1) and (t_{-1}, t_0) are quite different from each other.

computed center of curvature g. Assume that the normal vector $N(0)$ is only known within an angular tolerance of $\pm\epsilon$, see Fig. 2.12. The estimate for the center of curvature deviate by a distance $E = \|q - g\|$ from the previously computed center of curvature q.

Consider the situation as shown in Fig. 2.12: δ denotes the *turning angle*, i.e. the angle between the vector $\alpha(t_1) - \alpha(0)$ and the tangent $T(0)$ at $\alpha(0)$. This angle is the same as the angle formed by the straight line in normal direction through $\alpha(0)$ and the bisector $b_1(s)$. The angle δ is a simple integral of the curvature [83], and is given by

$$\delta = \int_0^{t_1} \kappa(t)dt = \kappa(0)\, t\, \left(1 + \frac{\kappa'(0)}{2\kappa(0)}\, t + \mathcal{O}(t^2)\right). \tag{2.6}$$

The distance $E = \|q - g\|$ is then related to the angles δ and ϵ and the computed radius of curvature $r_1 = \|q - \alpha(0)\|$ by

$$\frac{E}{r_1} = \frac{\sin \epsilon}{\sin(\pi - \delta - \epsilon)} \approx \frac{\epsilon}{\delta} \approx \frac{\epsilon}{\kappa(0)\, t}. \tag{2.7}$$

The approximation is valid if ϵ/δ, ϵ and δ are small.

For the approximation of the center of curvature by intersecting local Voronoi cells with straight lines in normal direction in $2D$ we conclude:
(a) The approximation converges, and the error is linear in the quality of the discretisation, measured in terms of κ'/κ.

(b) Imprecision of the curve normals leads to an error which is of the order of the maximal error in the normal angle compared to the turning angle per edge. If the error in normal angle is purely due to limited numerical precision whereas the turning angle remains small but finite, the error in the curvature center estimate is small. Discretising almost flat parts of the curve with short edges leads to problems.

Medial surface points coincident with centers of curvatures (analysed in this appendix) lead to the largest uncertainty. As is clear from Fig. 2.12, uncertainty in normal directions is most significant in this case. The precision analysis presented here therefore represents an upper estimate for the errors.

The results described above are almost immediately applicable to the $3D$ case: For a given vertex $p \in S$, one now has to identify all n nearest neighbours $\{p_i \in S\}$ of p. Nearest neighbours in this context means all vertices $p \in V$ which are connected by an edge of the Delaunay triangulation to p and are close to p as measured along a path on S.

For each nearest-neighbour p_i, one intersects the straight line in normal direction through p with the perpendicular bisector between p and p_i (which is in this case a plane containing the corresponding Voronoi facet). Again, the local Voronoi cell is defined as the set of perpendicular bisectors between p and all neighbouring points.

We define a planar curve α to be a unit speed curve lying within the intersection of S with a plane containing the surface normal $N(p)$, the point p and the point p_i. We define T_α as the tangent to α in p. The curvature of α at the point p is then (up to a sign change) the normal curvature $\mathbf{K}_p(T_\alpha)$ of S in the direction of T_α, see Corollary 16.8 in [83]. Thus, the $2D$ analysis above is equally applicable to the approximation of $\mathbf{K}_p(T_\alpha)$.

Intersecting all n nearest-neighbour Voronoi facets yields an approximation to the smallest of the positive radii of curvature (which is the relevant one for MS purposes). The quality of this approximation is then related to the curvature properties of curves $\alpha \subset S$ by the above $2D$ curvature analysis (We neglect effects of the neighbour vertices not sampling every direction from p).

The analysis presented here shows that our algorithm is robust for surface data with only minor imprecision in point and normal coordinates. The susceptibility to noise arises from the intersection of the long and thin Voronoi cells with the straight lines in normal direction. We mention that an MS approximation using the poles does not show this sensitivity.

2.7   Other MS algorithms and domain representations

Other algorithms for the computation of the MS and related line skeletons exist. Also a different representation of a domain, as a binary 3D data set, is commonly used. This section provides a brief overview of these alternatives. Common skeletonisation procedures for the computation of centered line graphs and skeletons are described in chapter 3.

Computations of MS that determine the locus of singularities of the weak solutions of Hamilton-Jacobi PDEs modeling wave-propagation exist, see e.g. [115, 81].

A different representation for the domain is via discrete binary 3D images or arrays, called *voxelised representations* (A *voxel* is the 3D equivalent of a 2D pixel). Space is subdivided into cubic voxel lattice, and each voxel is assigned either 0 or 1. The voxels at the interface between 0 and 1 then represent the surface.

Computation of medial surfaces for voxelised data sets is difficult. This is an immediate consequence of the conceptual sensitivities of the MS to the shape of the domain, in particular to the normal direction of the boundary surface S. In voxelised space, normal directions are evidently rational directions (as vector components are integers) and discretised. Further, even the notion of a sphere in voxel space presents some ambiguity.

For this representation MS algorithms based on thinning (or burning) ideas have been suggested [130, 75]. Wave-propagation ideas and cellular automata have been used [68]. An approach based on Chamfer distances is given in [173]. Another idea based on distance fields is presented in [22].

MS computation of polyhedral structures, where corners and edges are explicit features of the object rather than artefacts due to the discretisation, have been demonstrated [35].

Line graphs on the medial surface

The MS lies centered within the channels of a labyrinth, somehow reminiscent of a graph model of the labyrinth. Yet, it is a set of 2D surface patches. This chapter discusses the reduction of the MS to a true line graph consisting of 1D space curves and retaining as much of the geometry as a line graph can.

> The concept of skeletal graphs appears to be a useful one. It provides a picturesque model of both the symmetry and the connectedness [...].
> (A. Schoen, 1970)

This comment, by Alan Schoen, refers to skeletal graphs of infinite periodic minimal surfaces, i.e. symmetric structures of clearly labyrinthine character with constant vanishing mean curvature. By *skeletal graph* he means a network of (presumably straight) line segments meeting in nodes of connectedness of at least three and contained in the labyrinthine regions.[1]

This chapter gives a more rigorous definition for a line skeleton of a labyrinthine domain than Schoen's. It demonstrates that, for the case of strictly hyperbolic labyrinths such as IPMS, the so-defined line graph is indeed useful and describes both the geometry and the topology correctly. However, we also show that there are labyrinthine domains for which no definition of a line skeleton can simultaneously capture correctly the topology and geometry of the domain.

Our definition of a line skeleton puts emphasis on the fact that its edges – that are not necessarily straight lines – are geometrically centered in the channels of the labyrinths.

---

[1]With this, somewhat lax definition, he realises that "it is not true that the topological structure of a given IPMS implies the existence of a unique pair of dual skeletal graphs for that surface, unless it is stipulated that the two skeletal graphs of an IPMS have the same space group as the IPMS". His particular attention was on some notion of duality between the two graphs of the two separate labyrinth. In particular, his focus was on methods for constructing IPMS from two dual skeletal graphs. For one-parameter families of IPMS with changing node-connectivity, such as the rPD family (6-coordinated at the Primitive surface and 4-coordinated at the Diamond surface), Schoen's line graph definition is not sufficient to capture this change.

"Geometrically centered" means that the line graph traces paths through the labyrinth channels that are as distant as possible from the surface. Topological equivalence between line graph and the labyrinth may be lacking in cases where topology and geometry cannot be reconciled. In particular, depending on the cross-sectional shape, a labyrinth channel may contain more than one "parallel" line graph segments.

The suggested approach consists of an analysis of the Euclidean distance map D (EDM) that assigns to each point in the domain the distance to the bounding surface. In most cases, the line skeleton connects maxima of this distance field by following its "ridge lines". The minimum along a ridge-line, between two maxima, are critical inflection points of the EDM. They serve as a starting points for the ridge lines. At any point on a segment of the graph shall the graph point be a local maximum of the EDM in the plane perpendicular to the graph segment at that point. The principle is analogous to tracing ridge lines in two-dimensional topographies.

Note that this definition does not rule out multiply-connected nodes which are not maxima. Higher-connected saddles and even non-critical points can also be nodes of the graph.

As the MS is already centered in a less strict sense (the EDM decreases in perpendicular directions but may increase in directions tangential to the MS) it is clear that the geometrically centered line skeleton has to be contained in the MS.

We describe an algorithm that determines this line graph for domains that are represented by (triangulations of) their bounding surface. In that case, the Euclidean distance map is intimately related to the MS distance function. Our approach consists in carrying out the complete analysis of the Euclidean distance map by analysing the MS distance function on S or MS. The lack of differentiability of the distance function and Euclidean distance map do not cause a problem for our definition or algorithm.

Our algorithm makes no assumptions with respect to a specific symmetry, shape or topology of the labyrinth and is designed to work both on exact surface data, e.g. from parameterisations of mathematical models, and on experimental data, e.g. from tomographic images. In the later case, however, it is subject to the noise sensitivity to noise that is inherent to the definition of the MS. For experimental data, we have so far not achieved an automated implementation of the algorithm – in particular a robust detection of the saddle points of D is difficult. Nevertheless, tracing individual segments of graphs of experimental data sets is already a helpful tool.

In general, a line graph cannot represent the complete geometry of a labyrinth. The MS is already the optimal skeletonisation of a labyrinth in that it retains all topological and geometric information. In that sense, any further reduction to a line graph is

indeed only a picturesque model. However, in many instances a 1D line skeleton or graph provides sufficient structural information about the labyrinth. Effectively, reduction of the MS to a line graph corresponds to approximation of a labyrinth by a network of tubes of circular cross-section and varying radius.

This chapter is organised as follows: Section 3.1 gives a short overview of existing techniques. Sections 3.3 and 3.4 discuss the Euclidean distance map, its relation to the MS distance function and the concept of geometrically centered curves as prerequisites for the definition of the line graph. Section 3.5 defines the line graph as "lines of steepest ascent" connecting local maxima of the distance function. The properties of this line graph are illustrated by analysis of those cases where a compromise between topological and geometric requirements arises. Section 3.6 provides numerical details about the detection of saddle points of the Euclidean distance map and lines of steepest ascent. Finally, section 3.7 addresses the question of what the geometric requirements for a domain are so that both requirements of topological equivalence to the domain and geometric centeredness are met without compromise.

3.1   Related Work

The generation of line skeletons or centerlines of labyrinthine models is required for some applications, e.g. in virtual navigation through channel systems in non invasive surgery [223], in network models for fluid flow through porous materials [13, 200] or animation control in computer visualisation [75]. It is also, implicitly, often assumed in the description of regular space partitions, such as IPMS, where the name of the surface may be derived from the underlying network graph [183].

Most algorithmic approaches to line skeletonisations are for the case of voxelised binary data sets[2]. There are two classes of basic methods, "Topological thinning" and "Distance Transform methods".

Topological thinning is a method that, starting from the solid domain C, iteratively removes voxels from the outside of the domain such that the topology of C remains the same, until the domain has been shrunk as much as possible yielding a (line) skeleton. The topological equivalence of the skeleton and the original domain is ensured by the rule that a voxel on the boundary of the domain is only removed if the number of holes, cavities and connected parts of the domain remain the same.

---

[2]A *voxelised binary data set* is the 3D equivalent of a binary image where each pixel assumes either of the values 0 or 1. A voxelised representation of a domain C is hence a division of space into $n_x \times n_y \times n_z$ cubes, called "voxels", and an assignment of values to each voxel such that all voxels inside C are set to 1, and all voxels not contained in C are set to 0.

The geometrical centeredness of the line skeleton is not guaranteed when using a purely topological method. A crude way of incorporating it to some extent is the use of an "onion-peeling" idea, where voxels are processed in layers. In general, this method does not lead to a centered skeleton with respect to the Euclidean metric. "Distance-ordered thinning" incorporates a removal order given by the Euclidean distance map of the domain which ensures that the line skeleton is centered – under the proviso that the labyrinth allows for a topology preserving <u>and</u> centered skeleton.

A major problem for line graph algorithms based on thinning of voxelised data sets is the "end point criterion". It provides rules which determine voxels that may be removed without altering the topology, but shall be conserved for geometric reasons, such as the point p' in Fig. 3.2.

The literature on 3D thinning is too comprehensive to be reviewed in this context. We refer to the references in [130, 144, 22].

Topological thinning methods are useful in that they guarantee the strict equivalence of the domain topology and the line graph topology (holes, components, cavities). An additional favourable aspect is that noise of the data set does not influence the (connected components of the) line graph very much – provided it does not produce topological artifacts.

A drawback of topological thinning methods is the lack of guarantee that the skeleton is geometrically centered – even in those cases where no compromise between topological equivalence and geometrical centeredness is necessary[3]. Where a compromise is necessary, as e.g. in the case doughnut vs. disk in Fig. 3.9, this class of algorithms retains the topological requirement and not the geometric one.

Distance Transform methods compute the Euclidean distance map of the voxels in the domain C, i.e. the distance to the nearest voxel in the other phase. The line graph is then defined as a set of curves, maximally centered in some sense, that connect the local maxima of the distance map [222, 75, 158].

The resulting skeleton is geometrically centered, at the expense of topological equivalence between the domain and the line graph (in particular, a channel with bone-like cross section as in Fig. 3.8 produces two parallel skeleton lines, but it is reduced to a single line by thinning algorithms).

Fast computation of Euclidean distance maps is now feasible [179, 34]. Sensitivity to undulations of the bounding surface of the domain and noise, leading to numerous critical points and hence segments of the graph, need to be addressed.

Our definition of a line graph is closely related to the distance transform methods.

---

[3]Although in such cases, distance ordering can overcome this problem
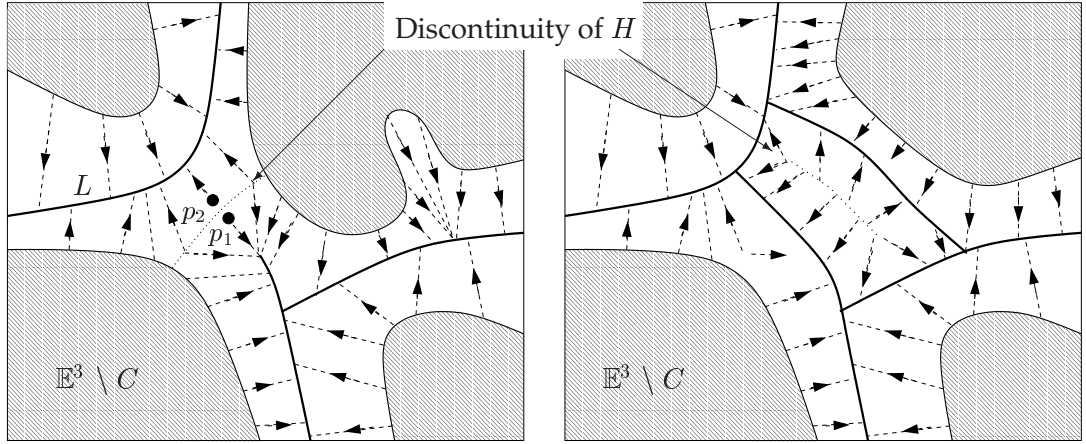
Figure 3.1: Two examples where the line graph L is not a strong deformation retract of the domain C. (Left) C has a channel that is not traversed by a segment of L. Any retraction H of C onto L has points where it is not continuous. (Right) C has a channel that is crossed by two "parallel" segments of L. Both retractions are discontinuous on lines in the figure.

In contrast to the works mentioned above, our numerical analysis is for triangulated representations of the domain.

Very little literature on algorithmic approaches to <u>line</u> skeleton generation exists for the case of domains represented as triangulated surfaces.

3.2 Topological equivalence of the domain and its line graph

Discussion of the homotopy relation between a domain and its line skeleton is ubiquitous in the literature. This section gives a summary of this aspect.

A domain C and its line graph L are homotopic if they can be continuously deformed into each other – by shrinking or swelling but without tearing or coalescing. That is, every channel of C has exactly one graph segment running through it, and C and L (and $\mathbb{E}^3 \setminus C$ and $\mathbb{E}^3 \setminus L$) have equivalent holes, components and cavities.

In a mathematical formulation, homotopy equivalence between a domain C and its line graph L is requires that L is a strong deformation retract of C. This means that the domain can be shrunk to the line graph <u>in a continuous way</u>.

Let I be the closed interval $[0, 1]$. Let L be a subspace of a topological space C. Then L is called a *strong deformation retract* of C if there exists a continuous map $H : D \times I \to D$ such that for any $p \in D$ and $q \in L$ the relations $H(p, 0) = p$, $H(p, 1) \in L$, and $H(q, t) = q$ hold for all $t \in I$ [195, 155].

We illustrate with two examples, shown in Fig. 3.1, why it is sensible to require a line graph to be a strong deformation retract of the domain if preservation of topological properties is the crucial condition.

The first example is illustrated in Fig. 3.1 (left). If the domain C has a channel – in the sense that $\mathbb{E}^3 \setminus C$ has a doughnut-like hole – that is not penetrated by a segment of the line graph L, then no strong deformation retraction H can be found – the continuity requirement is always violated on a topological disk, or at least some of its points, spanning the channel. In this case $\mathbb{E}^3 \setminus C$ has a (doughnut-like) hole, whereas $\mathbb{E}^3 \setminus L$ does not.

Our line graph algorithm, presented in the subsequent sections, never violates the equivalence of the domain C and the line graph L in this way; all channels of C are traversed by at least one line graph segment.

The second type of violation of the homotopy equivalence is shown in Fig. 3.1 (right): If the domain C has a channel that is crossed by more than one segment of the line graph L, again there is no strong deformation retraction H. The line graph L forms a ring that is not surrounding a connected section of $\mathbb{E}^3 \setminus C$, it forms a ring that could topologically shrink to a point and vanish. The retraction H again exhibits a discontinuity. In this example, L has a hole (or ring) that C does not have.

Our line graph algorithm will allow for such cases that arise e.g. for channels with a bone-shaped cross-section such as shown in Fig. 3.8.

Algorithms based on thinning typically ensure that the line graph is a strong deformation retract of the domain, by assessing at each step (voxel removal) if the connectivity and Euler characteristic is preserved [130, 143].

3.3   Euclidean distance maps and geometrically centered curves

The definition of a line graph proposed later in this chapter produces a skeleton that is as well-centered in the channel labyrinth as possible. The definition relies on the notion of "geometrically centered" curves which in turn are defined with reference to the Euclidean distance map D. These concepts are now formalised.

Given a domain C bounded by a surface S in $\mathbb{E}^3$ the Euclidean distance map (EDM) is the function

$$D : C \subset \mathbb{E}^3 \to \mathbb{R}^+, \qquad p \mapsto D(p) = \min_{q \in \partial C} |p - q| \tag{3.1}$$
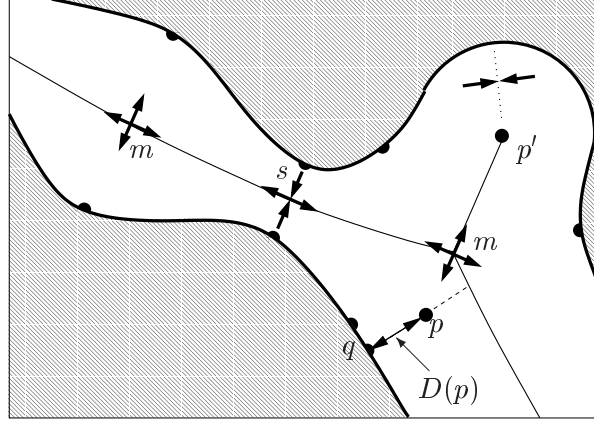
Figure 3.2: Euclidean distance map of the domain C (white): The Euclidean distance map assigns to a point $p \in C$ the distance to the closest point, denoted q, on $S = \partial C$. On the MS of C, the Euclidean distance map D corresponds to the distance function d. Saddles and maxima of D are on the MS. The dotted line to p' is a an example of a geometrically centered line that is not on the MS. The thick arrows indicate directions of increasing EDM D.

where $|.|$ denotes the Euclidean distance in $\mathbb{E}^3$. Hence, $D(p)$ is the distance from a point $p \in C$ to its closest point on the bounding surface of the domain [39, 221, 171].[4]

For points p on the MS, the Euclidean distance map and the distance function at corresponding points $q \in S$, with $\mathrm{ms}(q) = p$, are identical: $D(p) = d(q)$.

The Euclidean distance map D has a gradient of constant amplitude $|\nabla D| = 1$ on $C \setminus \mathrm{ms}(C)$, and is not differentiable on $\mathrm{ms}(C)$ (Trivially, for a point $p \in C \setminus \mathrm{ms}(C)$ the gradient of the EDM is $(\nabla D)(p) = N(q)$ where $q \in S = \partial C$ is the point on S that minimises $|p - q|$ and $N = N(q)$ the surface normal vector of p pointing into the domain C. Because of the assumption that $p \notin \mathrm{ms}(C)$ it is assured that q is unique)

Because of this fact, a definition of critical points using the differential or the condition that $\nabla D = 0$ is not sensible for the EDM. Instead, we define a point $p \in \mathbb{E}^3$ as a *critical point of rank n* of D if there are n linearly independent vectors v_i such that $D(p + r\,v_i)$ has a maximum at $r = 0$ <u>and</u> $3 - n$ linearly independent vectors v_i such that $D(p + r\,v_i)$ has a minimum at $r = 0$.

With this notation maxima and minima are $n = 3$ and $n = 0$ critical points, and $n = 2$ critical points shall be called saddle points. It is immediately clear that maxima and saddle points are on the MS of C.

---

[4]For voxelised representations, the EDM for a voxel in one phase is the minimum distance from a voxel $p \in S$ to the nearest voxel of the other phase, i.e. of $\mathbb{E}^3 \setminus C$ rather than ∂C.
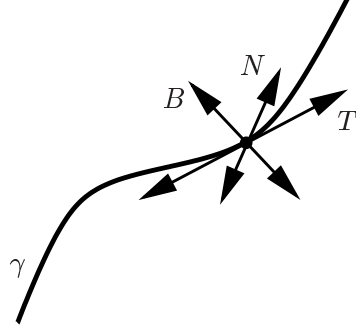
Figure 3.3: Illustration of the definition of *geometrically centered*: A space curve $\gamma(t) : [0,1] \to \mathbb{E}^3$ is *geometrically centered* with respect to the EDM $D : \mathbb{E}^3 \to \mathbb{R}^+$ if any $p \in \gamma$ is a local maximum of (or at least constant in) the EDM in the plane perpendicular to γ at p, i.e. in the plane spanned by the normal $\pm N$ and binormal $\pm B = N \times T$ of γ.

Geometrically centered space curves

A space curve $\gamma : [0,1] \to \mathbb{E}^3$ is *geometrically centered* within the domain C if for any value $0 < t < 1$ the point $p = \gamma(t)$ is a local maximum of D (or at least constant) in the plane spanned by the normal $N(t)$ and the binormal $B(t)$ of the space curve γ, i.e. in the plane perpendicular to γ at $\gamma(t)$ (see Fig. 3.3).

A geometrically centered curve α is not necessarily on the MS, e.g. a radial line emanating from a point p on a spherical cap of S is geometrically centered, see Fig. 3.2. A geometrically centered curve passes through a section of a labyrinth such that, at least locally, the distance, in perpendicular direction, to the boundaries of the domain is always kept maximal. This is the guiding idea behind the definition.

If γ is a geometrically centered curved and $p_c = \gamma(t_c)$ a minimum of D along γ, then p_c is a saddle point of D. Following γ in either direction from p_c leads to a maximum of D. More precisely, it eventually leads to a maximum, but may pass through other saddle points. This is analogous to a ridge line in a topography that terminates at the saddle point of another ridge line.

3.4   Relation between saddle points of d and D

The distance function d on the surface S and the Euclidean distance map D in $\mathbb{E}^3$, and in particular their "gradients", bear a close relationship. For domains represented by
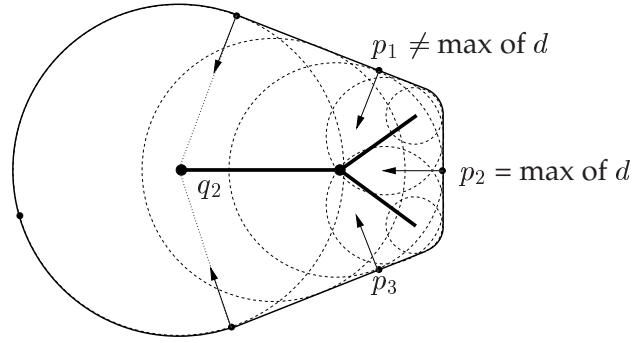
Figure 3.4: Illustration of a situation where a point p_2 is a maximum of d on S, but the corresponding point $\mathrm{ms}(p_2)$ is not a maximum of D: The outline S is a composition of straight lines and circular arcs. The point p_2 is a maximum of d whereas p_1 and p_3 are not. The points on S corresponding to the maximum q_2 of the Euclidean distance map D are all part of a circular arc (one connected subset of S).

triangulations of their bounding surface S, the distance function d on S is the more natural representation. Our detection of saddle points of the Euclidean distance map D relies on the relation between ∇D and $\mathrm{ms}(\nabla d)$. In this section, we define saddles and maxima of d on S using the concept of Hopf singularities of d. The relation between saddles of D and saddles of d is explained. In particular, we will see that there are saddles q of D whose counterparts $p \in S$ with $\mathrm{ms}(p) = q$ are not saddle points of d. Less intuitively, there are also saddles $p \in S$ of d with corresponding MS points $q = \mathrm{ms}(p)$ that are not saddles of D.

We consider the distance function

$$d : S \,(\text{or MS}) \to \mathbb{R}^+ \tag{3.2}$$

as defined in eq. 2.1. In this chapter we restrict ourselves to surfaces S that are smooth manifolds in $\mathbb{E}^3$. We also consider the "gradient function" $\nabla d : S \to T_{()}S$ that assigns to each point $p \in S$ the direction of steepest ascent of d; this direction is evidently a vector in the tangent plane T_pS of S at p.

We denote this function "gradient function" in inverted commas since the distance function d does not necessarily possess continuous derivatives. Therefore, the canonical definition of the gradient as partial or directional derivatives fails. However, the direction of steepest ascent is guaranteed to exist as d is at least continuous. The second requirement for our definition of the gradient function is that a tangent field exists for all points $p \in S$. This is assured as we assume S to be a smooth manifold.
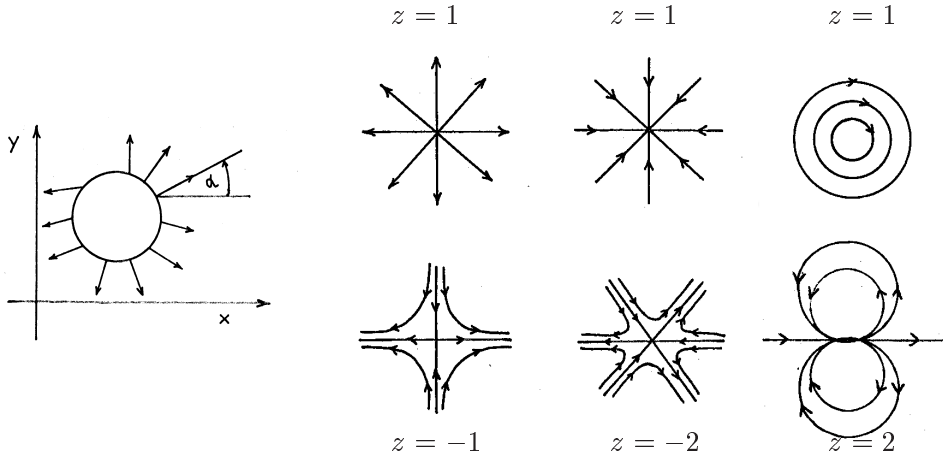
Figure 3.5: Definition of the index z of singularities of the vector field ∇d in the plane. (adapted from Hopf [92])

Definition of saddle points of d via the Hopf index

Saddle points of d are defined through consideration of the gradient ∇d: The vector field ∇d is continuous except at a finite number of points that are called the singular points of d. The index of a singularity is defined by the following construction that we explain for the simpler case where S is a plane (see Fig. 3.5): The angle α that ∇d subtends with a fixed vector T in (the tangent plane of) S is evaluated at all points on a closed path C on S around a singular point p. The integrated total change of α along the closed path C is an integer multiple $2\pi j$ of 2π because of the continuity. The integral multiple j is called the index of the singularity. The so-defined index does not depend on the particular path as long as the path does not contain any other singularity than p.

For the case of a non-planar surface S the definition of the integrated change of angle needs to be refined: The notion of a fixed vector T in the tangent space of S does not carry over to a non-planar manifold S where the tangent space $T_p S$ depends on p. Instead of integrating the angle that ∇d subtends with a fixed direction, one integrates the change of the angle between ∇d and a second non-singular test vector field along a simple closed curve on S around p. Again it turns out that this definition is independent of the particular test vector field.

Maxima and minima of d are singularities of ∇d with index +1. A *saddle point* is a singular point $p \in S$ with index -1, and a monkey saddle a singular point with index -2. Because ∇d is derived as a gradient-like field, singular points with positive indices

greater than 1 do not occur [92].

Saddles at normal MS points are saddles of both D and d

The relation between saddles of D and saddles of d is simple only in one special case: A MS point that has exactly two corresponding surface points ("normal") and is a saddle of D corresponds to two saddle points of d on S.

Saddles of d that are not saddles of D

A simple 2D example for a point that is a maximum on S but not a maximum of D on MS is shown in Fig. 3.4. If the diagram is considered as the cross-section of a straight cylinder of varying cross-sectional size but constant cross-sectional shape, and such that the paper plane represents the minimal cross-sectional size, then p_2 is a saddle point of d on S, but $ms(p_2)$ is not a critical point of D.

This case arises e.g. in the case of the infinite periodic Gyroid minimal surface, see Fig. 5.9. The point S_3, the small green sphere on the MS on the edge of the triangle on the two-fold rotational axis, corresponds to three points on the Gyroid surface. Two of them are not special points of d, but the third one, also on the two-fold axis away from the MS, is a saddle point with Hopf index -1. On S, there are two paths of steepest ascent emanating from this point that map to paths running along the edge of the triangle (where the blue and red "sails" meet) to the two maxima at the vertices of the triangle. This path is not a path of steepest ascent of D in $\mathbb{E}^3$.

Fig. 3.4 also demonstrates that a maximum (or another critical points) of the 3D Euclidean distance map D, that by definition lies on the MS, may correspond to a finite subset s (or a set of finite subsets) of S rather than just a number of isolated contact points. Hence, procedures to detect critical points of d must accommodate for that scenario.

A similar case actually arises when analysing Schwarz' Primitive surface whose MS and line graph is shown in Fig. 5.7. The planar constrictions in 100 planes are nearly circular, with radius variations of only 3.3% – in contrast to the value of 0.4% given by [183]. Hence, variations of the distance function on the surface points representing the ring are very small and hard to detect. The common approximation of the Primitive surface as the zero-level set of $\cos x + \cos y + \cos z = 0$ has perfectly circular constrictions, and the MS correspondingly shrinks to a point and the corresponding set of points on S be a ring of degenerate points.
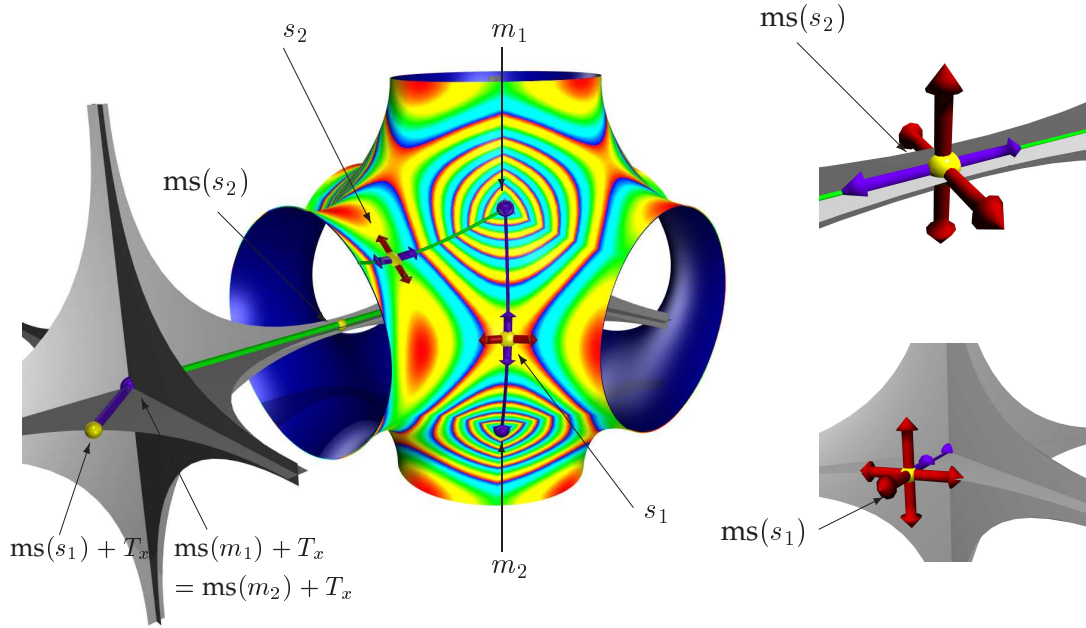
Figure 3.6: Saddle points of d on S are not necessarily saddles of D: (Left) Shown is a portion of the Primitive surface and a (different) portion of the MS of the P surface. The color scheme on one side of the surface indicates the isodistance lines on S (see page 193), the other side is colored blue. Also shown are two saddle points s_1 and s_2 and two maxima m_1 and m_2 of d on S. The blue and red arrows on S at s_1 and s_2 indicate directions, tangential to S, of maximal increase and decrease of d, respectively. The blue line on S is a path of steepest ascent from s_1 to m_1 and to m_2. The blue line on MS is the same line mapped onto MS – and corresponds to the lines of steepest ascent of D (However, as the surface occludes the portion of the MS that contains $\mathrm{ms}(s_1)$ and $\mathrm{ms}(m_1) = \mathrm{ms}(m_2)$, the corresponding line on the neighbouring translational unit cell is shown) Note that the two path to m_1 and m_2 coincide on MS. (Right) close up representations of $\mathrm{ms}(s_1)$ and $\mathrm{ms}(s_2)$. Blue and red arrows indicate directions in which the Euclidean distance function D increases and decreases, respectively. The directions corresponding to the on-surface directions from the left image are part of these arrows. For s_2 the four directions on S correspond to four distinct directions on MS. This is a necessary condition for $\mathrm{ms}(s_2)$ to be a saddle point. In contrast, for s_1 the two directions of increasing d on S coincide on MS. $\mathrm{ms}(s_1)$ is not a saddle point. From the definition of the MS it is evident that directions not tangential to MS always represent decreasing Euclidean distance function D.

A second situation in which a saddle of d is not a saddle of D is illustrated in Fig. 3.6: There are saddle points of d on S with Hopf index -1 that map onto points on the boundary of the MS such that the two directions $\pm T^-$ in which the d maximally decreases map onto the edge of the MS, and the two directions $\pm T^+ \in T_p S$ in which the d maximally increases map onto each other pointing into the MS patch.

The paths of steepest ascent emanating from such a saddle point typically terminate at

two maxima m_1 and m_2 that map onto the same point on the MS $ms(m_1) = ms(m_2)$.

A saddle of D that is not a saddle of d

We now show the inverse, less intuitive and more complicated case where all points $p \in S$ that map onto a saddle point q of D, i.e. $ms(p_i) = q$, are non-critical points p_i and in particular not saddles. Fig. 3.7 provides the illustration. The image on the top left gives a (flawed but useful) planar analogy: The point q is a saddle point of D in C^5, at a branch point of the medial axis with two angles slightly larger than $\pi/2$ and a third one close to π. The points p_2 and p_4, that both map onto q are not saddles of d; rather d increases continuously and monotonously at both.[6] The point q, corresponding to p_2 and p_4 is a saddle point by virtue of the images (arrows on MS) of their gradients $\nabla d(p_2)$ and $\nabla d(p_4)$ (arrows on S) pointing in different directions on the MS.

The example is flawed, as the third point p_1 always is a minimum of d – and hence there is a critical point p on MS that corresponds to the saddle q of D. This cannot be avoided in the plane. In 3D, however, this situation can occur without this caveat. The example we use to illustrate this situation is taken from the I-WP surface, to be more precise the I-labyrinth, described in chapter 5. It is also similar to the MS of the cubic Diamond surface.

In Fig. 3.7 (right) a portion of the MS of a hypothetical domain C with skin S is shown that contains a straight edge, the thick black line, with a point q at its center. The left half of the edge is at the intersection of three nearly triangular and flat surface patches, that subtend angles $2\pi/3$ with each other. The right half results from inversion in $\mathbb{E}^3$ of the left half in q, i.e. the flat patches are rotated by $\pi/3$ around the axis compared to those on the left half. Near the edge center, where the surface patches narrow down to the point q, small "webs" are spanned between the edges of pairs of adjacent patches, from the edge of a triangular patch on the left (L_1 to the edges of the patches on the right at $\pm\pi/3$ (R_1 and R_2). This arrangement creates six compartments around the edge, three of which are visible in the figure near the edge center. In particular, the point q on MS has six corresponding points p_i on S.

For each of these compartments, e.g. the light gray one in the foreground, there is a single, simply-connected surface patch $\tilde{S} \subset S$ that maps onto that compartment. The point $p_i \in \tilde{S}$ with $ms(p_i) = q$ on this patch is not a special point of the distance function d. Yet, when the six points p_i from the different patches collapse onto q, then the arrangement of their gradients makes the point q a saddle point of D.

---

[5]A saddle point of D in 2D is a point with two directions of increasing EDM and two decreasing ones.
[6]This is not possible if the medial axis branch point angle is less than $\pi/2$.
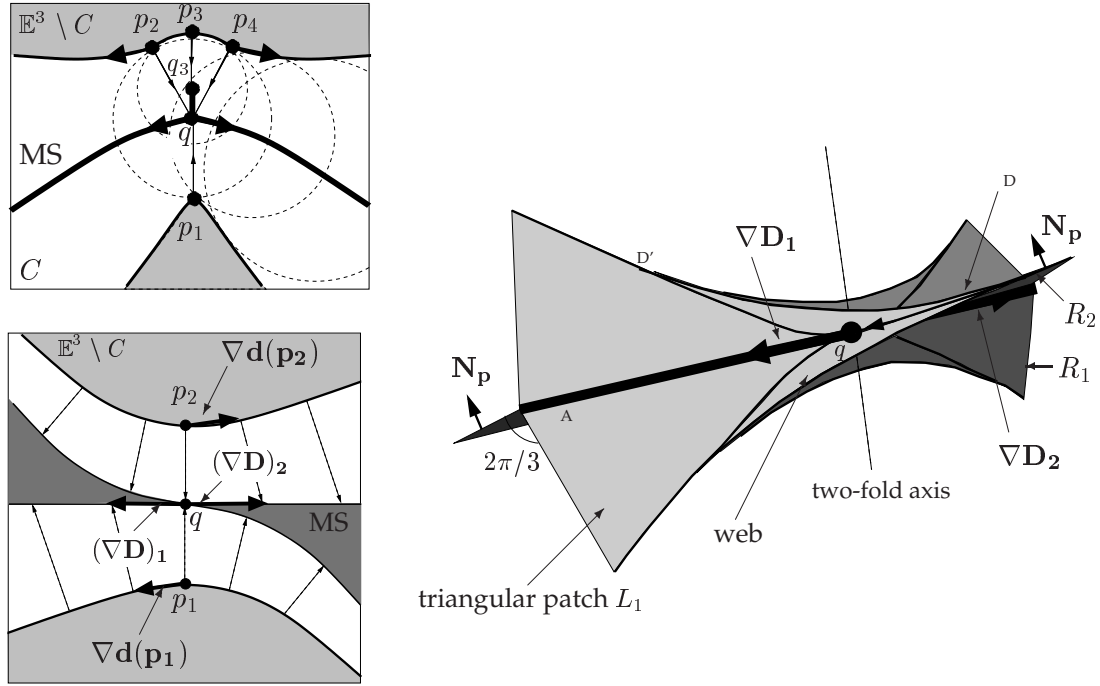
Figure 3.7: A saddle of the Euclidean distance map D that does not correspond to any saddle (or minima or maxima) of the MS distance function on S: (Top left) Planar example where two of three surface points corresponding to a saddle point of D on MS are normal points. The domain is shown in white. (Right) Hypothetical MS of a structure very similar to the cubic Diamond IPMS. Details are described in the main text. (Bottom left) Cross-section through the plane from the left figure that contains the straight edge with q at its center and with normal vector N_p.

Fig. 3.7 (Left, bottom) clarifies this situation, showing the cross-section through the plane with normal N_P: The patch $\tilde{S}$ contains a plane line that maps onto the planar path γ from A to q along the edge and then, along the edge of the corresponding surface patch half-way in between, to D (for clarity, an equivalent point D' is also shown). The cross-section through the plane with normal N_P contains both the path γ on S and its image ms(γ) on MS. It becomes clear that the points p_1 and p_2 are not special points of d; in particular their gradients are well defined vectors $\nabla d(p_{1/2})$ on S. In direction of $\gamma'(p_i)$ through p_i, the distance function is monotonous. Yet, when the gradients are mapped on the MS, they point in opposite directions away from q, thus making q a saddle point of D.

This situation is realised for the "innen-zentriert" labyrinth of the unbalanced I-WP surface (In Fig. 5.10, bottom, the equivalent situation is covered by the yellow spheres). It is also very similar to the MS of the Diamond surface where, at first, we thought this situation was realised. Yet, in that case, the point q is actually an ever so slight max-

imum and an additional saddle point – both of d and D – on the edge exists; see chapter 5.5. This example here is hypothetical in that the surface generating this MS is not known, and may not even exist. Yet, because of the tiny difference to the Diamond case we suspect it does.

For any practical purpose, e.g. detection of saddle points of D via detection of saddle points of d, the Diamond case has to be considered identical to the one discussed here.

The true relation between saddles of d and D

The implication of this result for the detection of saddles of D by analysing the function d on S is severe: it means that the set of saddles of D is not just a subset (and certainly not identical) to the images under ms of all saddle points of d. This means that the natural representation of d as a function on S is not sufficient to characterise the critical point structure of D. In addition, knowledge of the set of points that collapse onto a point on the MS is necessary.

However, an equivalence relation between gradients of D and gradients of d exists: restricted to that subvolume of space that corresponds to a patch of S (i.e. the volume foliated by (reduced) parallel surfaces of S) the direction of strongest increase of D at a point q corresponds to the direction of the gradient d on S.

Bearing this in mind, it becomes clear that a saddle q of D either corresponds to a saddle point of d, or the gradient images $\mathrm{ms}(\nabla d(p_i))$ of the two or more points $p_i \in S$ with $\mathrm{ms}(p_i) = q$ point in distinctly different directions. This is very useful for the saddle point detection described below.

3.5 Formal definition of a geometrically centered line graph

This section gives our definition of the line graph, and outlines some of its properties, advantages and shortcomings. Our definition leads to a geometrically centered graph, at the expense of a guarantee of the homotopy equivalence between S and the line graph. However, it is assured that every channel is traversed by *at least* one line graph segment.

We define a line graph to be a finite set of n finite curves $\alpha_i : [0, 1] \to \mathbb{E}^3$ such that

1. every segment is fully contained in the MS and is geometrically centered in C and emanates from a saddle point of D, and

2. all geometrically centered curves emanating from a saddle point D are part of the line graph.
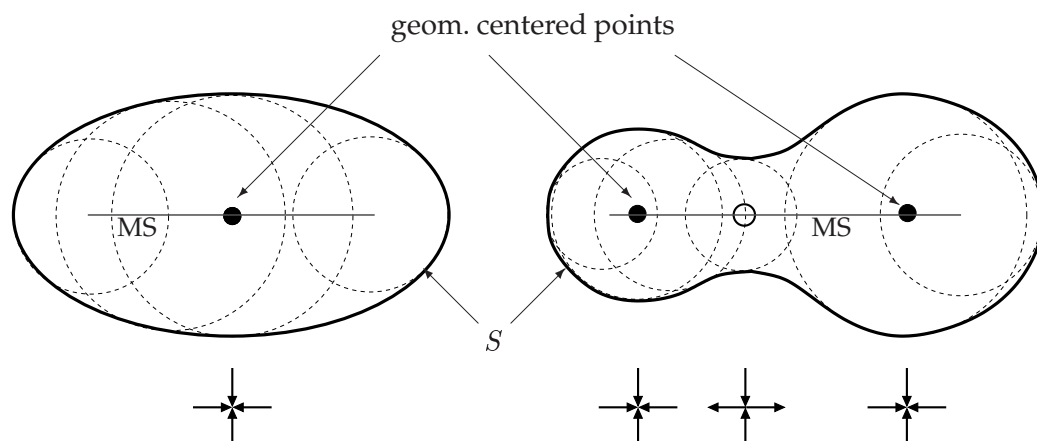
Figure 3.8: Illustration for the fact that a single channel can be traversed by more than one geometrically centred curve: Shown are the cross-sections of two "throats" of a labyrinth that extend in perpendicular direction in and out of the page. The solid disks indicate the positions of geometrically centred curves through the throats. The arrows indicate directions of increasing distance function D near these positions. In the case of the channel with elliptic cross-section there is only one geometrically centred curve that is, quite intuitively, positioned in the centre of the ellipse. In the case of the throat with bone-shaped cross-section, there are two such positions. If no more than one segment may run through the channel, one would presumably expect the curve to run through the center (the open circle) which is not geometrically centred.

As said before, this definition puts strong emphasis on the geometric centeredness of the line graph in the domain C. The edges are paths of maximal distance to S through C. A sphere – of varying radius that always adapts to the maximal size that fits into the domain C – follows the segments of the so defined line graph as it moves through the domain. The saddle points are the bottle-necks along the paths.

Note that we have not explicitly specified the end points of the segments. The reason for that is the fact that the end point, though most often a maximum of D, may also be another saddle (as for the rhombohedral Gyroid with $\phi_0 = 0.35\pi$, see Fig. 6.7). Also there is the possibility of degeneracy of parts of the segments (as in Fig. 3.10) before reaching its end point.

This definition of a line graph was inspired by the work of Richard Bader [11] who defined a molecular bond, rigorously, as the critical paths between saddle points and maxima of the electron density. The possibility of two distinct "parallel" path connecting the same two maxima (atoms) can be ruled out for physical reasons. An important difference is that the electron density is differentiable everywhere apart from at the positions of the atoms themselves.
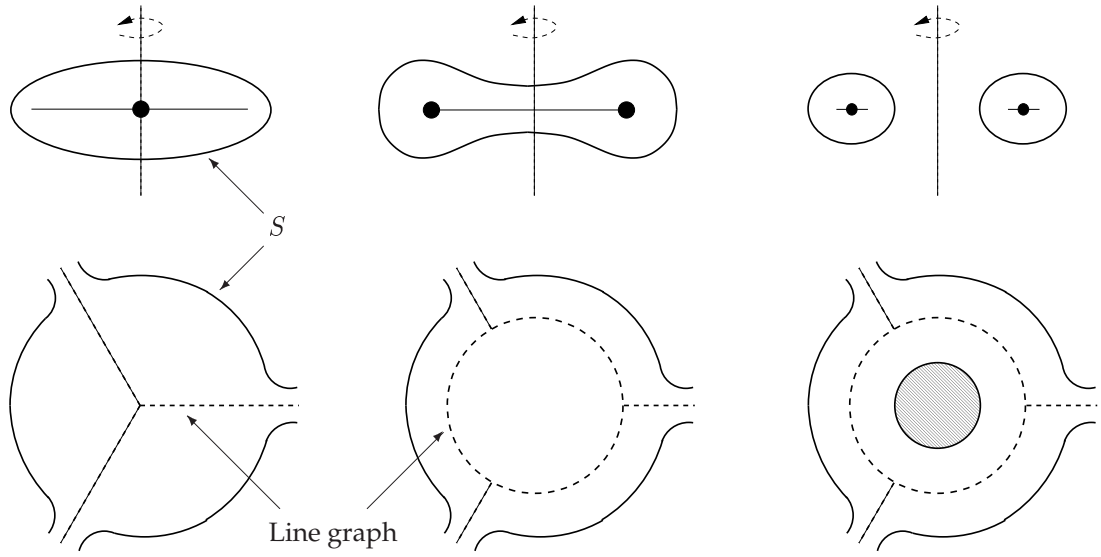
Figure 3.9: Three different triple labyrinth junctions showing that surface topology and graph topology do not necessarily match. (Top) cross section of three rotationally symmetric "pores". Not shown are the three tunnels joining the "pore" at three equidistant angles. (Bottom) top view of the pores together with the three emanating tunnels (that are assumed to be of circular cross section and joining the pore surface smoothly). Also shown, as dashed lines, are the graphs generated by tracing geometrically centered lines.

Topological non-equivalence of C and its line graph

The drawback of this definition is that the topology of the line graph defined in this way and that of the domain C may be different: a single channel may be traversed by more than one, "parallel", graph segment (Consider the example in Fig. 3.8).

Another example demonstrating that homotopy equivalence between the domain surface and the line graph (as defined by geometrically centered lines) can in general not be assumed is shown in Fig. 3.9: three channels, of say circular cross section, join smoothly onto rotationally symmetric pores – ellipsoid, rotated bone and a doughnut. The ellipsoid and the bone have the same topology as a simple sphere, different from the doughnut. Nevertheless, they yield two different line graphs. The doughnut, in turn, has the same line graph as the rotated bone. In particular, the line graph of the rotated bone contains rings that can be contracted to a point. The ellipsoid and the rotated bone can be smoothly transformed into each other, with a sharp transition when the graph jumps from the single three-coordinated node to a triplet of three-connected nodes.
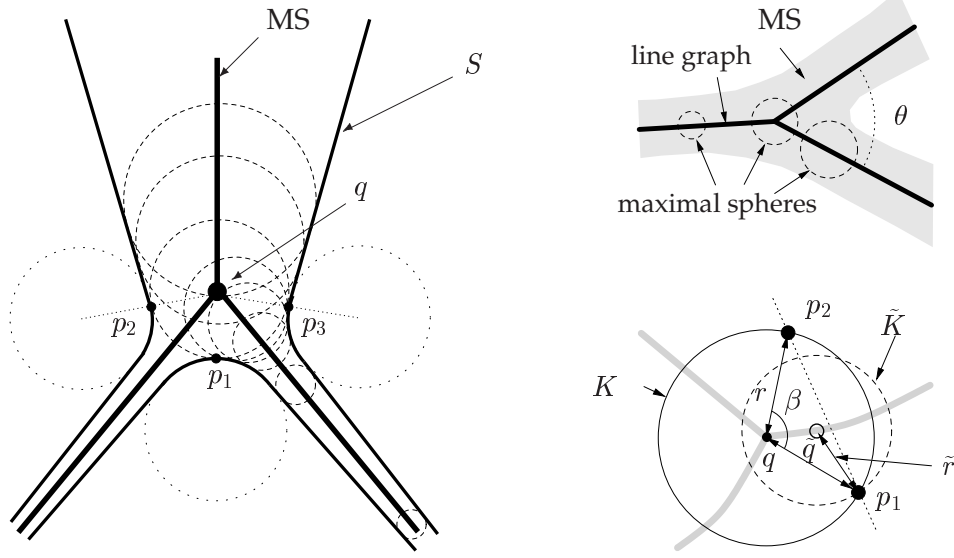
Figure 3.10: (Left) A 2D example where the medial axis has a junction, a three-coordinated point that is not a critical point of the distance function d. The thick black line is the medial axis of the outline given by the thinner solid black line. Dashed circles are maximal disks, dotted circles only serve to clarify the construction. (Bottom right) A triple junction of a planar MA with two edges with increasing d and one with decreasing d cannot exist. (Top right) A planar ribbon-like MS of a three-dimensional network of ellipse-shaped channels with a Y-junction of that type can exist.

Degenerate edges

Two segments of the line graph may follow, for parts of their lengths, the same path.

The geometric position of nodes of the line graph is not necessarily coincidental to the position of critical points of D: The notion that the line graph traces critical paths of the distance function, starting at saddle points and ending – eventually – at maxima or saddles, seems to suggest that its nodes are critical points of d. This is not correct as the example in Fig. 3.10 demonstrates.

The construction is as follows: A maximal disk B centered at q is drawn in the plane. Then three auxiliary balls are drawn that all touch B, one right below and another two as mirror images on the right and left of B slightly lower than q. The outline S is then a composition of circular arcs on the auxiliary balls plus straight lines tangential to the balls as shown in the figure.

It is easily verified that the thick black line is indeed the medial axis of S and that q is not a maximum or inflection point of D (or d). Any procedure that traces critical paths of D (or d), starting from saddles aiming for maxima, may detect the geometrically correct line graph, but will miss the junction as a topological feature. This

construction can be extended to 3D, simply by keeping the same line graph as the MS of the envelope of a set of spheres with radius given by the 2D distance function.

The reverse situation of a line splitting at a non-critical point does not occur in 2D. In 2D, a geometrically centered curve emanating from a saddle of D cannot split into two separate channels at a three-node that is *not* a critical point of D. The argument, illustrated in Fig. 3.10 (right) is based on analysis of possible maximal disk sizes in the vicinity of an MS point with 3 corresponding surface points.

A maximal sphere K of a domain C, centered at q, corresponding to the two surface points p_1 and p_2, has radius r. A second maximal disk $\tilde{K}$ in C is centered at a point $\tilde{q}$, within the triangle $\triangle(q, p_1, p_2)$ and is w.l.o.g. assumed to be closer to p_1 than p_2. Regardless of the shape of C, its radius has to be smaller than r as long as the opening angle β is less than π. Otherwise it would not be maximal as it would contain the point p_1.

This means that the MS distance function d can only increase (or even remain constant) along an MA segment in the direction of an opening angle β equal or greater to π. From that, it follows that at any point on the MA there can be at most two directions of increasing d on the MA. If there are two, $\beta = \pi$ must hold, the two directions are colinear and the points on ∂C corresponding to q are exactly the two points p_1 and p_2. That means that a triple junction with one thinning channel and two expanding channels is not possible.

The three-dimensional case is different. A situation as depicted in Fig. 3.10 (top right) where the MS is a flat ribbon that splits into two and the line graph "Y"-shaped on it, can exhibit a triple junction of the line graph without an $n > 2$ MS point. The maximal spheres within the ribbon all have two corresponding points on S above and below. Our implementation of the line graph does not cope with this situation, which can be aggravated by a vanishing angle θ between the two arms of the graph. The difficulty arises because it is only possible to assess how many segments emanate from a saddle, but not to locally test for the number of graph segments that hit a maxima. A possible solution may be to incorporate global topological information from different types of line graph algorithms such as thinning.

3.6   Computation of the line graph

This section discusses the implementation of the two essential steps to determine the line graph: (1) the detection of saddle points of D, and (2) the computation of finding lines of steepest ascent that connect the saddle points to the corresponding maxima.

Following the previous discussion in section 3.4 on saddle points of d and D, we detect saddles of D by detecting saddles of d and evaluating whether they correspond to saddles of D, <u>and</u> by comparing the direction of the images on the MS of the gradient of d of all those points that collapse to a single MS point. Therefore, in a first section we describe a method to detect saddle points of d on triangulated surfaces S. Then the selection of those points that are also saddles of D is described.

We propose the following data structures: The sample points on S are stored together with values of their distance function and their corresponding point coordinates when mapped onto the MS. In addition, two proximity functions are provided that, given a point on S or the MS and a distance r, return all points on the MS and S in a sphere of radius r around the point p, respectively.

The question may be asked why a detection of saddle points of d is at all necessary. A detection of D saddles based on the detection of directions of increase of D is possible. Yet, use of surface based methods provides for more flexible parameters, such as the minimum angle between two neighbouring directions of steepest ascent out of a saddle point, and additional assessment of the properties of a point based on the MS degree.

3.6.1   Detection of saddle points of the distance function on S

A method to detect saddle points on S without explicit evaluation of derivatives is presented. Some of the notation is borrowed from Hopf [92].

As motivated earlier, saddle points are points with two or more directions of increasing distance function and a corresponding number of directions with decreasing distance function.

Assume, for the moment, that saddle points are single points on S rather than finite subsets of S (lines or even surface patches) on which the distance function d is constant.

We now discuss a method of detecting the saddle points that consists of the following steps: for each point p on S, with distance function $d_c = d(p)$, a circle c of radius r on S around p is determined. The distance function d is analysed as a function of the angle α between a point on c and an arbitrary, tangential reference direction, e.g. the direction of the distance function maximum on the circle. A point p cannot be a saddle point unless $d(\alpha) - d_c$ has at least two positive maxima and two negative minima[7]. A

---

[7]This approach obviously does not detect saddle points if the characteristic behaviour of d is restricted to a surface patch contained inside the circle.
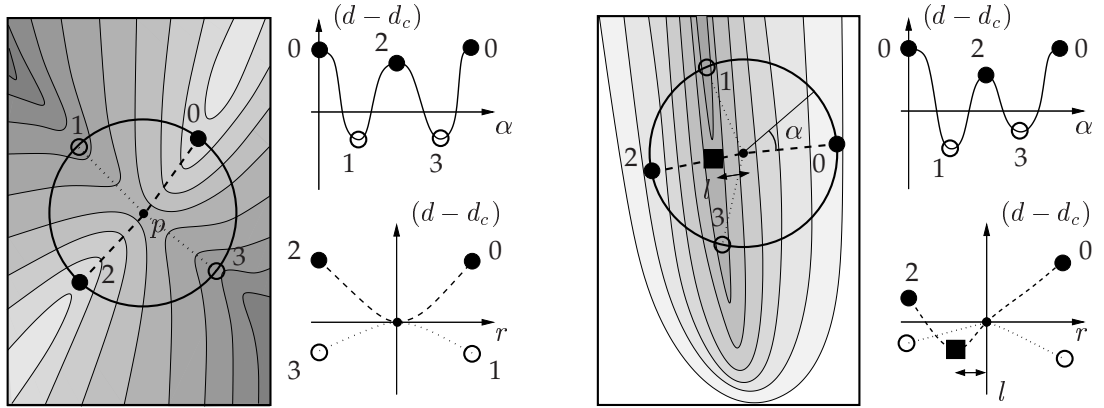
Figure 3.11: Detection of saddle points by analysis of the distance function on circles of finite radius r. Shown are portion of a surface S with iso-distance line. The distance function values are indicated by the grayscale where darker colors indicate lower values of d. (Left) The distance function $d(\alpha) - d_c$, with $d_c = d(p)$, on a circle around a saddle point p with Hopf index $z = -1$ has two positive maxima, points 0 and 2, and two negative minima, points 1 and 3, as a function of the angle alpha. Along a path on the surface connecting the two maxima (minima) via p, the distance function shows a minimum (maximum) at p. This behaviour is observed for all sufficiently small radii of the circle. (Right) A point p that is not a saddle point of d but for which, for finite radius r, the distance function $d(\alpha) - d_c$ also has two positive maxima and two negative minima. In contrast to a saddle point, the center point p does not simultaneously represent the minimum along the path connecting the maxima and the maximum along the path connecting the minima. Analysis of the distance l from this minima (the filled square) and maxima (in this case the point p itself) to the center point can be used to discard some of the saddle point candidates without the limit $r \to 0$.

point p is a saddle point if this holds true in the limit of vanishing r. See Fig. 3.11 for an illustration.

For triangulated surface data we define a circle of radius r around a point $p \in S$ as the intersection points of all edges of the triangulation with a sphere of radius r. We implicitely assume that the circle is sufficiently small so that the intersection points all stem from the same neighbourhood of p – and not from other patches of S that happen to cross the sphere. This procedure is linear – albeit with a large prefactor – in the total system size provided r is not of the same order as the dimensions of the whole surface.

Note that for the definition of singularities the circle is only required to be a simple closed curve on S. For numerical purposes, in particular to set noise thresholds, a geometric circle is favourable. We define a circle as the set of points in a sufficiently large neighbourhood of p on S that have 3D Euclidean distance r from p (rather than

geodesic, in-surface, distance). Hence the circle is the intersection of S with a 3D sphere of radius r around p.

However, exhibition of two positive maxima and two negative minima of d on a circle with <u>finite radius r</u> around a point p is not a sufficient condition for p to be a saddle point. Many other such configurations exist: First, all points in the vicinity (closer than r) of a genuine saddle point p will display that property. Second, points on the flanks of a valley, as in Fig. 3.11 (left), can lead to the same behaviour, as can points in the vicinity of anisotropic minima or maxima of d.

Using very small circles for the saddle point detection is numerically impractical. Both noise and finite resolution on S, of the order of the average edge length of the triangulation, impair this procedure. Note that the variations in d that one tries to detect are small compared to the difference between the global extrema of d; in the smooth case, saddle points have vanishing first derivatives of d, and therefore the typical distance function values on a circle of sufficiently small radius r increase as $\mathcal{O}(r^2)$.

Therefore, we now present alternative criteria to eliminate points that have two or more positive maxima and negative minima d on the circle but that are not saddle points: first, such points in the vicinity of minima or maxima are eliminated by testing the inside of the circle[8] for extrema.

Furthermore, we make the assumption that, inside the test circle, the straight line from the point p to the maximum (minimum) p_m on the test circle[9] represents the ridge (valley) lines. Then, for a saddle point, the minimum (maximum) of d along these lines should be the point p itself.

Points where the distance l between the minimum (maximum) along those radial lines and the center point exceeds a threshold tolerance that accomodates for noise, cannot be saddle points; see Fig. 3.11 (right). These points can be eliminated from the list of candidates for saddle points.

If these constraints are taken into account with thresholds, one still identifies clusters of points rather than individual triangulation vertices as saddle points. Therefore, in a final step we identify all clusters of such candidates and reduce them to single points by making another assumption. In principle, out of each cluster one may identify the saddle point as the point for which the sum of distances (or squared distances) l between the $-2(z+1)$ maxima and minima on the radial lines defined above is minimal

---

[8]For the actual implementation this means all triangulation vertices inside a sphere with a slightly reduced radius compared to r

[9]"Straight line" in this context should denote the geodesic. In our implementation it is given by the intersection points $\{q_i\}$ of all edges of the triangulation inside the sphere of radius r around p with the plane through p and p_m that also contains the normal direction $N(p)$, for which $0 \leq \langle q_i - p, p_m - p \rangle / r \leq 1$ (i.e. lie in between p and p_m).

```
Algorithm Detect Saddle points
   Input:
      Triangulation of S with distance function d
      r = Test circle radius
```
β_{min} = minimum angle between maxima of d on test circle
f_{ext} = fraction of max. d_{max} for a point to be *positive*
l_{max} = maximum distance of extremum on rays from saddle point

```
   /* find candidates for saddle points in S
```
$V := \emptyset$
```
   For all points p in S
      Compute circle c of radius r around p
```
Determine distance function $d^r(\alpha) := d - d(p)$ on c as function of α
Determine absolute maximum d_{max} and minimum d_{min} of d^r
Det. n positive maxima $\{d_i^+\}$ at $\{\alpha_i^+\}$ of d^r with $d^r(d_i^+) > f_{ext}\,d_{max}$
     and at least one point with $d^r < f_{ext}\,d_{min}$ between any 2 maxima.
Determine corresponding set of n negative minima $\{d_i^-\}$ at $\{\alpha_i^-\}$
If $n > 1$ **and** $\mod(\alpha_i^+ - \alpha_j^+, 2\pi) > \beta_{min}$
     $V = V \cup \{p\}$

```
   /* analyse distance function on ray from p to max/min
   For all points p in V
      Det. paths P_i from p to maxima (minima) of d^r on test circle
      Det. distance l_i from minima (maxima) on these paths to p
```
If $\sum |l_i|/n > l_{max}$
```
      Remove p from V

   /* identify clusters of saddle points
```
$SC = \emptyset$
```
   For all p in V
```
Identify clusters $\phi = \{SC_i\}$ with points q with $|p - q| \le r$.
If $\phi = \emptyset$
```
         Append new cluster to SC that contains p
```
Else
```
         Merge all clusters in φ and append p

   /* Reduce clusters to individual points
```
$V = \emptyset$ = list of saddle points
```
   For each cluster φ
      For each point p in φ
         Det. all n paths P_i from p to max (min) of d^r on test circle
         average-l = 0
         For pair of paths P_1 and P_2
```
Fit $a\,(x - b)^2 + c$ to d^r along the combined path
```
            average-l += b/n
      Append point with minimal average-l to list V of saddle points
```

Figure 3.12: Description of the algorithm to detect saddle points of d on S.

(z is the Hopf index). Numerically this is sensitive, and often the data needs to be fitted. The assumption we make is that along the radial lines the distance function fits a quadratic function $a\,(x-b)^2 + b$ in the distance x to p. The distance l is then $l = |b|$.

The saddle point identification process is summarised in Fig. 3.12.

Problems and Alternatives

Two problems associated with this approach are the following: Saddle points that form a line or even a surface patch of constant distance function are only detected if their spatial extent is smaller than the radius of the test circle r. This could be overcome allowing for non-circular paths, e.g. by starting with a circle but then growing further in those directions where the distance function does not exceed a prescribed threshold.

Also, the approach presented is not a multi-scale method. If the surface S has regions of different characteristic length scales, problems will be encountered. An approach where the test circle radius is more dynamic may be more suitable for that problem.

It is inherently a local method for a problem that has global implications: The distance function d induces two partitions of S into surface patches P_i through a watershed type algorithm [211]. The first (second) partition is into "bassins of maxima (minima) of d", i.e. every point $p \in S$ is assigned to the maximum (minimum) which can be reached along a path P along which the distance function d increases (decreases) monotonically. The set of points where the boundaries of the patches of these two distinct partitions coincide corresponds exactly to the set of saddle points.

This fact suggest an alternative procedure to detect the saddle points that avoids the possibility of global inconsistencies – which, due to its local nature, our approach cannot guarantee: compute the two partitions of S mentioned above and define the overlap of the two sets as the saddle points of S.

Finally, we mention that the global aspect of the problem gives rise to a fascinating theorem due to Hopf [92]: "The sum of the indices of all singularities of a regular vectorfield is equal to the characteristic of the surface":

$$\sum_j z_j = \chi(S) \tag{3.3}$$

where S is "a closed surface possessing continuous first derivatives at every point" and the sum is over all singularities of the vector field on S. A regular vector field is

a "field of tangent vectors (of unit length) defined and continuous at all but a finite number of points on this surface. These points are called singular points."[92][10].

At least on periodic surfaces, that can be regarded as closed surfaces if compactified [94], this theorem applies to the distance map d on S – providing a test for global consistency of the detected critical points.

3.6.2 Saddle points of the Euclidean distance map D in $\mathbb{E}^3$

After the preliminary discussion of the previous two sections, an identification procedure for saddle points of D is easy to implement.

For each point on the MS all directions of steepest ascent are determined: These are the images of the directions of steepest ascent on S at the corresponding surface points p_i ($\mathrm{ms}(p_i) = q$), i.e. the image $\mathrm{ms}(\nabla d(p_i)$ of the gradient of d on S and, for points p_i that are saddle points with Hopf-index $n \leq -1$, the images of the directions of maximal increase.
With appropriate thresholding, a point is then called a saddle point if the maximal angle between any pair of these directions exceeds a threshold-value. This threshold value is the minimal angle between the emanating edges from a saddle point.

With a double-cover representation of the MS, with the triangulations of the two sides not inter-connected except at the MS boundaries, identification of all surface points corresponding to an MS point q is difficult. Our solution to this problem is using a proximity test on the MS coordinates to detect nearby MS points. Alternatively, a single-sided MS representation may be more suitable, and can be obtained from the Voronoi diagram.

Finally, it is important to note that the saddle point identification process presented here is based on inherently local tests. This is foolish given the global implications of the saddle point and extrema structure of D. A combination of global approaches (such as watersheds) with the presented local method is likely to yield a more robust version of the saddle point detection. This is in particular desirable for experimental data, where a local method tends to produce many artefacts.

3.6.3 Detection of lines of steepest ascent

Once the saddle points are identified lines of steepest ascent are easily determined. Effectively, one advances the end point of the path on the MS by iteratively determin-

---

[10]An instructive discussion of the corresponding situation for the elevation on the globe is presented in Maxwell's "On Hills and Dales" [148].
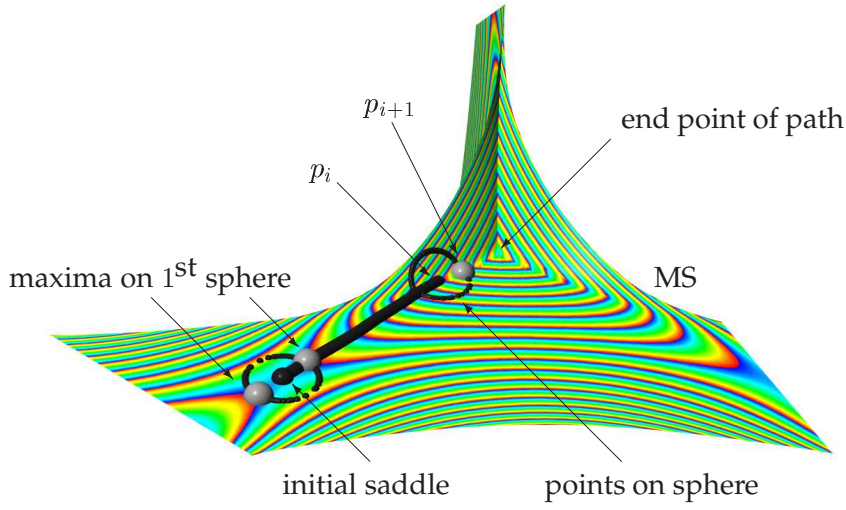
Figure 3.13: Tracing lines of steepest ascent starting from a saddle point of D. Shown is a patch of the MS (see page 193 for a description of the color scheme), of the tD surface, together with an intermediate step in the process of tracing a line graph segment. Starting from a saddle of D, the path is iteratively advanced by determining the maximum on the distance function on a sphere with radius equal to the desired step size (for practical purposes, one may exclude points in a small angle interval around the previous point). The point p_{i+1} is the maximum on the circle around p_i. From a single saddle, at least two line graph segments emerge. If the MS is flat in the vicinity of p_i, the points on the sphere form a circle around p_i. This is not the case if the MS is curved, or if p_i is on a branch line. Eventually, a maximum of D is reached.

ing maxima on the "circles" with radius equal to the desired step lengths around a saddle point s and setting the new end point to that maximum. This is repeated until a local maximum, or another saddle, of d is reached. See Fig. 3.13 for an illustration.

More precisely, for each saddle $s \in$ MS of D one determines the directions of maximally increasing distance function given as points $m_i \in$ MS on the sphere around the point s. The path emanating from s in direction of m_1 shall be determined. The path of steepest ascent P is intialised as $P = \{s, m_1\}$ with $n = 2$ elements. Iteratively, the points C of MS on a sphere in $\mathbb{E}^3$ around the end point p of P and of radius equal to the desired stepsize r are determined.[11] Also, the points C' that are contained in this sphere are determined. If the points C' contain a maximum (or possibly another saddle) m of D, the end point of the path is found and appended to P. Otherwise, the maximum p_{i+1} of D among the points C is appended to the path: $P = P \cup p_{i+1}$.

---

[11]Note that if p is on or near a branch line of MS, these points do not represent a circle, but rather circle segments or curves on a sphere. Furthermore, even if MS is not branched in the vicinity of p, the points still do not represent a geodesic circle on MS. However, as the task consists in integrating a function, D, defined on $\mathbb{E}^3$ rather than MS the stepsize should correspond to a distance in $\mathbb{E}^3$ and not a geodesic in-surface distance on MS.

The task of detecting a line $\mathbf{x} : [0,1] \rightarrow MS$ of steepest ascent is analogous to the problem of solving the equation

$$\nabla D = \frac{\partial \mathbf{x}}{\partial t} \quad \text{subject to} \quad \mathbf{x}(t=0) = s \quad \text{and} \quad \frac{\partial \mathbf{x}}{\partial t}(t=1) = t_s \qquad (3.4)$$

if D is a smooth function for which the gradient is well-defined. The point s is the saddle point of D from which the line graph segment $\mathbf{x}$ emanates, and t_s one of the directions of strongest increase out of the saddle s (the direction to the maximum on the first circle).[12]

The algorithmic definition, in contrast to the differential one, carries over to the case of a function D that does not necessarily possess continuous derivatives. In the smooth case, it yields an approximation to the solution of eq. 3.4. The quality of the approximation is obviously dependent on the stepsize r, i.e. the distance by which x is advanced in each step. It becomes an exact solution when $r \rightarrow 0$. However, in that limit noise, the finite sampling of D on the MS and imprecision in the calculation of D are more prominent than for larger stepsizes.

3.7 Representability of a labyrinth by a line graph

Much of the discussion in this chapter has focussed on the fundamental problem that geometric and topological requirements for a line graph cannot always be achieved simultaneously. This points to two questions: first, what are the labyrinths for which a line graph can be topologically equivalent to the domain <u>and</u> geometrically centered at the same time? Second, can a "quality measure" be found indicating how well a line graph represents a labyrinth? This section comments on these two issues.

Concerning the first question we notice that the examples where geometric and topological requirements could not be reconciled are domains with boundaries that are, at least on parts of their bounding surfaces S, not hyperbolic, i.e. have positive Gaussian curvature. In particular, labyrinth shapes with channels that are lengthwise divided into two streams by a narrow region that runs along the middle of a channel, such as

---

[12]For the case of the smooth function map D, the definition and classification of saddle points, maxima and minima can be made more precise, and is part of standard textbooks: A critical point is a point p where the gradient of the distance map D vanishes : $\nabla D(p) = 0$. If the point p is a maximum, minimum or a saddle point depends on the second derivative of D. The second derivative is represented by the 3×3 symmetric Hessian matrix of D. Its three eigenvectors are called principal axes of curvature as the magnitudes of the three second derivatives of D calculated with respect to these axes are extremised. The number of positive and negative eigenvalues of the Hessian then determines if the point is a saddle, minimum or maximum. Degeneracy, i.e. rank of the Hessian smaller than 3, need to be considered separately. This discussion is taken from Bader [11].

the bone-shaped cross-section in Fig. 3.14, seem impossible for a strictly hyperbolic bounding surface. Similarly, the pore with three connected channels and a distance function minimum at its center in Fig. 3.10 (middle) is inherently not hyperbolic.[13]

Furthermore, labyrinths with strictly hyperbolic bounding surface never have "dead-ends", i.e. channels that do not connect; some parts of a dead end necessarily have positive Gaussian curvature.

Based on these observations, and on the empirical evidence that the line graphs of all analysed IPMS have not required a compromise between the topological and geometric requirements, we suspect that labyrinths with strictly hyperbolic bounding surfaces, $K \leq 0$, allow for geometrically centered line graphs that have the same homotopy type as the labyrinths themselves.

For the discussion of the second issue, a measure assessing how well a labyrinth can be approximated by a line graph, it is useful to consider the reconstructability of the domain from the line graph and the relation to the MS: For a labyrinth that is essentially the union of balls (of varying diameter) centered on 1D space curves[14] the medial surface degenerates to a set of connected 1D space curves. By our definition the medial surface and the line graph are identical in this case. The union of maximal spheres on the line graph provides a complete reconstruction of the labyrinth.

In the essence, representing a labyrinth by a line graph corresponds to representing the labyrinth as a network of (possibly overlapping[15]) tubes with circular cross-section.

A possible measure to assess how well and how efficiently, in terms of space filling, a line graph represents the geometry of the labyrinth is given by comparision of the volume of the reconstructed and the original domain: Let V^o denote the total volume of the original domain, and V^r the volume of the union of maximal spheres on the line graph (the reconstructed domain). The volume of space that is covered by maximal spheres from more than one line graph segment is denoted V_d, see Fig. 3.14.

The volumes necessary for these two measures are difficult to compute for domains

---

[13]A somewhat similar situation appears at the triple-junction of the cubic Gyroid IPMS which represents a strictly hyperbolic geometry, see Fig. 5.9. At the triple junction, which corresponds to the only flat points of the Gyroid, the distance function has a saddle point with Hopf index -2, i.e. three directions of increasing and decreasing distance function values, respectively. In fact, the directions of decreasing distance function are almost constant. Even under distortions of the labyrinths, given by the one-parameter families tG and rG, no minimum of d is created which would lead to a ring of the line graph.

[14]There are obviously some restrictions on the radii and radius variations of the balls. Mathematically speaking, the labyrinth shall be one whose bounding surface is a canal surface.

[15]The tubes certainly overlap in the vicinity of the nodes of line graph. However, they may also overlap in other cases, e.g. spheres from the two geometrically centered line graphs in a channel with bone-like cross-section may overlap depending on the proximity and diameter of the two geometric centers.

Cross-section of a channel with
two parallel line graph segments

Side view of a channel with two
neighbouring maximal spheres

S

V^r V^d line graph   not part of V^d
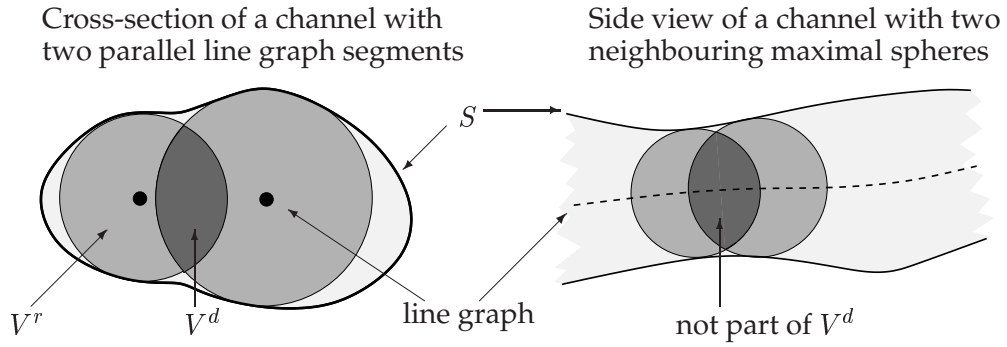
Figure 3.14: Different subvolumes defined for the measure assessing representability by a line graph. (Left) Maximal spheres on "parallel" graph segments may overlap; this is a sign of bad representation of the domain by a line graph. (Right) Neighbouring spheres on the same line graph segment always overlap, even if the line graph is a perfect representation of the domain.

represented as triangulations of the bounding surface. However, they are easy to compute for voxelised data sets.

Finally, the topological equivalence of the line graph and the domain can measured in terms of the number of rings in the line graph that can be shrunk to a point. As the line graph runs through all channels, and has the same number of components as D, the number of redundant rings is a good measure for the topological equivalence.

3.8   Images of line graph edges on S and watershed partitions

The line graph, and its "dual" graph connecting saddle points to minima, induce a watershed-like partition of both the domain C and the surface S. A few comments on this partition, and of the relation between graph segments and their preimages on the surface S are discussed.

The line graph constructed in this chapter consists contains the maxima of the Euclidean distance map D and lines between them. On any line between a pair of maxima there is always at least one saddle point of the D. In this way rings of sequences of maxima and saddle points are defined. A number of rings of this type may be the faces of a generalised polygon (with curved egdes and faces). Such a complex always encloses a minimum of D. It is precisely in this way that the line graph reproduces the watershed partition of space.

In a similar way, connections from saddle points to minima of D induce a dual partition where maxima of D are enclosed by generalised polygons that have saddles and maxima of D as the vertices of their edges. Note that this partition is not necessarily

one wherer each cell contains a node of the graph. A maximum of D does not need to be a node of the line graph, or vice versa. See for example the discussion of the Gyroid labyrinth in chapter 5.

A similar partition, but one dimension lower, is afforded by a network of lines of steepest ascent (descent) of the MS distance function d on S. The domain boundary $S = \partial C$ is segmented into surface patches containing a maximum (minimum) inside and saddle points and minima (maxima) of d on their bounding curves. This network of lines of steepest ascent is shown on the Primitive surface in Fig. 5.7.

It is possible, and has been suggested by us [184], to define the line graph of C as the network of lines of steepest ascent on S projected onto the MS. This network contains additional segments resulting from saddle points of d that are not saddles of D.

Geometrically, a relation between the line graph defined above and this latter line graph exists – due to the connection between maxima and saddles of D and d. If the equivalent paths of the line graph defined in this chapter and the image of the network of lines of steepest ascent on S are congruent, needs to be assessed carefully. In principle, the MS transformation may affect the gradient direction, which would result in a different path followed by the two paths. However, in particular for the cubic IPMS, no difference between the geometric paths of equivalent segments exist.

Concluding remarks

This chapter has elucidated many of the sensitive issues related to the definition of a line graph. In contrast to the MS construction, which is conceptually very robust and unambigiously defined, the definition of a line graph is subject to preference for topological or geometric representation and personal taste.

We have presented a definition that is clearly biased towards producing a geometrically centered line graph at the expense of homotopy equivalence between the domain and its line graph.

The computation of it relies strongly on the correct identification of saddles and maxima of D. Our method of detection relies on a local criterion, although adapted to cope with noise. A combination method that incorporates knowledge of the global combinatorial structure with the local geometric information would be desirable.

For the following chapters on line graphs of infinite periodic minimal surfaces, the method presented here allows for a reliable and sensitive characterisation of the graph connectivity and geometry that a topological method could not provide. For the section on experimental data, this chapter has set the principle by which we would like

to assign the line graph to a labyrinth even though its computation on the whole data set by an automated process without manual inspection is not possible.

With the definition provided we will be able to show that the line graph of many hyperbolic labyrinths is indeed well defined and a very picturesque model – if not even a little more.

Representations of Infinite Periodic Minimal Surfaces

This chapter describes the parametrisation of IPMS and the generation of discretised representations of their asymmetric unit-patches. Its main intention is to present a practical summary of the methods applied to generate IPMS representations on which the medial surface analysis can be carried out.

First, the key properties of and history of research into IPMS are summarised. The Weierstrass parametrisation for minimal surfaces is described, and illustrated with two specific examples. A catalogue of the Weierstrass functions and symmetry relations combined with a brief description is given for all IPMS analysed in the subsequent chapters 5 and 6.

Second, an algorithm to generate evenly triangulated representations of Fächenstücke of IPMS is introduced where all triangles are as close to equilateral (and of equal size) as possible. The approach is to coarsen a very dense but uneven sampling to generate a coarser but even triangulation. One of the key ideas is to implement a Monte Carlo method to find the most even triangulation.

4.1 Basic properties of IPMS

We consider infinite periodic minimal surfaces (IPMS) immersed in three dimensional Euclidean space $\mathbb{E}^3$. These are periodic, with three independent translational lattice vectors, and have constant vanishing mean curvature. In addition, we also require them to be embedded, i.e. free of self-intersections.[1]

---

[1]The term minimal is slightly misleading. The condition of vanishing mean curvature is equivalent to a vanishing derivative of the surface area functional under all infinitesimal normal variations of any bounded subsets of the surface. A normal variation is a deformation of the surface that can be expressed as $p(u, v) + \epsilon\, h(u, v)\, N(u, v)$ where h is a smooth real-valued function. The surface itself, i.e. $\epsilon = 0$, is a

An IMPS is always the common boundary of two distinct, individually connected but not simply connected, solid regions that are themselves triply-periodic. These solid regions are referred to as *labyrinths* and are defined as the two components of the complement of the surface in $\mathbb{E}^3$. This property of partitioning space into two continuous infinite components justifies the term *bicontinuous*, introduced by Scriven [189].

In general, the two distinct labyrinths can be different, both geometrically and topologically. A IPMS whose two labyrinths are congruent is called *balanced*, a name suggested by Fischer and Koch [57]. All IPMS with in-surface rotational axes, including in particular all those with asymmetric patches bounded by polygons, are balanced.

Because of the translational periodicity, analysis of properties of IPMS can always be restricted to the unit cell. If the IPMS has extra symmetries, its smallest representative fraction is even smaller[2]: Such an asymmetric unit patch is defined as a smallest surface patch from which any extended fraction of the IPMS can be obtained by application of congruence transformations in Euclidean space. The set of operations that needs to be applied in order to build a translational unit cell from the asymmetric unit patch is given by the 3D Euclidean space group of the IPMS.

If the surface is not balanced, the assignment of a space group to a IPMS is unambiguous. If the surface is balanced, however, an ambivalence arises: either one considers the *black-and-white* space group of the oriented surface or the space group of the non-oriented surface.

The former treats the two sides of the surface, or the two labyrinths, as different. Hence it contains no operations that map points within one labyrinth into the other. An asymmetric unit patch with a given normal orientation leads to a translational unit cell with a correctly oriented normal field. This is the appropriate space group for any analysis that involves out-of-surface properties – such as medial surfaces and normal fields.

On the other hand, the non-oriented space group treats both sides of the surface as equivalent. It contains operations that exchange the two sides of the surface, and hence the two labyrinths. For an analysis of purely intrinsic surface properties, such as Gaussian curvature, this is the appropriate description.

As is the case for all minimal surfaces, any IPMS can be parametrised locally using the Enneper-Weierstrass representation[3] that is attributed to A. Enneper [53] and K. Weierstraß [215]. Section 4.3 provides the details necessary for the work presented

---

critical point of the area, but not necessarily a minimum, see e.g. [47, 48].

[2]Whether a IPMS can exhibit translational symmetry alone is still an open question [91].

[3]In the following called Weierstrass representation.

here.

All minimal surface have an important isometry, known as the Bonnet transform, that is most easily understood in the context of the Weierstrass parametrisation. It consists in changing the complex phase of three functions, whose real parts are guaranteed to give the coordinates of a minimal surface, without changing the intrinsic geometric properties of the surface and hence its minimality. This produces a transformation that generates a whole surface family for any given minimal surface. In general, this transformation produces self-intersecting minimal surface families, with isolated members that are free of self-intersections. The typical examples are the family containing the helicoid and the catenoid, and the IPMS family containing the cubic Primitive, Diamond and Gyroid surfaces.

Two powerful statements about *linear asymptotes* and *plane lines of curvature* of minimal surfaces exist, and have been eminent in the description of IPMS. A linear asymptote is a surface geodesic that is a straight line. A plane line of curvature is a surface geodesic that is a planar curve (Def. from [64]). Any straight line embedded in an IPMS is a two-fold rotation axis, and any plane line of curvature (a planar geodesic) is a mirror plane of the global minimal surface [185].

4.2   History of and literature on IPMS

This section gives a short historical perspective on the mathematical description, parametrisation and discovery of IPMS. For details on the field of minimal surfaces in general we refer to [160, 45]. References to articles describing the relevance of IPMS in physical systems is given in chapter 5.

The first description of IPMS dates back to Riemann [174], Schwarz [185] and Neovius [157] in the late 19th century. Among the surfaces described by Schwarz are the IPMS now known as the Primitive (P), the Diamond (D), the Hexagonal (H) and the CLP surfaces. It is less well acknowledged that he has also described some of deformations of these surfaces, such as the rPD surface family. Neovius, a pupil of Schwarz, described a surface that is now called Neovius surface or C(P)[4]. All of these surfaces can be obtained by continuation of surface patches that are bounded by either straight lines or mirror planes. All of them contain an infinite number of straight lines, hence in-surface two-fold rotation axes, making these surfaces balanced. Neovius' and Schwarz' descriptions were based on Weierstrass-Enneper parametrisations of these surfaces.

---

[4]In Schoen's nomenclature it is the complement of the P surface [183].

Apart from Steßmann, who made further investigation into IPMS with patches bounded by four-sided polygons [206], the field of IPMS remained neglected for much of the 20th century.

In the 1960s Schoen [183] proposed another 12 surfaces without formal existence proofs, among them the Gyroid and the I-WP surface. He applied a wealth of mathematical ideas combined with Plateau-type soap film experiments. The Gyroid was a product of experiments with shearable plastic models, an experimental realisation of the Bonnet transform. The Gyroid was the first IPMS without embedded linear asymptotes or plane lines of curvature. He discovered the I-WP surface, bounded by a four-sided kaleidoskopic (mirror) cell, by realising that its adjoint surface patch is a Plateau border problem. He also introduced the concepts of complimentary surfaces (sharing the same set of straight lines) and labyrinth graphs.[5]

It is well known that an infinite number of IPMS exist [169].

In conjunction with increasing awareness among material scientists that IPMS and related surfaces form the basis of structure in many biological, chemical and physical systems (see the introduction) research into IPMS intensified in the 1980s, with many important contributions published in physical journals:

Fogden, Hyde, Lidin and others [134, 94, 135, 64, 65] established that the Weierstrass function of a large class of IPMS is essentially a product of factors $(\omega - \omega_i)^{-k}$ where ω_i are the branch points in the complex plane, i.e. the stereographic projection of the flat points in the Gauss map. The exponent k is dependent of the topology of the IPMS. Using this approach, an exhaustive enumeration of the so-called regular class IPMS was possible [64, 65].

Fischer and Koch [57, 119, 58, 120, 121, 59, 60] present a systematic crystallographic treatment of IPMS that contain in-surface two-fold rotation axes. Their results and new surfaces are based on analysis of the relative orientation and position of two-fold rotation axes in crystallographic space groups.

Karcher found a number of new surfaces using the conjugate surface method and the concept of handle insertion [112, 113]. This method is, as was Schoen's method, based on the realisation that a patch bounded by plain lines of curvature has a $\pi/2$-Bonnet associated patch bounded by straight lines. It is therefore equivalent to a Plateau problem. Karcher also established, by mathematical proofs, the existence of Schoen's surfaces [111].

---

[5]Karcher credits Schoen with "making [IPMS] popular in the natural sciences". Furthermore, Schoen filed an application for a patent for some IPMS entitled "Honeycomb Core Structures of Minimal Surface Tubule Sections", NASA case no. ERC-10, 363, serial no. 57253, 22. July, 1970

Brakke's program *Surface Evolver* [23] added an important numerical tool to the investigation of IPMS. It evolves triangulated representations of surfaces towards minimal energy, for example minimal mean curvature by a gradient descent method. It thus makes numerical soap film experiments possible.

Analysis of Bonnet associates of known IPMS was carried out by a number of authors in the 1990s, with the aim of finding analogies of the Gyroid which is a Bonnet relative of the Primitive and Diamond surfaces. Lidin and Larsson [136] analysed IPMS of hexagonal symmetry and found one hexagonal gyroid-like surface without linear asymptotes or plane lines of curvature, later named *Lidinoid* by Karcher [113]. Lidin and co-workers [135] found that the I-WP surface does not have any embedded Bonnet associates, and Fogden [61, 62] obtained the same conclusion for the F-RD and C(P) surfaces. Oguey and Sadoc [161] presented a more abstract analysis of crystallographic aspects of the Bonnet transform of IPMS showing that the isometric family of Bonnet-related minimal surfaces can be realised as a single surface in $\mathbb{E}^6$. Lidin [133] analyses point symmetry relations of Bonnet associates. All of these works are based on Weierstrass-Enneper representations of the respective surfaces.

Fogden *et al.* [63] and Fogden and Hyde [66] analysed one-parameter families of (embedded) IPMS, including rhombohedral and tetragonal deformations of the gyroid and pathsways between the cubic Primitive, Gyroid and Diamond surfaces, again based on the Weierstrass representation.

Fogden and Hyde [66] provide details of the expression of the Weierstrass integrals as elliptic integrals for rhombohedral and tetragonal distortions of the Gyroid, and Cvijović and Klinowski [36, 37, 38] give a similar analysis for a number of known IPMS.

Minimal surfaces are not the only hyperbolic and periodic space partitions. Implicit parametrisations as level-sets of sums over Fourier modes [213, 212, 217] provide ease of use and a wide range of surface families and topologies. Also there are good approximations of IPMS of this type, that are mathematically easier to handle than the Weierstrass-equations. Other classes include constant mean-curvature surfaces [84].

4.3   Weierstrass parametrisation of IPMS

The Weierstrass parametrisation is a parametrisation of a minimal surface $\mathcal{S}$ from the complex plane $\mathbb{C}$ into $\mathbb{E}^3$. The Euclidean coordinates are given as line integrals in the complex plane $\mathbb{C}$. It is a local parametrisation that maps simply connected regions of

$\mathbb{C}$ onto neighbourhoods of the surface in $\mathbb{E}^3$. However, using analytic continuation, and with the Riemann surface of the integrand as domain of integration, it represents a global parametrisation of $\mathcal{S}$.

The Weierstrass parametrisation is attributed to A. Enneper [53] and K. Weierstraß [215]. It is a subject of classical minimal surface theory. Comprehensive accounts of the Weierstrass-Enneper representation are given in [160, 45, 203].

The strength of the Weierstrass parametrisation is due to the following theorem (see e.g. [160], paragraph 156): The embedding of all minimal surfaces in $\mathbb{E}^3$ can be parametrised with a non-vanishing analytic $R(\omega)$, called Weierstrass function, via

$$
\begin{aligned}
x(\omega) &= x_0 + \mathrm{Re}\left(e^{\imath\theta}\int_{\omega_0}^{\omega}\left(1-\omega'^2\right)R(\omega')\right) \\
y(\omega) &= y_0 + \mathrm{Re}\left(e^{\imath\theta}\int_{\omega_0}^{\omega}\imath(1+\omega'^2)\,R(\omega')\right) \\
z(\omega) &= z_0 + \mathrm{Re}\left(e^{\imath\theta}\int_{\omega_0}^{\omega}2\,\omega'\,R(\omega')\right)
\end{aligned}
\tag{4.1}
$$

The angle θ is called the Bonnet angle.

The *Weierstrass function*, $R(\omega)$, completely determines all differential geometric properties of the surface S. The first and second fundamental forms, the Gaussian curvature and the metric are all given as simple expressions in $R(\omega)$ – and are independent of the Bonnet angle θ. In particular, the line element ds on the surface is given by

$$
ds = (1+|\omega|^2)\,|R(\omega)|\,|d\omega|.
\tag{4.2}
$$

Note that it diverges at the poles of $R(\omega)$.

The essential reason why the Weierstrass parametrisation is, a priori, only a local one becomes apparent from consideration of its inverse:

The Weierstrass parametrisation is the inverse of the composition of two simple maps from the surface onto the complex plane. This composition is given by $\sigma \circ \nu$ where σ is the stereographic projection and ν the Gauss map. The Gauss map maps a point on the Surface $\mathcal{S}$ onto its normal vector, pictured as its endpoint lying on the unit sphere $\mathbb{S}^2$,

$$
\nu : \mathcal{S} \to \mathbb{S}^2, \qquad p \mapsto N(p).
\tag{4.3}
$$
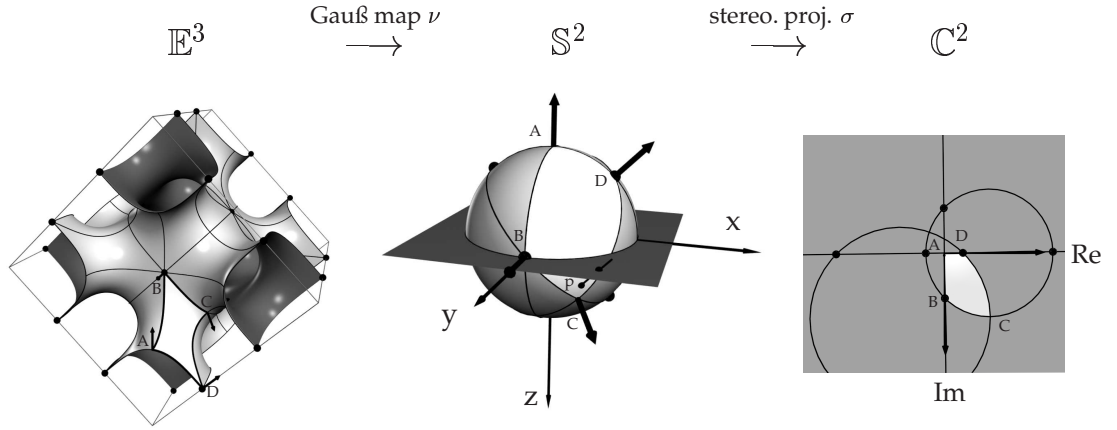
Figure 4.1: The Weierstrass parametrisation as the inverse of Gauss map and stereographic projection: (Left) A translational cubic unit cell of the I-WP surface in $\mathbb{E}^3$. One kaleidoscopic patch (from which the translational unit cell can be reconstructed by successive mirror inflections) is colored white and the normals at its four corner points A, B, C and D are indicated by small arrows. The lines on the surface indicate mirror planes. Flat points are marked with black spheres. (Middle) Gauss map of the kaleidoscopic patch on the unit sphere $\mathbb{S}^2$ together with the great-arc circles bounding it. The equatorial plane is the complex plane $\mathbb{C}$. The thin black line in the first quadrant – through the $(0, 0, 1)$ and a point p on the sphere – illustrates how the stereographic projection maps p onto $\mathbb{C}$. (Right) The kaleidoscopic patch after stereographic projection in the complex plane $\mathbb{C}$. The great circle arcs on $\mathbb{S}^2$ become circles and straight lines in $\mathbb{C}$. The small black dots indicate the location of the six branch points which are images of the flat points under $\sigma \circ \nu$.

The second is the stereographic projection, that maps a point on the unit sphere onto the complex plane. A point $p \in \mathbb{S}^2$ maps onto the intersection of the ray emanating from the north pole that passes through p with the equatorial plane, considered as the complex plane $\mathbb{C}$

$$\sigma : \mathbb{S}^2 \to \mathbb{C}, \qquad p = (x, y, z) \mapsto x/(1 - z) + \imath\, y/(1 - z) \tag{4.4}$$

Fig. 4.1 illustrates this composition for the cubic I-WP surface.

The Gauss map transforms the translational unit cell onto the unit sphere, but is not a bijection (a one-to-one correspondence). In the I-WP example, for a point q on the unit sphere $\mathbb{S}^2$ that does not correspond to a flatpoint, there are three distinct points $p_i \in \mathcal{S}$ with $i = 0, 1, 2$ with $\nu(p_i) = q$. If one wanted to make the Gauss map bijective, one would thus have to map $\mathcal{S}$ onto a triple covering of the unit sphere.

Plane lines of curvature and linear asymptotes in $\mathcal{S}$ (both of which are geodesics in
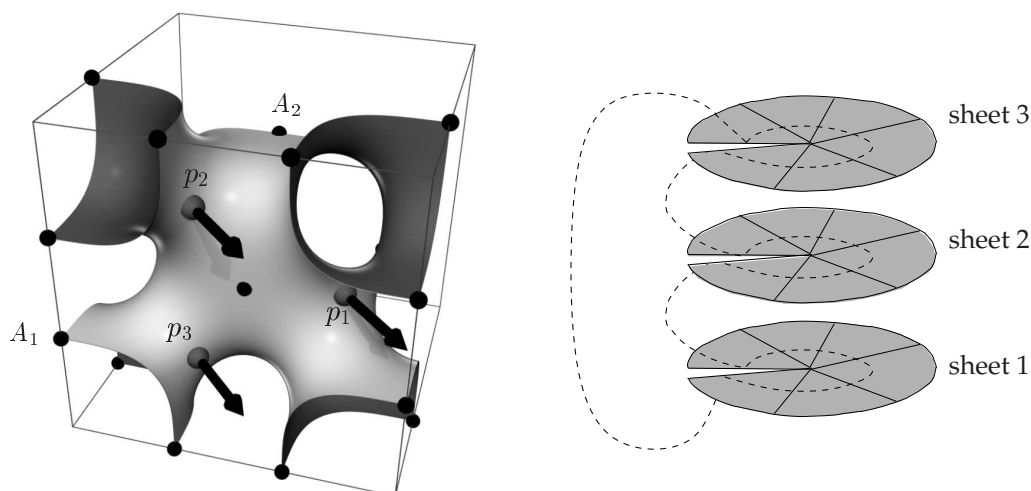
Figure 4.2: (Left) Three points p_1, p_2 and p_3 on the primitive translational unit cell of the I-WP surface with identical surface normal directions. A translational symmetry of the surface is (1/2, 1/2, 1/2) which transforms A_1 into A_2. This transformation demonstrates why the conventional cubic unit cell is not a primitive translational unit cell. (Right) Sketch of the Riemann surface of the cubic root function. It consists in 3 copies of the complex plane, sheets 1–3, that are sliced along the negative real axis. They are connected to each other as indicated by the dashed line.

$\mathcal{S}$) map onto great-circle arcs on the unit sphere[6]. All in-surface symmetries are preserved (excluding e.g. inversion in $\mathbb{E}^3$ in a point that is not on the surface).

Stereographic projection then maps the unit sphere onto the complex plane, shown on the right. This map is a bijection – the north pole maps to complex infinity. Great-circle arcs map onto circles (or straight lines through the origin). Hence, the kaleidoskopic patch from $\mathcal{S}$ maps onto a subset of $\mathbb{C}$ bounded by rays through the origin and circular arcs.

This example shows that the compositions of maps from the surface onto the complex plane is not bijective. This can, conceptually, be remedied by mapping the surface onto a multi-sheeted Riemann surface of R over $\mathbb{C}$ (their number corresponds to the number of covers of the sphere). Taking the Riemann surface as domain of integration for the Weierstrass parametrisation, the parametrisation can be extended to a global one. See Fig. 4.2 for an illustration.

The concept of Riemann surfaces is a general geometric construction in analytic function theory to deal with multi-valued inverses of analytic functions, such as the square

---

[6]For plane lines of curvature this result follows immediately from the fact that all normals along the plane line of curvature are contained in a plane. That plane has to cut the unit sphere in a great circle.

or cubic root. Essentially, multiple copies, *sheets*, of the domain of a function f with multi-valued inverse f^{-1} are joined, along branch cuts, so that the multiple values of $f^{-1}(y)$ are on separate sheets. See e.g. [165] for details on the Riemann surface.

For all examples discussed in this thesis, the Weierstrass function has the common form

$$R(\omega) = \left(\prod_{i=0}^{n} (\omega - \omega_i) \right)^{-b/(b+1)} \tag{4.5}$$

where n is the number of branch points (images of the finite flat points under $\sigma \circ \nu$), ω_i is the i-th branch point and b the order of the branch points[7]. The order of the branch points is the number of points in the unit cell with a given normal direction. Within the restricted class of surfaces considered here, this number is the same for any normal direction, other than those corresponding to flat points.

The Weierstrass function $R(\omega)$ has branch cuts, i.e. lines connecting the branch points, where $R(\omega)$ is not continuous as a function in $\mathbb{C}$. If $R(\omega)$ was defined on the Riemann surface, a multiple interconnected covering of the complex plane, these branch cuts represent the connections between the separate sheets. $R(\omega)$, and the Weierstrass parametrisation would be continuous there by virtue of changing to a different sheet.

If one ignores the multi-sheeted nature of the Riemann surface crossing a branch-cut corresponds to jumping from one of the n points with that exact normal vector to another one on the surface. Hence, for numerical integration one needs to know the branch cut structure of the Weierstrass function, and the effect of crossing branch cuts.

Symmetry considerations yield the domain in $\mathbb{C}$ that corresponds to an asymmetric unit patch. The following short description explains the principle (for details see [45]): First, the Gauss map of a translational unit of the surface is a dense cover of a (small, integral) number of unit spheres (because the genus minus 1 of the surface, which is always an integer, corresponds to the number of covers of the sphere). The Gauss maps of all asymmetric unit patches (differently oriented in space so that together they form the translational unit) are congruent. They form a tiling of a number of copies of the unit sphere. If all edges of the asymmetric unit are either plane lines of curvature or linear asymptotes (mapping onto great arc circles in $\mathbb{S}^2$ and onto circles or rays through the origin in $\mathbb{C}$) it is clear that the tiles in the complex plane are bounded by these circles or rays. See [64] for a discussion of many aspects of this tiling problem.

---

[7]This form has been established by Fogden and Hyde [64, 65, 61]. Their formulation is more general, in that different branch points may have different orders. However, all of the surfaces discussed in this thesis can be parametrised by this simpler formula.
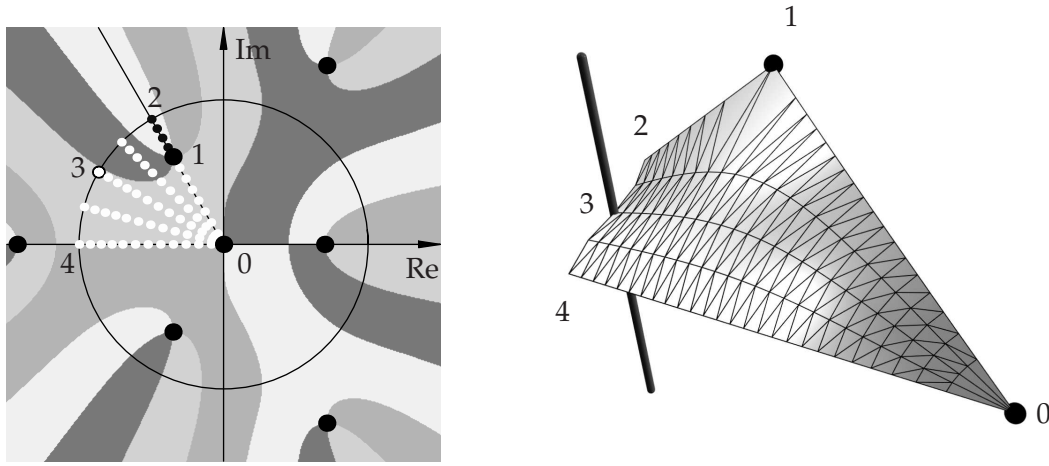
Figure 4.3: Weierstrass integration of asymmetric unit patch for the rPD surface family. (left) Complex plane with color mapping of sign of real and imaginary part of $g = \omega \, (\omega^3 - \omega_0^3) \, (\omega^3 + \omega_0^{-3})$. Branch cuts are the boundary between darkest gray ($\text{Re}(g) < 0$ and $\text{Im}(g) < 0$) and white ($\text{Re}(g) < 0$ and $\text{Im}(g) \geq 0$), in particular passing through the asymmetric patch ending at point 1.

In general, the tiles have to be chosen such that upon application of all symmetries the entire Riemann surface is covered exactly once.

4.4   Numerical integration

To obtain an asymmetric unit patch of a IPMS, a grid of points on the corresponding domain in the complex plane is created. Then each of these points is integrated to give a point on the surface. The difficulties in this approach arise from the branch cuts of R – that may cross the asymmetric unit patch. The branch points themselves are not a major problem as they are integrable singularities.

The actual numerical integration only requires standard techniques from numerical analysis. It is conveniently carried out using e.g. the *NIntegrate* command of the Mathematica software package [218]. It transforms the contour integrals to ordinary integrals of a single variable by choosing a particular parametrisation of the contour[8]. It then uses an adaptive Gaussian integration scheme with error estimation based on evaluation at Kronrod points (see e.g. ref. [40]).

---

[8]Conveniently this parametrisation can be influenced by giving specific intermediate path points. This is helpful when avoiding branch cuts and branch points.

We are illustrating the problems associated with branch cuts using the rPD surface (with $r_0 < 1$) as an example. Fig. 4.3 shows both the domain of integration together with a set of sample points and the resulting asymmetric unit patch in $\mathbb{E}^3$. All branch points are of order 1, leading to a double-sheeted Riemann surface of the Weierstrass function

$$R(\omega, \omega_0) = [\omega \left(\omega^3 - \omega_0^3\right) \left(\omega^3 + \omega_0^{-3}\right)]^{-1/2} \tag{4.6}$$

Branch cuts of R are all points in $\mathbb{C}$ where the polynomial $g(\omega, \omega_0) = \omega \left(\omega^3 - \omega_0^3\right) \left(\omega^3 + \omega_0^{-3}\right)$ is real and negative. An easy way to visualise them is to color the complex plane according to the sign of the real and imaginary part of the Weierstrass function, as in Fig. 4.3. The branch cuts are then easily identified as the boundaries between regions of $\mathrm{Re}(g) < 0, \mathrm{Im}(g) \geq 0$ (white in Fig. 4.3) and $\mathrm{Re}(g) < 0, \mathrm{Im}(g) < 0$ (dark gray).

A line integral along a path that does not cross any branch cuts is path independent. This is guaranteed by Cauchy's integral theorem that a contour integral along a closed path C in a simply connected region $R \subset \mathbb{C}$ over a function $f(z)$ that is analytic in R vanishes (see e.g. [165]). This means that we can choose an integration path that avoids the vicinity of branch points unless the end point is close to a singularity. For the rPD domain we choose e.g. integration along two straight segments from 0 to $0.5 \exp(\imath\, 3/4 \, \pi)$ for all white points, i.e. for all points that lie on the same branch.

Path integrals along a path that crosses branch cuts are problematic, e.g. the paths to all white points ω in Fig. 4.3. The problem is not the numerical problem of handling the integration over a discontinuity. That problem may be well-defined, and could be overcome by avoiding the branch cut by changing the integration path, for example from 0 to $\imath$ and from $\imath$ to ω.

The fundamental problem is that the analytic continuation of $R(z)$ across the branch cut (and that is the one yielding continuous paths on the minimal surface) is defined on the second branch of the Riemann surface. Crossing the branch cut should correspond to changing to the second branch. The branch structure of the rPD Weierstrass function is inherited from the square root function. Its two branches are defined by the two distinct values for the square root of a complex number $z = r \exp(\imath\, \theta)$

$$z^{1/2} = r^{1/2} \, e^{\imath\, \theta_0/2} \qquad \text{or} \quad z^{1/2} = r^{1/2} \, e^{\imath\, (\theta_0 + 2\pi)/2} \tag{4.7}$$

with $\theta_0 \in (-\pi/2, \pi/2]$. The first solution is often called the *principal branch*. Without jumping to the other sheet (but changing the path to avoid the branch cut), the points on the other side of the branch cut do not continuously connect, but form a sep-

arate patch (on the IPMS), but not on the asymmetric unit patch (for the rPD, they are inverted in the flat point in $\mathbb{E}^3$).

Indeed, in the example, we can explicitly implement the change of the branch by redefining the square root function to be

$$
\overline{\sqrt{z}} = \overline{\sqrt{r\,e^{\imath\,\theta}}} = \begin{cases} r^{1/2}\,e^{\imath\,(\theta_0 + 2\pi)/2} = e^{\imath\,\pi}\,\sqrt{z} & \text{if } \mathrm{Im}(z) > 0 \text{ and } \mathrm{Re}(z) < 0 \\ r^{1/2}\,e^{\imath\,\theta_0/2} = \sqrt{z} & \text{otherwise} \end{cases} \tag{4.8}
$$

for the points within the domain of the asymmetric unit patch, where θ_0 is the same as above.

The difficulty in this approach is the identification of branch lines or, in other words, the assignment of points in the domain of the unit patch to their branch. A systematic approach is difficult, but the visual analysis suggested here works well for the cases considered in this thesis.

Distortion of the sample point grid

A less fundamental but practically very important issue is the choice of sample points in $\mathbb{C}$. It is clear from the distortion of the length element, eq. (4.2), that the Weierstrass parametrisation is not isometric; distances are not preserved. In particular, this distortion becomes infinite at the poles.

This unisometry leads to considerable distortion of the sample point grid in the complex plane $\mathbb{C}$ upon integration. In Fig. 4.3 the points in the complex plane $r_i\,\exp(\imath\,\phi_i)$ are chosen on concentric circles around the origin with constant radial and angular intervals Δr and $\Delta \phi$. The distortion near the flat points 0 and 1 is clearly visible.

In many instances one wants to obtain an evenly spaced sampling on the surface, possibly even with a specific topology of the triangulation (e.g. a rectangular mesh). It is difficult to determine the corresponding sample points in $\mathbb{C}$, because of the distortion of point-point distances and because of the change in shape of the boundary polygon. In the rPD case a triangle is mapped onto a four-edge polygon.

It is, however, easy to generate a triangulation where the distance between nearest points is always smaller than a parameter δ. This is achieved, for example, by recursively and locally subdividing an initial coarse grid until it fulfills the requirement. It is also easy to generate a boundary polygon of the asymmetric unit patch with that property. In that case it is important to include poles on edges as vertices of the dis-

cretisation in order to properly resolve the resulting corners of the patch (e.g. point 1 in Fig. 4.3).

In Section 4.6 we describe an algorithm that coarsens a dense triangulation of this type to give a triangulation of almost equilateral triangles.

Symmetry requirements for the sample points

A further requirement for the sample points on the boundary of the asymmetric unit patch is that they comply with the symmetry group of the surface. Edges (or one edge) of the boundary polygon of the asymmetric unit patch that, upon application of one of the operations of the symmetry group, are mapped onto each other (or itself), are required to have matching discretisations.

This is trivially fulfilled for any discretisation of edges that are plane lines of curvature (mirror planes) or linear asymptotes (in-surface two-fold rotation axes).

A non-trivial example are the edges (2,3) and (3,4). In Fig. 4.3: an out of surface two-fold rotation maps (2,3) onto (4,3). The sample points for these two edges have to be chosen such that they match exactly upon application of that two-fold rotation. In this particular case, the discretisation shown does fulfill this requirement.

4.5 Parametrisations of specific IPMS

This section provides details of all those IPMS and their parametrisations that are analysed in the subsequent chapters. The results are summarised in Tables 4.2, 4.3 and 4.1, and Figure 4.4 that list symmetry positions. flat and corner points of the asymmetric unit patches of the Primitive, Gyroid, Diamond, I-WP, rG, rPD, tD and tG surfaces.

4.5.1 The cubic Primitive, Diamond and Gyroid surfaces

The most well-known and best studied IPMS are without a doubt the cubic Primitive, Diamond and Gyroid surfaces. Their common Weierstrass function is

$$R(\omega) = \left(1 - 14\,\omega^4 + \omega^8\right)^{-1/2}. \tag{4.9}$$

The three different surfaces are distinguished by their Bonnet angles of 0, $\pi/2$ and $1/\tan(K'/K) \approx 38.0147740^o$ for the Diamond, Primitive and Gyroid surface, respectively. $K = K(1/2)$ is the complete elliptic integral of the first kind.

(a) P, D and G   (b) I-WP   (c) tD ($r_0 = 1/3$)

(d) tG ($\phi_0 = -\pi/6$)   (e) rG ($\phi_0 = -3/8\pi$)   (f) rG ($\phi_0 = -1/12\pi$)
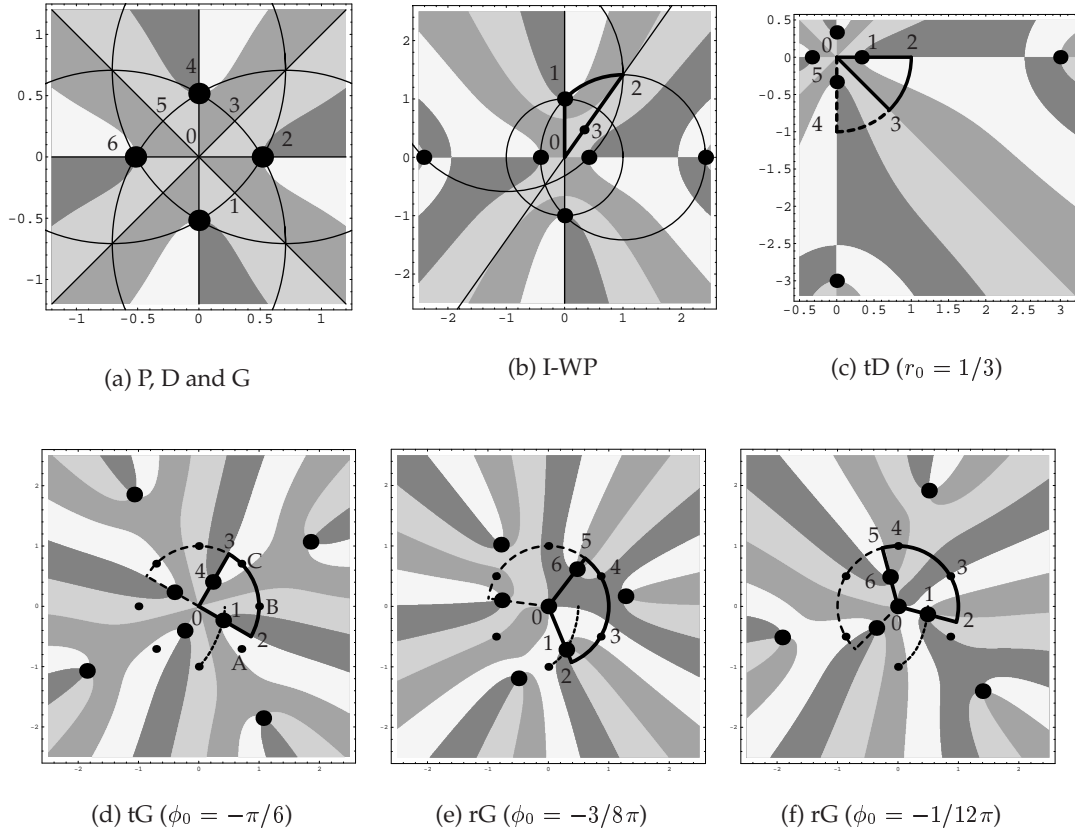
Figure 4.4: Domains of integration and location of branch cuts for the IPMS asymmetric unit patches discussed in section 4.5. Branch cuts are boundaries between white and the darkest gray. The big black points are branch points. Thick black lines are boundaries of the domain of integration for the asymmetric unit patch of the non-oriented space group, dashed lines of the oriented one.

For the Primitive surface, a domain of integration for the non-oriented space group is bounded by the circle of radius $\sqrt{2}$ at $1/\sqrt{2}\,(-1-i)$, the real axis and the diagonal through the first quadrant, the polygon (0–2–3–0) in Fig. 4.4. For the oriented space group the domain is twice as large, and can be the chosen to be the same as for the non-oriented space group plus its image under reflection in the real axis, (0–1–2–3–0). For the Diamond surface, the domain of integration for the non-oriented space group is the same as for the Primitive surface. The domain for the non-oriented domain is more conveniently chosen to be bounded by polygon (0–2–3–4–0) as this yields a Flächenstück that is contained in the crystallographic unit volume.

For the Gyroid, the domain for the non-oriented space group has to be chosen twice as large as for the Primitive and Diamond surfaces. It can be chosen to be bounded

		non-oriented spacegroup			oriented spacegroup		
Index	$\omega \in \mathbb{C}$	Cryst. coord.	Sym	Wyck	Cryst. coord	Sym	Wyck

Primitive		$Im\bar{3}m$		a=2.15652	$Pm\bar{3}m$		a'=a=2.15652
$x_1 = 0.3249, y_2 = 0.1751, x_2 = 1/4, y_2 = 1/4, \omega_1(\alpha) = -1/\sqrt{2}(1+\imath) + \sqrt{2}e^{\imath(\pi/6+\alpha)}$							
0	0	(1/2, 1/4, 0)	$\bar{4}m2$	12d	$(1/2, y_2, 0)$	mm2	12h
$0 \to 2$	$[0, (\sqrt{3}-1)/\sqrt{2}]$	(x, 1/4, x+1/2)	2	48i	(x, 1/4, x+1/2)	–	–
2	$(\sqrt{3}-1)/\sqrt{2}$	(1/4, 1/4, 1/4)	$\bar{3}m$	8c	(x_2, x_2, x_2)	3m	8g
$2 \to 3$	$\omega_1([0, \pi/6])$	(x, x, z)	m	48k	(x, x, z)	m	24m
3	$(\sqrt{2}-1)e^{\imath\pi/4}$	$(x_1, x_1, 0)$	mm2	24h	$(x_1, x_1, 0)$	mm2	12i
$0 \to 3$	$[0, \sqrt{2}-1]e^{\imath\pi/4}$	(x, y, 0)	m	48j	(x, y, 0)	m	24k
1	$(\sqrt{2}-1)e^{-\imath\pi/4}$	$(1/2, y_2, y_2)$	mm2	24h	$(1/2, y_2, y_2)$	mm2	12j
$2 \to 1$	$[\omega_1([0, \pi/6])]^*$	(x, y, y)	m	48k	(x, y, y)	m	24m
$0 \to 1$	$[0, \sqrt{2}-1]e^{\imath\pi/4}$	(1/2, y, z)	m	48k	(1/2, y, z)	m	24l

Diamond		$Pn\bar{3}m$ (origin at $\bar{4}3m$)		a=1.68575	$Fd\bar{3}m$ (origin at $\bar{4}3m$)		a'=2a = 3.37150
$\omega_1 = (\sqrt{3}-1)/\sqrt{2}, \omega_1(\alpha) = -1/\sqrt{2}(1+\imath)+\sqrt{2}e^{\imath(\pi/6+\alpha)}$							
0	0	(1/2, 1/2, 0)	$\bar{4}2m$	6d	(1/4, 1/4, 0)	2mm	48f
$0 \to 2$	$[0, \omega_1]$	(x, x, z)	m	24k	(x, x, z)	m	96g
2	ω_1	(1/4, 1/4, -1/4)	$\bar{3}m$	4c	(1/8, 1/8, -1/8)	3m	32e
$2 \to 3$	$\omega_1 e^{\imath[0, \pi/2]}$	(x, 1/4, x-1/2)	2	24j	(x+3/8, 1/8, x+1/8)	–	–
3	$(\sqrt{2}-1)e^{\imath\pi/4}$	(1/2, 1/4, 0)	222	12f	(1/4, 1/8, 0)	2	96h
$0 \to 3$	$[0, (\sqrt{2}-1)]e^{\imath\pi/4}$	(1/2, y, 0)	2	24h	(1/4, y, 0)	–	–
4	$\imath\omega_1$	(3/4, 1/4, 1/4)	$\bar{3}m$	4c	(3/8, 1/8, 1/8)	3m	32e
$0 \to 4$	$[0, \imath\omega_1]$	(x+1/2, -x+1/2, z)	m	24k	(x+1/2, -x, z)	m	96g

Gyroid		$Ia\bar{3}d$		a=2.65624	$I4_1 32$		a=2.65624
x_1=0.3375							
0	0	(0, 3/4, 1/8)	$\bar{4}$	24d	(0, 3/4, 1/4)	2	24f
2	ω_1	(0, 1/2, 0)	$\bar{3}$	16a	(0, 1/2, 0)	3	16e
3	$(\sqrt{2}-1)e^{\imath\pi/4}$	$(-1/4+x_1, 5/8, 1/2-x_1)$	2	48g	$(-1/4+x_1, 5/8, 1/2-x_1)$	2	24h
4	$\imath\omega_1$	(1/4, 3/4, 1/4)	$\bar{3}$	16a	(1/4, 3/4, 1/4)	3	16e
5	$(\sqrt{2}-1)e^{\imath 3\pi/4}$	$(1/8, 1/2+x_1, -1/4+x_1)$	2	48g	$(1/8, 1/2+x_1, -1/4+x_1)$	2	24h
6	$-\omega_1$	(0, 1, 0)	$\bar{3}$	16a	(0, 1, 0)	3	16e

I-WP		–			$Im\bar{3}m$		$a = 3.15491$
$x_0=0.2748, z_0=0.1667, y_0=1/2-x_0, x_1=0.1374, \omega_2(\alpha)=1+\sqrt{2}e^{\imath\alpha}$							
0	0	–	–	–	$(x_0, x_0, 0)$	mm2	24h
$0 \to 1$	$[0, \imath]$	–	–	–	(x, x, z)	m	48k
1	$\imath$	–	–	–	$(1/2, 1/2, z_0)$	4mm	12e
$1 \to 2$	$\omega_2([\pi/2, 3\pi/4])$	–	–	–	(1/2, y, z)	m	48j
2	$1 + \sqrt{2}\imath$	–	–	–	$(1/2, y_0, y_0)$	mm2	24h
3	$1/3 + \sqrt{2}/3\imath$	–	–	–	$(1/2-x_1, 1/4, x_1)$	2	48i

Table 4.1: Symmetry of the edges and corners of the asymmetric unit patches of the cubic Primitive, Diamond, Gyroid and I-WP surfaces. The lattice constants refer to the parameterisations as in eqs. (4.9) and (4.13). As the boundary of the asymmetric unit patch of the Gyroid consists in points in general position (except for the vertices and the points 3 and 5) its edges are not explicitly listed here. The symbol * denotes complex conjugation.

by the polygon (0–2–3–4–0). The patch for the oriented space group is again twice as large, that is the polygon (0–2–3–4–5–6–0).

4.5.2   The rhombohedral rPD surface family

The rPD surface family is a one-parameter family of IPMS of rhombohedral symmetry. For two singular values of the free parameter it corresponds to the cubic Diamond and Primitive surface, respectively. It hence represents a continuous pathway of embedded minimal surfaces between these two cubic surfaces.

It is the minimal surface spanning two parallel, horizontal equilateral triangles at distance c apart that are rotated by 60° around the vertical axis. By repeated two-fold rotations about the straight lines in $\mathbb{E}^3$ the rPD is generated from that catenoidal surface element [119].

Fogden and Hyde describe that "rhombohedral distortions [the rPD surface] of the D and P surfaces are obtained by pulling along the z-axis [...] (in the $[\overline{1}1\overline{1}]$ direction), stretching the screwed triangular catenoidal units [...]". By "stretching" they mean an anisotropic scaling (stretching) of the polygonal boundary of the catenoidal units and subsequent evaluation of the correct minimal surface for that boundary polygon. A stretch of the minimal surface patch, in the sense that the three point coordinates are simply multiplied with different factors, does not yield a minimal surface – $H = 0$ is trivially violated.

The rPD Weierstrass function is given by eq. (4.6) [185, 65, 66]. It possesses 8 first order branch points at 0, ∞ and $r_0 \exp(\imath \phi_i)$ and $1/r_0 \exp(\imath (\phi_i + \pi/3))$ with $\phi_i = 0$, $2\pi/3$, $4\pi/3$ (see Fig. 4.3). Changing the real parameter $r_0 \in [0, \infty]$ gives a continuous family of embedded IPMS where $r_0 = 1/\sqrt{2}$ gives the cubic Diamond surface and $r_0 = \sqrt{2}$ the cubic Primitive surface.

The space group of the non-oriented and oriented rPD surface is both $R\overline{3}m$, but the lattice parameter c is doubled in the latter case. Table 4.2 indicates the relation between the points on the complex plane and the symmetry sites in $\mathbb{E}^3$.

The domain of the asymmetric unit patch is a $\pi/3$ wedge inside the unit circle centered at 0. The angles $\pi/3$, π, $\pi/2$ and $\pi/2$ at the points 0, 1, 2, 3, and 4 (in Fig. 4.3) in the complex plane lead to an asymmetric patch with angles $\pi/6$, $\pi/2$, $\pi/2$ and $\pi/2$ at the respective points. The edge (0,1) is a plane line of curvature, (1,2) a linear asymptote, (2,4) neither of them but with a two-fold rotational axis in surface normal direction at point 3, and finally edge (4,0) is a linear asymptote.

Note that the domain of integration given in reference . [65] yields a Flächenstück

Index	$\omega \in \mathbb{C}$	non-oriented spacegroup			oriented spacegroup		
		Cryst. coord.	Sym	Wyck	Cryst. coord	Sym	Wyck
rG		$R\overline{3}c$, origin at $\overline{3}c$, hex. axes, $a = a(\phi_0)$, $c = c(\phi_0)$			$R32$, or. 32, hexagonal axes, a'=a, c'=c		
z_1=-1/4, x_1=1/6, z_2=-1/12, x_2=1/6, y_2=1/3, z_3=-1/2							
0	0	(0,0,0)	$\overline{3}.$	6b	$(0,0,z_1)$	3.	6c
1	$r_0\, e^{\imath \omega_0}$	(-1/6, 1/6, 1/6)	$\overline{1}$	18d	$(-x_1,x_1,z_2)$	1	18f
2	$e^{\imath \omega_0}$	variable	1	36f	variable	1	18f
3	$e^{\imath \pm \frac{1}{6}\pi}$	(0, y, 1/4)	.2	18e	(0,y,0)	.2	9d
4	$e^{\imath(\frac{1}{4}\pm\frac{1}{6})\pi}$	(x, 1/3, 1/12)	.2	18e	(x, 1/3, -1/6)	.2	9e
5	$e^{\imath(\omega_0+\frac{2}{3}\pi)}$	variable	1	36f	variable	1	18f
6	$r_0\, e^{\imath(\omega_0+\frac{2}{3}\pi)}$	(1/6, 1/3, -1/6)	$\overline{1}$	18d	(x_2, y_2, z_3)	1	18f
rPD		$R\overline{3}m$ (a,c), hexagonal axes			$R\overline{3}m$, hex. axes, $a' = a$, $c' = 2c$		
0	0	(0, 0, 0)	$\overline{3}m$	3a	$(2/3,1/3,0.1\overline{6})$	$3m$	6c
	$[0, r_0]\, e^{\imath\, 2\pi/3}$	(x, 2x, z)	m	18h	$(2\overline{x},\overline{x},z)$	m	18h
1	$r_0\, e^{\imath\, 2\pi/3}$	(1/6, 1/3, 1/3)	$2/m$	9e	$(-0.\overline{3},-0.1\overline{6},-0.1\overline{6})$	m	18h
	$[r_0, 1]\, e^{\imath\, 2\pi/3}$	(-1/3+x, 1/3, 1/3)	2	18f	$(0.\overline{3},0.\overline{3}+x,-0.1\overline{6})$	1	36i
2	$e^{\imath\, 2\pi/3}$	(-1/3+x, 1/3, 1/3)	2	18f	$(0.\overline{3},0.\overline{3}+x,-0.1\overline{6})$	1	36i
3	$e^{\imath\, 5\pi/6}$	(1/3, 2/3+y, 1/6)	2	18g	$(0.\overline{3},0.\overline{3},0)$	2	18f
4	$-\imath$	(x, x, 0)	2	18f	$(0.3+x,0.\overline{3},0.1\overline{6})$	1	36i
	$[-1, 0]\, \imath$	(x, x, 0)	2	18f	$(0.3+x,0.\overline{3},0.1\overline{6})$	1	36i

Table 4.2: Symmetry positions of (some of the) corners, special sites and edges of the asymmetric unit patches of the rPD and rG IPMS discussed in section 4.5. The notation $[a, b]\, e^{\imath \alpha}$ means $r\, e^{\imath \alpha}$ with $r \in [a, b]$, and similarly $r\, e^{\imath\, [c,d]}$ means $r\, e^{\imath \alpha}$ with $\alpha \in [c, d]$. The coordinates are crystallographic coordinates, for one of the possible asymmetric unit patches. Space group notation as in [85]. The indices refer to the points in Fig. 4.3 for the rPD, and in Fig. 4.4 for the rG.

twice as large. Their Flächenstück is bounded by linear asymptotes or plane lines of curvature on all four sides. It is, however, not asymmetric.

The domain as indicated here, and in similar form in [66], also does not extend to infinity. This has obvious advantages for the numerical integration and discretisation of the grid. The disadvantage is that a two ostensibly distinct cases arise, $r_0 > 1$ and $r_0 \leq 1$, distinguished by either a flat point on the real axis or one on the $e^{2/3\pi\imath}$ ray being within the domain. Alternatively, the domain could be chosen to be the $\pi/6$ wedge starting at $e^{2/3\pi\imath}$ and extending to complex infinity. In this case the two cases could be treated in a uniform manner. Also, the Fächenstück is then completely contained within the triangular prism that constitutes the asymmetric unit of the $R\overline{3}m$ space group.

The rPD family is self-adjoint, i.e. its members with $r_0 > 1$ have $\pi/2$ Bonnet-associates among the members with $r_0 < 1$. In particular, the cubic Primitive surface is the adjoint of the cubic Diamond surface.

Details of the integration are discussed in section 4.3.

4.5.3   The rhombohedral rG surface family

The rG surface is a one-parameter family of surfaces that contains the cubic Gyroid as one of its members. Its description is due to Fogden *et al.* [63, 66]. As the cubic Gyroid it does not contain any straight lines or mirror planes. It is of rhombohedral symmetry, i.e. if compared with the cubic case it only retains the three-fold and one two-fold rotation[9]. It is balanced, and the symmetry operation exchanging its two sides is a three-fold inversion rotation $\overline{3}$.

The Weierstrass function for the rG is given by

$$R(\omega, \omega_0) = \left[\omega\left(\omega^3 - \omega_0^3\right)\left(\omega^3 + \omega_0^{-3}\right)\right]^{-1/2} \tag{4.10}$$

where $\omega_0 = r_0 \exp(\imath \phi_0)$. Constraints for the lock-in of the surface into the $R\overline{3}c$ space group eliminate two of the three, a priori free, parameters r_0, ϕ_0 and θ. If, as in [66], one chooses ϕ_0 as the free parameter θ and r_0 follow as the (numerical) solution of two transcendental equations (see the appendix of [66]). The free parameter ϕ_0 is restricted to the interval $-\pi/2 \leq \phi_0 \leq 0$. Tab. 4.2 lists coordinates and symmetries of the corners of the asymmetric unit patch.

Note that the rG Weierstrass function is identical to that of the rPD surface, eq. 4.6. The two surface families are distinguished by different relations between the Bonnet angle ϕ and ω_0. However, the end point of the rG surface with ω_0 on the real axis corresponds to a member of the rPD surface.

The space group of the non-oriented rG surface is $R\overline{3}c$, and the space group of the oriented rG surface $R32$. for both space groups, crystallographic hexagonal coordinates $\{X, Y, Z\}$ and Euclidean coordinates $\{x, y, z\}$ are related by the equation

$$\{x, y, z\} = \left\{-\frac{\sqrt{3}\,a}{2}(X - Y),\ -\frac{a}{2}(X + Y),\ c\,Z\right\}. \tag{4.11}$$

Note though that the origin is chosen differently for the two space groups (related by a translation in c direction). While the origin of the non-oriented rG surface in the $R\overline{3}c$ space group (No. 167, hexagonal axes) is on the surface at the flat points with vertical normals (i.e. in c-direction), the origin of the oriented rG surface in the $R32$ space group (No. 155, hexagonal axes) is inside the labyrinth channels, at one of the types of line graph nodes (the big yellow spheres on the medial surface in Fig. 6.7).

---

[9]It retains one two-fold axis (18e) in the space group $R\overline{3}c$ of the non-oriented surface that includes interchanges of the two sides of the surface. The space group $R32$ of the oriented surface has two distinct two-fold axes.

The (non-oriented) asymmetric unit patch is a $2\pi/3$ wedge between the rays $r\,\exp(\imath\,\phi_0$ and $r\,\exp(\imath\,(\phi_0+2\pi/3$ contained within the unit circle. Branch cuts cross the asymmetric unit patch, and change with varying ϕ_0, making the numerical integration difficult. A redefinition of the square root function as in eq. (4.8), or the fact that points on the different branches are related by an inversion in the origin solves this problem.

The boundary of the coordinate grid needs to be symmetric with respect to the two-fold rotation axes as $\exp(-\imath\pi/6)$, $\exp(\imath\pi/6)$ and $\imath$ – depending on which of this actually lie within the domain of the asymmetric unit patch.

4.5.4 The tetragonal tD and tP surface families

The surface families tD and tP arise as tetragonal distortions, i.e. retaining 4-fold rotational symmetry, of the cubic Diamond and Primitive surfaces. These one-parameter families are adjoints of each other.

The parametrisations of tD and tP are well-known [185, 36, 65, 66]. The Weierstrass function is given by

$$R(\omega, \omega_0) = e^{\imath\,\theta}\,[(\omega^4 - \omega_0^4)(\omega^4 - \omega_0^{-4})]^{-1/2} \tag{4.12}$$

where $\omega_0 = r_0 \in [0, 1]$. For the tD family the Bonnet angle is $\theta = 0$, for the tP family $\theta = \pi/2$.

The symmetry group of the non-oriented tD family is $P4_2/nnm$, and that of the oriented surface is $I4_1/amd$. A portion of the tD surface in $P4_2/nnm$ orientation (origin choice 1 in space group No. 134 in [85]) is transformed into $I4_1/amd$ orientation (origin choice 1 in space group No. 141) by the following steps: (1) mirror inflection in the (010) plane[10], (2) rotation in clockwise sense around the [001] axis by $5\pi/4$[11], and (3) translation by $c/2$ (referring to $P4_2/nnm$) along the [00-1] axis. The lattice parameters in the different space groups are related by $a(I4_1/amd) = \sqrt{2}\,a(P4_2/nnm)$ and $c(I4_1/amd) = 2\,c(P4_2/nnm)$.

For $r_0 = \sqrt{2 - \sqrt{3}} \approx 0.517638$ the tD [tP] surface is congruent to the cubic Diamond [Primitive] surface.

Numerical integration is straightforward. As all edges of the asymmetric unit patch are either mirror planes or in-surface two-fold rotation axes any discretisation will

---

[10]Note that this plane is not a mirror plane of the symmetry group.

[11]$\pi/4$ rotation is sufficient to map the surfaces onto each other. The additional π rotation ensures that the conventional asymmetric unit cell of $P4_2/nnm$ is rotated into a subvolume of the $I4_1/amd$ asymmetric unit cell

		non-oriented spacegroup			oriented spacegroup		
Index	$\omega \in \mathbb{C}$	Cryst. coord.	Sym	Wyck	Cryst. coord	Sym	Wyck
tD		$P4_2/nnn$, origin at $\overline{4}2m$, $a = a(r_0)$, $c = c(r_0)$			$I4_1/amd$, origin at $\overline{4}m2$, $a' = \sqrt{2}\,a$, $c' = \sqrt{2}\,c$		
$z_1 = -1/4,\ y_1 = 1/4,\ z_2 = -1/8,\ y_2 = 1/4,\ x_3 = -1/4,\ y_3 = 1/4,\ z_3 = -3/8,\ x_4 = -1/4,\ z_4 = -3/8$							
0	0	$(0,0,0)$	$\overline{4}2m$	2a	$(0,0,z_1)$	2mm.	8e
$0 \to 1$	$[0,r_0]$	(x,x,z)	..m	8m	$(0,x,y)$	.m.	16h
1	r_0	$(1/4,1/4,1/4)$	..2/m	4f	$(0,y_1,z_2)$	.m.	16h
$1 \to 2$	$[r_0,1]$	$(x,\ x+1/2,\ 1/4)$	..2	8k	$(x,\ 1/4,\ \text{-}1/8)$	–	32i
2	1	$(0,1/2,1/4)$	2.22	4d	$(1/4,\ y_2,\ \text{-}1/8)$	.2.	16f
$2 \to 3$	$e^{i\,[0,-\pi/4]}$	$(0,1/2,z)$	2..	8h	$(1/4,\ 1/4,\ z)$	–	32i
3	$e^{-i\,\pi/4}$	$(0,1/2,0)$	222.	4c	$(x_3+1/2,\ \text{-}x_3,\ \text{-}1/4)$	..2	16g
$3 \to 0$	$[0,1]\,e^{-i\,\pi/4}$	$(0,y,0)$	.2.	8i	$(x,\ x,\ \text{-}1/4)$	–	32i
$3 \to 4$	$e^{i\,[-\pi/4,-\pi/2]}$				$(1/4,\ 1/4,\ z)$	–	32i
4	$e^{-i\,\pi/2}$				$(\text{-}x_4,\ 1/4,\ \text{-}3/8)$	.2.	16f
$4 \to 5$	$[1,r_0]\,e^{-i\,\pi/2}$				$(x_4,\ y,\ z_4)$	–	32i
5	$r_0\,e^{-i\,\pi/2}$				$(0,\ y_3,\ z_3)$	.m.	16h
$5 \to 0$	$[0,1]\,e^{-i\,\pi/2}$				$(x,\ 0,\ z)$	.m.	16h
tG		$I4_1/acd$, origin at $\overline{4}c2_1$, $a=a(\phi_0)$, $c=c(\phi_0)$			$I4_122$, origin at 222, $a'=a$, $c'=c$		
$y_0 = y_0(\phi_0),\ z_0 = -1/4,\ x_2=0,\ y_2=1/4,\ z_2=\text{-}1/8,\ x_4=\text{-}1/4,\ y_4=0,\ z_4=\text{-}3/8$							
0	0	$(0,0,0)$	$\overline{4}..$	8a	$(0,0,z_0)$	2..	8c
1	$r_0\,e^{i\,\phi_0}$	$(0,1/4,1/8)$	$\overline{1}$	16c	(x_2,y_2,z_2)	–	16g
2	$e^{i\,\phi_0}$	(x,y,z)	–	32g	(x,y,z)	–	16g
A	$e^{-i\,\pi/4}$	$(\text{-}x_1+1/2,\ x_1+1/2,\ 1/4)$	..2	16f	$(\text{-}x_3,\ x_3,\ 0)$	..2	8e
B	1	$(\text{-}1/4,-y_0+1/2,1/8)$	.2.	16e	$(\text{-}1/4,-y_0,\text{-}1/8)$	.2.	8f
3	$e^{i\,(\phi_0+\pi/2)}$	(x,y,z)	–	32g	(x,y,z)	–	16g
4	$r_0\,e^{i\,(\phi_0+\pi/2)}$	$(\text{-}1/4,\ 0,\ \text{-}1/8)$	$\overline{1}$	16c	$(x_4,\ y_4,\ z_4)$	–	16g

Table 4.3: Symmetry positions of (some of the) corners, special sites and edges of the asymmetric unit patches of the tetragonal tG and tD surfaces. Point indices refer to the points in Fig. 4.4.

continue seamlessly across the asymmetric patches.

4.5.5   The tetragonal distortion tG of the Gyroid

The tG surface is a one-parameter family of surfaces that contains the cubic Gyroid. It is of tetragonal symmetry. It can hence be viewed as a tetragonal distortion of the Gyroid, i.e. retaining the vertical four-fold axis but loosing the diagonal three-fold axes. Its two terminal points are members of the tD and tP families, respectively. Therefore, together with these two families it offers an alternative pathway of continuous and embedded IPMS between the three cubic surfaces P, D and G.

Its description is due to Fogden *et al.* [66, 63].

The Weierstrass function is the same as given in eq. (4.12). The free parameter can be chosen as ϕ_0. The other two, a priori free variables, r_0 and the Bonnet angle θ, then

follow as functions of ϕ_0 from the symmetry constraints formulated in appendix B of reference [66].

In order to fit into the space group $I4_1/acd$ of the non-oriented tG surface, the asymmetric unit patch given in the appendix of reference [66] has to be rotated by $\pi/2$ such that $y(\omega_0) = a/4$ and $x(\omega_0) = 0$.

The discretisation of the boundary of the asymmetric unit patch has to be compliant with the two-fold symmetry axes (normal to the surface) at $\exp(\imath\,\Phi)$ with $\Phi = -\pi/4, 0, \pi/4$ (points A, B and C in the Fig. 4.4 and Tab. 4.3).

The space group of the oriented tG surfaces is $I4_122$. The asymmetric unit patch of this space group consists of the asymmetric unit patch of the $I4_1/acd$ asymmetric unit patch plus a copy of it after application of the orientation-reversing four-fold inversion symmetry around the origin (point 0 in the Fig. 4.4 and Tab. 4.3). It is also translated along the negative z-axis by $c/4$. The translational unit-cells of both space groups are the same, hence also the two lattice parameters a and c.

The member that is congruent to the cubic Gyroid is $\varphi_0 = -\pi/4$.

4.5.6   The cubic I-WP surface

The I-WP surface is of cubic symmetry, $Im\overline{3}m$, and is not balanced. Figs. 4.1 and 4.2 illustrate the translational unit cell. Among the surfaces discussed here, it is the only one with branch points of order 2, hence with a three-sheeted Riemann surface.

It was first described by Schoen [183], and its Weierstrass parametrisation has been discussed in [135, 65, 38]. The name was given by Schoen, "I" for innen-zentriert (body centered) and "WP" for wrapped-parcel. This is according to his usual naming convention where the name is composed of two parts describing the symmetry or shape of the two labyrinth.

We here describe the orientation as in [135].

The asymmetric unit patch is a patch in the first quadrant of the complex plane bounded by the imaginary axis, the circle centered at 1 of radius $\sqrt{2}$ and the ray from the origin and through $1 + \imath\sqrt{2}$, see Fig. 4.4 (b). The first and second of these arcs are plane lines of curvature, whereas the third is somewhat arbitrary but contains the out-of-surface two-fold rotation point at $1/3 + \imath\sqrt{2}/3$.

Many representations in the literature [135, 65, 38] describe the kaleidoskopic patch (bounded by 4 plane lines of curvatures) that is twice as large. It is the kaleidoscopic patch that is shown in Fig. 4.2 as it is more easily recognised by the eye. However, it is not asymmetric.

The Weierstrass function is

$$R(\omega) = (\omega^6 - 5\omega^4 - 5\omega^2 + 1)^{-2/3} \tag{4.13}$$

and the Bonnet angle is $\theta = 0$.

The numerical integration is straightforward as the asymmetric unit patch (or for this purpose the kaleidoscopic patch) do not contain any branch cuts.

Some care needs to be taken to ensure that the discretisation of the edge from 0 to $1 + \imath\sqrt{2}$ displays the two-fold rotational symmetry of the point $1/3 + \imath\sqrt{2}/3$. A simple discretisation with identical step size on either side does not work. One way is to generate a discretisation on the straight line in $\mathbb{C}$ from 0 to $1/3 + \imath\sqrt{2}/3$ and apply a composition of inverse stereographic projection, the two-fold rotation and stereographic projection to these sample points.

4.6 Even triangulations of IPMS

This section describes a method for generating a triangulation of the asymmetric unit patch S of a IPMS where all triangles are as close as possible to being equilateral and of identical size (in $\mathbb{E}^3$.

Generation of such representations of IPMS is necessary in the context of this research as the medial surface algorithm presented in chapter 2 requires well-sampled input data. Strictly speaking, it requires an input where the distance between nearest sample points on the surface is dependent on the medial surface distance at the point. However, as the analysis presented here is not aimed at resolving features at varying length scales, a sample with uniform nearest point distance (in $\mathbb{E}^3$) is sufficient.

The idea is to put a relatively coarse but even triangulation onto a subset of a dense but uneven set of points sampling an asymmetric unitpatch. In the cases discussed here, the underlying dense set of points is created by application of the Weierstrass parametrisation described above.

The algorithm starts from the boundary of the patch and iteratively builds a triangulation with specified approximate edge length r on a subset of the dense but uneven set of points sampling the asymmetric patch. It consists of three steps:

(1) The boundary polygon of the dense sample is determined and discretised with

(a) Boundary polygon BP

(b) Ideal point far from BP

(c) Boundary Intersection

(d) Update BP and P

(e) Ideal point close to BP

(f) Nearest BP vertex

(g) Complete with defects

(h) Monte Carlo step

(i) After MC smoothing
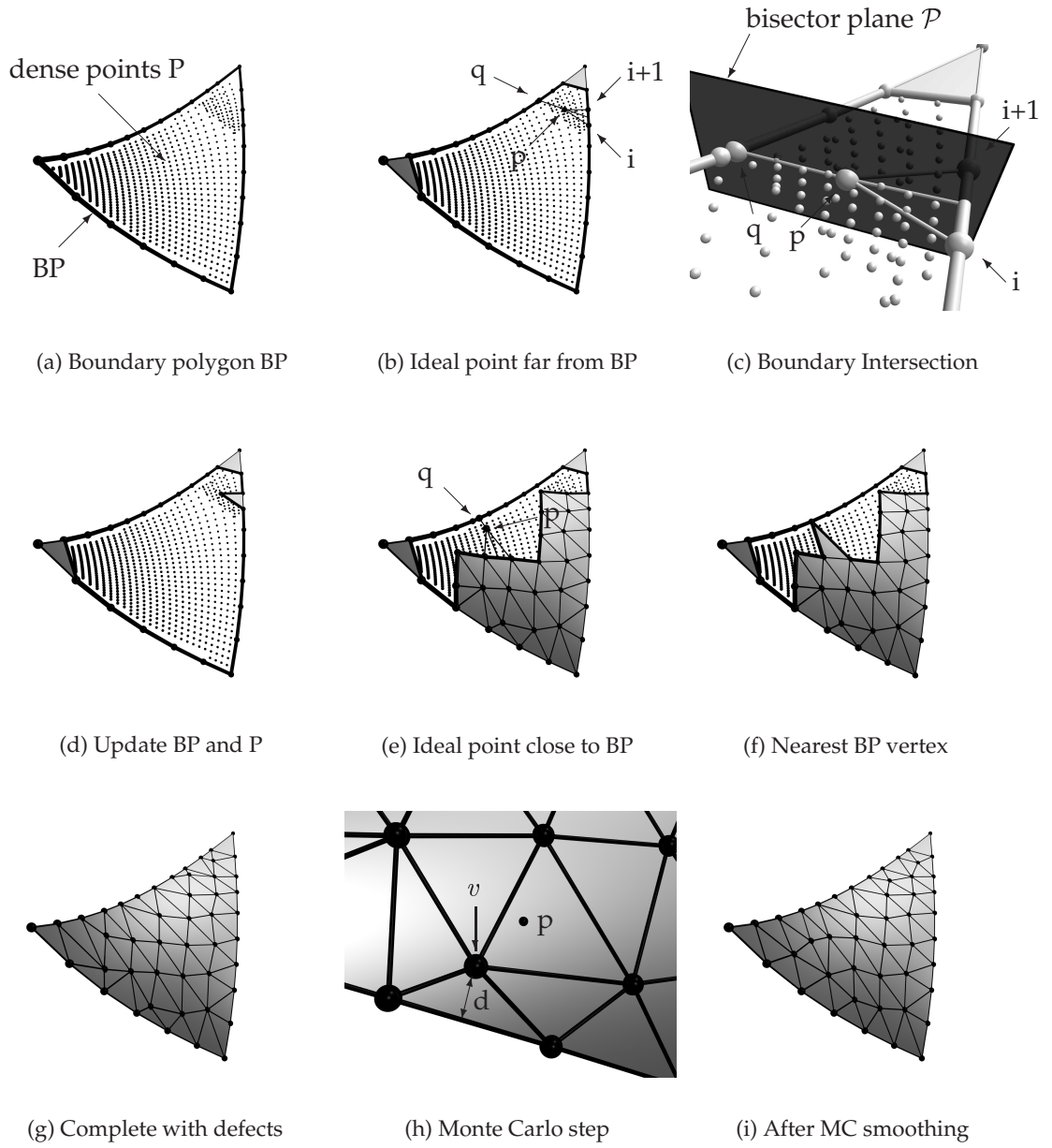
Figure 4.5: Illustration of the algorithm to evenly triangulate patches of IPMS.

point-point distance approximately equal to r. Corners and symmetries[12] are preserved.

(2) An edge e of the boundary polygon is chosen. The vertex p of the dense triangulation is determined that, together with e, forms the most perfect equilateral triangle.

---

[12]I.e. if the symmetry group of the IPMS contains operations that map a part of the boundary polygon onto a different part of the boundary polygon (or onto the same part in a different orientation) then the discretisation displays the same symmetries.

```
Algorithm EvenTriangulation
  Initialise empty set of new vertices :  V = ∅
  Initialise empty set of new triangles :  P = ∅

  /* discretise boundary polygon
  Discretised sets Bᵢ with edge length |Bᵢ|/int(|Bᵢ|/r) ≈ r
  Form closed boundary polygon BP from sets Bᵢ.
  Initiate set of boundaries BPS = {BP}
  Append points of BP to V.
  Remove points p with d(BP,p) < hₘ from P.

  /* build initial triangulation
  while BPS ≠ ∅ do
    BP = BPS[0]
    if BP is triangle then
      T = △(BP[0], BP[1], BP[2])
    else if ∃i : VertexAngle(BP[i]) < αc then
      T = △(BP[i-1], BP[i], BP[i+1])
    else
      Choose random edge e=(i,i+1) of BP
      q = NearestBoundaryIntersectPoint(e)
      if d(e,q) < h + hₘ then
        j = NearestBoundaryVertex(q, e)
        T = △(BP[i], BP[i+1], BP[j])
      else
        p = CreateIdealEquilateralVertex(e)
        V = V ∪ p
        T = △(BP[i], BP[i+1], p)
    Append T to P
    Remove points p with d(T,p) < hₘ from P.
    Update boundary polygon BP

  /* Monte Carlo smoothing
  Restore original point set P
  for all t in {0.5, 0.2, 0.1, 0.05}
    repeat n times
      choose random vertex v from V \ B
      d = MinAdjacentTriangleHeight(v)
      ΔF = AverageEdgeLengthFluc()
      choose random vertex p from P with |p − v| < d
      δF = AverageEdgeLengthFluc(v → p) - ΔF
      if exp[δf/(t ΔF)] < Random([0,1]) do
        replace v with d in P
```

Figure 4.6: Description of the algorithm to evenly triangulate patches of IPMS.

All vertices that lie 'within' the obtained triangle T are removed from the dense triangulation, with the exception of p. The triangle T is appended to a list representing the eventual triangulation. The edge e in the boundary polygon is replaced by the two

other edges of the triangle T . This process is repeated until the boundary polygon vanishes, i.e. until the whole patch is triangulated.

(3) A Monte Carlo procedure is used to even out differences in edge length. The 'energy functional' is given by the square of the average edge length. Repeatedly, a random point v of the new triangulation and a second random point p of the original dense triangulation in the vicinity of v are chosen. v is replaced by p according to a Monte Carlo criterion and only if the move does not produce overlapping triangles.

A property of this algorithm that is most important for our application is the following: all vertices of the obtained triangulation are vertices of the initial dense triangulation. The algorithm does not manipulate the coordinates (or any other property, e.g. normals) of any points; if the original points were exact points on the surface, then that evidently holds true for all points in the final triangulation. This is an important difference to surface smoothing algorithms that manipulate the coordinates of the vertices.

We find that for the surface patches presented in this thesis, application of this algorithm produces a triangulation where the typical square root of the mean square deviation of the edge length is approximately 0.1 in units of the average edge length. This is obtained if the initial triangulation if the maximal point point distance in the underlying dense triangulation is approximately 0.1 of the average edge length of the final triangulation.

Detailed description of algorithm

The input data consists in a set P of points sampling the surface $S \subset \mathbb{E}^3$, a set $\{B_i\}$ of sequences of points representing the boundary of the patch S and a parameter r specifying the desired average edge length for the final triangulation.

The requirements for the set P are that it is a good sample in the following sense: for any point $q \in S$ there is a point $p \in P$ such that $|p - q| < \kappa r$ where $\kappa \approx 0.1$ is a constant. It is also required that each point $p_i \in P$ has an associated normal direction n_i that is, approximately, the surface normal direction of S at the point p_i.

The set B is required to be a set of sequences $\{B_i\}$ of points on the boundary ∂S of S that fullfil the same criterion as the point set P plus an additional requirement that guarantees correct symmetry properties of the patch in the final triangulation:
The boundary ∂S is subdivided into subsets U_i with the following property: if a symmetry operation $T : \mathbb{E}^3 \rightarrow \mathbb{E}^3$ (of the IPMS) maps one of those subsets, say U_1, onto

∂S, then the image of U_1 under T is exactly one of the subsets U_i.

Beginning and end point of these subsets have to be part of the sequences B_i. More-over, if $T(U_i) = U_j$ then for all points $B_i[k]$ and $B_j[k]$ of their discretisations $T(B_i[k]) = B_j[k]$ is required.

The purpose of these conditions on B is to guarantee that the discretised patches yield a continuous triangulation of the IPMS upon application of the symmetry group – with vertices and edges on the boundary of one patch seamlessly joining with vertices and edges of the neighbouring patch.

All these requirements are easily fulfilled if B and P are obtained from mathematical parametrisations, such as the Weierstrass integrals, and if the symmetries of the IPMS are known.

The pseudo code in Fig. 4.6 and the illustrations in Fig. 4.5 together with the following clarifications explain the algorithm.

It is necessary to maintain a set of boundary polygons even though there is only one inital boundary polygon. Addition of a new triangle may therefore split the boundary polygon into two separate boundary polygons, as in Fig. 4.5 (f).

The distance function (point from edge, point from triangle) used throughout the algorithms denote distance from the geometric entity and not only from its vertices; e.g. points with $d(BP, p) < h_m$ all lie within a cylinder of radius h_m around the edges of BP.

The removal of points $d(BP, p) < h_m$ from the dense vertex set P ensures that the minimal triangle height h_m is not exceeded by any of the triangles of the final triangulation.

The vertex angle VertexAngle(BP[i]) is the oriented angle of the boundary polygon at the vertex i on the inside of BP. A critical angle $\alpha_c \approx \pi/3$ gives the threshold below which a vertex of BP is considered a sharp corner.

The function NearestBoundaryIntersectPoint(e) provides the nearest point on BP (in general not one of its vertices) in perpendicular direction from the edge e in the following

sense, see Fig. 4.5 (c): All intersection points $\{q_i\}$ of the perpendicular bisector plane of the edge e with BP are computed (There may be several if BP is not convex). Out of these q_i the nearest one q is the one that is minimises the distance $d(e, q_i)$ from the edge e and is in direction $n_i \times e_{ij}$ from the edge e, where $n(i)$ is the surface point normal of the vertex BP[i].

If the distance $d(e, q)$ from this nearest intersection point to the center of the edge e is smaller than the desired triangle height $\sqrt{2}\, r$ plus the minimal triangle height h_m required then the the third vertex of the triangle adjacent to e should not be a new point inside the patch but rather the nearest point on BP. The function NearestBoundaryIntersectPoint(q, e) then finds the nearest BP vertex to q that is not one of the two vertices of the original edge e.

CreateIdealEquilateralVertex(e) creates a point $p \in \mathbb{E}^3$ approximately on S such that the $\triangle(i, p, i+1)$ is of triangle height $\sqrt{2}\, r$. The point p is at $(p_i + p_{i+1})/2 + \sqrt{2}\, r\, (n \times e)/|n \times e|$. n is the edge normal, i.e. the average of the surface normals of the two edge vertices, and e the edge directional vector. p is approximately on S depending on the accuracy of the surface normals and the triangle length r compared to the curvature.

The update of the boundary polygon BP depends on what type of triangle has been added: If BP was a single triangle, then BP vanishes altogether. If the added triangle fills in a sharp corner (i-1, i, i+1) of BP then the edges (i-1, i) and (i, i+1) are replaced by a single edge (i-1, i+1). If the new triangle is the old edge e=(i,i+1) of BP plus a newly added point p then the edge (i, i+1) in BP is replaced by two edges (i,p) and (p,i+1), see Fig. 4.5 (d). If the new triangle is the old edge e=(i,i+1) plus a furter vertex p of BP then, again, the edge (i, i+1) in BP is replaced by two edges (i,p) and (p,i+1). Furthermore, BP is split up into two polygons at the vertex p that are both single closed loops, see Fig. 4.5 (f).

The triangles obtained by application of this algorithm to this point are nearly equilateral if the third vertex is from generation of a vertex by CreateIdealEquilateralVertex. The other steps do not create equilateral triangles – "they fill in where no perfect triangle can be created". The idea is to smooth out these irregularities via a Monte Carlo approach, combined with an annealing idea.

A measure for the deviations from evenness of the triangulation is provided by the fluctuations of the edge length of all triangles. This motivates the use of this measure

as an 'energy functional'

$$H(\mathcal{T}) = \sum_{\text{edges}} (l - \bar{l})^2 \tag{4.14}$$

where l is the length of the edge and $\bar{l}$ the average edge length over all edges of the triangulation.

A standard Monte Carlo (MC) approach is used to find the constellation that minimises this functional. An MC step consists in choosing a random vertex p of the triangulation that is not on the boundary of the patch (This additional condition ensures that the symmetry properties are preserved). Then a random vertex of the dense sample that lies within the set of adjacent triangles is chosen; this is most easily verified by computing d and ensuring the distance criterion, and ensures that changing p to v does not generate overlapping triangles.

The normalisation in the exponential factor is provided by the average edge length multiplied by an artificial temperature factor. AverageEdgeLengthFluc gives the square of the fluctuations of the edge length.

MS Analysis of cubic IPMS

This chapter discusses MS related properties of the cubic P(rimitive), D(iamond) and G(yroid) infinite periodic minimal surfaces (IPMS). We describe their geometry and demonstrate that the commonly accepted line skeletons – the simple cubic, the Diamond and the Y^*graph – are geometrically centered. An unexpected result here is that the three-coordinated nodes of the Gyroid are not at the widest point of its line graph (saddle points of D), but at the narrowest.

We argue that the degree of variation of the distance function on a IPMS provides a measure for *surface homogeneity*, in addition to the more common analysis of curvature fluctuations. The underlying idea is to extend an infinitesimal tiling of the surface to a tiling of $\mathbb{E}^3$ by infinitesimally narrow but macroscopically long cells. Each of the $\mathbb{E}^3$-tiles is the space foliated by a surface tile under transport in normal direction until it collapses on the MS. The less these $\mathbb{E}^3$-tiles vary in length or tilt, the more homogeneous the surface.

We show that the G surface is, in the sense of this measure and at least among these three surfaces, the most homogeneous (albeit not perfectly homogeneous) space partition with respect to packing properties. The G is followed by the D surface and then the P surface in terms of global homogeneity. This result is shown to be valid for three sensible length scale normalisations: isometric surfaces, surface-to-volume ratio of unity, and the same average distance function value. Consideration of packing properties is particularly important for these three surface forms because they are very similar (or identical) in terms of their curvature properties for all three length scale normalisations presented.

In addition to the three isomorphic P, D and G surfaces of genus 3, data for the cubic but not balanced I-WP surface of genus 4 is presented. One of its two labyrinths (the "WP" or wrapped-package network, christened "nbo" net by O'Keeffee[1]) turns out to

---

[1] See the homepage, http://okeeffe-ws1.la.asu.edu/RCSR/home.htm, of the Reticular Chemistry Structure Resource.

be as homogeneous in terms of channel diameter variations as the cubic Gyroid. The geometry and properties of the WP-labyrinth MS are similar to the Gyroid case, in that the nodes of the geometrically centered graph (which is shown to be the 4-connected graph with nodes at cubic face-centers) are saddle points of the Euclidean distance map D (EDM). This line graph differs from one that has recently been assumed in a line-defect study in smectic blue phases [43, 44].

The chapter is organised as follows: Section 5.1 defines our notion of surface homogeneity based on variations of the MS distance function values over the surface and gives some details on its computation. Section 5.2 summarises the origin of homogeneous surfaces and of the frustration between packing requirements and curvature homogeneity in liquid crystal self-assembly. Section 5.3 and 5.4 presents homogeneity data for the four cubic surfaces in the form of distance function histograms. Section 5.5 describes the details of the geometry of the four cubic surfaces, and the resulting line graphs, followed by some conclusive remarks.

5.1   Homogeneity and packing frustration

Space partitions based on embedded hyperbolic surfaces that divide $\mathbb{E}^3$ into two intertwined labyrinth are inherently inhomogeneous – both as far as intrinsic and extrinsic properties are concerned. The hyperbolic analogue of a sphere or a cylinder, where all points are identical in curvature and extrinsic properties (such as distance to the center), does not exist. The degree of homogeneity varies between surfaces, and measures for curvature inhomogeneity have been suggested and applied to discern between competing surfaces. In this section we introduce a measure that quantifies the extrinsic homogeneity by analysing variations of the channel diameter throughout the labyrinth. With reference to the energetics of mesophase formation we use the term "packing frustration".

Homogeneity and variations of Gaussian curvature have been studied by a number of authors: Hyde introduced the term *homogeneity* to account for energy differences between bicontinuous surfactant-water mesostructures of various symmetries modeled by IPMS [98, 95, 99]. Fogden and Hyde [66] have published second moments of the distribution of Gaussian curvatures of continuous families of IPMS. Schwarz and Gompper have published distributions of the Gaussian curvature distribution for a variety of cubic IPMS [188]. The relevance of curvature homogeneity in Helfrich systems is documented in [88, 95, 187].

Curvature inhomogeneity is the degree of variation of curvature over the surface. As a surface in $\mathbb{E}^3$ is completely characterised by its mean and Gaussian curvatures H and K, this reduces to variations of the Gaussian curvature for the case of IPMS (that by definition have $H = 0$ everywhere). A surface of constant Gaussian curvature is in this sense perfectly homogeneous. For positive and vanishing K the sphere and the cylinder are perfectly homogeneous. However, based on a very general mathematical result, no surface with negative and constant K can be immersed in $\mathbb{E}^3$ [90, 203]. Hence, a system striving for homogeneous and hyperbolic surface structure is necessarily frustrated.

The issue of global homogeneity is related to curvature inhomogeneity (but not fully determined by it). Global homogeneity is a measure of the homogeneity of the space tiling induced by a surface: We invoke the idea of a tiling of space by small volume elements, associated with small surface elements. A perfectly homogeneous space partition is one that allows a tiling of space by identical volume elements. A measure of the degree of homogeneity of inhomogeneous surfaces is given by the amplitude of variations in the size and shape of the volume elements.

The volume elements are defined in the following way. Given a small surface element dA on the surface S, the associated volume element is the space foliated by all parallel area elements $dA(r)$. The parallel area element $dA(r)$ is that part of the surface element dA after translation along its normal by a distance r that has not collapsed onto the MS, i.e. that fraction of the translated dA for which $r \leq d$ holds.

A strong relation between the surface element dA and the corresponding volume element dV exists. By virtue of the theorem of Steiner [181] the size of the parallel area elements $dA(r)$ of the surface element dA at point $p \in S$ is given as an expansion in mean curvature H and Gaussian curvature K
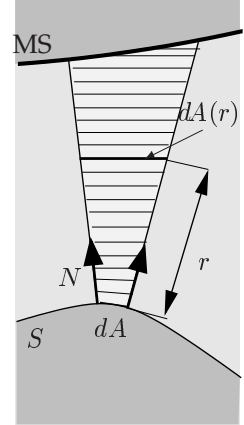
Figure 5.1:

$$dA(r) = dA(p)\left(1 + H(p)r + \frac{K(p)r^2}{2}\right).\tag{5.1}$$

For a finite surface element this formula only holds for $r < min_{p \in dA}d(p)$, that is until the first of its points collapses onto the MS. Even if dA is infinitesimal some care needs to be exercised as d is, as a function of S, not necessarily smooth.

Curvature inhomogeneity and global homogeneity can then be separately measured: the former as variations of the curvature, the latter as variations of the length of the

volume elements (i.e. the MS distance function). In this thesis, we consider solely the latter issue.

Our measure of homogeneity consists of the distribution $P(d)$ of the distance function over S, in particular its width (as for example measured by the standard deviation).

$$\Delta d = \sqrt{\langle (d - \langle d \rangle)^2 \rangle} = \sqrt{\langle d^2 \rangle - \langle d \rangle^2} \qquad \text{with} \quad \langle d^k \rangle = \int_{r=0}^{d_{max}} r^k \, P(r) dr. \qquad (5.2)$$

Volume- and area-weighted distributions of MS distances

A distribution of MS distances over the surface, or its second moment, yields a description of the packing frustration as outlined above. This section describes the computation of this distribution for triangulated data and the possible normalisations. Two sensible normalisations for this distribution are conceivable: either by the surface area of the interface or by the labyrinth volume (A trivial frequency distribution $F(d)$ that simply counts the number of sample points on S with distance function within the range $d + \Delta d$ is meaningless as the distribution of points on S is in general uneven and not representative of the metric of S).

From a differential geometric point of view, the most sensible distribution of d over S is one that is normalised by the total surface area of the surface S

$$P^A(d) = \frac{1}{A} \int_S da \, \delta(d' - d(p)) \qquad (5.3)$$

where $A = \int_S da$ is the total area of the surface S. In the remainder of this thesis, we refer to this area-weighted distribution as $P(d)$.

The second alternative is a normalisation to the total volume of the labyrinth, which may be a more relevant normalisation for situations where the volume is fixed rather than the total area. Using the partition presented in Figure 5.1) the domain is subdivided into volume elements of infinitesimal width but finite length, each of which is associated with points on S and hence with a distance function value d. Then the distribution, normalised by the total volume[2], is

$$P^V(d) = \frac{1}{V(C)} \int_C dV \, \delta(d' - d(p)) \qquad (5.4)$$

where C is the domain and $V(C)$ its total volume measure.

---

[2]Total volume here refers to the domain C, i.e. for a IPMS one of the two labyrinths. For a balanced IPMS that is identical to half the total volume.
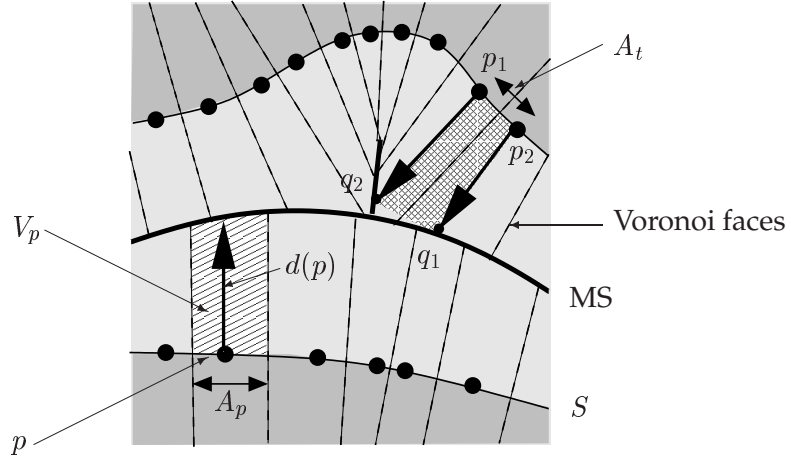
Figure 5.2: Normalisation of the distribution of MS distances by surface area or labyrinth volume:

In Section 5.4 we will show that the qualitative behaviour of these distributions, for the four investigated IPMS, is the same with either of the two weightings. The quantitative differences are small, owing to the similar surface-to-volume ratio of the investigated surfaces.

Computation of weights for triangulated domain representation

Numerically the distributions are easily evaluated once a triangulation of S and MS coordinates for all points of S are determined (for both area- and volume-weighted distributions). Two methods that yield the same result in the dense sampling limit can be used, one slightly more accurate at finite sampling density, the other one easier to implement. See Figure 5.2 as an illustration for the following notations.

For a vertex $p \in S$ we define $V_p = \mathrm{Vol}(C \cap C_V(p))$ as the volume of that part of the Voronoi cell $C_V(p)$ of p that is inside the domain C. This volume is the discrete analogue of the volume elements defined above in Figure 5.1. The discrete area element A_p is given as that part of (the triangulation of) S that is contained inside the Voronoi cell $C_V(p)$.[3]

An approximation to the distributions $P^A(x)$ and $P^V(x)$ is then calculated for each x and given a discretisation Δd, by summing the areas A_p (or volumes V_p) of all points p with $d \leq x < d + \Delta d$. We expect this approximation to converge well as the surface

---

[3]Here we assume sufficiently high sampling density of the surface S. If the sampling density is too low, it is possible that $C_V(p)$ may intersect with remote patches of S. This may be the case if, for example, the spacing between vertices in a narrow channel of C is too large. The assumption is that the surface patch inside $C_V(p)$ always contains p.

patch A_p appears to be the patch best represented by the point p.[4]

It involves, however, computation of intersections of polygonal cells and surfaces which is comparatively difficult to implement. Another difficulty appears for symmetric and periodic structures where the analysis can be restricted to the asymmetric unit-patch. Then the cells on the boundary of the patch need to be assigned a weight smaller than one to account for boundary effects.

A method that is easier to implement consists of going through all triangles rather than points of the triangulation. It yields the same result in the dense sampling limit, but is likely to give a slightly worse approximation for coarser triangulations.

We define the area element A_t as the area of a triangle t of the triangulation in 3D (or the length of an edge in 2D). The volume V_t is the volume of the cell given by the three vertices p_1, p_2 and p_3 of the triangle t together with their images $q_i = ms(p_i)$ on the MS.[5] Note that at finite sampling the face made up of the MS points need not be contained in the MS, as is illustrated in Figure 5.2.

A distribution of distance function values, either volume or area normalised, can be easily computed with these definitions. The distance function value that is assigned to a triangle of the triangulation is the average of the distance function values of its three vertices.

We finally mention that another type of distribution is interesting, although less relevant to the problem of surface homogeneity: $P_M(r)$ is the fraction of the total cell volume for which the distance D to the closest point on S is $r \leq D < r + \Delta d$. In fact, this measure is a distribution of the Euclidean distance map. Also, the points of identical distance function values are obviously reduced parallel surface sheets of S. This in turn means that $P_M(r)$ is the first Minkowski functional (the area) of the reduced parallel surfaces of S as a function r.

Effect of noise and small perturbations on the distance distribution

The MS construction can been criticised for its sensitivities to small changes of the surface shape. In particular, only a small deformation of the surface is necessary to

---

[4]In some sense this association is reminiscent of the natural surface coordinates introduced by Boissonnat and Cazals [21].

[5]A slight problem arises as some of the faces are not necessarily planar. For example, the face p_1, p_2, q_1, q_2 is only planar if the normal of p_1 lies in the plane spanned by the edge p_1 to p_2 and the surface normal of p_2. If that is not the case and that facet is buckled, the volume is not unambiguously defined. One needs to triangulate these faces. This can be done in a consistent way such that the cells, as an ensemble, tile space. The error made due to this arbitrary choice is small in the dense sampling limit. Alternatively, a construction of the volume by foliation of space with parallel surface elements avoids this problem altogether.

induce spurious branches of the MS that come much closer to the surface than the MS of the original surface does (see Chapter 2). The distribution of distances is evidently subject to the same sensitivities, a small bump in the surface (see the elephant on page 16) can radically decrease d in its vicinity, but never increase it.

Note that this sensitivity applies to the distribution of (Gaussian) curvatures in the same way. Nevertheless, they have proven to be very useful. The argument in the curvature case is that any curvature above a certain threshold can be disregarded as noise. That same argument applies to the case of the distribution of distance function values, in particular if the normalisation is to the total surface area rather than to the volume.[6] We nevertheless need to demonstrate that our algorithm for the MS computation is robust with respect to small changes, and that the distribution of distances we obtain is indeed the correct result

Figure 5.3: MS distance distribution of a noisy oblate ellipsoid.

for the particular labyrinth in the infinite sampling limit. To that purpose, Figure 5.3 shows an analysis for the case of an oblate ellipsoid given by $(x/3)^2 + (y/2)^2 + z^2 = 1$: Connected small black dots are data for a high-resolution ellipsoid (n=2.4×10^4 vertices) for which the MS is computed by intersecting straight lines in surface normal direction through the surface points with the $z = 0$ plane. Large symbols indicate data computed with our algorithm. Data is presented for a relatively coarse triangulation (n=2.2×10^3) with exact normals (open circles) and without (open squares) and one where random numbers in $[-0.03\,l, 0.03\,l]$ are added to the surface coordinates (filled diamonds). The number l is the average triangle length.

We conclude that the distributions from our algorithm are indeed reliable approximations to the MS distance function distribution if the data stems from mathematical parameterisations. For experimental data, the quality of the distributions needs to be treated with the same caution as the MS construction itself.

---

[6]In both cases, this argument fails for multi-scale analyses. In those cases, setting an appropriate threshold becomes impossible. Fortunately, the preferred curvature model does not allow for variations of the curvature over many length scales.

5.2   Relevance to liquid crystalline mesophase formation

The relevance of the notion of homogeneity to a variety of self-assembly processes rests on the assumption of a preferred molecular shape. The mesophase that forms for a molecule of a given shape is the one where the deviations of the individual molecular shape from the preferred one are minimised while the global constraints imposed by the composition are fulfilled.

The literature on liquid crystalline mesophase formation is vast and cannot be reviewed in this chapter. Much of the material is contained in textbooks [99, 117, 56, 123]. The original work by Larsson [125], Fontell [69] remain invaluable references. Numerous reviews on bicontinuous mesophase formation [142, 97, 70, 190] and interface and curvature models [178] exist.

A brief introduction to mesophase formation in amphiphilic systems

The best-documented systems for which homogeneity arguments have been applied are amphiphilic lyotropic mesophases in surfactant-oil-water mixtures. Amphiphilic molecules (like natural lipids or synthetic surfactants and tensides) are schizophrenic molecules, in that they are made of two parts – a hydrophilic *headgroup* and one or more hydrophobic *tail(s)*.

Hydrophobic and hydrophilic components tend to demix, as hydrophobic molecules are expelled from water-like environments. Yet macroscopic phase separation is made impossible by the covalent bonding between the two parts. However, micro-geometries exist where local interfaces globally shield the hydrophobic parts from the hydrophilic ones. Among the wealth of geometries found in such systems are the relatively mundane *micelles*, arrays of spheres of oil in aqueous solution with a layer of amphiphilic molecules lining the interface – headgroups outside, tails inside. Also found are regular arrays of cylinders (hexagonal phases) of either oil in water or water in oil, and alternating flat layers of water and oil (*lamellae*). The amphiphilic molecules always assemble to form an the interface, with their headgroups towards the water phase and their tails into the oil phase.

The interfaces discussed in this thesis are hyperbolic bicontinuous surfaces, partitioning space into two intertwined yet disconnected labyrinths on either side. Typically, hydrophobic interfaces consist of a double layer of amphiphilic molecules (*bilayer*) wrapped onto the surface, either with the polar hydrophilic headgroups towards two water-filled channels separated by a hydrophobic layer (Type 2), or with the the hydrophobic tails sticking into two oil-filled channels with and the headgroup

assembling on the interface. These geometries can be adopted both by binary (water-amphiphiles mixtures) and by ternary systems (mixtures of water, oil and surfactants). In ternary systems, monolayer assembly is a further possibility where an oil channel is separated from a water channel by a layer of amphiphilic molecules.[7]

The concept of a preferred molecular shape

To a first approximation, amphiphilic molecules may be regarded as building blocks of a certain molecular shape, deviations from which are energetically penalised. The typical picture is that of a molecule of a disk-like hydrophilic headgroup of area A, with a hydrophobic tail attached to it that is characterised by a typical length and a typical width. These assumptions lead to the now-famous dimensionless *shape parameter $s = V/(a\,l)$* introduced by Israelachvili, Mitchell and Ninham [103] and critically reviewed in [207].

The so-defined shape parameter is related to curvature properties of the interface by the formula for the volume of the *parallel body* of a surface S, that is the volume foliated by parallel surfaces to S up to a distance l,

$$s^{\pm} := \frac{V^{\pm}}{A\,l^{\pm}} = 1 \mp H\,l + \frac{K\,l^2}{3} \tag{5.5}$$

where H and K are the mean and Gaussian curvature of the interface, and the superscript $\pm$ indicates that the shape parameter for the two different sides may be different. In particular, if the interface is a bilayer of identical molecules, the relation $s^{+} = s^{-}$ immediately dictates $H = 0$, that means a minimal surface.

This superficial discussion heuristically motivates curvature energy functionals of the form $E = k/2(H - c_0)^2 + \overline{k}K$ with bending moduli k, saddle-splay $\overline{k}$ and spontaneous curvature c_0. This functional is attributed to Canham [25] and Helfrich [87].

This expressions is also not restricted to the amphiphilic self-assembly case, but has been derived in similar form for block-copolymers [101], surfactant films with spontaneous curvature [67], and thin films of isotropic linear elastic material [122]. The simplest model for a surfactant molecule, a ball-and-spring model, is discussed in [167]. A review is given in [178].

---

[7]Note that the distinction between monolayers and bilayers is one of convenience only, as is argued in [96, 164, 102]: A bilayer can always be regarded as two monolayers, and assuming the existence of punctures, bilayer geometries can be transformed into monolayer geometries without tearing and gluing.
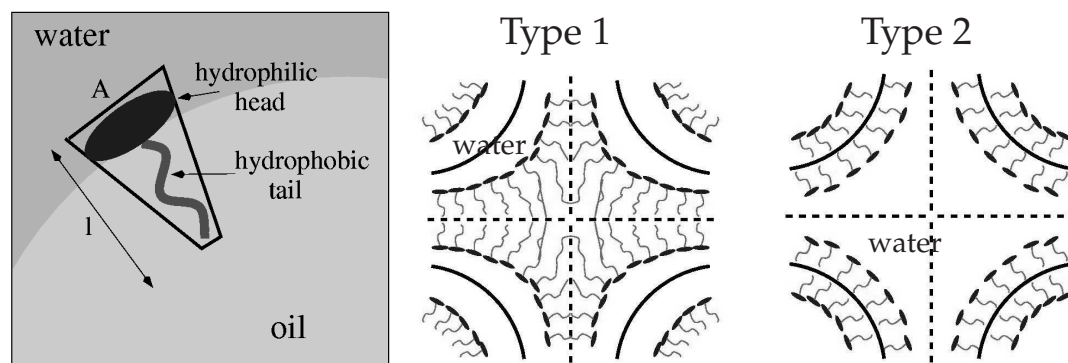
Figure 5.4: Surfactants and lipid molecules may be characterised by the shape parameter $V/(Al)$ where A is the head group area, l the average chain length and V the volume per molecule. These amphiphilic molecules rearrange water and oil in such a way that they pack with their tails in the oil-phase and their headgroup towards the water. Two types of mesophases are distinguished, illustrated by a cross-section through the P surface. Type II where two water-channels are separated by a hydrophobic bilayer, and Type I, where a layer of water separates two hydrophobic channels. These hydrophobic regions can be hydrocarbon chains with or with additional oil. The dashed lines, the cross-section of the MS, can be considered as the chaotic zones.

Chain stretching contributions – frustration

The picture of the preferred molecular shape suggests a preferred bending of the interface (dependent on the wedge angle of the idealised molecule) evident in the curvature contribution of the Helfrich functional. However this picture also suggests a preferred length of the molecule, again under the assumption of monodispersity.

A number of authors have adopted a harmonic contribution, $(l - l_0)^2$, of deviations from a nominal average length l_0 of the hydrocarbon chains [116, 5, 50, 188].

For Type 1 bilayer phases, bending and stretching contributions are somewhat linked, and frustrated. This is due to the fact that a parallel surface (constant l) of an minimal surface has variations in H and thus deviates from the preferred curvature c_0. Vice versa, a constant H interface related to a minimal surface (with average distance l_0) has necessarily variations in thickness [5, 28].

This result immediately follows from intrinsic properties only, and is the first indication of the importance of fluctuations of the Gaussian curvature. Energetically penalised deviations in mean curvature from the c_0 of the interface, parallel to a minimal surface, result from non-constant Gaussian curvature K on the minimal surface. The fact that fluctuations of K are a relevant measure determinant of the stability of

mesophase formation has been stated in [88, 95, 24] and more recently quantified by computation of distributions of K in [186, 187, 188].

A rather expected result is that chain stretching is prohibitive for small chains, whereas for large chains bending and stretching contributions are comparable. Pure curvature models are appropriate in the limit of small chain length compared to the average radius of curvature [178, 188] or more precisely the channel diameter.

Duesing *et al.* use this idea to quantify packing frustration in inverse hexagonal, micellar phases and bicontinuous phases (i.e. Type 2 [50]). Given a curvature-optimised interface (among the bicontinuous structures they only consider the D surface), they model the chain stretching contribution by a harmonic term $(l - l_0)^2$. They obtain an expression that penalises variations of the distance from the surface to its line skeleton. We argue that the MS distance function is a more suitable choice.

For Type 1 bilayer phases, global packing properties (as opposed to analysis of fluctuations of the distance between $H = const$ interfaces) can be more important if the chain length is of the same order as the channel diameter, i.e. the MS distance function. In that case, the tails overlap; in overly simplistic terms, the overlap volume is somehow related to the chain ends that penetrate further than the distance to the MS.

Relevance of the MS

In this thesis we refrain from proposing a specific model free-energy functional that incorporates MS measures. Instead we describe these properties in purely geometric terms. The biggest obstacle in formulating a free-energy functional is to incorporate the relative importance of stretching and bending. This translates into the difficulty of finding the correct length scale that is set by the complex interplay of these forces and the constraints imposed by the chemical composition.

In our view the elucidation of geometric principles, in this case that of variations of the channel thickness, is more important than the detailed quantitative analysis based on models that, owing to the intricacies of the physical system, incorporate many parameters, few of which can be measured directly. At the very least, gaining an understanding of the geometric principles is a necessary precursor to such calculations.

In many mesophases the average molecular chain length is not *much* smaller than the typical channel radius (used here as the macroscopic length scale). The curvature expansions are strictly valid in the limit of vanishing bilayer thickness only.[8] Typical

---

[8]Note that, given the possibility of surface transformations preserving minimality, incorporation of higher order terms is necessary even in this limit for consistency with thermodynamic stability [24].

relations of the ratio between channel radii and surfactant chain length are 1:1 to 2:1 (e.g. the unit-cell length of the $Im\bar{3}m$ phase in DDAB-cyclohexane-water is 116 $\mathring{A}$, with approximately 600 atoms per unit-cell and a chain length of 10-13$\mathring{A}$. The ratio of the minimum diameter 116/4 of the P surface to the chain length is roughly 1:2 [15].). Given such large ratios, the success of the curvature approaches must be considered an amazing result and extrinsic properties should be considered more carefully.

In addition, Luzatti *et al.* have presented experimental evidence for the existence of what they call *chaotic zones* [139, 142]: The lateral order of the flexible hydrocarbon chains [9] decreases gradually as one ventures deeper into the hydrophobic phase away from the interface. The hydrocarbon core of the structure, located at maximal distance from the surface itself, is occupied with a high concentration of CH_3 end-groups, anchored at different parts of the interface. There the packing is inevitably disordered. Similarly, in the water phase the dipoles are strongly ordered in the vicinity of the polar/apolar interface. This orientational order decreases with distance from the interface, defining the centers of the water channels (or polar chaotic zones). Their assignment of chaotic zones of the cubic IPMS are the respective line graphs, yet the construction is reminiscent of the MS construction which may be a more general model for these zones.

Confocal domains frequently found in lamellar or smectic liquid crystals (see [117] for an overview) also related to the MS construction. These are line singularities of the evolute to an interface, and constitute topological defects in a variety of liquid-crystalline phases. These singularities result from parallel transport along the surface normal to the center of curvature, a process which involves different patches of the surface passing through each other, whereas the MS construction obviously does not allow for that.

These phenomena suggest that an analysis of extrinsic properties of space partitions yields insight into the mechanisms of self-assembly and the relief of frustration, in addition to the common interface curvature descriptions. The remainder of this chapter aims to provide this description for the most frequently encountered cubic IPMS. By representing the data in three alternative normalisations, we provide the possibility of comparison of these geometric results under different physical constraints setting the length scale.

---

[9]See [27] for a review of the discussion about the flexibility of the chains.

5.3   Relative length scales of IPMS

The length scale is a free parameter of minimal surfaces which are free to swell without changing their mean curvature. It is typically set by physical considerations (volume/surface area, preferred curvature, preferred chain length). Comparison of scale-dependent IPMS characteristics, such as Gaussian curvature and distance functions, is meaningless without suitable adjustment of the length scale.

For a system where the length scale is determined by the preferred curvature of an interface, the length scale of the compared IPMS should correspond to identical (average Gaussian) curvature. For this normalisation the average Gaussian curvature $\langle K \rangle$ can be calculated by the useful relation to the genus g (or the Euler-Poincaré characteristic χ) of the surface and the total surface area, the Gauß-Bonnet theorem:

$$\int_S K \, dA = 2\pi \, \chi \qquad \text{with} \quad \chi = 2(1-g). \tag{5.6}$$

This theorem holds true for any oriented and compact surface (see for example [48] or most differential geometry text books).
The genus is a topological invariant of a compact surface, indicating the number of handles of a closed manifold (0 for a sphere, 1 for a doughnut, 2 for a pretzel) . For IPMS the genus is usually given for a translational unit-cell (to be more precise, a unit cell embedded in a flat three-torus T^3 to get rid of all translations [94, 58, 183]).
Note that it depends on the size of the chosen unit-cell. For example, the translational unit-cell of the I-WP surface is twice the size of the smallest possible translational unit-cell[10]. Therefore, its Euler-Poincaré characteristic is -12 (genus 7) although I-WP surface is a IPMS of genus 4 ($\chi = -6$).

Alternatively, the length scale may be set by the surface to volume ratio. This situation applies, for example, to a type 2 bilayer phase in a binary mixture where, globally, the volume filled with hydrophobic components relative to the surface area is fixed by the composition of the mixture [24].

The third alternative is most relevant to block-copolymer self-assembly. In that case, the copolymer blocks fill the complete labyrinth.
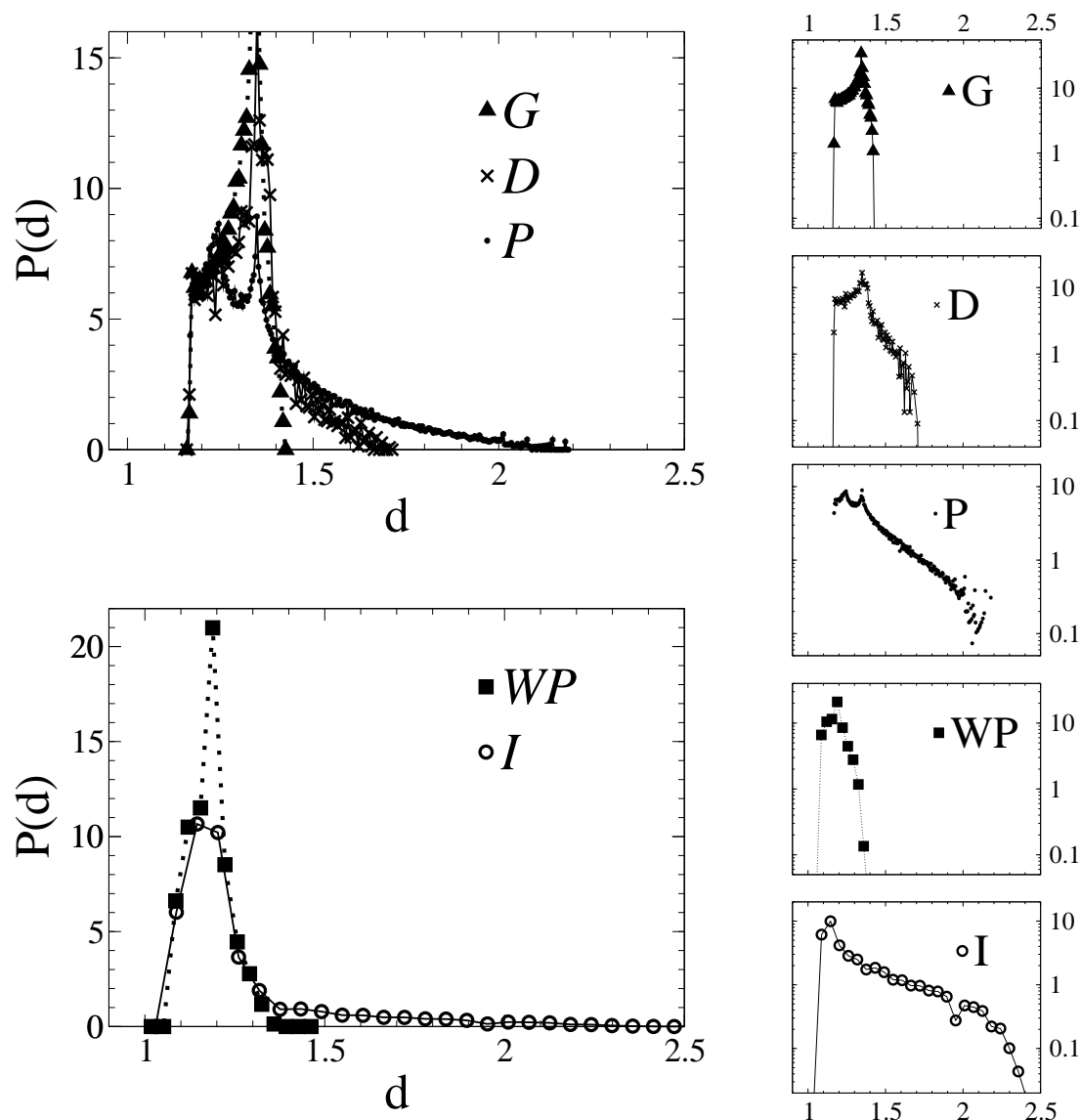
Figure 5.5: Area-weighted distributions of the MS distance function for isometric cubic G, D and P surfaces, and the two distinct channels of a cubic IW-P surface scaled to have the same average Gaussian curvature as the P, D and G surfaces. The width of the distribution is a measure of the relative homogeneity of the surfaces. See Tab. 5.1 for averages, standard deviations, minima and maxima of the distributions. The plots on the right show the same data (and all distances with non-zero frequency) on a logarithmic vertical axis (the horizontal axes are identical for all five figures).

5.4 Relative homogeneity of the P, D and G surfaces

This section presents the result for the stretching homogeneity of the cubic P, D, G and I-WP surfaces. We show that the Gyroid minimises the fluctuation of the distance

---
[10]Since the translation along (1/2, 1/2, 1/2) is a congruence transformation

$V/A = 1$								
	a	$\langle d \rangle$	Δd	d_{max}	d_{min}	V/A	A	$\langle K \rangle$
P	4.711	1.31	0.19	2.03	1.09	1	1.084	-0.483
D	7.660	1.30	0.10	1.66	1.14	1	1.17280	-0.446
G	6.204	1.30	0.06	1.42	1.17	1	2.479	-0.422
I-WP (WP)	7.485	1.23	0.06	2.12	1.41	1	2.022	-0.357
I-WP (I)	6.447	1.21	0.25	2.15	0.97	1	1.500	-0.523
I-WP (both)	6.927	1.22	0.21	2.31	1.04	1	1.732	-0.453

$\langle d \rangle = 1.30$								
	a	$\langle d \rangle$	Δd	d_{max}	d_{min}	V/A	A	$\langle K \rangle$
P	4.672	1.30	0.18	2.02	1.08	0.992	1.067	-0.491
D	7.689	1.30	0.10	1.66	1.14	1.003	1.182	-0.443
G	6.204	1.30	0.06	1.42	1.17	1.000	2.479	-0.422
I-WP (WP)	7.918	1.30	0.06	1.49	1.19	1.059	2.263	-0.347
I-WP (I)	6.940	1.30	0.27	2.31	1.04	1.076	1.738	-0.452
I-WP (both)	7.457	1.30	0.23	2.49	1.12	1.076	2.007	-0.39

$\langle K \rangle = -0.422$								
	a	$\langle d \rangle$	Δd	d_{max}	d_{min}	V/A	A	$\langle K \rangle$
P	5.037	1.40	0.20	2.18	1.17	1.249	1.239	-0.422
D	7.875	1.33	0.10	1.71	1.17	1.201	1.239	-0.422
G	6.204	1.30	0.06	1.42	1.17	1.000	2.479	-0.422
I-WP (WP)	7.177	1.18	0.06	1.35	1.08	0.959	1.859	-0.422
I-WP (I)	7.177	1.34	0.28	2.39	1.08	1.113	1.859	-0.422
I-WP (both)	7.177	1.25	0.22	2.39	1.08	1.036	1.859	-0.422

Scale-independent parameters					
	Space group	χ/tuc	multiplicity	$n_\triangle/\text{ap}$	Φ
P	$Pm\bar{3}m$	-4	48	6×10^3	1/2
D	$Fd\bar{3}m$	-16	192	6×10^3	1/2
G	$I4_1 32$			1.3×10^4	1/2
I-WP (both)	–	-24	184	1.2×10^3	1/2
I-WP (I)	$Im\bar{3}m$	-12	96	6.4×10^2	0.537
I-WP (WP)	$Im\bar{3}m$	-12	96	6.4×10^2	0.463

Table 5.1: Homogeneity of the P, D and G surfaces for different scaling of the length scale. The fluctuations Δd are defined in eq. 5.2, and the lattice parameter a refers to the space groups $Pm\bar{3}m$ (P), $Fd\bar{3}m$ (D) and $I4_1 32$ (G) of the oriented surfaces. The Bonnet related data is scaled such that $V/A = 1$ for the P surface, and $\langle d \rangle = 1.31$ is chosen such that the values for the G surface are identical in all three normalisations of the length scale. V is the volumne of the channel whose MS is analysed. For the P, D and G surfaces, this is identical to $1/2\, a^3$ and $\Phi\, a^3$ for the I-WP surface where ϕ is the volume fraction of the channel.

function over its surface and has the narrowest distribution. The values for the P and D surfaces and the average value of the two distinct sides of the I-WP are distinctly less homogeneous. However the "wrapped-parcel" channel of the I-WP by itself is as homogeneous as the Gyroid. The order of homogeneity of the surfaces does not depend on the choice of length scale normalisations (average curvature, area-to-volume ratio or MS distance function value).

The distributions of d for all surfaces is shown in Figure 5.5, and their averages, maxima, minima and fluctuations are summarised in Tab. 5.1. The distributions are area-weighted in the sense of eq. (5.3). The normalisation of the length scale is such the values for the Gyroid are identical in all three normalisations. The surface-to-volume ratio is defined as the area of the surface within a translational unit-cell to the volume of the channel inside that unit-cell, i.e. $1/2$ of the volume for the G, D and P surfaces and 0.463 and (1-0.463) of the total volume for the two distinct I-WP networks.
For the I-WP we also show the data of a hypothetical balanced I-WP surface of twice the area and volume, made up of one copy of each labyrinth. For the distribution of d this corresponds to averaging of the two individual contributions.
The data for $\langle K \rangle = \mathrm{const} = -0.422$ is for isometric G, D and P surfaces.

Effect of variation of the sampling density of S on the distance distribution

The distance distribution as computed by our algorithm does not change significantly if the resolution of the triangulation (still assumed to be exact surface points) changes. Figure 5.6 shows the distance distribution for the P surface for different resolutions of the asymmetric unit-patch. Although the finer details of the distribution, in particular its two peaks corresponding to the two saddle points S_1 and S_2 of the following section, are only resolved for higher resolution, the overall features of the distribution are similar for all resolutions.[11]

Volume-weighted versus area-weighted averages and fluctuations

The second issue (not to be confused with the choice of appropriate length scale of the compared structures) is the normalisation or weighting of the frequency distributions. The data presented in Figure 5.5 and Tab. 5.1 is for area-weighted data as in eq. (5.3). Instead of contributing the area of each small area element on the surface, each data point can instead contribute the volume of its associated narrow volume

---

[11]The length scale of the distribution shown is that of the Weierstrass-representation in eq. (4.9) and eq. (4.1) without any further scaling.
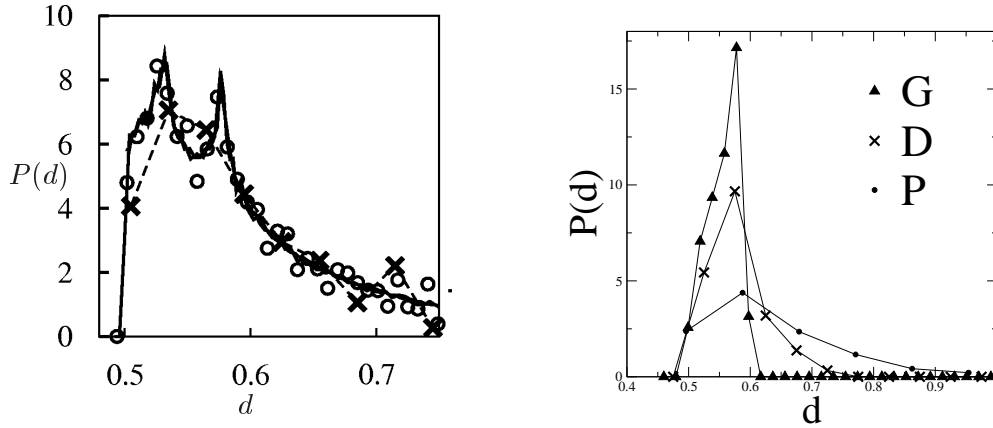
Figure 5.6: (Left) Patch of the P surface with 10^5, 10^4, 10^3 and 10^2 vertices. (Right) Volume-weighted distribution of distances for the P, D and G surfaces. The resolution of this data is much lower than on the left.

element (see Figure 5.1) to the frequency distribution. Then the distribution becomes that of eq. (5.4).

This weighting does not change the maximal or minimal values of the distribution, but does have an effect on average and standard deviation. In general, for the relatively curvature homogeneous IPMS discussed here this volume-weighted distribution increases the frequencies of large distance function values, by virtue of the simple formula $V = A \cdot (1 + K\, l^2/3)$. The differences between area-weighted and volume-weighted distributions are small for the cubic IPMS, as shown in Figure 5.6 (right). We expect this to hold true for any truly IPMS, as the distribution of d cannot have infinite tails that could affect averages in unexpected ways.

5.5   MS geometry of the cubic P, D and G surfaces

This section describes the detailed geometry of the MS of the cubic P, D, G and I-WP surfaces. The geometric features found here also appear (in less symmetric form) in many of the continuous IPMS families discussed in the subsequent chapter.

The cubic P surface

The P surface bounds a labyrinth that is well characterised by a simple cubic lattice. The nodes, with six emanating edges that are mutually perpendicular and along the lattice directions, are the biggest cavities of the labyrinth. The constrictions, in be-
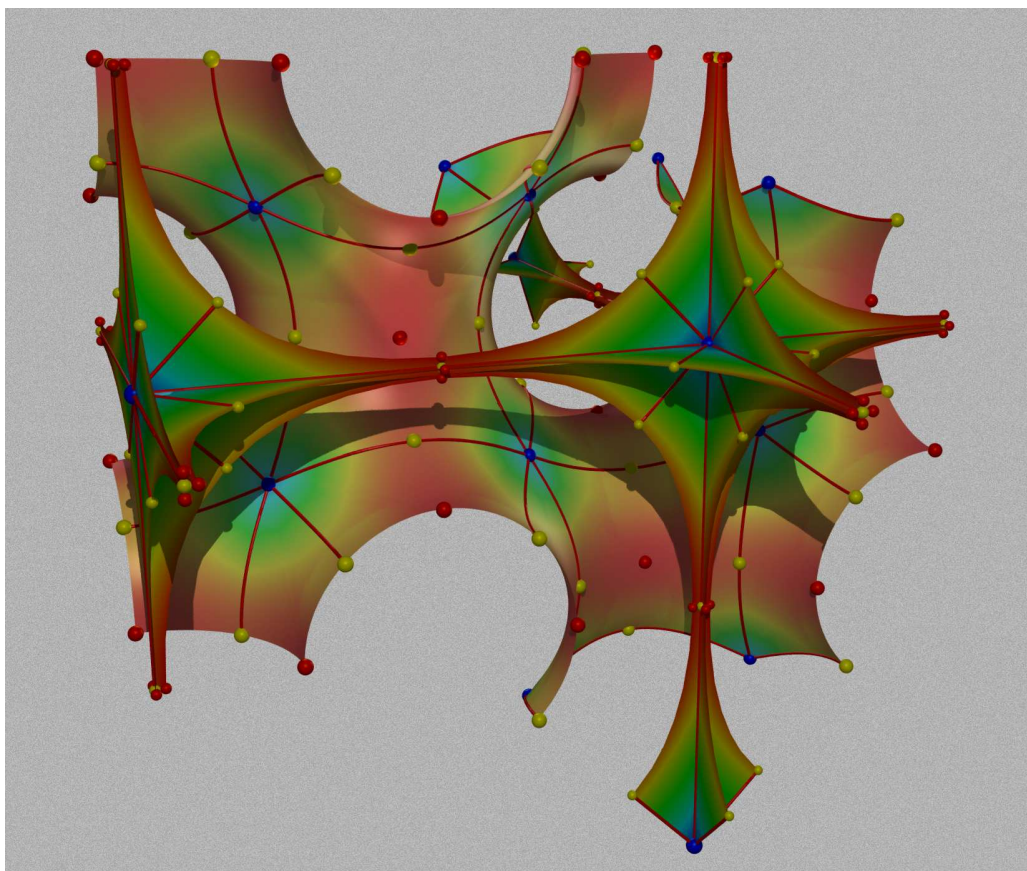
Figure 5.7: Portion of a medial surface of the P(rimitive) IPMS, together with the IPMS. Both the IPMS and the MS are coloured according to values of the distance function d: red indicates small d values and blue large values. Red, yellow and blue spheres indicate minima, saddle points and maxima of the distance function d, respectively. The red lines on the surface are ridge lines of d connecting saddles to maxima, and the red lines on the medial surface their images under ms.

tween two adjacent nodes, are nearly circular. At each node three mutually perpendicular mirror planes coincide. The edges run along the intersection of two perpendicular mirror planes.[12]

The MS of the P surface, illustrated in Figure 5.7, is geometrically simple and intuitively clear. It consists of the simple cubic line graph together with surface patches fully contained in the mirror planes. At the nodes, twelve such patches meet. Pairs of the emanating line graph edges have flat surface patches ("webs") spanned between them. The free boundaries of the MS patches are, by definition of the MS, points with

---

[12]Note that there are additional mirror planes at $\pi/4$ angles, both at the nodes and along the edges.

$d(p) = r_c(p)$.[13] Near the constrictions, half-way along the edges, these surface patches become narrower (closer to the line graph edges). Yet they do not shrink to a point, but retains a cross-like cross-section. This is a reflection of the fact that the constriction – which corresponds to a plane line of curvature on S in a (mirror) plane perpendicular to the edge with normals contained in that plane – is not perfectly circular. Along the constriction d varies between 0.5340 and 0.577, of variation of approximately 4%.[14].

The MS of the P surface can be computed (almost) analytically. For any point $p \in S$ that is contained in those mirror planes that contain the line graph edges, the corresponding MS point $q = ms(p)$ is the center of curvature: $q = p + r_c(p) N(p)$. These points form the free boundary of the MS that correspond to lines of maximal curvature[15]. For any other point $p \in S$ on the surface the corresponding MS point $q = ms(p)$ is found by intersecting the straight lines in normal direction through p with the nearest global mirror plane.

Note that the presence of mirror planes is not sufficient to deduce that MS points are necessarily contained in it. For example, the cubic D surface has three mirror planes intersecting along the line graph edges, yet some of the MS points are not contained in any of those mirror planes.

The MS distance function is maximal at the nodes of the simple cubic graph (blue spheres in Figure 5.7). The mid point of the graph edges is a saddle point of the Euclidean distance map D. The minimum of d on the MS also corresponds to a point on the constriction (red points).

Note that there is only one type of maxima and minima, but two crystallographically distinct saddle points: S_1 in 100 (on Schoen's line graph) and S_2 in 110 direction from the maximum (on the MS, see also Tab. 5.2).

The line graph calculated by the method described in Chapter 3 reproduces exactly the simple cubic graph that is commonly accepted as the line graph of the P surface. Figure 5.7 shows some additional edges, from points on the free boundary of the MS patches to the maxima of D. These connect saddle points of the MS distance function d (on S or MS) that do not correspond to saddle points of the Euclidean distance map D to maxima of d (or D), see also Chapter 3.6.2 and 3.8.

---

[13]For a hyperbolic surface with unit normal field N pointing into the domain C, the radius of curvature r_c is defined here as the positive radius of curvature of S. Only curvature towards the normal can induce MS points (on the MS of C, i.e. in normal direction of N).

[14]Schoen [183] erroneously quotes this number as 0.4%.

[15]On a hyperbolic surface with $r_c(p)$ defined as the positive radius of curvature and the positive unit normal $N(p)$ pointing into the domain C, a curve α on S is a line of maximal curvature if the following conditions apply: the directional derivative $\nabla r_c : T_p S \to \mathbb{R}$ of r_c has one vanishing eigenvalue with eigenvector t_0, in the tangential plane $T_p S$ at p, in direction of the tangent of α. It is a ridge line of the curvature.

An interesting correlation between the critical points of d for the P surface and its distribution of MS distances can be made. The two peaks of the bimodal distribution of distances in Figure 5.5 correspond to the two saddle points S_1 and S_2 of d.

The cubic D surface

Reduction of the MS of the cubic D surface to a line graph reveals that the Diamond network ("dia" in O'Keeffe's notation[16]) is indeed the geometrically centered line skeleton of the cubic D surface. The geometry of its MS is more subtle than for the P surface. First, some parts of the MS do not lie in the global mirror planes, although most do. Second, the distribution of MS distance along the Diamond graph has maxima not only at the nodes but also at the edge centers, even though these are very weak.

Figure 5.8 shows the geometry of the MS. The red lines (along [111] directions of the corresponding space group $Fd\bar{3}m$ of the oriented D surface, see Tab. 5.2) correspond to one of the two interpenetrating diamond lattices commonly accepted as labyrinth graphs of the D surface [183]. The blue spheres indicate the main distance function maxima located at the nodes of the line graph, and the small red spheres its minima. The MS can be approximated by an assembly of almost flat webs spanning the six pairs of graph edges (from the node to the middle of the edge) emanating from each node, and each of these webs is contained in one of the global mirror planes. The two sets of three webs meeting at the center of each graph edge subtend angles of 60° with each other.

The top right image is a close-up of the MS in the vicinity the middle of a graph edge. The graph edges are on three-fold symmetry axes, with inversion centers at their midpoints (blue spheres). Each of the yellow spheres S_1 (saddles of d on the free boundary of the MS that are not saddles of the Euclidean distance map D) lie on a two-fold axis through this inversion center). The medial surface webs do not shrink to a single point as one moves along the graph edge, but rather each of the webs splits up into two webs (at $\pm 60^o$). It is only in this region that the MS is not contained within global mirror planes of the surface. The yellow and green spheres indicate saddle points of the distance function and the blue sphere a very weak maximum of the distance function. Critical paths connect the node max Max_1 to the saddle S_2 on the edge (red line), S_2 to Max_2 (green line).

The graph shows the distance function on a $(1\bar{1}0)$ plane intersection of S (i.e. the mir-

---

[16]See the homepage, http://okeeffe-ws1.la.asu.edu/RCSR/home.htm, of the Reticular Chemistry Structure Resource.
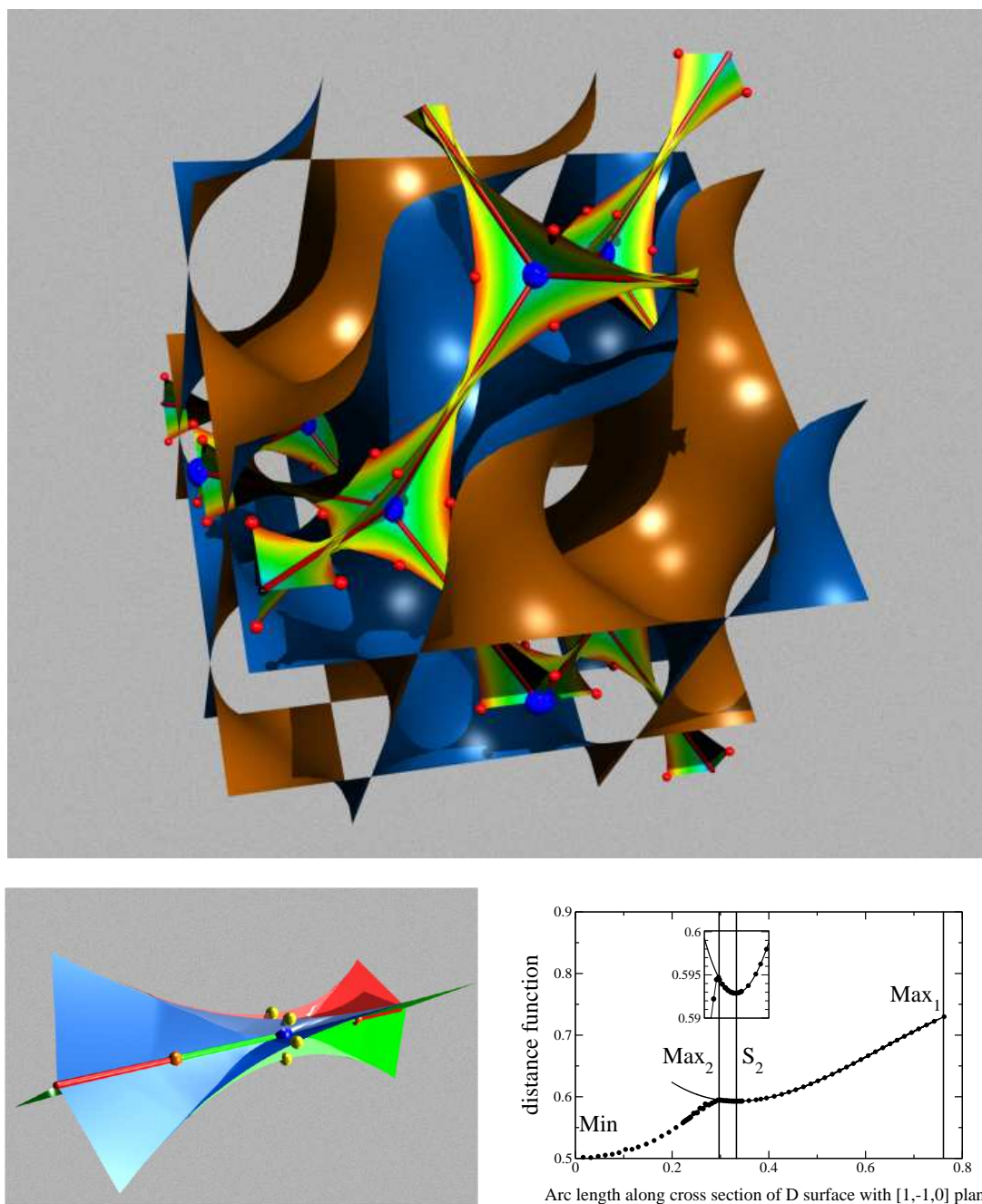
Figure 5.8: D surface: (Left) A fragment of the D IPMS is shown, together with the medial surface of one of its two channel labyrinths.

ror plane relating the two blue planes. The graph corresponds to distance function values on the line graph on MS). Dots are data computed with our algorithm, whereas the full curve is the length of lines directed along surface normals between the surface vertices and the global mirror planes. In this way, exact distance values for the region

from the graph nodes to the edge center can be computed, clearly demonstrating that the blue sphere is indeed a weak maximum and the orange sphere a saddle point.

The cubic G surface

The MS geometry of the Gyroid is distinctly different from those of the P and D surfaces, see Fig. 5.9. At a first glance, its MS seems to be ribbon-like, displaying no clearly discernible branch lines where MS patches meet. The MS appears as an assembly of triangles, twisted at their common vertices and with sail-like MS patches smoothly connecting edges of neighbouring triangles. More detailed analysis reveals that branch lines exist.

The Y^* (or Laves or srs) graph, commonly accepted as the line skeleton of the Gyroid, is indeed geometrically centered. However its three-coordinated nodes are not at points of maximal channel diameter (Euclidean Distance Map), but at saddles of D with three directions of increasing and decreasing EDM, respectively (Hopf index -2). The points of maximal distance function are located at the mid-points of the graph edges.

Figure 5.9 illustrates the MS of the G surface. The conventional labyrinth graph (blue thick lines) for the G surface connects nearest pairs of points of intersection of these two-fold axes through straight lines [183]. These are a subset of the ridge lines of the distance function, though, in contrast to the P and D surfaces, the nodes of the channel graph are not the maxima of the distance function (the maxima, blue spheres, are in the middle of the edges). There are three different types of saddle points of the distance function: saddle singularities of Hopf index -2 at the nodes of the graph (large yellow spheres), S_1, as well as two types S_2 (small yellow spheres), and S_3 (green) of saddle singularities of Hopf index -1. The critical paths connecting S_3 to the maximum and S_2 to the maximum are not shown. The top right image (with arbitrary color coding) illustrates that the medial surface is an assembly of nearly planar triangles (green) plus *webs* spanned between the edges of neighbouring triangles. Pairs of adjacent triangles share common vertices and are twisted by $\cos^{-1}(1/3) \approx 70.53°$ around the common two-fold rotational axis containing the the labyrinth graph, consistent with symmetries of the G surface. Calculations indicate that the triangular portions of the MS deviate from planarity by only $\pm 0.75\%$ of the triangle edge length. The figure on the bottom right shows one of the triangles of the MS with the saddle point in its center and three maxima located at each of its corners beneath a surface graph with height indicating the value of the distance function at the site immediately below, on the projected triangle.
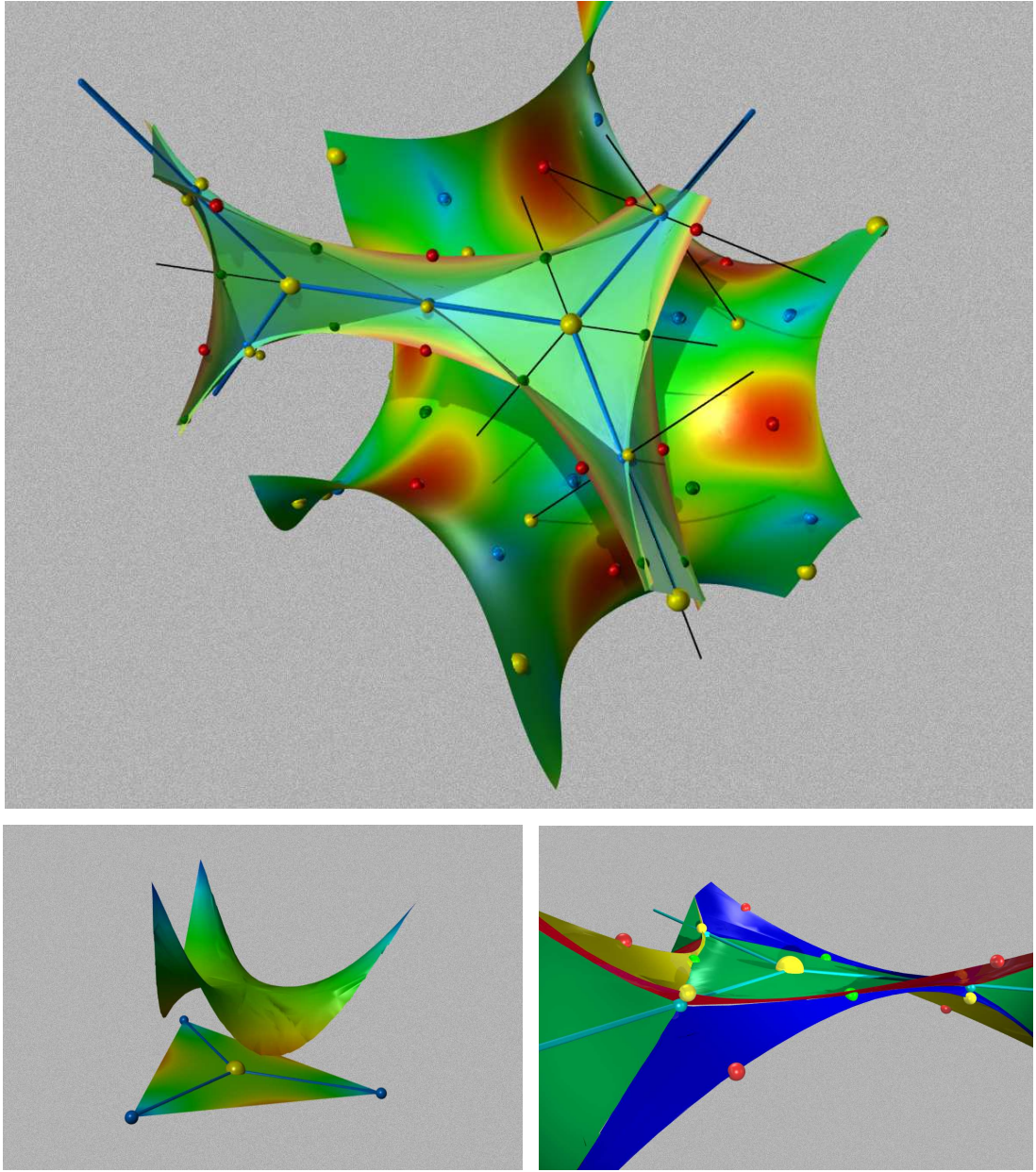
Figure 5.9: Medial Surface of the G(yroid) IPMS coloured according to the scheme described in Figure 5.7. The thin black lines are some of the two-fold rotational symmetry axes of the G surface. Note in particular that the three-coordinated node of the line graph (big yellow sphere on MS) is *not* a maximum of the distance function d (or the Euclidean distance map D), but a saddle point of those functions. The maxima of D (or d) are the mid-points of the edges of the line graph (small blue spheres). Bottom left: Illustration of the distance function: Shown is one of the (nearly) flat triangular patches of the MS together with the surface given by $q + D(q)M(q)$ where q are MS points and $M(q)$ the constant MS normal.

5.6   MS geometry of the I-WP surface

The I-WP surface divides space into two non-congruent labyrinth. Each gives rise to
a MS that is clearly distinct from the other. Both MS are made up of surface patches
mostly contained in the global mirror planes. The *I* MS is similar in character to those
of the D and P surfaces in that it has branch lines along the line graph edges and clear
maxima at the 8-connected node. The WP MS, on the other hand, is reminiscent of the
Gyroid in that its 4-connected nodes are saddles of Hopf-index -3 and its line graph
edges are two-fold rotation axes contained in the MS, but not along branch lines.

"I" for Innenzentriert

The MS of the body-centered I-labyrinth (O'Keeffe's "bcu" graph) is shown in Figure
5.10 (bottom). It contains the body-diagonals as its branch lines. They also consti-
tute the line graph that is (trivially because of the mirrors and the three-fold rotation)
geometrically centered. The MS patches are webs that span all adjacent pairs of body-
diagonals of a cube of size $a/2$ (the body centered cube with the four yellow spheres
at its corners).
There is only one type of node which is eight-connected and a distinct maximum of
the EDM D (or d), located at the eight corners of the cubic translational unit-cell and
its body center.
The points at (1/4, 1/4, 1/4) are at the middle of the line graph edges, and are inver-
sion centers of the space group ($.\overline{3}m$, 8c in $Im\overline{3}m$). The MS nearly shrinks to almost to
a point (yellow spheres), and the flat MS patches in either direction of the edge are ro-
tated by $\pi/3$ compared to each other (Similar to the D surface MS yet stronger). They
appear to be saddle points of D.

In the vicinity of these saddle points some transition structure from the two sets of
twisted MS patches is necessary. It appears from high resolution analysis to be similar
to the D surface MS sails spanning the edges of adjacent MS patches, yet the size of
the region where this happens is much smaller than in the D surface case. Careful
analysis suggests that the transition is very similar to the case drawn in the linegraph
chapter in Figure 3.7. The edge mid-point is, in contrast to the D surface case, indeed
a saddle of D but not of d, denoted S_1.
There are additional saddles of d, but not of D, that are in equivalent positions to the
saddles S_2 of the D surface, see Figure 5.8. Hence we give them the same name.
The curvature maxima correspond to the minima Min of D and d and are located on
the boundary of the MS, still in the immediate vicinity of the edge centers. Note that
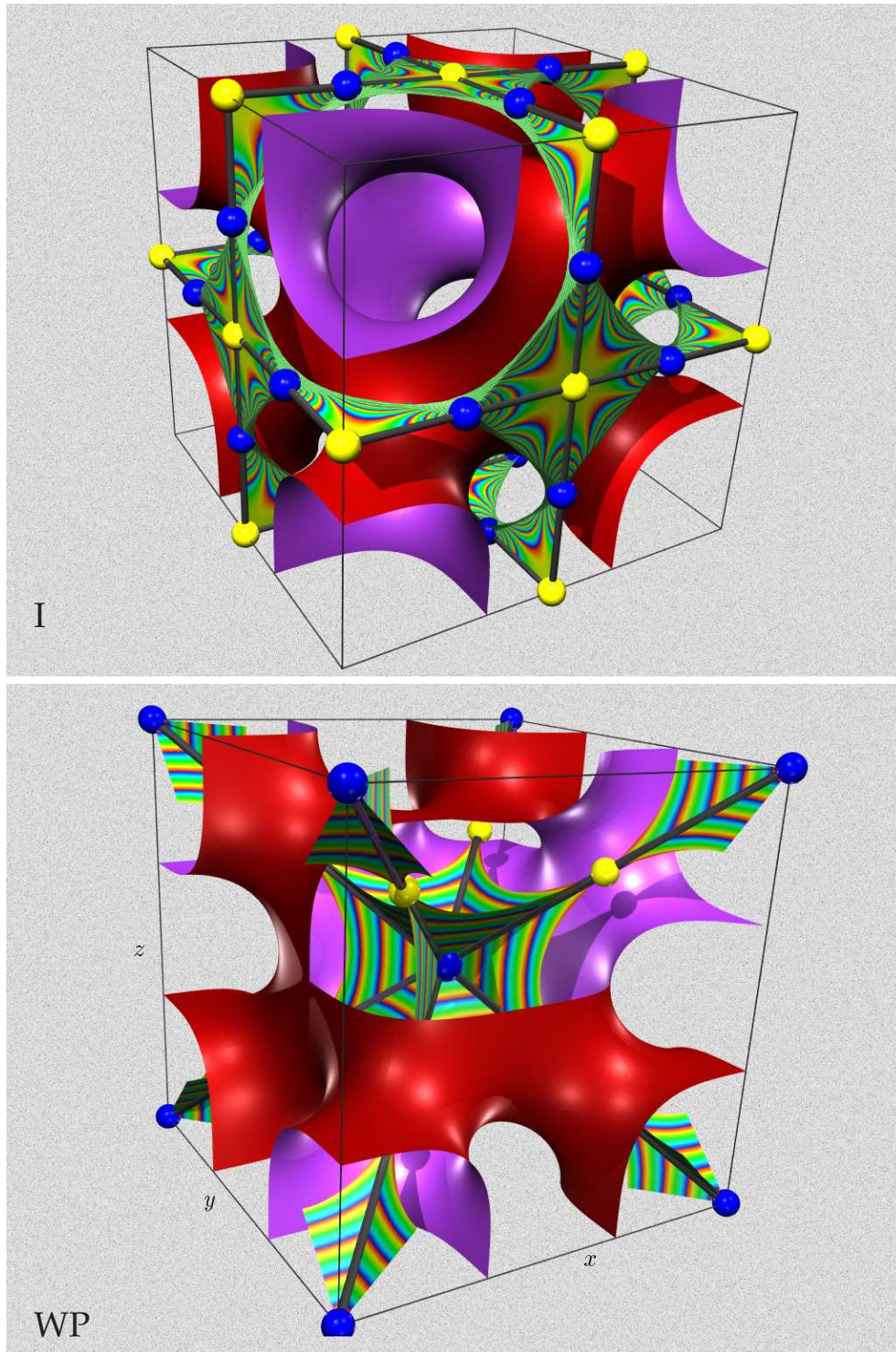
Figure 5.10: The two MS in either of the two geometrically different channels of the I-WP IPMS: (Top) MS of the WP side (Bottom) MS of the *I* side (Here, the surface itself is cut open along [001], [010] and [110] planes for enhanced visibility of the MS).

even this minimum is still very close (both in distance in real space and in distance function value) to the edge center.

Another saddle S_3 of d but not D is on the MS boundary half-way along the boundary of the webs in between the two corresponding saddle points S_1. This is the analogon of S_3 in the D surface case.

"WP" for Wrapped Parcels

The MS of the WP labyrinth of the I-WP surface (O'Keeffe's "nbo" network) is very different to that of the I labyrinth. That difference is reflected in its MS. Essentially, the MS is a collection of almost quadrilateral flat surface patches, joined at the corners incorporating a $\pi/2$ twist around their common axis. Similarly to the D surface, small sails span the edges of neighbouring quadrilateral patches (i.e. again the MS does not shrink to a point). The four-connected planar nodes of the line graph are saddle points of d or D, whereas the midpoints of the edges are maxima of the distance function. Figure 5.10 (top) shows an illustration.

The line graph of the WP labyrinth consists of edges connecting four-connected nodes at $[0, 0, 1/2]$ ($4/mm.m$, 6b) sites connected to each other by edges in (100) direction. The nodes are the yellow spheres in Figure 5.10 (top). The edge midpoints are at $[1/4, 0, 1/2]$ ($\overline{4}m.2$, 12d, blue spheres). The incident edges at each node are coplanar, and planes between neighbouring nodes are twisted by $\pi/2$ around the edge.

The MS is best visualised as flat squares whose midedge points are at $[1/2\pm1/4, 0, 1/2]$ and $[1/2, 0, 1/2 \pm 1/4]$ with the four-node at its center. These flat patches are propagated through space by the diagonal two-folds $1/4, y, \overline{y} + 1/2$ (..2) through the midedge points – inducing the $\pi/2$ twist between neighbouring patches. Small sails span adjacent edges of these four-patches and contain a part of the diagonal two-fold axes.

The distance function (or Euclidean distance map) maxima at the midedge points have substantially higher values ($d = 0.59$) than the four-nodes ($d = 0.525$).

5.7 Final thoughts

This chapter offers a complete description of the MS geometry of the ubiquitous cubic G, D and P surfaces of genus 3 and the I-WP surface of genus 4.

In terms of surface homogeneity, we have demonstrated that the degree of variation of channel size, as defined by the MS distance function, provides a new homogeneity

measure according to which the Gyroid is more homogeneous than the cubic D surface which, in turn, is more homogeneous than the cubic P surface. We have shown that this result is valid for three different length scale normalisations where the average curvature, the average distance function and the surface to volume ratio, respectively, are kept constant. This analysis is based on properties that cannot be derived from intrinsic characteristics alone.

We have also shown that, somewhat surprisingly, the "Wrapped-Parcel" channel of the I-WP surface is as homogeneous as the cubic Gyroid, whereas the "I" channel is slightly less homogeneous than the cubic P surface.

This result underlines the special role of the G surface among the balanced low-genus IPMS. It provides simple geometric evidence for the superior embedding of the G compared to the P and D surfaces.

In terms of the MS geometry we have shown that the commonly accepted line graphs of all four surfaces, set by symmetry considerations, are indeed geometrically centered line skeletons, as defined in Chapter 3. However, the line graph nodes for the cubic Gyroid and the WP labyrinth of the I-WP surface do not define the widest apertures on the surface, but the narrowest. The corresponding widest points are at the midpoints of the straight line graph edges. Indeed they correspond to normal MS points (i.e. resulting from the collapse of exactly two surface points), whereas the P and D surface nodes (that are maxima of the EDM) are branchpoints at the intersection of multiple MS patches.

This finding provides a counter-example to the assumption that is occasionally suggested [198], that a network inside a labyrinth connects multiply connected wide pores via narrower tunnels.

In the case of the WP labyrinth of the I-WP surface, the geometrically centered line graph is clearly shown to be the one with edges along [100] directions, and four-connected planar nodes at the face-centers of the translational unit-cell. Recently, a different graph inside the labyrinth, yet not homotopic to the domain, has been mentioned as the WP line graph, in work suggesting a new model for smectic blue phases with line defects [43, 44]. In these articles an "optimal line defect structure" is guessed with three-connected nodes at the (1/4,0,1/2) sites and two types of edges – resembling closely the boundary of the MS squares, close to lines where the MS points correspond to centers of curvature.

point	complex plane ω	on surface S Coordinates	Sym	Wyck
Primitive, $Pm\overline{3}m$, $a = 2.15652$, $\phi = \pi/2$ $y_2=0.1751$, $x_1=0.3249$				
Max	w_1	$[\frac{1}{4}, \frac{1}{4}, \frac{1}{4}]$	$3m$	8g
Min	0	$[\frac{1}{2}, \frac{1}{4}, 0]$	$mm2$	12h
S_1	w_5	$[\frac{1}{2}, y_2, y_2]$	$mm2$	12j
S_2	w_2	$[x_1, x_1, 0]$	$mm2$	12i
Diamond, $Fd\overline{3}m$ (origin at $\overline{4}3m$), $a = 3.37150$, $\phi = 0$ $x_3=0.1846$, $x_5=0.1910$, y_5=-0.0247				
Max_1	w_1	$[\frac{1}{8}, \frac{1}{8}, -\frac{1}{8}]$	$3m$	32e
Min	0	$[\frac{1}{4}, \frac{1}{4}, 0]$	$2mm$	48f
S_1	w_2	$[\frac{1}{4}, \frac{1}{8}, 0]$	2	96h
S_2	w_3	$[x_3, x_3, z_3]$	m	96g
Max_2	w_4	$[x_5, x_5, y_5]$	m	96g
Gyroid, $I4_132$, $a = 2.65624$, $\phi \approx 38.015^o$ $x_1=0.124$, $y_1=0.702$, $z_1=0.176$, $x_4=0.491$, $x_3=0.3375$, $x_4=0.491$, y_5=-0.1625				
Max	w_6	$[x_1, y_1, z_1]$	1	48i
S_1	w_1	$[0, \frac{1}{2}, 0]$	3	16e
Min	0	$[0, \frac{3}{4}, \frac{1}{8}]$	2	24f
S_2	w_2	$[-\frac{1}{4} + x_3, \frac{5}{8}, \frac{1}{2} - x_3]$	2	24h
S_3	w_5	$[\frac{1}{8}, 1 + y_5, \frac{1}{4} + y_5]$	2	24g
I of I-WP, $Im\overline{3}m$ (origin at $m\overline{3}m$), $a = 3.15491$, $\phi = 0$ $z_0=0.1667$, $x_2=0.321$, $y_0 = 1/2 - x_0$, $x_1=0.1374$, $x_6=0.41$, $y_6=0.20$				
Max	$\imath$	$[0, 0, \frac{1}{2} - z_0]$	$4mm$	12e
S_1		$[x_2, x_2, z_2]$	m	48k
S_2	$1/3 + \sqrt{2}/3\,\imath$	$[1/2 - x_1, 1/4, x_1]$	2	48i
S_3	$1 + \sqrt{2}\,\imath$	$[1/2, y_0, y_0]$	$mm2$	24h
Min		$[x_6, y_6, y_6]$	$..m$	48k
WP of I-WP, $Im\overline{3}m$ (origin at $m\overline{3}m$), $a = 3.15491$, $\phi = 0$ $y_8=0.303$, $z_8=0.181$, $z_0=0.1667$				
Max^w		$[1/2, y_8, z_8]$	m	48j
S_1^w	$\imath$	$[0, 0, \frac{1}{2} - z_0]$	$4mm$	12e

Table 5.2: Crystallographic coordinates of minima, maxima and saddle points of d (coordinates), together with the point group symmetry of the site (Sym) and its Wyckoff symbol (Wyck). Crystallographic coordinates refer to the space group [85] of the domain C (i.e. the "black-white group" of the oriented surface). Corresponding absolute values of the distance function d and the radius $r_c = 1/\sqrt{-K}$ (where K is the Gaussian curvature) are listed, for unit cells of lattice parameter a (Unit cells are scaled such that the three surfaces are isometric). The numerical values for coordinates are correct to ± 2 in the last given digit, unless otherwise indicated.

point	position on MS			d	r_c
	Coordinates	Sym	Wyck		
Primitive, $A_0 = 0.2272$, $V_0 = a^3/(2 \cdot 48) = 0.104$, $\langle d \rangle = 0.60$					
$y_1 = 0.018$, $x_2 = 0.136$					
Max	$[0,0,0]$	$m\overline{3}m$	1a	0.9338	∞
Min	$[\frac{1}{2}, y_1, 0]$	$mm2$	12h	0.500	0.5000
S_1	$[\frac{1}{2}, 0, 0]$	$4/mmm$	3d	0.5340	0.5774
S_2	$[x_2, x_2, 0]$	$mm2$	12i	0.577	0.5774
Diamond, $A_0 = 0.2272$, $V_0 = a^3/(2 \cdot 192) = 0.100$, $\langle d \rangle = 0.57$					
$z_1 = 0.1483$, $x_2 = 0.004$, $x_4 = 0.1129$					
Max_1	$[0,0,0]$	$\overline{4}3m$	8a	0.7230	∞
Min	$[\frac{1}{4}, \frac{1}{4}, z_1]$	$2mm$	48f	0.5000	0.5000
S_1	$[\frac{1}{8} + x_2, \frac{1}{8}, \frac{1}{8} - x_2]$	2	96h	0.5774	0.5774
S_2	$[x_4, x_4, x_4]$	$3m$	32e	0.5929	0.6547
Max_2	$[\frac{1}{8}, \frac{1}{8}, \frac{1}{8}]$	$\overline{3}m$	16c	0.5949	0.615
Gyroid, $A_0 = 0.4544$, $V_0 = 0.197$, $\langle d \rangle = 0.56$					
$z_2 = -0.064$, $x_4 = 0.491$, $y_6 = -0.311$					
Max	$[\frac{1}{4}, \frac{5}{8}, 0]$	222	12d	0.609	0.683
S_1	$[\frac{1}{8}, \frac{5}{8}, -\frac{1}{8}]$	32	8b	0.575	∞
Min	$[0, \frac{3}{4}, z_2]$	2	24f	0.500	0.5000
S_2	$[-\frac{1}{4} + x_4, \frac{5}{8}, \frac{1}{2} - x_4]$	2	24h	0.577	0.5774
S_3	$[\frac{1}{8}, 1 + y_6, \frac{1}{4} + y_6]$	2	24g	0.558	0.5774
I **of I-WP**, $A_0 = 0.3593$, $V_0 = 0.537 \cdot a^3/96 = 0.1758$, $\langle d \rangle = 0.59$					
$x_3 = 0.25$, $y_4 = 0.34$, $x_7 = 0.31$, $y_7 = 0.29$					
Max	$[0,0,0]$	$m\overline{3}m$	2a	1.05	∞
S_1	$[x_3, x_3, x_3]$	$.\overline{3}m$	8c	0.50	0.51
S_2	$\approx [x_3, x_3, x_3]$	2	48i	0.50	0.500
S_3	$[1/2, y_4, y_4]$	$mm2$	24h	0.50	0.500
Min	$[x_7, y_7, y_7]$	$..m$	48k	0.48	0.47
WP of I-WP, $A_0 = 0.3593$, $V_0 = 0.463 \cdot a^3/96 = 0.1514$, $\langle d \rangle = 0.52$					
Max^w	$[1/2, 1/4, 0]$	$\overline{4}m.2$	12	0.59	0.756
S_1^w	$[0, 0, 1/2]$	$4/mm.m$	6b	0.525	∞

Table 5.2 (continued from page 126): The area of the asymmetric unit-patch, A_0, area-weighted average distance, $\langle d \rangle$ and the volume associated with the asymmetric unit-patch, V_0, are also listed. V_0 is the volume foliated by reduced parallel surfaces in positive normal direction from the surface, i.e. the volume on one side of the original surface. The surface coordinates are obtained from usual Weierstrass representation for minimal surfaces as in [64, 160] plus roto-translation in $\mathbb{E}^3$. The Weierstrass functions are given in eq.4.9 and eq. 4.13 with Bonnet angle ϕ. The complex variable w indicates the preimage in the complex plane of the respective points ($w1 = (\sqrt{3} - 1)/\sqrt{2}$, $w_2 = (\sqrt{2} - 1)\exp(\imath\pi/4)$, $w_3 = 0.3178$, $w_4 = 0.2863$, $w_5 = (\sqrt{2} - 1)\exp(\imath 3\pi/4)$, $w_6 = 0.3644\exp(\imath\, 0.4177\,\pi)$).

Medial Surface Analysis of continuous IPMS families

Continuous families of IPMS formed by crystallographic deformations of the cubic Primitive, Diamond and Gyroid surfaces are known. This chapter describes their MS geometry, extrinsic surface homogeneity measures and transient line graph structures. These surfaces offer pathways between the cubic IPMS, maintaining minimality and channel topology throughout the evolution. In contrast to the Bonnet-transformation (where intermediates between cubic cases are self-intersecting) all members of these surface families are free of self-intersections. The surface families discussed here are the tetragonal tD and tG surfaces, and the rhombohedral rPD and rG families, parametrised and analysed in terms of intrinsic properties by Fogden, Hyde *et al.* [66, 65, 63].

We present an analysis of their packing homogeneity by characterising the distribution of MS distances by their averages $\langle d \rangle (r)$ and fluctuations $\Delta d(r)$, in the same spirit as the previous chapter. This analysis reveals that the cubic Gyroid and the cubic Diamond surfaces are maximally homogeneous within the families that contain them (the rG and tG for the Gyroid, and the rPD and tD for the Diamond). In contrast, the cubic primitive surface represents an inflection point of $\Delta d(r)$ of the rPD surface. Thus it has degradations that are more homogeneous in a packing sense. In particular, along the rPD the homogeneity decreases monotonically from the cubic Primitive to the cubic Diamond.

The implications of this finding to the mesophase formation in bicontinuous liquid crystalline phases are evident. First, continuous families of embedded IPMS provide a model for transitions of systems in which all of the three cubic Gyroid, Primitive and Diamond phases form dependent on the concentration.[1] This transition has been

---

[1]Such a system has been described recently [208, 205]. It is a saturated 2:1 (mol:mol) fatty acid/phophatidylcholine mixture in water in which the Gyroid, Diamond and Primitive phases form

shown to be very fast between the G and D phase indicating little tearing and fusion of the bilayer [205].

Second, the prevalence of cubic IPMS in self-assembled mesophases in lipid, surfactant and copolymer mesophases demands exploration. In these systems, symmetry is at best a secondary consequence of the optimal shape. The issue why they tend to form phases with cubic symmetry is best addressed by studying surface families that are in general *not* cubic, but comprise singular members with cubic symmetry. Also, the occasional occurrence of non-cubic phases in systems, where the individual building blocks are less symmetric and hence not so well captured by curvature-based descriptions, emphasises the need for consideration of extrinsic surface properties (c.f. the ABC triblock copolymer in chapter 7 and [12, 54]).

Another aspect of our analysis concerns the transition of the line graphs corresponding to the IPMS labyrinths, in particular in terms of coordination number at the nodes. Some of these transitions involve changes of the node-connectivity of the networks, that are three-, four- and six-connected for the cubic Gyroid, Diamond and Primitive surfaces.[2]

Transitions between differently coordinated graphs have been described in great detail, in particular for for the case of IPMS by Charvolin and Sadoc. An example is the classical transition from a four-node to two three-nodes by insertion of an additional edge – which is often drawn schematically with equal incident angles between edges at the nodes. If the transition of the graph is illustrative of the transition of a channel system in which it is contained, the line graph should be centered within the labyrinth (as is the graph defined in Chapter 3).
We show in this chapter that the topological and geometric transitions of the line graphs of the tG and rG labyrinths involve very uneven incident angles of the edges. An example is a four-connected node consisting in two pairs of tangentially incident edges, somewhat in contrast to the common picture described above.

The first part of this chapter gives our results regarding the homogeneity of the surface families and gives a brief review of relevant literature (sections 6.1 and 6.2). The second part (section 6.3) contains detailed descriptions of the MS geometry and the topological and geometric properties of the line graph.

---

as the water content is increased.
  [2]In the remainder of this chapter, we sometimes refer to such transitions as topological when speaking about the graphs, although this is not the completely correct term.

6.1 Concepts and relevant literature

A surface or a member of a surface family?

The notion that there is *a* Primitive surface (or Gyroid, ...) is somewhat misleading. Rather, *the* Primitive surface is a (especially symmetric) member of a whole family of surfaces with a number of parameters distinguishing between the individual members. This fact is easily forgotten because of the overwhelming emphasis on symmetric structures, or hidden by the fact that expressions for the more general cases are lacking.[3]

In many cases (such as rPD, tD, tP) a *Flächenstück* that is bounded by straight lines can be identified. The subset of the surface bounded by that frame is obviously the solution of a Plateau "soap film" problem. In these cases, a surface family may simply be constructed by deformation of the frame in ways that avoid self-intersections when the patch is propagated through space by the two-fold rotations around its edges. For example, the rPD surface is obtained from propagating a soap film spanned between two parallel triangles twisted by 60° around their midpoint normal (a *triangular catenoidal neck*) by two-fold rotation. In that case, the distance c^* between the triangles is (determined by) the parameter r of the surface family.

All of the IPMS families described here are embedded for any value of their parameters, that is they are without self-intersections. In contrast, the celebrated Bonnet-transformation produces, for any minimal surface, a family of (in general) self-intersecting minimal surfaces (the Bonnet angle being the parameter of the surface family). In particular, members of the Bonnet-family containing the P, D and G surfaces is self-intersecting for all Bonnet angles apart from the ones corresponding to the cubic cases. Vice versa, the members of the Bonnet-family are evidently isometric to each other (identical in all intrinsic properties), which is not the case for any of the surface families discussed in this chapter. For example, without appropriate scaling, the end points (G and D) and all other members of the transition from the cubic Gyroid to the Diamond (or Primitive surface) via the rG and rPD surface families are not Bonnet related.[4]

For the self-assembly of lipids and surfactants, self-intersections correspond to tearing

---

[3]For example, generalisation of the cubic Gyroid (i.e. surface families containing the cubic Gyroid) were not known until the early 1990s [63], and believed not to exist [183]. Another example is the I-WP surface whose deformations fall outside the class of regular surfaces [65], and that is hence often considered as *a* surface rather than a continuum of surfaces by lack of knowledge of its generalisations. Yet, the existence of a single surface that does not allow for any deformations preserving minimality cannot be excluded.

[4]However, the cubic members, P and D, of the rPD family are Bonnet related due to the fact that the rPD is a self-adjoint family of surface with the D member being the adjoint equivalent of the P.

Figure 6.1: (Fig. 3 from [66]): "Layout of the three cubic IPMS and the pathways of their 3- and 4-fold generalisations and relatives. [...] The terminals (open circles) of the families are labeled 3 and 4, representing saddle towers of this symmetry (* denotes the adjoint), or h and c to indicate helicoid and catenoid." A slightly misleading aspect of this diagram is the position of the intersection between rG and rPD surface. It is at $r_0 = 0.49472$, which is in between the cubic Primitive and the helicoidal limit rather than in between the cubic Primitive and Diamond surface.

gluing of the bilayer. As the common assumption is that both have prohibitively large energy penalties, the viability of the Bonnet family as a physically viable pathway between the cubic members is questionable (Note however that in systems exhibiting two cubic phases the ratio of lattice dimensions between the two phases is experimentally often commensurate with the Bonnet transform [100]).

The parameterisations of the surfaces discussed here are given in chapter 4, alongside with some comments on related surface families such as nodal or constant mean curvature surfaces.

Continuous pathways between the cubic Gyroid, Diamond and Primitive surfaces

The surface families analyzed in this chapter all contain at least one of the cubic Primitive, Diamond or Gyroid surfaces and provide pathways between these three surfaces. Figure 6.1 (from [66]) illustrates the layout of the pathways traced by the tD, tG, tP, rPD, and rG surface (and a few others that are not considered in this thesis).[5]

These families allow the following two transitions between the cubic Diamond and cubic Gyroid surfaces (among others that are not considered here): (1) D via rPD to P

---

[5]The representation in Fig. 6.1 is slightly misleading in that the actual rhombohedral path from D ($r_0 = \sqrt{2}$ on the rPD) to G passes through the cubic P surface ($r_0 = 1/\sqrt{2}$ on rPD) before the junction with rG ($r_0 = 0.49472$ on rPD).

via rPD and rG to G, and (2) D via tD and tG to G.

Literature on non-cubic IPMS in liquid crystalline self-assembly

Discussion of the possibility of non-cubic bicontinuous phases based on IPMS in lipid or surfactant self-assembly or the geometry of transition structures between cubic phases has only started recently.

For self-assembly in lipid/surfactant mixtures, this is due to the overwhelming majority of equilibrium bicontinuous IPMS phases being cubic. One of the few non-cubic phases reported is the structure of the alveolar surface in lung tissue, modeled by the tetragonal CLP surface [126, 127]. Furthermore, Hyde and Fogden [100] speculate on the possibility of misidentification of phases because analyses based only on symmetry (as measured in SAXS) can not ascertain the topology of the phase. For example, hexagonal phases (now found for example in ionic amphiphile-water systems displaying limited diffraction peaks [33]) that are assumed to be hexagonal closed-packed arrays of micelles share the symmetry of the bicontinuous hexagonal H surface which is another candidate for their structure.

For block-copolymer systems, focus is on AB diblock copolymer blends in which cubic phases prevail. Even more, it is claimed that there is essentially only one type of cubic bicontinuous phase based on the Gyroid morphology [16]. Upon consideration of more general classes of copolymers, for example ABC linear or star-block copolymers, this focus is likely to shift. Non-cubic phases based on periodic hyperbolic surface forms have been found, see [12, 54] and chapter 7.

Reports on details of phase transitions between cubic IPMS phases in surfactant/lipid systems are also fairly recent [208, 205, 182, 168]. Based on time-resolved X-Ray diffraction, Squires *et al.* [205] suggest that the time-scale of the transition points to one without tearing and gluing of the membrane. Saturni *et al.* [182] and Pisani *et al.* [168] both comment that non-curvature contributions to the free-energy may play a crucial role in the transition.

Two similar topological models for the transition between different bicontinuous structures have been put forward [176, 177] and [17].

Fogden and Hyde analyze the tetragonal and rhombohedral IPMS families discussed in this chapter in terms of their intrinsic curvature properties [66]. They conclude that energetic penalties from increased curvature heterogeneity along the tetragonal families are relatively slight, leading to the possibility of non-cubic stable intermediates within those families and possible transition structures for cubic-to-cubic phase transitions.

Non-minimal surface families that model topologically identical transitions to the one considered here have been described. Leoni *et al* [131, 132] analyze phase transitions of inorganic crystals in terms of periodic zero-potential surfaces [212] and periodic nodal surfaces [213]. These are implicitly-defined surfaces given by enumeration of their Fourier series. Many of these are known to approximate IPMS, though they are not ideal.

The surface families parametrised by Fourier-modes are obviously larger than the families of minimal surfaces, as the condition of minimality is not imposed. For example, imposition of the condition of being part of the regular class of minimal surface [64, 65] makes a symmetry degradation in form of removal of mirror planes from the tD surface family possible only at the value $r_0 = 0.43188$. Surface families given by series of Fourier modes are not subject to that constraint and branch off anywhere.

6.2   Packing homogeneity via fluctuations of MS distances

This section presents measures of the relative packing homogeneity of the surface families. The measure for surface homogeneity is the one introduced in section 5.1. We restrict ourselves to an analysis of the standard deviations of the distribution of the MS distances, rather then presenting the distributions themselves.

The outcome of this analysis is that the cubic Gyroid and the cubic Diamond correspond to deep minima of the fluctuations of d around their average along all symmetry degradations considered (rPD and tD for the D, and rG and tG for the Gyroid). In contrast, the P surface is an inflection point of these variations (along the rPD), indicating reduced homogeneity.[6] This result is shown to be true for transitions that preserve volume to surface ratio and those that have constant average distance function.

Normalisation of the length scale

The length scale, as given by the Weierstrass parameterisation, of the individual members of continuous IPMS families is arbitrary, as explained in more detail in section 5.3. A sensible and physically relevant normalisation is required. In a model for the transition between two different liquid-crystalline mesophases, e.g. between the Primitive

---

[6]It is regrettable that we do not present data for the tP degradation. The only reason for the lack of it is shortage of time.

and the Diamond structures, the requirement may be constant surface to volume ratio, or constant average distance function (chain length), or constant average curvature (corresponding to the preferred curvature)[7]. For the alleged transition structure, such as via the rPD family, this requirement then provides the normalisation for the length scale (the arbitrary factor in the Weierstrass coordinates) of the surface.

In the context of transitions of liquid crystalline mesophases, a normalisation such that $V/A = 1$ is appropriate to describe transitions where the water content and the interface area, the sum of head group areas, does not change.

A normalisation such that $\langle d \rangle = 1$ suggests a preferred MS distance function value, corresponding to a preferred labyrinth channel radius, and therefore a preferred chain length.[8] This concept is a tempting one as an energy functional penalising deviations from the preferred, and hence on average adopted, chain length could easily be written down. However, it has to be considered that, at least for liquid crystalline self-assembly, chain stretching contributions are usually considered as an additional effect to interface bending.

Therefore, in a system with a preferred curvature (as given by the surfactant parameter) and a preferred MS distance function the balance between the two may lead to a length scale such that neither the average curvature is the preferred curvature, nor the average MS distance function the preferred one.
If this is the case, the preferred and average distance function (and the preferred and average curvature) are no longer the same, and the average squared deviations of d from the preferred distance function value are a composition of $\langle d \rangle$ and Δd, as explained below.

For the assessment of homogeneity in terms of fluctuations around $\langle d \rangle$, however, we show that the behavior is qualitatively similar for the two different normalisations. This demonstrates that our conclusions are not an artifact of the normalisation.

Preferred chain length not necessarily the average chain length

A reasonable model for chain stretching contributions to a toy energy functional is likely to penalise deviations of the chain length from a preferred chain length l_0 and not from the average chain length $\langle d \rangle$. In a system where the length scale is set by

---

[7]For this normalisation which may be argued to be the most physically relevant, no data is presented here. The curvature data is readily available, though, from the parameterisations in [66].

[8]Note that the relation between chain length and channel radius is not a trivial one in lipid or surfactant/oil/water self-assembly: It is only trivial in a system of type I with the additional constraint that the hydrophilic phase/film is assumed to be of constant (possibly vanishing) thickness, see Fig. 5.4. The concept is much more applicable to self-assembly of block co-polymer phases.

the preferred chain length the two lengths are equal, $\langle d \rangle = l_0$. In a system where the length scale is set by a different mechanism, the two lengths are in general different. For example, if chain stretching is considered as a correction to a bending energy functional, the length scale of the system adjusts to minimise the bending energy and not the preferred chain length.

However, even if $\langle d \rangle \neq l_0$, the data supplied is sufficient to compute the stretching contribution E_s in a simplistic harmonic model,

$$E_s \propto \int_S (d - l_0)^2 = \langle (d - l_0)^2 \rangle A. \tag{6.1}$$

Here $\langle . \rangle$ denotes area-weighted averaging over the surface S and A is the total area of S. One obtains,

$$
\begin{aligned}
\langle (d - l_0)^2 \rangle &= \left\langle [\langle d \rangle + (d - \langle d \rangle) - l_0]^2 \right\rangle \\
&= \left\langle ((\langle d \rangle - l_0) + (d - \langle d \rangle))^2 \right\rangle \\
&= \left\langle (\langle d \rangle - l_0)^2 + 2(\langle d \rangle - l_0)(d - \langle d \rangle) + (d - \langle d \rangle)^2 \right\rangle \\
&= \left\langle (\langle d \rangle - l_0)^2 \right\rangle + \langle 2(\langle d \rangle - l_0)(d - \langle d \rangle) \rangle + \left\langle (d - \langle d \rangle)^2 \right\rangle \\
&= (\langle d \rangle - l_0)^2 + 2(\langle d \rangle - l_0) \underbrace{(\langle d - \langle d \rangle \rangle)}_{=0} + \langle (d - \langle d \rangle)^2 \rangle \\
&= (\langle d \rangle - l_0)^2 + (\Delta d)^2
\end{aligned}
\tag{6.2}
$$

This result demonstrates that consideration of Δd has to go alongside consideration of $\langle d \rangle$ which is a quantity that changes as a function of the geometry in the sequence of members of a surface family, see for example Figure 6.2.

We refrain from further analyzing the IPMS in terms of this result, as it is not a purely geometric property of the surface, but depends on the specific details of the actual system. It highlights one of the biggest obstacles of free energy calculations for liquid crystalline systems, namely that the length scale is set by competing forces.

Fluctuations of d for the rPD, rG, tG and tD surfaces

Figs. 6.2 and 6.3 show data for the (area-weighted) average distance function value $\langle d \rangle$, as defined in eq. (5.2), the standard deviation $\Delta d = \sqrt{\langle (d - \langle d \rangle)^2 \rangle}$ of the distribution of d for the tD, tG, rG and rPD surface families. The data summarises the two

normalisations of the length to constant V/A or constant $\langle d \rangle$ for all members of the families.

In terms of the fluctuations of the distance function *around its average*, the distributions show clear minima at the cubic Gyroid and Diamond, along all families. The Primitive surface is an inflection point of these variations along rPD family[9].

For the tG family, the behavior of Δd is very simple: $\Delta d(\phi_0)$ exhibits a clear minimum at the cubic Gyroid ($\varphi_0 = \pi/4$). From there it monotonically decreases to its two limiting members at $\varphi_0 = 0$ (congruent to the tD family member for $r_0 \approx 0.43$) and $\varphi_0 = \pi/2$ (saddle tower). Both of these retain finite periods in all dimensions, hence $\langle d \rangle/(V/A)$ and Δd finite.
Similarly, in the rG case, the cubic Gyroid ($\varphi_0 = \pi/3$) is a deep global minimum of Δd, and the limiting members at $\varphi_0 = \pi/2$ (saddle tower) and at $\varphi_0 = 0$ (congruent to the rPD surface at $r_0 \approx 0.49472$) both have finite $\langle d \rangle$ and Δd.

Both of these emphasise, again, the robust homogeneity of the cubic Gyroid. Among its deformations analyzed here the cubic Gyroid clearly represents the most homogeneous IPMS in terms of packing.

The functional form is most interesting for the tD and the rPD case, due to their lower-periodic limit cases. For the tD, the cubic member (at $r_0 = \sqrt{2 - \sqrt{3}} \approx 0.51764$) is again a minimum of Δd, from which Δd rises in both directions. However it reaches maxima at $r_0 \approx 0.83$ and $r_0 \approx 0.39$. The latter one is very close, but at slightly smaller r_0, to the tG junction at $r_0 \approx 0.43188$. Beyond these maxima, the fluctuations Δd decline.
In the limit $r_0 \to 0$ the tD surface becomes the 1-periodic helicoid. $s(r_0) = \langle d \rangle/(V/A)$ declines from near 1.3 at the cubic member to (an extrapolated) 1.

With the interpretation of s as an average shape parameter, this corresponds well to the intuition that the helicoid is a double staircase with a ribbon-like MS that is stairwell-like as well, offset by π in phase. The MS structure and the distribution of d needs to be confirmed for the helicoid and the catenoid, and can probably be done analytically. Note that the helicoid still retains in-surface two-folds, is balanced and has two congruent MS.

---

[9]judged from analysis of higher resolution data, up to 5000 triangles in the unit patch, in the vicinity of this cubic member. However, the possibility of a very shallow minima cannot be excluded

[10]The rPD can also be embedded, as a non-oriented surface, in the space group $R\overline{3}c$ of the rhombohedral Gyroid [66]. The data shown (and this only affects the crystallographic axes) is for precisely this space group, as we had parameterised the rPD using the formulae of the rG. To fit into the real oriented space group $R\overline{3}m$ of the rPD, the c/a ratio increases by a factor of $2\sqrt{2}$. For the space group of the non-oriented rPD, this factor is $\sqrt{2}$.
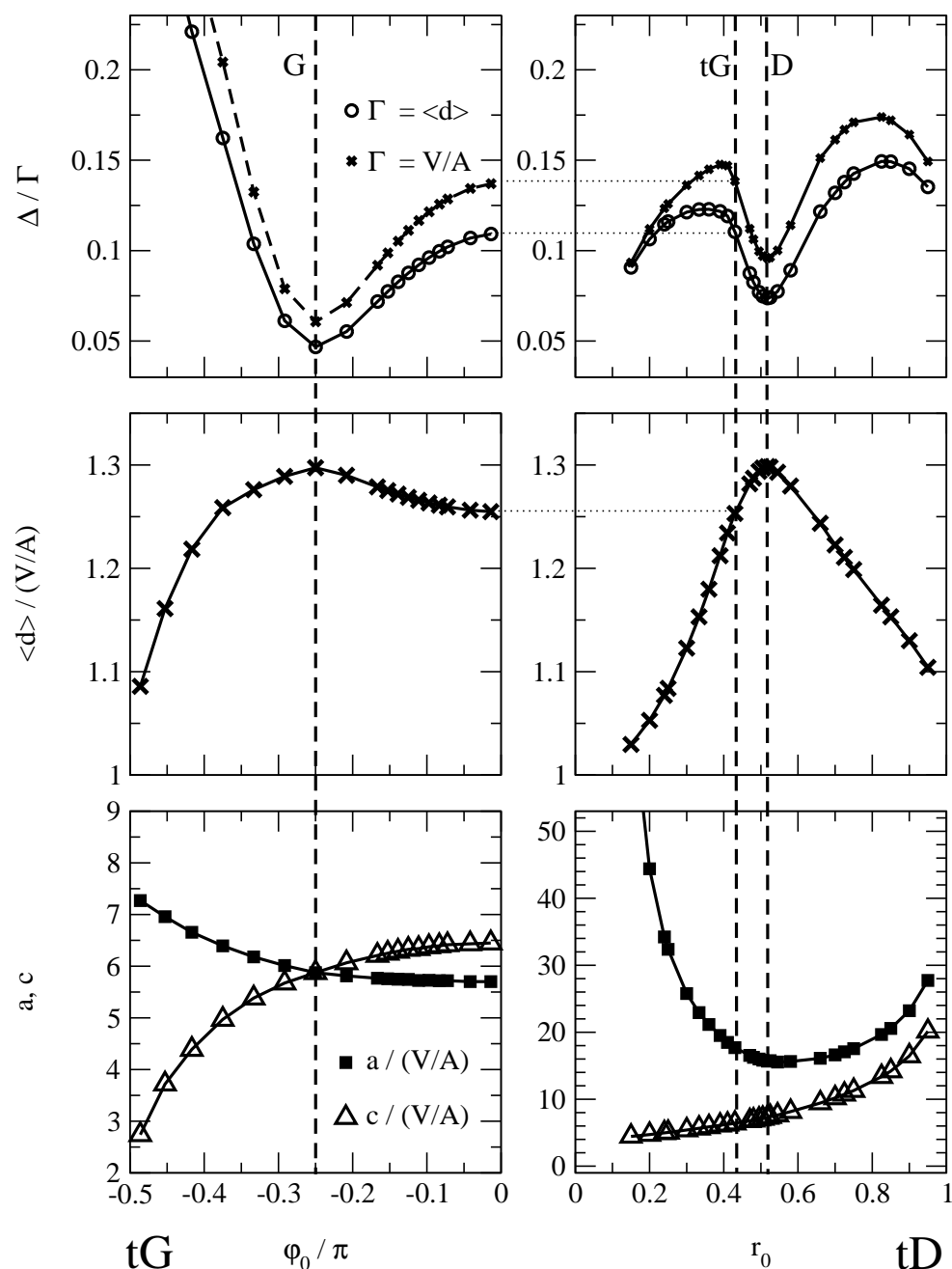
Figure 6.2: Fluctuation and average of the MS distance function for the members of the tG and tD surface families. Shown, as functions of the parameters of the surface families, are the standard deviation of distribution of MS distance function values (top), the average of that distribution (middle), and the corresponding crystallographic parameters a and c in the space groups $I4_122$ and $I4_1/amd$ for the tG and tD, respectively (bottom). The asymmetric patches of the surfaces are sampled by approximately 2500 (tG) and 1200 (tD) triangles. The x-axes are the same within each column.
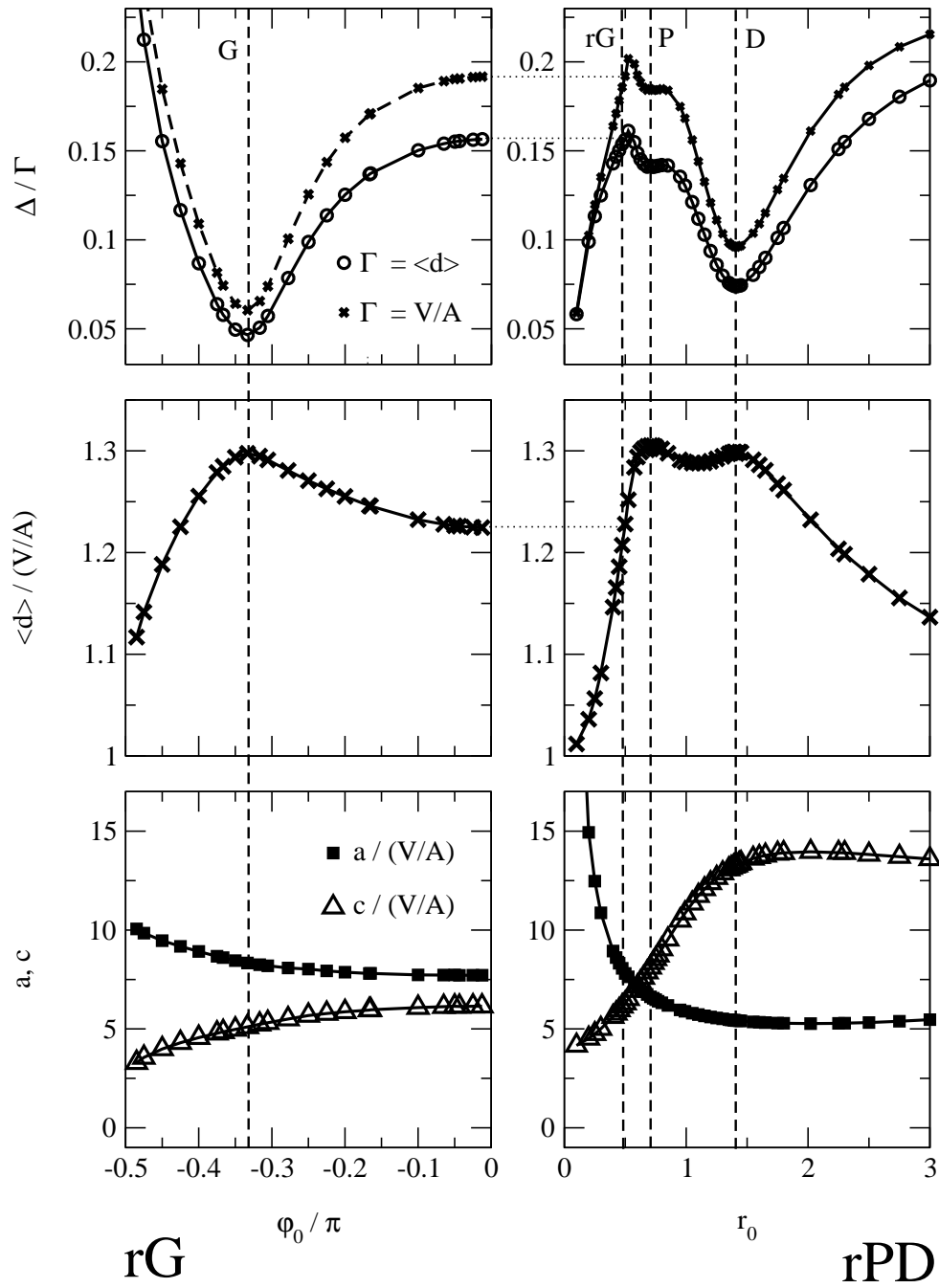
Figure 6.3: Fluctuation and average of the MS distance function for the members of the rG and rPD surface families. Shown are, as functions of the parameters of the surface families, the standard deviation of distribution of MS distance function values (top), the average of that distribution (middle), and the corresponding crystallographic parameters a and c in the space groups $R32$ and $R\bar{3}c$ for the rG and rPD[11], respectively (bottom). The asymmetric patches of the surface are sampled by approximately 2500 (rG) and 1000 (rPD) triangles. The x-axes are the same within each column.

The other limit, $r_0 \rightarrow 1$, is also accompanied by a steady decline of s towards approximately 1 and terminates in a saddle-tower. The MS consists in increasingly wide ribbons with increasingly flat distance profiles, reminiscent of a stacking of crossed lamellar ribbons.

Instability of the Primitive surface

The functional form of Δd of the rPD surface family exhibits a clear minimum at the cubic member corresponding to the diamond surface ($r_0 = \sqrt{2}$). Somewhat unexpected, the Primitive surface ($r_0 = 1/\sqrt{2}$) corresponds to an inflection point. Hence, there are rhombohedral deformations of the cubic Primitive surface that are more packing homogeneous than the Primitive surface itself. The maximum of the fluctuations actually corresponds to a surface very close to the rG surface family member that is part of the rPD family (with $r_0 = 0.49472$).

Definitive assessment of whether the cubic Primitive surface corresponds indeed to an inflection point of Δd, or rather to a very shallow minimum, is difficult. We have collected additional data, spaced at closer intervals and with higher resolution. The noise in the data is too large to make a clear decision. However, we believe it is an inflection point; if it is a minimum its depth is smaller than the symbol width of the data points.

In the limit $r_0 \rightarrow 0$, the rPD becomes the aperiodic catenoid. In this process, the surface loses its in-surface two-folds, is no longer balanced and has two distinct MS. It is evident that one side of the MS is a flat plane with a circular hole punched out with radius equal to twice the radius of the catenoid at its constriction (the MS point must correspond to the center of curvature). The other MS degenerates to the rotational axis. The MS structure of the rPD for $r_0 = 2.25$ in Fig. 6.6 already precludes these features, with thin vertical (almost degenerate) lines and flat horizontal pierced layers.

Implications for possible transition pathways

We conclude this section with speculation on the likelihood of transitions from the cubic Diamond surface to the cubic Gyroid surface. The surfaces discussed here offer two alternative routes between the Diamond and the Gyroid: D – rPD – P – rG (rhombohedral) or D – tD – tG (tetragonal).

Fogden and Hyde have already shown that the cost incurred by curvature heterogeneity along the tetragonal path is small. We have shown here that this transition

also involves smaller packing homogeneity than the rhombohedral path. Along the former, the fluctuations Δd and the deviations of the average shape parameter s from the approximate cubic 1.3 are small, in particular smaller than along the rhombohedral path. Thus, both local and global homogeneity favour a tetragonal pathway over a rhombohedral one.

6.3 Detailed description of some IPMS families

This section describes the geometry and shape of the MS and the geometrically centered line graphs of the tD, tG, rPD and rG families. The transitions of the MS are illustrated, and described in terms of the changes to the set of critical points of the Euclidean distance map (EDM) as their positions are[11] descriptive of the structure of the line graph.

Geometrically centered line graphs are computed by tracking ridge lines on the MS of the EDM D, starting from saddle points eventually leading to maxima (possibly via other saddles), see chapter 3 . The surfaces analysed in this chapter provide the main evidence for our conjecture that labyrinths bounded by hyperbolic periodic surfaces have unambiguously defined line graphs: The domains and their line graphs are homotopically equivalent for all surfaces analysed here.

We note that homotopic equivalence does not exclude interesting transitions between different coordination numbers at the nodes. Indeed, apart from the tD surface, we do observe such transitions for all families.

All crystallographic coordinates in this chapter refer to the space groups of the oriented surfaces as given in Tab. 4.2 in Chapter 4.

6.3.1 The tD surface family

The tetragonal distortion, i.e. stretching along the vertical four-fold rotation axis, of the cubic Diamond surface yields the tD surface family described in chapter 4.5.4. This family comprises the cubic Diamond surface as one of its members; another member is congruent to a member of the tG family.

The evolution of the MS as the free parameter r_0 is varied from 0 to 1 (shown in Fig. 6.4) clearly illustrates the changes in the character of the surface. The length scale

---

[11]More precisely, "turn out to be", as these properties cannot be assumed a priori
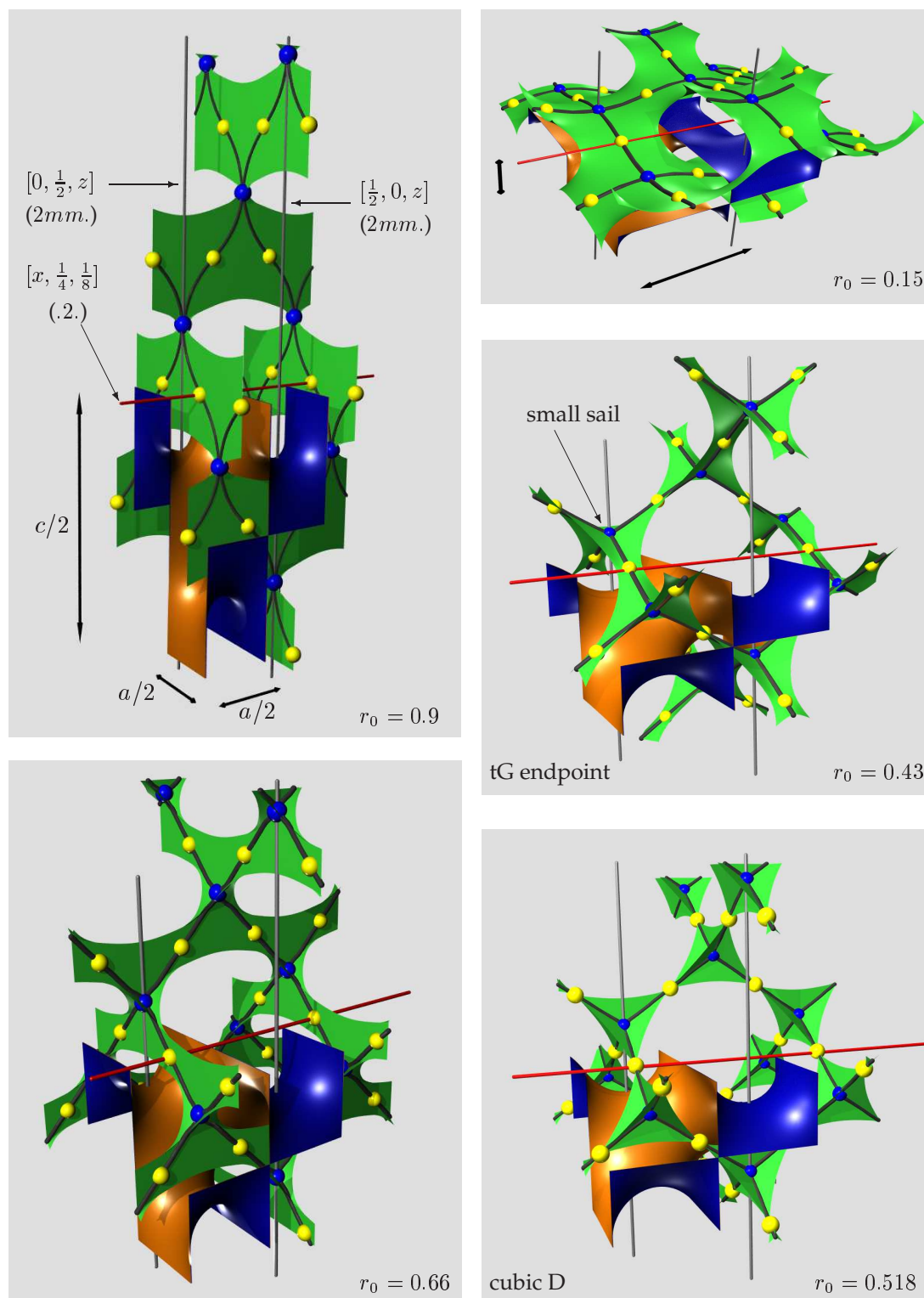
Figure 6.4: Evolution of the medial surface of the tD infinite periodic minimal surface: The tD surface patch shown is exactly one half of the translational unit cell in the $I4_1/amd$ space group and the portion of MS shown is a little more than one translational unit cell.

is normalized such that the crystallographic parameter a remains constant.[12] Yellow spheres are saddle points of the Euclidean distance map D, blue spheres are maxima. The black lines are the line graph as defined in chapter 3.

For all r_0 the crystallographic coordinates of maxima and saddle points of the Euclidean distance map D remain the same. Maxima are at $\overline{4}m2$ (4a), saddle points are at $2mm.$ (8e). The topological structure of the graph remains constant as well, in the sense that the same saddles are connected to the same maxima. Note that this could not be expected (a priori), and is, in general, not the case; see e.g. the analysis of the rPD family.

For small r_0, the MS resembles a checker-board pattern of wide ribbons in x and y directions, with alternating z-coordinates. Each $(a/2)^2$ patch of the ribbon connects to its two upper neighbors at $z + c/4$, in $\pm y$ direction, and to its to lower neighbors at $z - c/4$ in $\pm x$ direction. The MS exhibits no cusps. The MS is essentially a topologically complex lamellar division of space into horizontal layers.

Maxima are normal MS points: the two corresponding points on the surface are on the same vertical axis, above and below (point 0 in Tab. 4.3). Saddle points of the Euclidean distance map D, located on the .2. axes, are normal MS points as well. For arbitrary r_0, they do not correspond to the flat points of the surface, but to other surface points in the vertical mirror plane. The flat points at 8e, in the mirror planes, map onto MS points on the line graph edges. Only in the $r \to 0$ limit is their image the saddle point of D.

The line graph follows planar curves $(x, 0, z(x))$ and $(0, y, z(y))$ contained in the global mirror planes. They are not, however, straight lines.

As r_0 (and c) increases the cross-sectional shape (at the edge centers) becomes more and more circular. For $r_0 > 0.4 \pm 0.1$, the MS exhibits small "sails" that span the two opposite line graph edges emanating from a node – either both going up or down. As a consequence the points on the surface corresponding to the the maximum are no longer vertically above and below the maximum, but points on the graph edges. There are also four corresponding surface points instead of two.

The sails extend further towards the saddle points of D as r_0 increases further. Eventually, the saddles of D cease to be normal MS points.

For $r_0 = \sqrt{2 - \sqrt{3}} \approx 0.518$, the corresponding tD member is congruent to the cubic Diamond surface. At that point, the angles subtended by the edges emanating from

---

[12]The crystallographic parameters refer to the space group $I4_1/amd$ of the oriented surface. With the parameterisation given in chapter 4.5.4 a and c increase monotonically as r_0 varies from 0 to 1, with a remaining finite and $c \to \infty$ at $r_0 \to 1$. The ratio c/a increases monotonically, with $c/a \to \infty$ for $r_0 \to 1$.

the nodes are identical and tetrahedral. The sails between two opposite edges (pointing both upwards or both downwards) are now identical to the sails between two neighboring edges, one pointing down and one up (See chapter 5 on the MS of the cubic IPMS for more details on how the sails join near the saddle points of the EDM D).

The edges of the line graph are straight lines, and correspond to the cubic three-fold rotation axes. The flat point on the surface corresponds to the maximum of D.

Upon further increase of r_0 beyond the cubic case the vertical sails expand and start forming ribbon-like sheets in the mirror planes in x and y direction. The other sails shrink towards the maxima, and merely form transition structures between the perpendicular ribbons.

The maxima of D still correspond to points on the mirror planes, and have more than two corresponding surface points. The saddle points of D are the images of the surface points at sites 222. (4c)in the non-oriented space group, on the same horizontal two-fold axis .2. as the saddle points (point 3 in Tab. 4.3).

For large r_0, the MS of the tD surface family consists of a vertical stacking of parallel sets of ribbons (with normals pointing in x or y directions) of height $c/4$ with spacing between two neighboring parallel ribbons equal to a. The orientation of the parallel ribbons alternates from stack to stack. The connection between two perpendicular ribbons has almost shrunk to a point, although, in detail, the transitions are still formed by the sail-like arrangement.

Note that the line graph continues to zig-zag from saddle point to maxima – across the ribbons. This may seem counter-intuitive to the notion of a network representation given the fact that the ribbons contain straight lines in x or y direction that could be interpreted as channels. This again demonstrates the importance of a robust definition of labyrinth skeletons.

6.3.2   Tetragonal distortion of the Gyroid surface

The tetragonal distortion, i.e. stretching along the vertical four-fold rotation axis, of the cubic Gyroid surface yields the tG surface family described in chapter 4.5.5. This family includes the cubic Gyroid surface as one of its members. The end points of this family are part of the tD and tP surface families, respectively.

The tG family comprises members with different coordination numbers of the line skeletons. The end point on the tD surface is four-connected whereas the cubic Gyroid and the other end point on the tP family are three-connected. The transition of the line

graph is somewhat different to the idealised picture of two connected three-nodes forming a four-node by virtue of the connecting edge vanishing: in the tG case, two adjacent three-nodes each split into normal points (two-nodes) making the center of their connecting edge a four-node.

The evolution of the MS and the line graph, as the free parameter φ_0 varies from $-\pi/2$ to 0, is shown in Fig. 6.5. Symmetry positions refer to the space group $I4_122$ of the oriented tG surface. In the following, *saddle* (or monkey saddle, minimum, maximum) denotes a saddle (or monkey saddle, minimum, maximum) of the distance function d, defined on the tG surface or its medial surface.

The tG member for $\varphi_0 = -\pi/2$ is congruent to the member of the tP surface with $r_0 = 1$. In that limit, the tG surface is essentially an array of vertical tubes with rounded, nearly square cross-section, where diagonal neighbors are connected by horizontal periodic small and nearly circular holes.

The MS (on either side of the surface) is a collection of planar surface patches, contained in the diagonal mirror planes (of the tP surface). Four such patches meet perpendicularly along vertical 4_1 screw axes through the centers of the tP channels (e.g. $[1/4, 1/4, z]$). The distance function d on the MS along these lines is constant, as the corresponding points on the surface are parallel lines in the tP surface (e.g. $[0, 1/4, z]$). This value of the distance function is also the global maximum of d.

Medial surface patches penetrate the small holes connecting diagonal channels to each other. Even there, the MS remains flat, fully contained in the mirror planes and of finite width, indicating deviations of the holes from circularity. The point at the center of the holes is on the 8d two-fold axis (cyan straight line) and is a saddle point of d.

Along the vertical maximal 4_1 axes, the connections to diagonally neighboring channels are vertically offset by $c/4$ relative to each other. Hence, the line graph nodes, located where the straight and horizontal graph edges from the saddle point meet these vertical lines, are three-coordinated with one horizontal and two vertical directions.

As φ_0 increases, but remains smaller than $-(0.32 \pm 0.02)\pi$, the MS structure becomes more complicated. The 4_1 axes are no longer part of the MS; instead the MS "wobbles" around it. The line graph now follows a helical line around the 4_1 axis. The distance function on the MS (or Euclidean distance map) d is no longer degenerate in vertical direction, but shows alternating maxima and saddle points along the vertical parts of the line graph.

The MS patches penetrating the horizontal holes remain a single surface patch without branch lines, although with a developing kink. The points at the center of the horizontal holes remain saddle points of D. The line graph edges emanating from these

(a) $\varphi_0 = -0.49\pi$

(b) $\varphi_0 = -0.38\pi$

(c) $\varphi_0 = -0.26\pi$
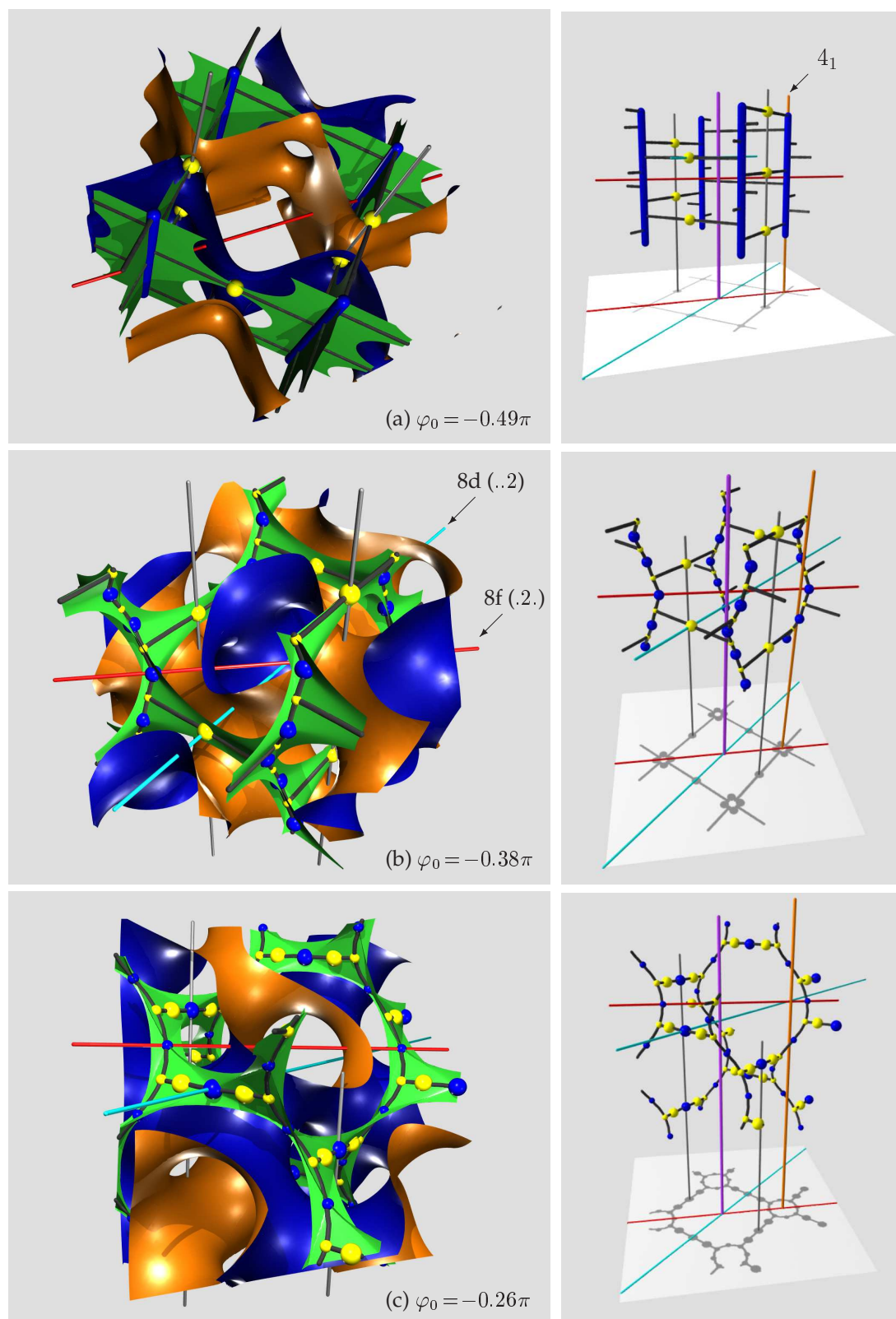
Figure 6.5: Evolution of the medial surface of the tG infinite periodic minimal surface.

(cubic Gyroid)   (d) $\varphi_0 = -\pi/4$

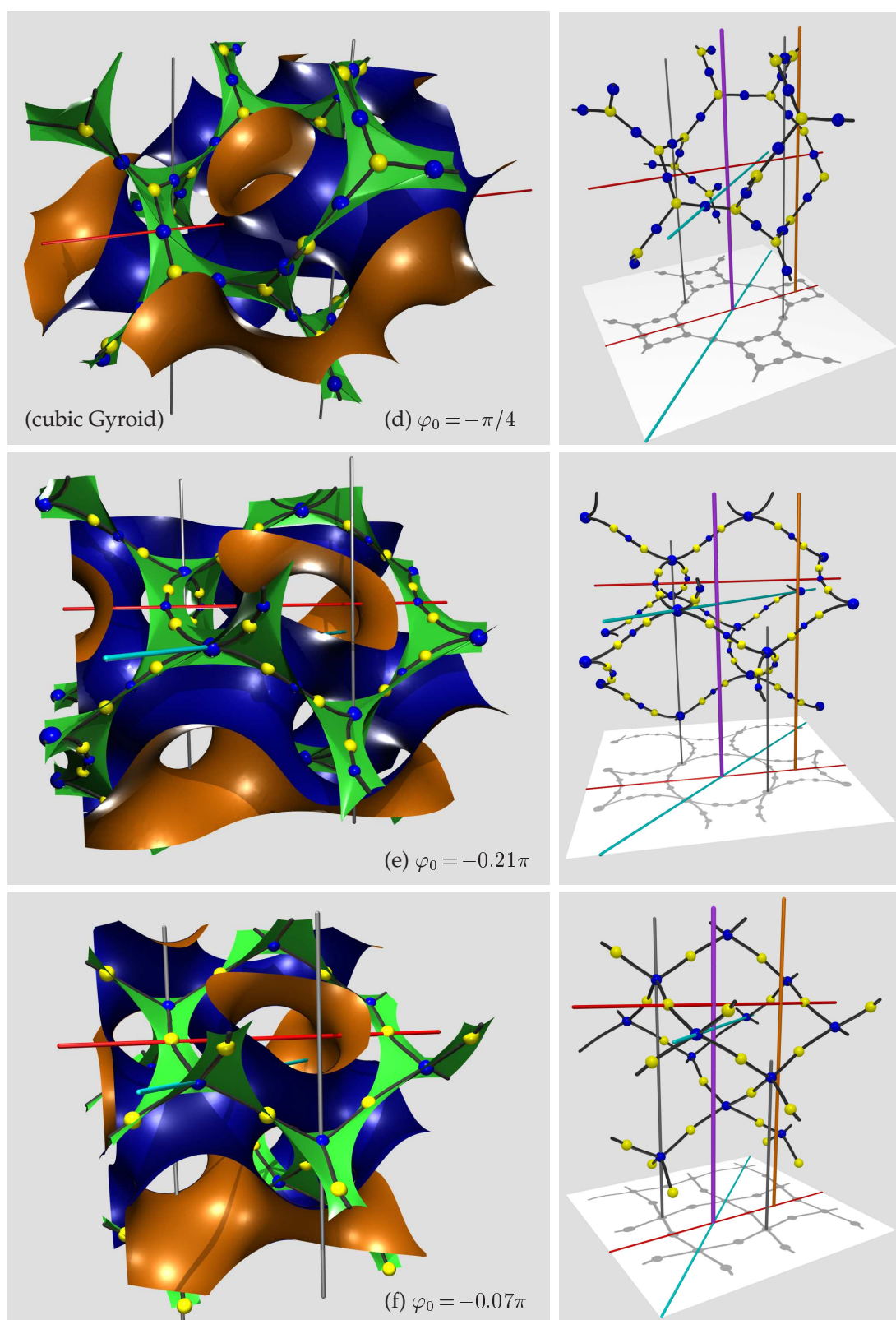(e) $\varphi_0 = -0.21\pi$

(f) $\varphi_0 = -0.07\pi$

Fig. 6.5 (continued)

saddles do terminate at (a second, symmetrically distinct set of) saddle points on the helical segments of the line graph (the small yellow spheres). The three-connected nature of the line graph is preserved. The incident angles at the node continue to be $\pi/2$ and π.

Upon further increase of φ_0 beyond $-(0.32 \pm 0.02)\pi$, the line graph point on the 8d two-fold axis becomes a maximum (big blue sphere) with two adjacent saddle points (big yellow spheres) instead of a single saddle. The maximum (small blue sphere) on the 8f two-fold axis remains. There are now two distinct saddle points of d and two distinct maxima. The two types of saddles move towards each other, rather than one of them moving and one of them staying fixed, as φ_0 gets closer to $-\pi/4$. The line graph remains three-connected.

At $\varphi_0 = -\pi/4$ the tG surface becomes the cubic Gyroid. The two saddles (geometrically distinct at lower values of φ_0) collapse onto a single point (on the cubic three-fold rotation axis). The new saddle is now a "monkey saddle" of d, i.e. with three directions of increasing distance function. By virtue of the three-fold symmetry, all maxima are now identical points.

The MS is now an assembly of flat triangles joined at the vertices (the maxima of D) with the monkey saddles of d at the centre. See chapter on the cubic Gyroid for further discussion.

The line graph is the Laves (or Y*) graph with straight edges that lie on the (additional) two-fold axes.

If φ_0 becomes greater than $\varphi_0 = -\pi/4$, the line graph becomes four-connected. The mechanism by which this split-up occurs is different from the standard picture where the length of a graph edges goes to 0, effectively merging two three-nodes to form a single four-node.

Instead, the monkey saddle splits up into two normal saddles that move towards the two maxima on the 8f sites, away from the maximum at the 8d axis. The line graph segment emanating from this saddle towards the maximum on the 8d site are (to the best resolution we can obtain) geometrically distinct lines. The only coincidental point is the maximum at their end points[13].

Note that this drastic change in the line graph structure is not paralleled by an equally drastic change in the MS. Apart from losing some symmetry (compared to the cubic

---

[13]Remember, as discussed on page 3.5 and in Fig. 3.10, that a node of a graph may be at a point on MS that is neither a maximum nor a saddle point of d. Therefore the claim made here relies on detailed analysis of the trajectory of the line graph segments connecting the saddles on the 8f axes to the maximum at the 8d site. It is based on analysis of high resolution data; the trajectory has been verified using increasingly small step sizes when tracing lines of maximal ascent on MS.

case) its structure remains very similar.

At $\varphi_0 = -(0.17\pm0.01)\pi$ the saddles collapse onto the maximum on the 8f axis, forming a single saddle point at that site. The MS is now a single surface patch in the vicinity of that point. Only one type of saddle and one type of maximum remain.

As $\varphi_0 \to 0$ the edges of the line graph approach the global mirror planes of the tD surface family. The tG surface member for $\varphi_0 = 0$ is congruent to the tD surface with $r_0 = 0.43188$.

6.3.3 The rhombohedral rPD family

The evolution of the MS structure and of the line graph of the rhombohedral rPD surface family is interesting despite the fairly high symmetry. The line graph undergoes a transition from six-connected to four-connected nodes. It also turns out to be an example where the images $ms(p_0)$ of the flat points $p_0 \in S$ do not correspond to nodes of the line graph. Analysis of the rPD medial surface also helps to elucidate the MS branch line structure of the cubic Primitive and especially the cubic Diamond surface, see Fig. 5.7 and Fig. 5.8.

Four special members of the rPD surface family are distinguished: $r_0 = 0$ is the helicoid and 1-periodic, $r_0 = 1/\sqrt{2}$ is the cubic P, $r_0 = \sqrt{2}$ is the cubic D and $r_0 \to \infty$ the catenoid (note that these points are pairwise adjoints of each other).

In the limit $r_0 = 0$, the MS of the rPD is the MS of the helicoid, i.e. a ribbon that ascents like a spiral staircase around a vertical axis. For finite r_0, e.g. $r_0 = 0.45$ shown in Fig. 6.6 (top left), the vertical rotation axis of the helicoid becomes a three-fold screw axis (in Fig. 6.6 this is the 3_1 axis). The MS still retains its ribbonlike character, i.e. it has no branch lines.

The nodes are six-coordinated with vertical MS normals on three-fold axes. They are clear maxima of the Euclidean distance map D, and correspond to flat points on the surface, vertically above and below the node. The second set of six flatpoints on the surface, half-way along the edges of the spanning triangles, does not map onto a node but to a point in between the saddle and the node. The line graph edges are contained in the mirror planes, but are clearly curved. This is necessarily the case, as they connect two MS points both with vertical normal direction but with different z-coordinates to each other.

As r_0 increases further, to $r_o = 0.65$ the c-axis becomes larger relative to the a-axis, and the MS develops a branched structure. The areas around the nodes are still flat (and unfortunately not visible in the picture), but a branching structure develops that
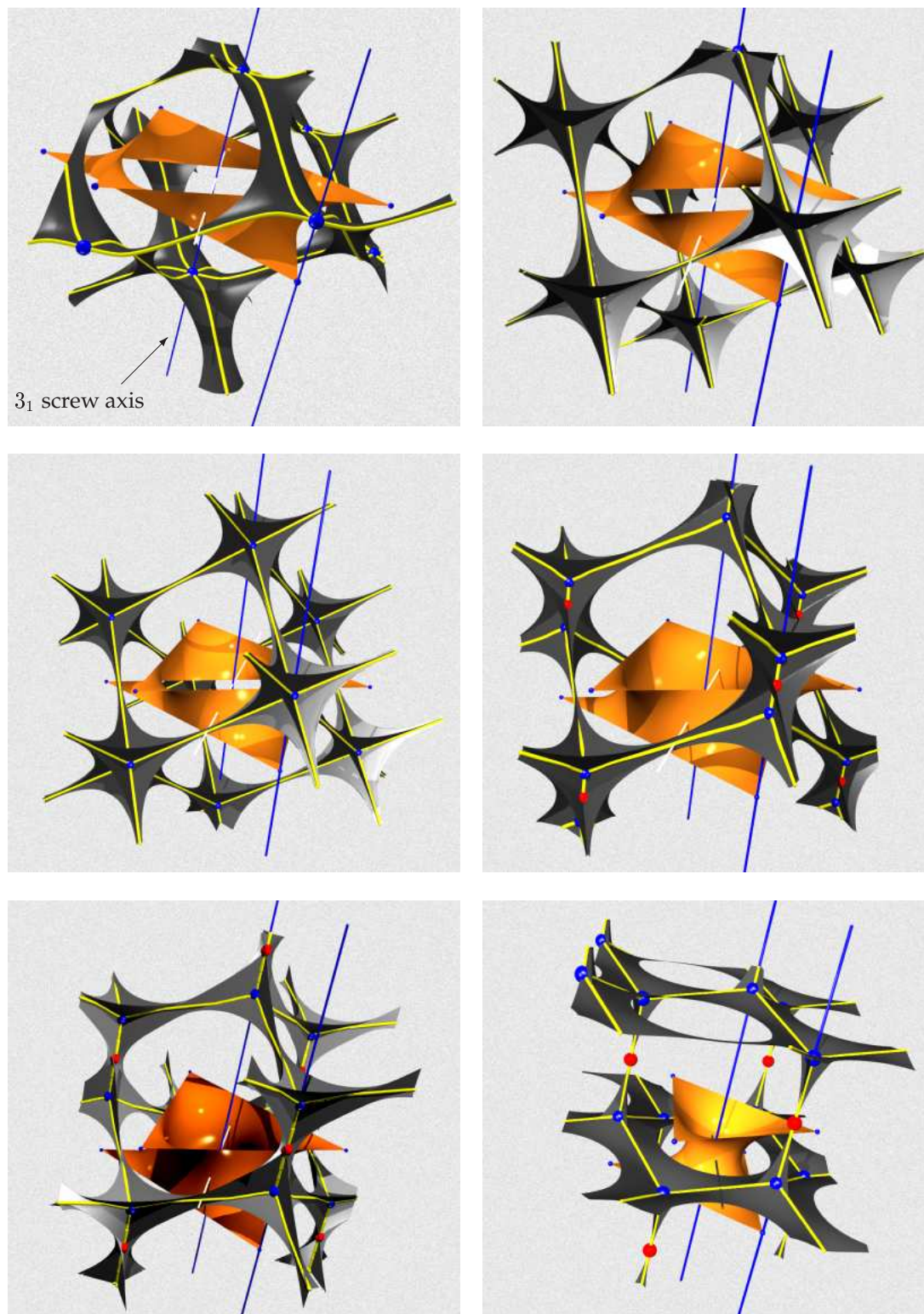
Figure 6.6: MS structure of the rPD surface family for the values (from top left) $r_0 = 0.45, 0.65$, $1/\sqrt{2}$ (P), 0.85, 1.05, 2.25

turns into the MS of the cubic P surface. Around the nodes, there are two vertical "openings" of the MS (the top one is bounded by the horizontal flat patch and three diagonal sails related by the 3-fold symmetry) and six horizontal openings, related by $\bar{3}$ symmetry around the node, which extend to the boundary of the flat patch (and do not reach the 3-fold axis). The images on the MS of the second set of flat points move closer to the nodes (The area around the nodes is still flat, as the distance between the vertically aligned flatpoints is still larger than the distance from the other flat points to the node). The line graph remains six-coordinated.

For $r_o = 1/\sqrt{2}$, the rPD is congruent to the cubic P surface, with the distance from the node to all 8 flatpoints identical and corresponding to the node on the MS. The two vertical and six horizontal openings are now congruent, pointing towards the eight corners of the unit cube.

Maximal 6-nodes turn into two non-maximal 4-nodes at $r_0 = 1/\sqrt{2}$

As r_o (and c/a) increases further, e.g. $r_0 = 0.85$, the vertical distance between the $\bar{3}$ sites and the vertical flatpoints becomes larger than the distance from the other six flat points to the $\bar{3}$ site. As a consequence, the two vertical openings no longer extend to this site, and the six horizontal openings develop a common branch line along the 3-fold axis.
Up to a certain $r_0 > 1/\sqrt{2}$, the $\bar{3}$ sites remain the only maxima of D, and the common point at of the top-opening with three of the horizontal ones (the new node) a normal point of D.
Even though the image of the vertical flat points is not a special point of D, the line graph passes through it, as it comes from the $2m$ sites, and turns sharply onto the 3-fold axis. As three diagonal edges meet here, this point is a 4-node of the line graph without being a maximum.

Upon further increase, the four-nodes move further apart. The images of the six non-vertical flat points move closer towards the graph nodes along the three-fold, away from the $\bar{3}$ site. The four-nodes turn into maxima of D. Yet, the $\bar{3}$ sites remain maximal points as well, and a new saddle point of D is created on the three-fold, in between $\bar{3}$ and the nodes.

The cross-over of the cubic Diamond MS between nodes seems sensible in the sequence of the rPD members

As r_0 approaches $\sqrt{2}$ and the rPD the cubic case, the MS shrinks near the midpoint on the edge, and grows near the nodes. Yet, it retains its structure even at the cubic case; it does not shrink to a point.

In the context of this transition, the peculiar shape of the MS of the cubic D makes more sense.[14]

Upon further increase of r_0 beyond the point of maximal c/a ratio at $r_0 = 2.02134$. The top and bottom opening becomes flatter. The MS becomes thinner around the vertical three-fold axes approaching the rotational axis of the catenoid to which the rPD eventually converges. The other MS patches become more horizontal, slowly but steadily approaching the outer MS shape of the catenoid, the pierced horizontal plane.

The $\overline{3}$ points become proper saddle points of D. The angles at the four-nodes of the line graph approach $\pi/2$ and $2\pi/3$, respectively.

6.3.4   The rombohedral Gyroid family

The rG surface family, parametrised with a free parameter $\varphi_0 \in [-\pi/2, 0]$, results from a "stretch" of the cubic Gyroid along one of the sets of three-fold axes. For $\varphi_0 = 0$ it corresponds to a member of the rPD surface family[15]; for $\varphi_0 = -\pi/3$ it is congruent to the cubic Gyroid; and for $\varphi_0 = -\pi/2$ it is a representation of Karcher's saddle tower [110].

We show that the rG has a three-coordinated line skeleton – with two distinct types of nodes – for all finite values of φ_0, but a six-coordinated endpoint, $\varphi_0 = 0$ on the rPD surface. However, the evolution features, at the cubic Gyroid, a simultaneous annilation of one type of three-coordinated node and creation of a different type.

Our analysis is presented with respect to the space group $R32$ of the oriented surface. An illustration of the evolution is presented in Fig. 6.7. On the left, a portion of the rG surface is shown, with one side colored orange and the other blue. A portion (more than the MS corresponding to the portion of the surface shown) of the MS is shown in green. The black lines are the line graph as defined in the previous chapters, yellow

---

[14]Upon initial inspection of low-resolution data of the cubic case only, we believed it to be an artefact of insufficient resolution.

[15]This member is, in terms of the free parameter r_0 of the rPD surface, *not* intermediate to the cubic Primitive and Diamond surfaces. Whereas the parameter corresponding to the cubic cases is $r_0 = \sqrt{2}$ and $r_0 = 1/\sqrt{2}$, the end point of the rG surface corresponds to the rPD surface with $r_0 = 0.4947$. The diagram in Fig. 6.1 is slightly misleading in that sense.

spheres are saddle points of the Euclidean distance map D and blue spheres maxima. The three vertical gray lines are three-fold rotation axes, and the horizontal red and purple lines are the two-fold rotation axes 9d and 9e, respectively.

On the right, the line skeleton and the critical points are shown together with the rotation axes and an additional three-fold screw axis (green) but without the surface or the MS. The graph and the critical points are projected onto the white horisontal square. For clarity, the horizontal directions of the two two-fold axes are also shown on this square.

For all finite values of φ_0, one of the two three-coordinated nodes remains in the channels on the vertical three-fold axes; the angles between the three incident edges – with horizontal tangents along (the red) two-fold axes at the node – is constant and $2\pi/3$. This node is a saddle point of Hopf-index -2, i.e. with three directions of increasing and decreasing distance function, respectively.

The other node is a maximum for $\varphi_0 > -\pi/3$, a saddle point for $-\pi/3 \geq \varphi_0 > -\pi/2$ and a degenerate –along the vertical screw axes – maximum for $\varphi_0 = -\pi/2$. One of the incident edges of this second type of node, emanating from the first type of node, is straight along a two-fold axis. The other two are symmetry related by that same two-fold rotation, and subtend an angle κ between 0 and $\pi/2$ with the imaginary continuation of the straight edge along the two-fold axis beyond the node.

The evolution is most easily understood by starting from the cubic case, $\varphi_0 = -\pi/3$ and examining $\varphi_0 \to 0$ and $\varphi_0 \to -\pi/2$ separately. As discussed above, the cubic case is the Laves graph (or "srs") with saddle points of D at the three-connected nodes and maxima of D at the center of the edges. The two types of nodes are symmetry related by virtue of the additional – compared to R32 – two two-fold axes through the centers of the edge.

When φ_0 decreases, the nodes on vertical 3-axes remain monkey saddles of D (big yellow spheres). All other three-coordinated vertices (the medium sized yellow spheres) slide along the red 9e two-fold axes away from the nodes on the 3-axes. This results in an increasing angle κ, i.e. the angles at the shifted three-node now are $\kappa > 2\pi/3$ and two times $(1-\kappa)\pi$. The node becomes a normal saddle, Hopf-index -1. Along the edge to the node on the vertical three-fold axis, an additional saddle of Hopf-index -1 emerges (small yellow spheres). The edge from the vertical 3-axes nodes to the second type of three-coordinated node is horizontal, straight and fully contained in the 9e two-fold axis. It connects a monkey saddle of D via a maximum and a normal saddle to a normal saddle.

The second type of edge emanating from the shifted node terminates at a maximum of D on the 9d two-fold axis (big blue spheres on the purple 9d axis). It is not straight,

$\varphi_0 = -0.49\pi$
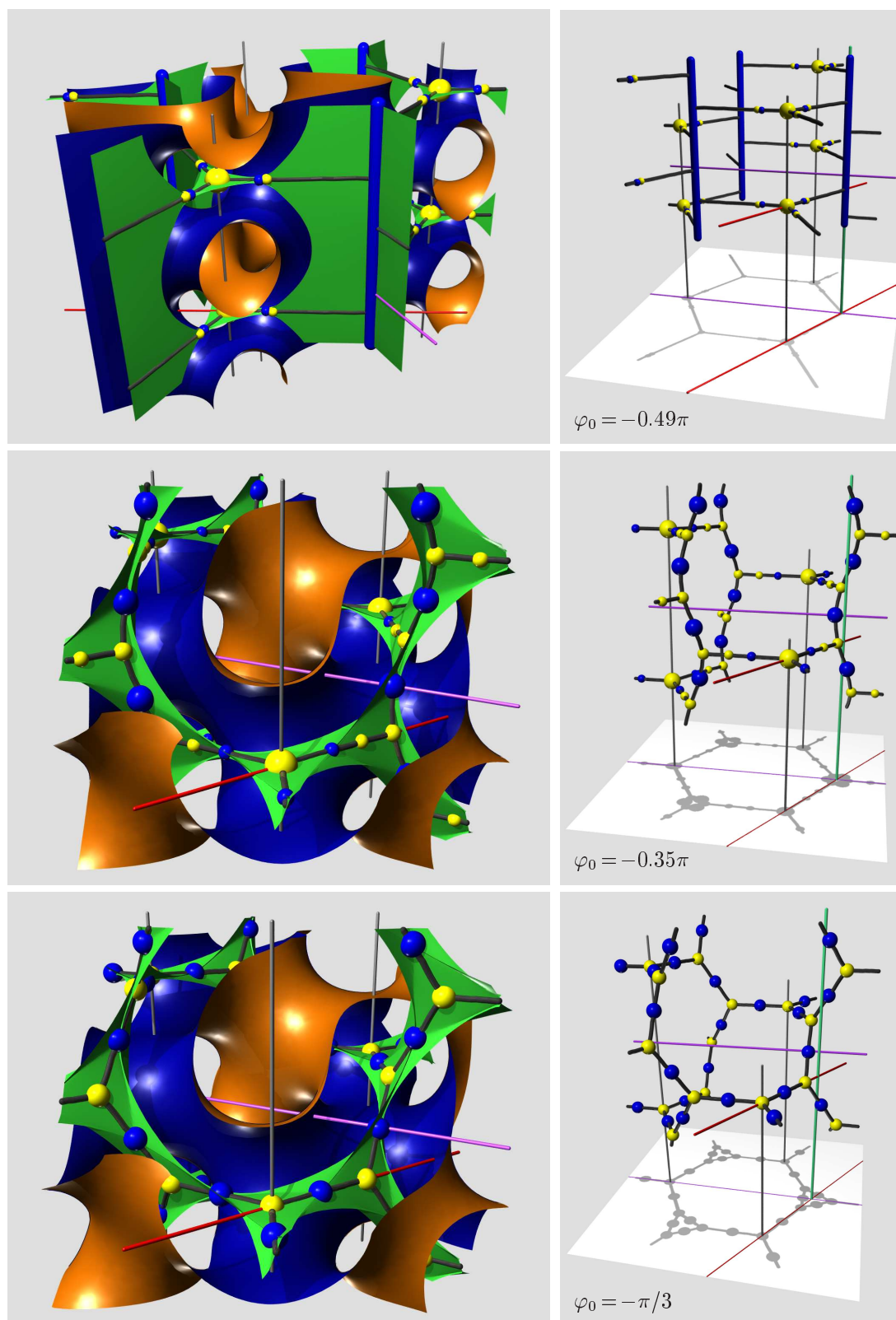
$\varphi_0 = -0.35\pi$

$\varphi_0 = -\pi/3$

Figure 6.7: Evolution of the medial surface of the rG infinite periodic minimal surface.

$\varphi_0 = -0.315\pi$

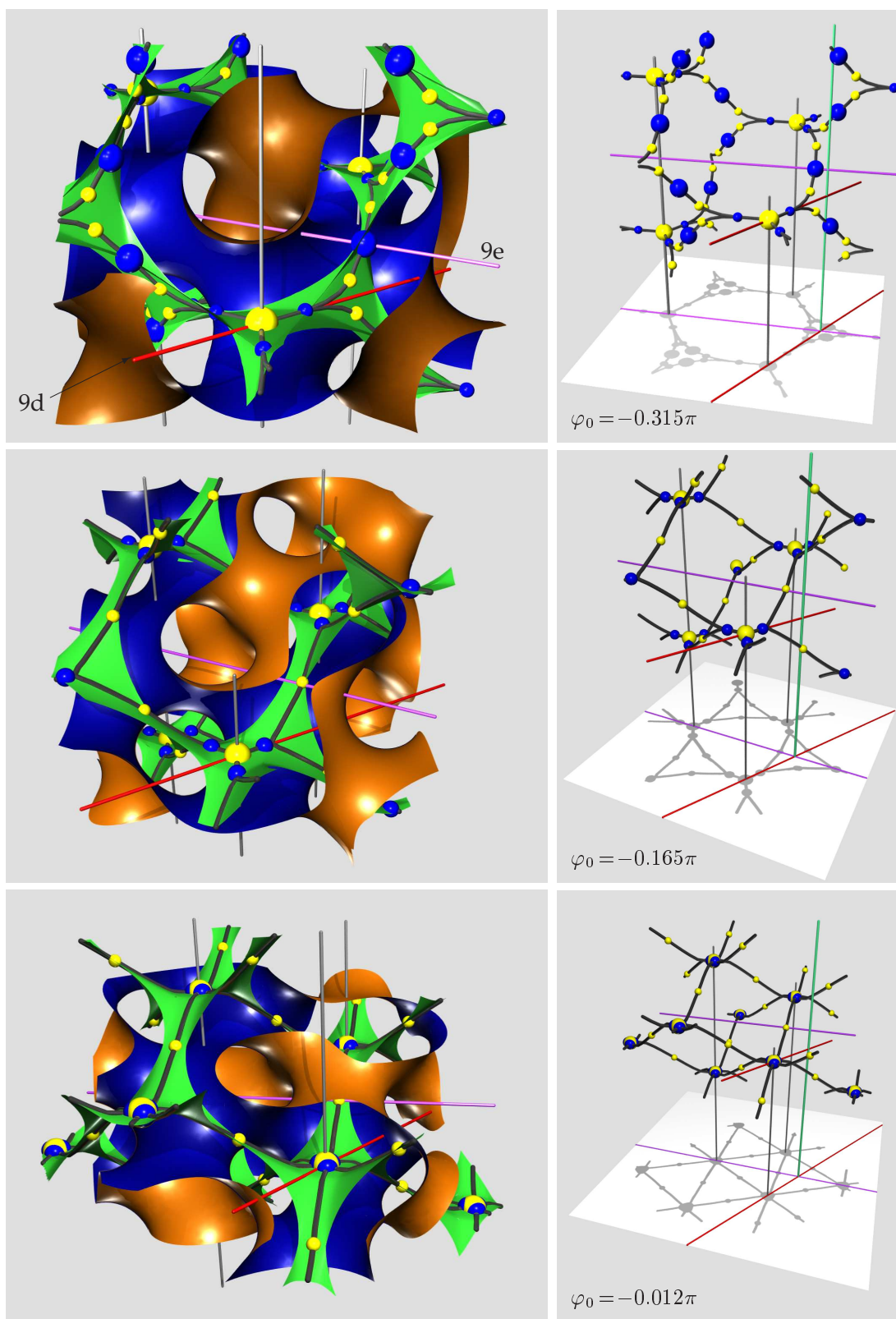$\varphi_0 = -0.165\pi$

$\varphi_0 = -0.012\pi$

Figure 6.7 (continued)
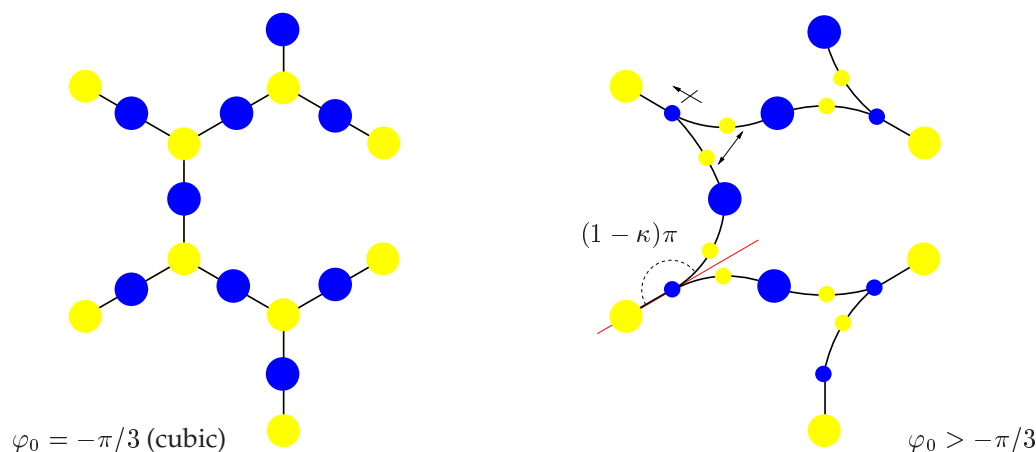
Figure 6.8: Illustration of the topological transition of the line graph of the rG surface family at the member corresponding to the cubic Gyroid.

and upon application of symmetry, yields a spiral that revolves around the vertical three-fold screw axes (green line).

This change in the line skeleton structure solely affects the geometry of the line skeleton but not its topology and connectedness.

As φ_0 decreases further, the revolution of the vertical elements of the line graph around the three-fold screw axes becomes tighter and the relative variations of d (or D) along those lines smaller. Eventually, at $\varphi_0 = \pi/2$ these edges become vertical and coincide with the screw axis. The distance function is then maximal along this axis and constant. The screw axis are now at the center of large vertical channels of triangular cross-section. One portion of the MS are three flat ribbons, running in vertical direction, with the screw axis being the branch line.

The other portion of the MS is still a flat horizontal triangle centered at the three-fold axes[16]. The point at its center remains a monkey saddle of D. The mid-edge maximum and saddle of D converge towards each other, but merge and form a single saddle point only in the limit $\varphi_0 = -\pi/2$.

The line graph now has one type of node with three symmetric edges in a horizontal plane subtending $2\pi/3$ angles with each other, and another type where a horizontal edge connects perpendicularly to a straight vertical line.

The other development from the cubic case, i.e. φ_0 increases from $-\pi/3$, features a topological transition of the line skeleton.

Again, at least for all finite values of φ_0, the three-coordinated nodes on the three-fold

---

[16]Note that the set of three-fold axes shown in Fig. 6.3.4 yields the set of corresponding three-fold screw axes upon rotation of $\pi/3$ around the vertical axis in the center of the axes.

axes remain monkey saddles of D and 3-nodes.

For φ_0 just above the cubic case, e.g. $\varphi_0 = -0.315\pi$, the three-nodes that are not on vertical three-fold axes split up into to normal saddle points (small yellow spheres), symmetry related by two-fold rotation around the red 9e axis. Two types of maxima exist: One is on the purple 9d axis in between two of the new simple saddles that is not the node of the graph (big blue spheres). The other one is on the 9e a axis and forms a node with three incident edges – two from the new saddles and one from the monkey saddle at the 3-fold axis (small blue spheres).

The lines of steepest ascent from the normal saddles, in direction of the three-fold axis, terminate at the maxima on the 9e axis. At the maximum, the angle between the 9e axis and these lines is very small, suggesting tangency of both the two edges and the two-fold axis. Two scenarios are possible: first, the two edges (from the two saddles) only end in the same point but are geometrically distinct elsewhere. The second possibility, which cannot be ruled out a priori as demonstrated in Fig. 3.10, is that both lines coincide before the maximum and from there follow a common path to the maximum.

Our analysis – with the caveat of limited, although very high, resolution in the immediate vicinity of the maximum – suggests that the first situation is realised, i.e. the two paths are geometrically distinct apart from their common endpoint at the maximum. This implies that a true topological transition takes place at the cubic case: A three-coordinated node splits up into two normal points, while simultaneously the points at the centers of the adjacent edges becomes a three-coordinated node.

Geometrically, the new graph is not very "equilibrated" in the sense that the angles of incident edges at the nodes are rather uneven – $2\pi/3$ at the nodes on the three-fold rotation axes, and $\pi - \kappa/2$ and κ a the second type of node.

As φ_0 increases further, the normal saddle points (small yellow spheres) move towards the maximum (big blue sphere) on the purple 9d axis. Eventually, at $\varphi_0 \approx -0.2$, coalesce with that maximum and form a single saddle on the 9d axis.

Simultaneously the other maximum (small blue sphere), now a three-node, moves towards the monkey saddles on the three-fold rotation axes. For all finite values of φ_0 it remains a maximum and at finite distance from the three-fold axes.[17]

At $\varphi_0 = 0$, the maximum has been swallowed by the monkey saddle on the three-fold axis, making that point a six-connected node of maximal distance function value.

---

[17] The situation at $\varphi_0 = 0.165$ is an example that the line graph is, in general, not centered with respect to the MS. The MS is almost ribbon-like and the line graph is not running along the middle of the ribbon but rather on one of its two edges.

Three curved edges descent and ascent, respectively. The rG surface displays the additional symmetries of the rPD surface, in particular additional vertical mirror planes. The line graph is contained in the mirror planes.[18]

6.4   Conclusion

The analysis of these surface families in terms of MS properties has demonstrated that the MS construction, the construction of a geometrically centered line and the analysis of the MS distance function provide a robust, non-trivial measure of labyrinth network geometry and topology, unavailable by other techniques.

A caution for graph models

The line graphs undergo the expected topological transitions that symmetry alone does not explain. However, the geometry and distance function values along the graph segments evolves in unexpected ways. In particular, there are
(a) the four-nodes of the rPD surface where the node is not a critical point of the Euclidean distance map D. The consequence of this is that the split of the six-connected node to two four-connected nodes happens in two stages: first, the node splits into two nodes with an edge connecting them but the maximum of the Euclidean distance function remains at the edge center; second, the edge center becomes a saddle point, and the two new nodes become maxima of the Euclidean distance function D. (b) The transition of a three-connected graph to a four-connected graph in the tG eventuates not by virtue of two neighbouring three-nodes merging, but by them individually splitting apart. The edge center between them becomes a four-node with two pairs of opposite graph segments with very small angle between them.

These cases elucidate the transition between generalised graphs (with curved edges) of different coordination numbers. For the investigated IPMS, they clearly show that changes in coordination number of the line graph incur strongly uneven geometric arrangements of the incident edges – in sharp contrast to the picture of a split up of four-nodes that is typically drawn.

---

[18]The result that this node is six-coordinated is clearly evidenced by our numerical analysis. The possibility of graph edges being pairwise coincidental before the end point at this maximum – leading to more nodes but three- instead of six-coordinated – can be confidently ruled out.

For graph models in general this means that emphasis on the topological transition between differently coordinated graphs, that constitutes by definition a sharp jump, must be treated with caution. The situation where the transition from a most symmetric 3-node (or n-node) to a most symmetric 4-node (or n-node) occurs is a ficticious one, at least if the graph at all represents the geometry of a labyrinth (and if similar results hold true for other space partitions).

Global homogeneity and average shape parameter

We have shown that the cubic Gyroid and Diamond surfaces minimises variations of the MS distance function among their tetragonal and rhombohedral distortions. This implies that they are stable structures if these fluctuations determine the energy functional. For the cubic Primitive this does not hold true as there is at least one deformation that leads to a more homogenous partition. Globally, the Gyroid is more homogeneous in a packing sense than the Diamond which is more homogeneous than the Primitive.

We have also shown that the variations of $\langle d \rangle / (V/A)$ (1.3 ± 0.1 in the vicinity of the cubic cases) are smaller than the variations in homogeneity Δd, which are 0.05, 0.10 and 0.19 for the G, D and P surface, respectively, scaled to give constant V/A. This implies that for these cases it is Δd and not $\langle d \rangle$ that makes the bigger contribution to the toy model $E_f \propto (d - l_0)^2$ for an energy functional.

The interpretation of these results in terms of mesophase assembly of surfactant mixtures is only straightforward in binary Type 2 systems. It is likely to be more relevant to self-assembly of copolymer phases where the channel diameter is of increased relevance.

Omissions and extensions

The analysis of this chapter is incomplete in a number of basic ways. The surfaces analysed should at least include all known tetragonal and rhombohedral distortions of the cubic IPMS, most notably the tP surface. Furthermore, the MS of the limiting helicoidal and catenoidal cases lends itself to almost analytic computation. Hence, the homogeneity properties of these cases could be computed with much higher precision – especially desirable since these are aperiodic and 1-periodic cases where the analysis needs to be extended to infinity.

As an extension, a similar analysis needs to be carried out on the other known families of IPMS to get a better understanding for the relative strength of the fluctuations.

Furthermore, if the surfaces are used as models for the transition behaviour between mesophases it is not clear that vanishing mean curvature is a property of the non-equilibrium phases. Therefore, extension to other hyperbolic space partitions is desirable.

A non-cubic network in a triblock copolymer blend

This chapter presents a MS analysis of the microdomain morphology of a linear triblock terpolymer phase, based on real space data from electron tomography. The microdomain morphology, as characterised by the shape of the domain of one of the three components (PDMS), consists in two intertwined, disjoint, identical, symmetric and periodic channel networks with three- and four-connected nodes. The symmetry of the network is orthorhombic and with a c/a ratio distinctly larger than one – making it one of the rare occurrences of non-cubic structures in systems that assemble in hyperbolic labyrinths.

The MS analysis proves to be a useful visual tool by providing a succinct yet sparse representation of the labyrinth that represents topology *and* geometry. Furthermore, a statistical analysis of MS properties (distance function, MS normals) of the network nodes provides evidence for the symmetry and periodicity of the network.

The polymer system is a linear triblock terpolymer made up of polystyrene (PS), Polyisoprene (PI) and polydimethylsilocane (PDMS).

A three-dimensional dataset of the PDMS phase is reconstructed from a tilt series of transmission electron microscopy (TEM) images. These images only resolve PDMS in contrast to PI and PS, but do not distinguish between PI from PS. After binarisation and triangulation of the interface between the PS/PI phase and the PDMS phase, an approximation of the MS inside the PDMS phase is computed, using distance and incident angle to discern MS parts that are only due to noise. This makes the MS a set of not necessarily connected triangles rather than a connected triangulation. This representation of the MS is not good enough to detect geometrically centered line graphs in an automated way. Yet it elucidates, both qualitatively and quantitatively, some of the subtleties of the symmetry of the labyrinth. In particular, it clearly demonstrates

that the four-nodes are four-connected, rather than being two nearby three-nodes connected by short edges.

This chapter is organised as follows: Section 7.1 provides a short review of the ideas behind self-assembly of co-polymers into hyperbolic network phases. Section 7.2 summarises sample synthesis, electron tomography imaging, and the MS computation. Section 7.3 contains a detailed discussion of symmetry, periodicity, shape and connectivity of the MS and the topological graph as deduced from the data. A discussion and summary is given in section 7.4.

7.1   Network phases of block co-polymers melts

Block copolymers are polymers where sequences of one type of monomers (*blocks*) are covalently bound to blocks of different types. The simplest example are AB diblock copolymers where a sequence of monomers of type A is connected to a sequence of monomers of type B. Triblock copolymers are made up of three different components A, B and C, that can be joined linearly or star-like. The latter architechture generates "mikto-arm" copolymers.

Block copolymers have been long known to self-assemble in solution into a number of different mesophases if the blocks are immiscible (i.e. have a tendency to phase-separate). This microphase separation is diven by chemical incompatibilities between the different blocks of the copolymer molecules. As the entropy of mixing is small in these systems, already a small chemical or structural difference between the components suffices to produce excess free-energy contributions that make mixing unfavorable. After evaporation of the solvent, a variety of mesophases result where the particular form and shape depend on the temperature and on the relative weight of the components.

These mesophases are characterised by the symmetry and topology of each microdomain (containing single block type). Similar to mesophase formation in surfactant/lipid-water-oil systems, spherical, cylindrical, lamellar and bicontinuous structures are found in AB diblock copolymer systems. However, in contrast to surfactant water systems, it has been claimed that out of all bicontinuous structures, the only one observed is the cubic Gyroid.

7.2 Sample synthesis, e^- - tomography, and MS computation

This section describes the synthesis of the sample, the acquisition of the spatial data as a voxelised electron tomography dataset and the computation of an approximation of the MS.

Sample synthesis by casting from polymer solution

The film specimen was prepared by casting from a 5 wt % polymer solution in toluene at room temperature, with slow evaporation of the solvent over 20 days. The cast film was used without annealing.

Using a Reichert Ultracut N ultramicrotome thin sections of the film were cut at -65° to -80° Celsius.

The copolymer was synthesised by Panagiota Fragouli and Hermis Iatrouthe within the group of Nikos Hadjichristidis at the University of Athens.

The triblock copolymer sample considered here is not amenable to mesostructural analysis by standard techniques, such as small angle X-ray scattering, due to the small domain size detected in electron microscopy. Therefore, 3D electron tomography is the best route to determination of the mesostructure.

3D electron tomography datasets with nanometer resolution

Electron tomography is the reconstruction of a three-dimensional structure from a tilt series of transmission electron microscopy (TEM) images [204, 72, 73, 128, 106]. The data analysed in this chapter is obtained from electron tomography and was reconstructed from a series of projections with tilt angles (around a common axis in the plane of the sample) ranging from -60° to 60° with 1° increment between successive projections. Because of the presence of silica atoms, contrast in transmission between the PDMS phase and the other two phases exists (but none between the PI and the PS phase). Energy filtering was used to obtain the zero-loss image that provides better contrast and resolution. TEM micrograph images were taken with a magnification of 25000, corresponding to a voxel size of 0.834 nm in the 3D reconstructed images.

A number of methods are used to investigate three-dimensional spatial structure on the nanometer-scale. Traditionally, the most common 2D microscopy techniques are scanning electron microscopy (SEM) and transmission electron microscopy (TEM) both of which provide images of surfaces, or ultra-thin sections. Volume imaging by serial slicing can produce 3D images (of materials that can be sliced into thin

slices) with approximately 20-50 nm resolution [199, 76]. Nanotomography, based on successive stripping of thin layers and simultaneous imaging by scanning tunneling microscopy, has been shown to yield resolutions of about 10 nm and has been successfully applied to block copolymer systems [145]. Laser confocal microscopy yields resolution of the order of 100 nm and can only be applied to optically transparent materials, see for example [216, 105] for an application to polymeric systems. By comparison, the resolution of conventional X-ray tomography systems is approximately 2 μm for conventional X-ray tubes [180] and 0.2 μm for synchrotron radiation [150].

The reconstruction of the 3D image from the tilt series is the inversion of the projections of the 3D structure onto the planes given by the sequence of tilt normal. Details on the so-called *filtered back-projection algorithm* (for parallel beams) used here can be found in the computer-tomography books [89, 109, 93], or more specifically about the implementation in [74].

Data collection and reconstruction was done at Kyoto University (Japan) by Satoshi Akasaka and Hirokazu Hasegawa. A JEOL JEM-2010FEF electron microscope equipped with an omega filter was used at magnification factor 25000. The accelerating voltage of the TEM was 200 kV, and a Gatan slow-scan CCD camera was used for the image data collection.

An energy filter was used to extract the zero-loss image, $\Delta E = 0$. Zero-loss images result from elastic electron collisions only. That is, only the fractions of the incident, transmitted and scattered electron beams that have the same wavelength are used. Zero-loss images are similar to conventional TEM images but are sharper and have higher contrast, as the inelastic scattering that produces chromatic aberration is eliminated [52].

7.2.1 Segmentation, volume fraction and triangulation of the interface

The tomographic reconstruction yields a 3D gray-scale dataset where each voxel is assigned a number that, in principle, corresponds to its density. The ideal situation, where each voxel adopts one of three values corresponding to either phase and where there are sharp transitions at the interface between two phases, is usually not achieved. At the least, the interfaces are blurred due to noise, finite sampling size, misalignments and reconstruction artifacts due to real inhomogeneities in the phases [93]. More often, the intensity function only converges to the bulk value of a specific phase deep inside that phase, far away from an interface. The process of turning the

gray-scale image into a binary image[1], where 1 corresponds to the PDMS phase and 0 to the union of the PS and PI phases, is called *segmentation* or *binarisation*. The volume fraction of the first phase, as represented in the binary dataset, is trivially computed as the number of voxels with intensity 1 divided by the total number of voxels.

The simplest segmentation scheme is based on a level-set segmentation, i.e. all voxels with intensity $I < I_c$ are assigned the value 1, all others the value 0. The threshold I_c is a parameter that can be tuned and determines the volume fraction. The volume fraction of the first phase monotonously increases as the threshold value I_c goes up. The problem with this segmentation process is its great sensitivity to noise, which leads to ragged interfaces and large numbers of small isolated clusters of one phase within the other.

Alternative and more sophisticated segmentation schemes have been derived based on propagation of an initial interface under a speed function [114, 146, 26] or by using the concept of watershed [211]. The segmentation applied to the dataset here is a combination of these ideas, called *converging active contours segmentation*, and is described in [194]. Note that with this technique the volume fraction is not an input parameter of the segmentation, rather the binary output data set is an optimal segmentation.

The processing of the gray-scale dataset consists in the following steps in this order: (1) sharpen edges using the *unsharp mask filter* [170] [2]; (2) noise reduction via anisotropic diffusion [166, 1]; (3) converging active contours segmentation [194]; (4) triangulation of the interface using marching cubes [137]; (5) decimation and smoothing using routines from the vtk library [3].

The volume fraction, as measured in the image segmented with the converging active contour method, is 12% for the complete data set. This is lower than the volume fraction of approximately 19 % expected from the the composition of the mixture. Differences between likely and actual volume fractions can occur for various reasons: first, the data set contains large regions of poorly resolved structure. Second, as is described later we find that the channel system geometry suggests that some parts of the PDMS phase are not represented in the binary image, whereas we detect fewer regions where the data shows channels that are should not be if the assumed model is correct. This leads to an overestimation. Third, the total extent of the data is only about 1.7 translational unit cells in the c-direction.[4] If the size of the data of a periodic

---

[1]In this specific case, the image could be turned into a ternary dataset. Since we do not aim to (and cannot without staining of the sample) resolve the PD and PS phases individually, we convert the dataset to a binary dataset.

[2]See also the GNU image manipulator manual, www.gimp.org

[3]See the Vizualisation Toolkit homepage: www.vtk.org

[4]This refers to the smallest unit cell possible, which is a monoclinic. Of the body-centered Imm2 unit

system is not an integer multiple of the translational unit cell, the volume fraction of the data set may not correspond to average volume fraction of the sample.

A triangulation of the bounding surface of the PDMS phase, referred to as the *labyrinth*, is obtained from the segmented (binary) dataset using the isosurface and smoothing function of the vTK library. In an additional step, the resulting triangulation is smoothed using the "Smooth" operation of the Houdini visualisation software[5].

The dataset to which the remainder of this chapter refers is a subset of the complete dataset. First, roughly 10% in each linear dimension, for which the MS is not defined as a consequence of the boundary, are removed. Second, half of the sample is not considered as it appears to have been bent macroscopically (as is revealed by a determination of all maxima of the MS distance function maxima that clearly lie on a lattice, one side of which is distorted). The size of the remaining subset is $180 \times 130 \times 180$ in units of the voxel edge length ($150 \times 101 \times 150 \text{nm}^3$). The (smoothed) triangulation of the PDMS labyrinth's bounding surface consists in approximately 1.3×10^5 triangles with an average edge length of 1.8 and standard deviation of the distribution of edge lengths 0.8. The sum of the areas of all triangles (an approximation of the total interface area) is $1.77 \times 10^5 \text{voxel}^2$ ($1.23 \times 10^5 \text{ nm}^2$).

7.2.2   Medial Surface computation

An approximation to the MS of the channels is obtained by Voronoi-based methods that take as input a triangulated representation of the bounding surface of the PDMS phase. A subset of the Voronoi diagram is used to approximate the MS. This subset consists of all Voronoi faces with incident angle for which the face normal (an approximation of the MS normal, and assumed to be pointing into the Voronoi cell) and the vector from the surface point to the pole (that vertex of the Voronoi cell $C_V(p)$ of a vertex p of the surface triangulation that is furthest away from p and inside the channel) form an angle no greater than a threshold angle α_{MS}. This threshold is chosen as $\alpha_{MS} = 60^o$. This procedure is somewhat reminiscent of the approach presented by Dey and Zhao [42]. It yields a sufficiently good representation for the analysis presented in this thesis.

---

cell used later, only about 0.8 of a lattice translation in c-direction is resolved.

[5]Houdini is a commercial 3D rendering and animation software package. It allows for very versatile transformations of triangulated surface data. See the web page of its producers: www.sidefx.com.

7.3 Medial Surface and Channel Geometry

This section describes the spatial structure of the channel network of the PDMS phase as derived from analysis of its MS. The MS is ribbon-like throughout (without branch lines) and resembles (with some distinct differences) a straight-edge graph of flat ribbons. We derive a line graph model (with straight edges) from the MS representation of the tomographic data. According to that model, the PDMS phase consists of two identical intertwined networks of 8-rings and 3- and 4-coordinated nodes of nearly orthorhombic symmetry. Further analysis of the MS (lattice directions and spacings, distance function values and MS normals of particular points) provides evidence for this claim. First, a description of the straight edge line graph is given as it is the easiest to visualise and already a good structural model. Then the MS geometry and shape is described.

Two intertwined (3,4) line graphs of orthorhombic symmetry

Our interpretation of the structure of the PDMS network, expressed as a line graph with straight edges, is as follows: The PDMS phase consists of two identical, intertwined, symmetric and periodic networks with four-connected and three-connected nodes (see Fig. 7.1 and Tab. 7.1 for an illustration).

These networks can be built from body- or face-centered symmetries depending on the orientation of the unit cell relative to the network. The networks are related to both Diamond and Y^* graphs (the channel graphs of the Diamond and the Gyroid surfaces, respectively). Splitting of every second layer of 4-connected Diamond nodes, or fusion of a subset of the 3-connected Y^* nodes, generates the 3- and 4-coordinated graph (described by O'Keeffe and Hyde [163], Fig. 7.78, p. 359).

We choose, for convenience only, the body centered unit cell for the further description of our analysis. One of these networks in that orientation in Fig. 7.1 is as follows: In one of the two networks, called graph 1, four-connected nodes sit on the eight corners and in the center (f_b^1) of a body centered translational unit cell. The emanating edges (two upwards and two downwards) connect to planar three-nodes, that reside horizontally centered in the faces of the unit cell at $[0, b/2, z]$ (t_c^1), or by virtue of the body-centered cell $[a/2, 0, z - 1/2]$, (t_b^1) and $[a/2, 0, z]$ (t_a^1), respectively. A vertical edge connects the pairs of vertically aligned three-nodes, e.g. t_a^1 to t_b^1.

Within the uncertainty of the available data, the second graph is geometrically identical to the first graph but oriented differently in space: The four 4-nodes of the translational unit are on the four vertical faces, and the vertical edges (and the three-nodes)
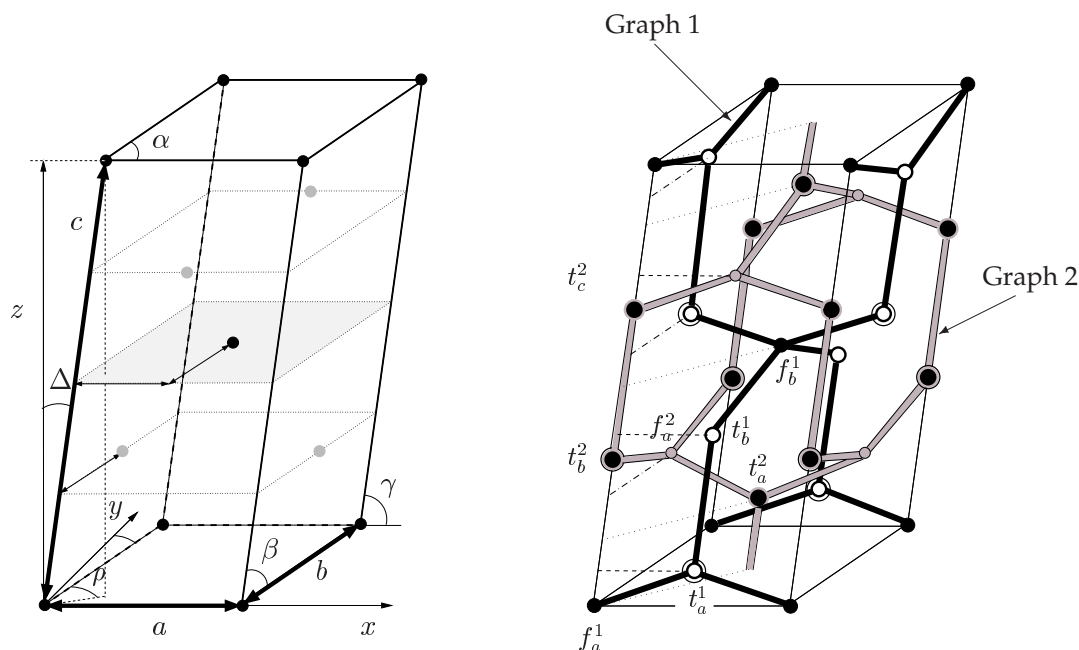
Figure 7.1: Model of the line graph (with straightened edges) of the PDMS network as extracted from the MS. Shown here is a monoclinic translational unit cell that corresponds to a tetragonal unitcell of the body-centered $I\bar{4}m2$ spacegroup upon lifting of the symmetry. (Left) Shown is one translational unit cell and the location of the four-nodes of the two separate graphs marked as black and gray points, respectively. Numerical values for the lattice directions and angles are given in Tab. 7.1. The crystallographic a-axis coincides with the Euclidean x-axis, and the b-axis is contained in the xy-plane. (Right) Shown are the two inter-penetrating graphs 1 and 2 together with their six distinct nodes (two 3-nodes and one 4-node each). As a visual aid, some lines along (100), (010) and (110) direction are shown as dashed, dash-dotted and dotted lines, respectively.

are one the straight vertical lines $0, 0, z$ and $1/2, 1/2, z$. Thus, the 4-nodes of the first graph align vertically with the 3-nodes of the other.

More symmetric embeddings of this line graph in tetragonal unitcells

More symmetric embeddings of this graph exist. Discussing these helps to elucidate the geometry and symmetry. This discussion is presented in Fig. 7.2 and in this section.

The ratio between the lattice parameters of the body-centered unit cell shown in Fig. 7.1 is approximately 1:0.8:4.6 (a:b:c). The angles between the lattice vectors are $\alpha = 80^o \pm 4^o$ ($\measuredangle a, b$), $\beta = 90^o \pm 6^o$ ($\measuredangle b, c$) and $\gamma = 85^o \pm 6^o$ ($\measuredangle a, c$). The deviations from $\pi/2$ are only significant in α. We assume the symmetry group to be at least monoclinic (as

Primitive lattice vectors of the $I\bar{4}m2$ space group			
	in voxel[a]	in nm	in Euclidean coordinates of the dataset[b]
a	43 ± 2	36.9 ± 2	$(-0.986 \pm 0.02, -0.050 \pm 0.02, -0.157 \pm 0.02)$
b	36 ± 2	30.0 ± 2	$(0.338 \pm 0.02, 0.080 \pm 0.02, 0.938 \pm 0.02)$
c	199 ± 2	166.0 ± 2	$(-0.12 \pm 0.02, -0.98 \pm 0.02, -0.15 \pm 0.02)$
z [c]	99 ± 3	82.6 ± 2.5	$(-0.02 \pm 0.01, 0.99 \pm 0.01, -0.10 \pm 0.01$

Angles between relevant directions of the unit cell[d]		
α	between a and b	$80^o \pm 4^o$
β	between b and c	$90^o \pm 6^o$
γ	between a and c	$85^o \pm 6^o$
�	between z and c	$6^o \pm 5^o$
ρ	between projection of c onto the ab plane and b	$\approx 90^o$

Positions of the nodes in the translational unit cell						
Node	ideal			experimental [e]		
f_b^1	$1/2$	$1/2$	$1/2$	0.37 ± 0.07	0.63 ± 0.07	0.50 ± 0.02
t_a^1	$1/2$	0	$z \in [0, 1/4]$	0.55 ± 0.08	-0.11 ± 0.06	0.13 ± 0.02
t_b^1	$1/2$	0	$z \in [1/4, 1/2]$	0.4 ± 0.1	-0.05 ± 0.05	0.40 ± 0.02
f_a^2	0	$1/2$	$1/4$	0.04 ± 0.04	0.38 ± 0.07	0.25 ± 0.02
t_a^2	$1/2$	$1/2$	$z \in [0, 1/4]$	0.56 ± 0.05	0.42 ± 0.05	0.10 ± 0.02
t_b^2	0	0	$z \in [1/4, 1/2]$	0.00 ± 0.04	0.00 ± 0.04	0.36 ± 0.02
t_c^2	0	0	$z \in [1/2, 3/4]$	0.25 ± 0.07	0.32 ± 0.07	0.64 ± 0.02

Table 7.1: Positions of the 3- and 4-nodes in the experimental dataset in the notation in the unitcell shown in Fig. 7.1. The assumed model for the connectivity of the nodes and the idealised positions is given in Fig. 7.1. The space group notation is as in [85]. Superscripts in brackets refer to Appendix 7.5 containing details of the fitting procedures.

two of the pairs of primitive vectors are perpendicular), with the likely possibility of an orthorhombic cell. Indeed, the symmetry could lift the symmetry to a tetragonal cell (a=b) without significant distortions.

This tetragonal network is precisely[6] the network considered by O'Keeffe and Hyde [163] with space group $I\bar{4}2$. Its formal description, with all edges of identical unit length and all angles tetrahedral (4-vertices) or trigonal (3-vertices) is:
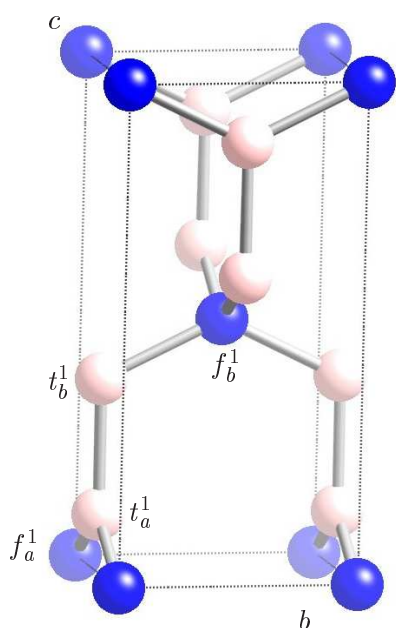
---

[6]With the minor exception that the coordinate axes a and b in O'Keeffe and Hyde are exchanged compared to ours.

Imm2 with a=37; b=31; c=166;

4-vertex f_a^1	:	(0, 0, 0)
3-vertex t_a^1	:	(1/2, 0, 0.12)
3-vertex t_b^1	:	(1/2, 0, 0.38)

F222 with adapted a, b ; c=166;

4-vertex f_a^1	:	(0, 0, 0)
3-vertex t_a^1	:	(1/4, 1/4, 0.12)
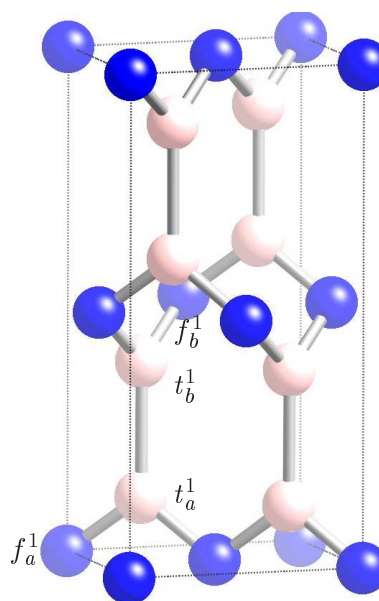
Figure 7.2: Graph 1, under the assumption of orthorhombicity, embedded in the $Imm2$ translational unitcell (left) and in the $F222$ translational unit (right).

$I\bar{4}m2$; a=1.8; c=3.744;

Net 1 :	4-vertices at (0, 0, 0)	(f_a^1)
	3-vertices at (1/2, 0, 0.3836)	(t_a^1)
Net 2 :	4-vertices at (0, 1/2, 1/4)	(f_a^2)
	3-vertices at (1/2, 1/2, 0.1336)	(t_a^2)

The two possible embeddings of this network in orthorhombic groups are in the body-centered $Imm2$ space group, or the face-centered $F222$ space group – both for the symmetry of one of the two networks only (shown in Fig. 7.2). The corresponding symmetry groups containing symmetry operations exchanging the two networks are $Imma$ and $Fddd$.

The symmetries of the two embeddings are clearly different, even though they give the same <u>line</u>-graph. The clear distinction between the two space groups is that $Imm2$ has mirrors, the $a = 0, 1/2$ and $b = 0, 1/2$ planes, that $F222$ lacks. Vice versa, $F222$ has horizontal two-fold rotation axes through the four-nodes in lattice vector direction of $F222$. The line graph with straight edges has all symmetries of both groups, but the MS does not.

Note that the orientation of the lattice vectors in the two space group is different. The a-axis [100] of the $Imm2$ space group corresponds to half the face diagonal [110] of the $F222$ space group. The c-axes of both space groups are identical.

The four-node is at the origin of the $Imm2$ space group and a $mm2$ sites. The two-fold axis is along the c-axis and the mirrors in the horizontal unitcell faces. In $F222$ the four-node is again at the origin. It has 222 site symmetry. The three two-fold axes are along the crystallographic primitive translations of $F222$. In particular, $F222$ contains two horizontal two-fold axis through the four-nodes, in [100] and [010] direction.

An important difference between $F222$ and $Imm2$ with respect to this graph, are the positions of the three-nodes. Note that there are two symmetrically distinct three-nodes in the $Imm2$ space group, t_a^1 and t_b^1, whose c coordinates are not a priori fixed (although in our data their respective c values are $1/4 \pm x$). . In the $F222$ spacegroup the two types of maxima are related by a two-fold horizontal two-fold rotation in the $c = 1/4$ plane. The set of three-nodes in the translational unit is symmetry-related in different ways for the $Imm2$ and the $F222$ spacegroups: in $Imm2$ by virtue of the body-center translation, t_1^c corresponds to t_1^a and t_1^c to t_1^d. In $F222$, they are all at equivalent sites, related by horizontal two-fold axes at $c = 1/4, 1/2, 3/4$.

The MS, as opposed to the line graph, does not share both symmetries. Its shape can in principle distinguish between the two possibilities. This aspect is discussed on page 180. Before this we discuss the shape of the MS and our analysis of the periodicity of the structure.

MS is ribbon-like and without branch lines

.

---

[8]Note that this is a projection of an array of half-unit cells with one layer of maxima, the layer of upwards facing three-nodes above and the layer of downwards facing three-nodes below. Even if c was perfectly vertical to a and b a larger number of layers would not produce the collapse shown here as the bending of the MS "edges" is different in the respective layers. The projection is not along the c axis either, but rather along the imaginary vertical axis $a \times b$ (the minimal requirement for a vertical two-fold axis to exist). The slight crystallographic distortions are also the reason for the green three-nodes to be slightly offset from the a-axis.
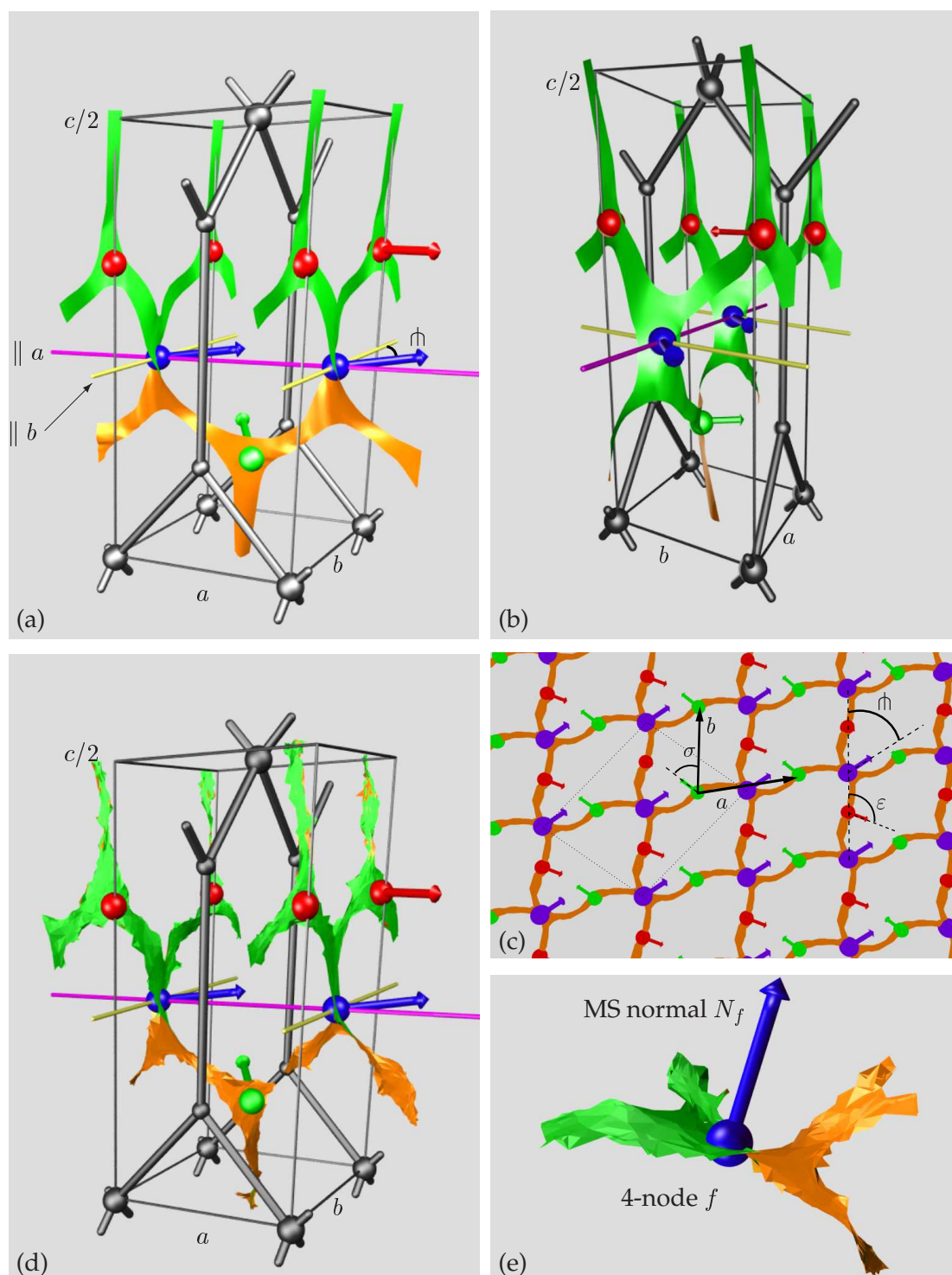
Figure 7.3: MS of the PDMS network: (a, b) Smooth surface, manually adapted, to the MS of half a translational unit cell of one of the two labyrinths in two different orientations. The MS is essentially a ribbon structure. One side is colored orange, the other side green. The second labyrinth is represented by its stylised line graph. The colored arrows represent the MS normals of the nodes. (c) Vertical projection of the MS onto the (001) plane.[8] The dotted four-gon is the $F222$ translational unit cell. (d) The same as a but showing the experimentally determined MS rather than the stylised MS. (e) Close-up of the (experimental) MS portion around one of the 4-nodes.

The shape of the MS is illustrated in Fig. 7.3. We describe only one of the two MS only. Our analysis does not detect any difference between the shape of the two MS, which supports the symmetry assignment.

The MS is made up of ribbons of varying width that follow the line graph, with the edges curved in space. The 4-nodes are on curved but simple surface patches without branch lines from which four ribbons emanate. The MS here twists to accommodate two ribbons going up (that eventually reach three-nodes in upwards $\pm b$ direction) and two going down (to the two adjacent downwards three-nodes in $\pm a$ direction). The MS is widest in the vicinity of the four-nodes. The four-nodes are clear local maxima of the distance function with small fluctuations over the different four-nodes of the sample.

In principle there may be two distinct types of three-nodes that are not related by symmetry and hence may exhibit differences in the shape of the channels (and their MS) in their vicinity. Out of the first class of three-nodes, called "three-downs" and represented by green spheres (t_a^2), one MS ribbon emanates vertically downwards, and two emanate diagonally upwards going to the four-nodes in $\pm a$ direction. Out of the nodes of the other class ("three-ups", red spheres, t_b^2) one MS ribbon emanates vertically upwards to go to a three-down, and two ribbons go diagonally downwards to the four-nodes in $\pm b$ direction.

Our analysis of the MS detects no significant differences in shape between the two types of three-nodes, or in the relative position to the four-nodes and the unit cell. This is an indication that the space group may indeed be one where a symmetry operation exists that exchanges the two types of three-nodes. We can restrict our analysis to one of the two saddle points.

The MS in the surrounding of the three-nodes is again a simple surface without branch lines with three ribbons emanating from it.

The three-nodes are statistically weak maxima of the distance function on the MS. The line graphs (geometrically centered, in the spirit of the discussion in chapter 3) emanate from distance function saddle points on the ribbons to the adjacent four-nodes. However, in some instances, they are monkey saddles (as in the cubic gyroid) or not special points of d at all.

The MS patches connecting three-nodes to four-nodes are clearly ribbons, reflecting the elliptic cross-section of the channels, wider in extent in c-direction than in ab-plane. Although these ribbons are not flat, their normals are mostly horizontal and the MS patches vertical patches (see the distributions of ζ_2 and ζ_3 in Fig. 7.4 on page 179).

The MS patches connecting three-nodes vertically are more difficult to assess. This is

mostly because their cross-section is more circular making the MS computation more noise-sensitive. They are also thinner, therefore with a constant resolution of the raw data, the sampling of the surface by vertices is worse.

It is clear though from consideration of their end points (the three-nodes) that they represent a twist of the MS ribbon by an angle corresponding to the difference between the MS normals of the two types of three-nodes, i.e. $\pi/2$ or more (see Fig. 7.3, in particular c).

None of the MS ribbons is flat even though the "end points" (a four-node and a three-node) are contained in the same vertical plane ($a = $ const or $b = $ const). This is evident in the projections of the MS ribbons in Fig. 7.3 (c). A two-fold symmetry around vertical axes through the three-nodes seems to exist mapping adjacent four-nodes (the end points of the ribbons) onto each other. This is consistent with both potential space groups).

In the following we will use the shape of the MS to support our claim of a *periodic* structure, and on page 183 to distinguish between the two possible symmetry assignments, $F222$ or $Imm2$.

Periodicity of the network by analysis of the positions of 4- and 3-nodes

The periodicity of the structure is best quantified by statistical analyis of the four-nodes, as they are the most distinct features of the MS of the PDMS networks. First, they are the only local maxima of the distance function with values in the range $4 < d < 7$. Second, the MS structure (shape and orientation) in their vicinity shows little variation between different realisations within the sample. We quantify this by analysis of the MS normal directions and distance function values of the maxima. Third, their positions in space clearly reveal an underlying periodic lattice, at least in a and b direction, with small fluctuations of the data points around the nominal positions on the fitted lattice.

All four-nodes are distance function maxima on the MS in the following sense. They are the set of MS points with maximal distance function among all points within a sphere of radius 10 voxels and with distance function value in the range $[4, 7]$ voxels. In other words, the subset of points on the MS with that property is essentially the set of four-nodes, with the exception of very few (likely erroneous) points, all of which lie in the poorly represented boundary region of the sample. In the following analysis we denote as the "four-nodes" exactly this set of these maximal points. We will later demonstrate that they indeed are four-connected nodes of the line skeleton.

The first observation is that the four-nodes lie on distinct planes, the $c = 0, 1/4, 1/2$

planes in Fig. 7.1. Our data set contains three distinct sets of four-nodes on three parallel planes, with the middle one, $c = 1/4$, containing points that lie on graph 1, and the other two, $c = 0$ and $c = 1/2$, containing four-nodes of graph 2. The plane normal directions of the individual planes, as determined from linear least square fits of a plane equations $\mathbf{n_i} \cdot \mathbf{x} = d_i$ to the data points of each plane, differ by an angle of less than 1 degree from their average, i.e. they are parallel within the limits of our analysis. The distances between them are $d = 48 \pm 3$ voxels, as determined by a renewed least square fit to the plane equation $\mathbf{n} \cdot \mathbf{x} = d_i$ where $\mathbf{n} = \langle \mathbf{n_i} \rangle$ is the average normal direction. The error is the standard variation of the distribution of vertical distances of the sample points from the corresponding planes.

The coordinate axes a and b, in the $Imma$ space group with one of the maxima as the origin, are the visually immediately evident straight lines (through these maxima) that are contained in the three parallel planes. The average directions of the straight line fits to aligned subsets of four-nodes yields the coordinate directions, given in Tab. 7.1, with small errors corresponding to the deviations of the data points from the fitted lines.
Analysis of the spacing between data points along these straight lines gives the translation lengths, again with small deviations.

An analysis of the positions of the three-nodes yields the same result within the error specified. However, the analysis is more difficult as the identification of the three-nodes is not as easy as for the four-nodes. Our data is not sufficient to ascertain if the three-nodes are maxima of d or saddles with Hopf-index -2 ("monkey saddles"). Furthermore, their distance function, approximately 2 ± 1, is much closer to the distance function along the ribbons of the MS. In principle, an automated identification of MS points at the center of three junctions is possible. However, in the present study the identification was based on visual selection of the points – allowing for the detection of pseudo-three-nodes as in Fig. 7.7. Linear least square fits to planes and lines through the three-nodes confirm the above result for the four-nodes within the limits of the error.

It remains to be demonstrated that the two translations, a and b, are indeed congruence transformations of the *labyrinth*, rather than only of the set of maxima and three-nodes. The strongest evidence is provided by a superposition of the sample under translations of integer multiples along a and b. The superposition of all, approximately 5×4 translational ab unitdomains (the volume given by $0 \leq a, b < 1$, $-\infty < c < \infty$) gives strong evidence that the data is consistent with this translational symmetry, based on visual inspection. Quantitative measures for the similarity of the superposed structures, based on Hausdorff-measures for example, is desirable but

view along [100]

view along [010]

view along [001]

graph 1 (black) and 2 (red)   both graphs and MS

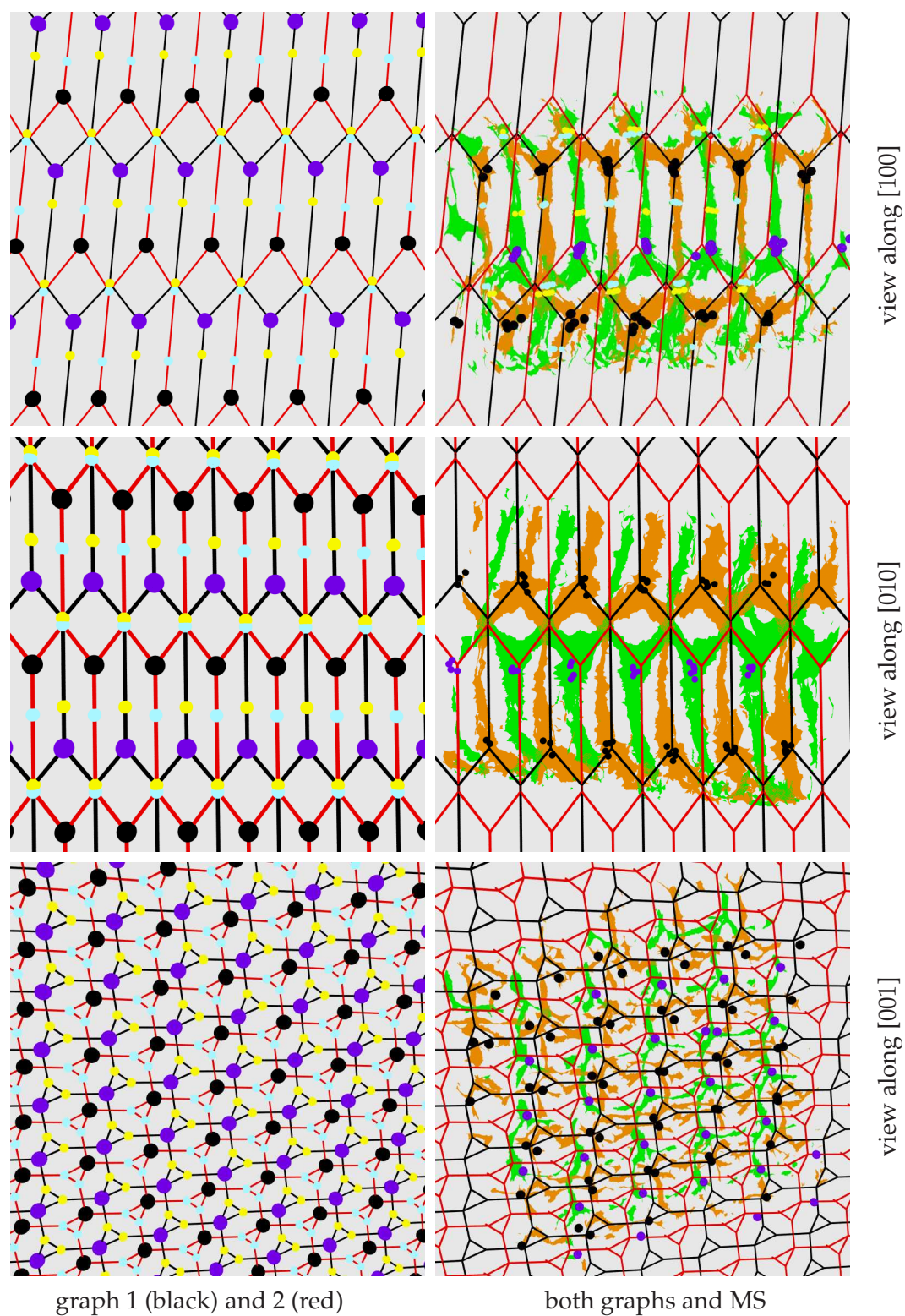**Figure 7.4:** Projections of the MS of the complete experimental Triblock Copolymer dataset onto three crystallographic planes. Continued on page 179.

view along [100]

view along [010]

view along [001]

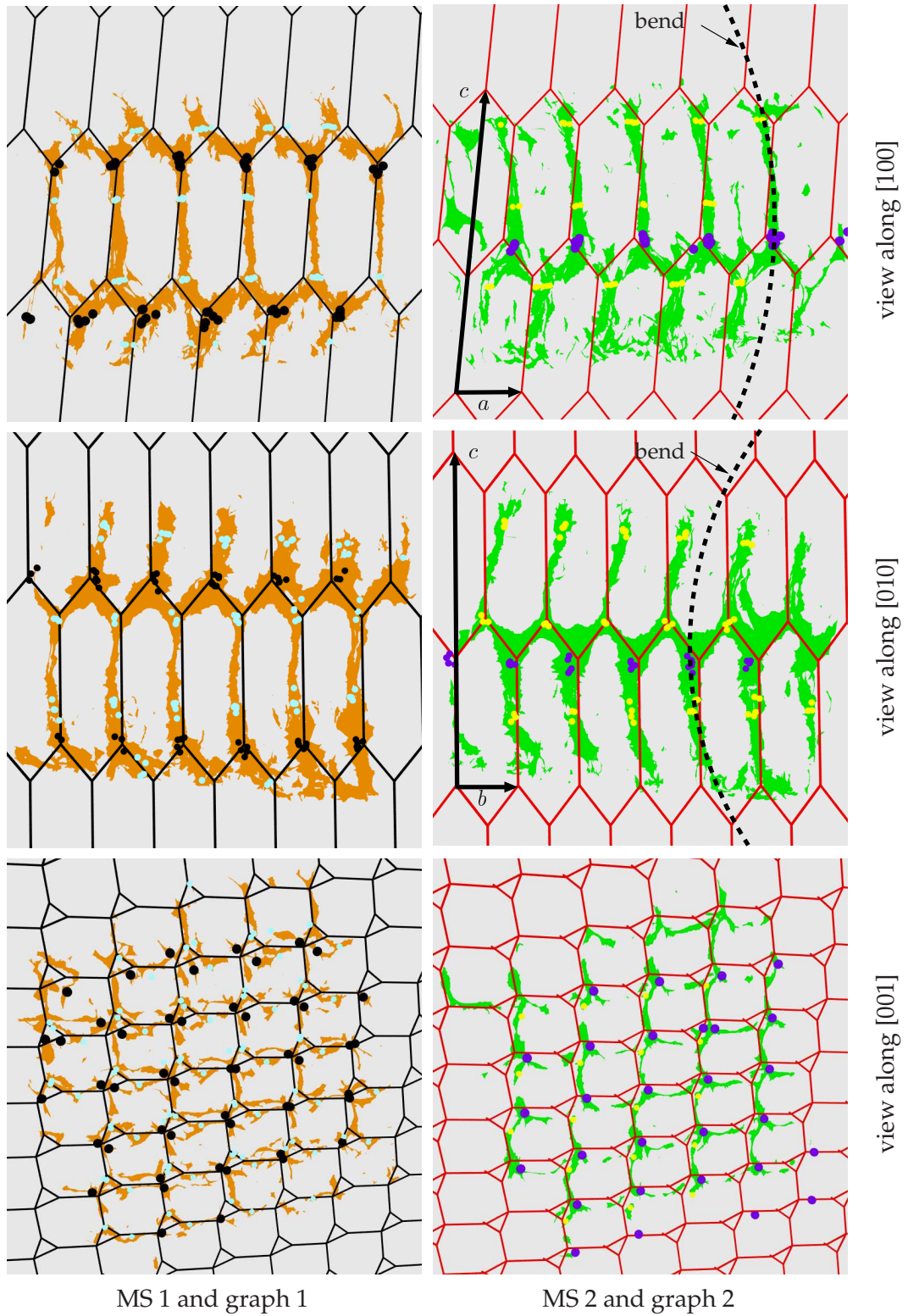MS 1 and graph 1   MS 2 and graph 2

Figure 7.4 (continued): The black arrows indicate the lattice vectors. The dashed circular arcs indicate heuristically the macroscopic bend.

seems difficult because of noise and missing parts of the labyrinths. It is doubtful if a figure like the Hausdorff distance (defined on page 21) provides a better indication of the degree of symmetry than the visual inspection.

We can nevertheless quantify in a basic sense that the local shape of the labyrinth is identical in the vicinity of the maxima. We show that the MS normals, indicating tangency directions, and the MS distance function values, indicating thickness of the labyrinth, are similar when compared between the different unitcells of the sample. Figure 7.5 shows the variation of the MS normal and the distance function at the four- and three-nodes. For the sake of simplicity the data presented are restricted to the respective points of graph 2.

The variations of the distance function between the different four-nodes (three-nodes) are small compared to the complete range of distance function values, approximately $[0.5, 5.5]$. Similarly, the deviations of the MS normals around the averaged normal directions among all four-nodes (three-nodes) within one plane are small with statistically $\pm 10^o$.

The periodicity in the third direction, c, proves more difficult to ascertain from the available dataset. Because of the limited height of the sample, the only translation in a linearly independent direction of a and b, for which several pairs of corresponding points exist, is not the $c - axis$ of the body-centered cell. It is the translation c' from the origin to the body-center in the $Imm2$ ($Imma$) spacegroup, i.e. point f_a^1 to point f_b^1 in Fig. 7.1. The three lattice vectors a, b and c' form a monoclinic translational unitcell.

Alternatively, making the assumption that the four-nodes of graph 1 align with the vertical edges of graph 2, and hence with the three-nodes, the c axis direction is determined from statistical analysis of the translations $f_a^1 \rightarrow t_b^2$ and $f_a^1 \rightarrow t_b^2$.

Once the direction is determined, a simple trigonometric relation between the perpendicular distance between the maximal planes and the c provides the length of the translational vector c in the $Imm2$ (or $Imma$ orientation).

Numerical values for the directions and lengths of a, b and c are given in Tab. 7.1.

MS Space group more likely $Fddd$ than $Imma$

As discussed on page 172, the (straight-edge) line graph model that we propose to represent the PDMS phase labyrinth can be embedded in a few different space groups. Assuming that the deviations of α and β from $\pi/2$ are not significant, the ambiguity reduces to a choice between the $Imm2$ ($Imma$) and the $F222$ ($Fddd$) space group without (with) symmetries exchanging the two networks, see Fig. 7.2. Here we present
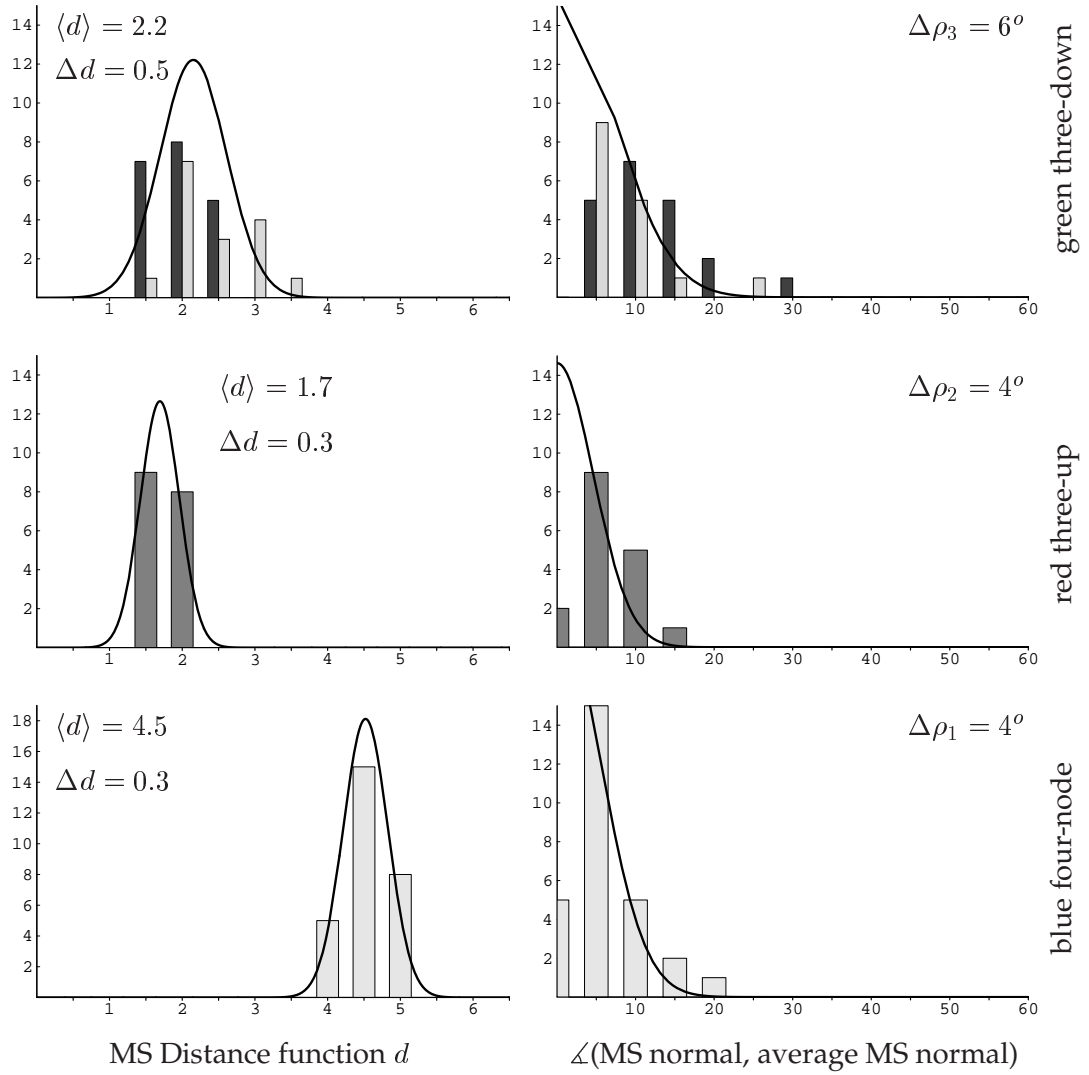
Figure 7.5: Distribution of MS distances and angles between MS normals and coordinate axes at the 4-nodes and 3-nodes of the PDMS network. Shown are distributions for the nodes at equivalent positions (assuming Imma symmetry) to the nodes shown in Fig. 7.3, i.e. all of them are on graph 2. The y-axes give the number of nodes in the sample with values in $[x-dx, x+dx]$ intervals ($dx = 0.5$ for the distance function, and $dx = 5^o$ for the angles). Shown are the distribution of distance function values and the angle between the node MS normal and the average of all MS normals at these nodes (on this page). The diagrams on page 182 show the distribution of the angle (in clockwise direction around the ab plane normal $\mathbf{a} \times \mathbf{b}$ which is almost parallel to c) between the node MS normal and the b-axis and the distribution of the MS normal angle to the c-axis.(continued on page 182)
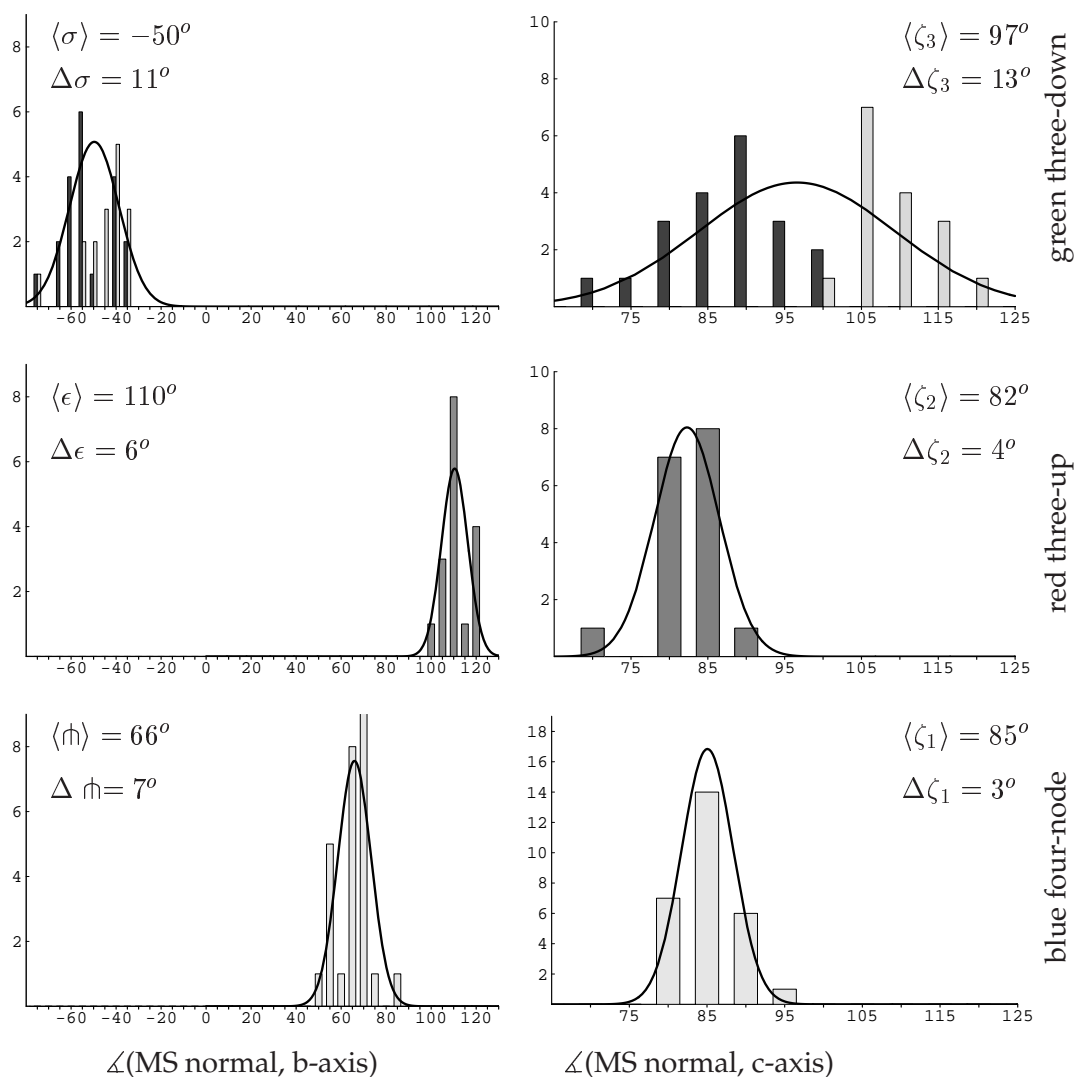
Figure 7.5 (continued from page 181): The graphs represent normal distribution centered at the average $\langle . \rangle$ of the distributions and of width equal to the standard deviation Δ. (For the angle to the average it represents a half-normal distribution as the average is clearly zero). For the three-down nodes, edge interval is represented by two bars, indicating the distributions of the two separate layers in which three-downs appear on graph 2 (points in the same layer as point 9 in Fig. 7.6 are light-gray, points in the layer of points 8 and 4 represented by black). We attribute the bimodal nature of the distribution of angles ζ_3 to the macroscopic bent, that bends the normals of the lower plane (black) upwards, whereas it bends the normals of the top plane (gray) downwards.

arguments for both assignments, based on analysis of MS shape and MS normal directions at the four- and three-nodes and the distances between pairs of three- and four-nodes. The analysis is presented in the space groups of a single network, for the sake of simplicity. The presented arguments slightly favour $F222$, although a definitive conclusion cannot be made until additional datasets are analysed.

Recall the discussion of the symmetry of the two different embeddings in $Fddd$ and $Imma$ orientation – or the equivalent space groups without the symmetry elements exchanging the two graphs, $F222$ and $Imm2$ – on page 172.

The shape of the MS in the vicinity suggests two-fold symmetry rather than mirror symmetry, for two reasons:
 (1) The picture of a wide twisted ribbon (rather than a branched structure) that splits

up into four ribbons, radiating statistically in $[011]$, $[0\bar{1}1]$, $[10\bar{1}]$, $[\bar{1}0\bar{1}]$ directions, cannot have a mirror symmetry unless the MS shrinks to a point. Our MS computation does not show a branched structure. The caveat of this argument is that the influence of the small monoclinic distortion in the data (that we here assume as an artefact of the sample preparation) on the MS shape is difficult to assess. The possibility that the MS of the truly tetragonal MS is branched cannot be totally excluded.
 (2) The MS normal at the four-nodes has to coincide with one of the horizontal two-

fold directions if $F222$ is the correct symmetry. If $Imm2$ was the correct symmetry, the normal would have to be colinear with either of the crystallographic directions. Fig. 7.5 shows that the angle $\zeta_1 \approx 85^o$ between the c-axis and the MS normal at the four-nodes is close to $\pi/2$, that is the MS normals at the four-nodes are indeed horizontal. The angle ⋔ between the MS normal and the $Imm2$ b-axis is 66°, hence the normal is in between a and b, although not quite on the face diagonal of $Imma$ (the coordinate axes of $F222$). Again, the influence of the monoclinic deformation of the data on this as is difficult to assess.

A further observation that favours the assignment of $F222$ as the correct space group is the cross-sectional shape of the three-nodes, see Fig.7.3 (c). The MS ribbons near the three-nodes are not contained in the crystallographic planes [100] and [010], but seem to exhibit vertical two-fold symmetry around axes through the three-nodes. This is corroborated by analysis of the angles of the MS normals with the b-axis, see Fig. 7.5. The MS normals are horizontal[9] and the angles to the b-axis of the two distinct three-nodes are $(-50 \pm 11)^o$ and $(110 \pm 6)^o$, and thus not vertical to the coordinate planes (the mirror planes of $Imm2$). Note also that at the orientation of the normals at the

---

[9]subject to the macroscopic bend, see the Figure caption.

two distinct three-nodes is roughly consistent with that two-fold rotation of the $F222$ that exchanges the two points.

A more indirect argument, that relies less on the actual shape of the MS, is provided by analysis of the edge lengths from the four-node to the three-nodes. It is based on the different symmetry relation of the three-nodes in the translational unitcell, discussed on page 173. In $F222$ all three-nodes are at symmetrically equivalent sites; in particular the ones just above and below the maxima (e.g. points 1 and 3 in Fig.7.6) are related by the horizontal two-fold symmetries. In $Imm2$ no relation between them exists, they are free to slide along the vertical $mm2$ axes and point 1 and 3 are not symmetry related. That means that the distances between the four-node and the two three-nodes may be different from each other. An analysis of these lengths reveals that the downward distances are slightly larger (36 ± 5 and 37 ± 3) than the upward distances (32 ± 3 and 28 ± 3). This seems to be in favour of the $Imm2$ group, yet the distances are too small to be significant given the assumption on the orthorhombicity. On the other hand, the fact that all three-nodes seem to be of similar MS shape (orientation, shape, distance function) suggests that there is a symmetry relation between them. This is an argument in favour of $F222$. Besides, even if the symmetry were $Imm2$ and the three-nodes symmetrically distinct, one may expect the structure to as homogeneous as possible. This is likely to yield identical edge lengths for both edges.

Finally, in a computer visualisation, a two-fold rotation of the dataset around the $F222$ [100] axis (corresponding to the [110] axis in $Imm2$) is certainly closer to being a true congruence transform of the dataset than any mirror operation. Wether that holds true if the deviations from orthorhmbicity are included cannot be ascertained from our data.

In conclusion, given the deviations from orthorhombicity, that are considered to be due to sample deformations during preparation, the MS shape does not unambigiously indicate the space group of the network. The observed properties of the MS are all commensurate with an assignment of the $F222$ space group, but the changes required for $Imm2$ are small enough to be feasible.

Evidence for the topological correctness of the MS

This last section of the description of the MS and line graph analysis of the data describes our identification of topological aspects of the labyrinth. Our assessment of the topological structure as two intertwined disjoint 3- and 4-coordinated networks is hampered by two issues: First, based upon visual inspection of the MS structure (and the structure of the labyrinth) a number of pairs of dead-end channels of the data are
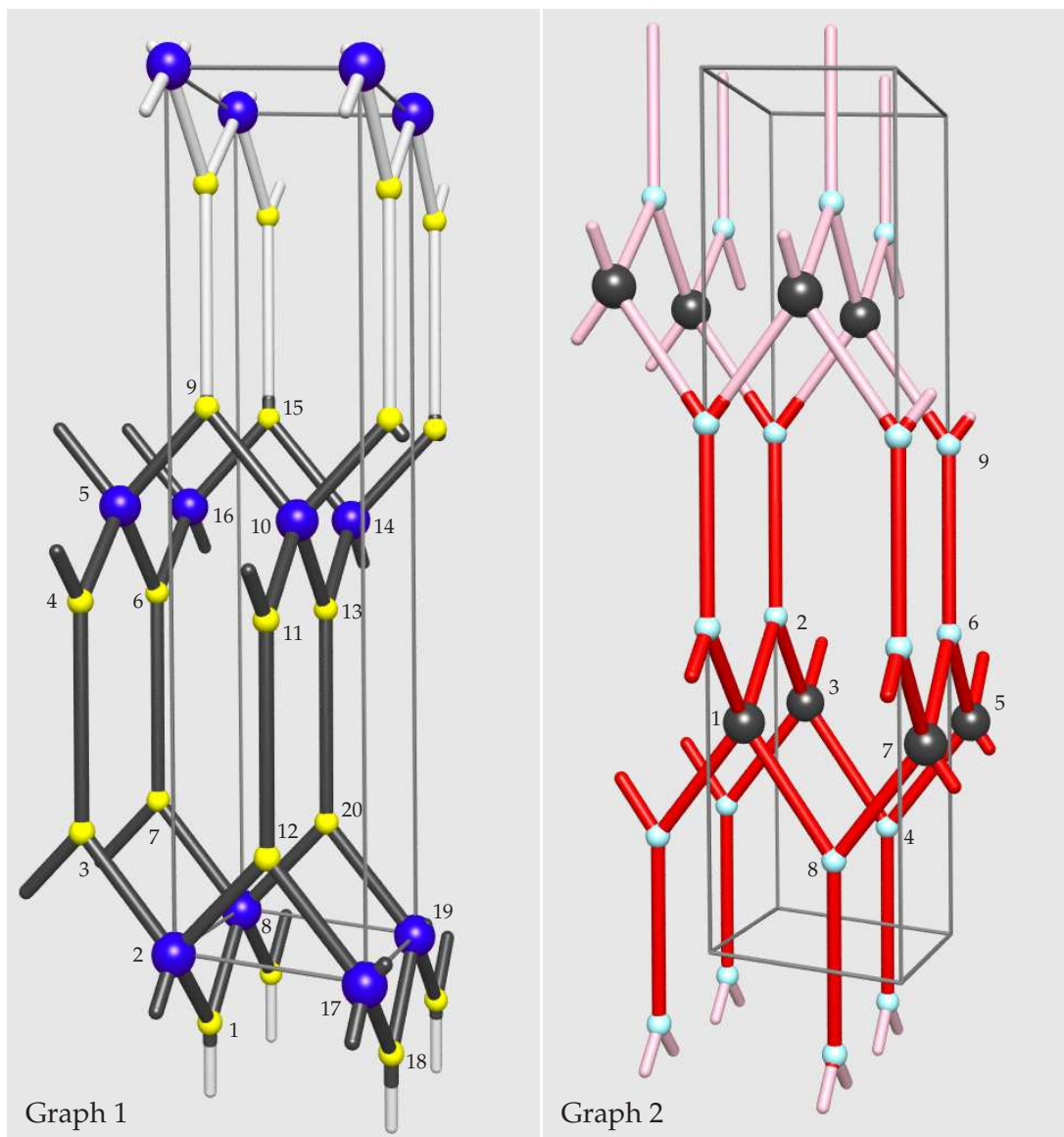
Figure 7.6: Portion of the two intertwined (3,4) graphs that corresponds to slightly more than a translational unitcell in the Imma space group. The portion that is contained within the tomographic sample is colored in black (red) whereas the fraction that is outside of the tomographic dataset is colored gray (pink). Eight-rings R_a (1-8,1), R_b (2-5,9-12,2) and the two R_c rings (6,5,9,10,13-16,6 and 8,1,2,12,17-20,8) of the first graph and one ring R_c (1-8) are contained within the boundary of the sample. Note that a monoclinic cell, with c axis corresponding to the vector from point 2 to 10 in the left image, is completely embedded in the tomographic data.

assumed to represent connected channels even though they are not in the dataset. Second, the size of the dataset in c direction is only 1.5 unitcells of the monoclinic unitcell (corresponding to 0.75 of the bodycentered $Imm2$ unitcell). Third, too a lesser degree a few dead-end channels, of considerable length, are discarded as artefacts.

The size of the analysed dataset is strongly constrained in the c direction. Fig. 7.6 shows the fraction of the networks that are represented: For Graph 1 (the black one in both Fig. 7.4 and Fig. 7.6) two vertical rings R_a and R_b and two horizontal R_c rings are completely represented in the data, although the latter are in the very noisy boundary regions of the dataset. For the other graph, no complete vertical ring is contained in the dataset, but the horizontal R_c rings are embedded vertically centered within the dataset and hence of good quality.
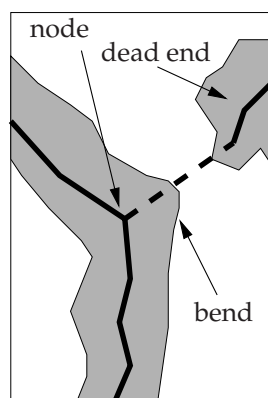

Figure 7.7:

The more important source of uncertainty is the fact that many of the graph edges do not correspond to channels in the segmented binary data, i.e. there are graph edges that connect two PDMS phase regions of the data even though there is not a continuous connection in the binary data. The decision to place additional edges is based on visual inspection of the individual situations, and is used here in conjunction with the proposed model to verify if the edges of the model network may have counterparts in the real data. An edge is assumed to be present if the MS geometry looks as if it should be continuous rather than disjoint, leading to a connecting edge.

Often the situation is one as depicted in Fig. 7.7: The geometry of the channels, or their MS, suggests that a connection exists. An example is a situation where a dead-end of the PDMS phase network extends close (but does not connect) to another part of the channel network which, in that region near the putative node, exhibits a bent. See also Fig. 7.3 for a clear example where a similar situation occurs in the data.

Many of the edges connecting 3-nodes to 4-nodes, particularly those near either of the sample boundaries in the c direction, are of this type. As this process is nearly impossible to automate and involves manual assessment, it does not yield a completely objective result.

It may be useful to compare the obtained graph structure to that obtained on a different segmentation of the same data set. A segmentation of the same dataset that is biased more towards recognising voxels as PDMS rather than the other phase (e.g. through a higher threshold in a simple graylevel-thresholding segmentation) should tend to

close of most of these gaps. It has to be kept in mind though that the initial segmentation was an optimal one;therefore the alternative segmentation does not only close the gaps but also tends produces more artefacts.

Alternatively, or in addition, an erosion-dilation procedure may be used. It is a method that swells the structure (possible merging to near dead ends) and then skins of the same number of voxels, but preserving the new topology. If a two dead-ends connect in the swelling to form a (thick) connection, that connection remains in intact during the skinning. Dead-ends that almost connect should connect under application of this procedure.

The situation where a channel that exists in the binary dataset is not represented in the MS, due to elimination of MS faces based on angle or distance criteria, is taken care of by comparison with a line graph obtained by topological thinning.

In summary, our claim of the network topology to be two intertwined 3- and 4-coordinated networks relies heavily on the geometry and visual appearance of the fragments of the labyrinths or its MS. A homotopy equivalence between the triangulation of the interface surface data and the suggested graph is not in place. In particular in the boundary areas of the dataset in c direction, there are many parts where the data set does not allow for a unique identification of the topology.

Despite this caveat, using the combination of (fragmented) topological information and the geometric shape information contained in the MS and the distance function, we have been able to identify a consistent topological and geometric model of this network phase. This is of particular value as X-ray or electron-scattering data for this specific copolymer system is not available.

7.4 Discussion

Observation of a non-cubic phase in self-assembled phases in block copolymer systems is rare. Reports of non-cubic structures in other linear ABC triblock copolymer systems have only been published recently [12, 54]. Their analyses employed a variety of measurements (small-angle X-ray scattering, transmission electron microscopy, static birefringence,dynamical mechanical spectroscopy), but not electron-tomography. Therefore the analysis presented here provides for the first time real space data of the geometry and topology.

The network models that have been derived in those two papers are different from the one we claim as the spatial structure. Their model is that of a single network of three-coordinated nodes of symmetry $Fddd$ whereas our analysis suggests a system

of two intertwined identical networks of 3- and 4-coordinated nodes.

It is important to note that mesostructural identification based on symmetry constraints and analysis of TEM 2D slices only must be treated wit caution, as many topologies can be constructed within a given symmetry. Indeed, the work of Epps *et al.* seems to ignore that possibility.

The question wether the spatial structure is that of a single network or that of two double networks of one phase (here PDMS) embedded in the matrix of the two other phases (PS/PI) has repercussions for the self-assembly mechanism. In the case of a double network, the possibility of self-assembly similar to the Double-Gyroid phase is possible, with a minimal surface providing the interface that separates two microdomains of identical composition.

For a domain given by a single domain this picture does not apply in the case of ABC triblock copolymers, as the natural location for the $H = 0$ interface is lacking. The partition of space into domains is clearly an assymetric one.

From a computational point of view this chapter has demonstrated that MS computations of experimental datasets are possible and can shed light on complex morphologies whose structures are impossible to decipher otherwise. This holds true despite the fragility of the MS construction. First, as a visual aid to a three-dimensional representation on a computer the much sparser representation of a labyrinth, compared to a representation as its bounding surface, makes the overall structure very easy to discern. The MS remains a geometrical rather than a topological representation that makes shape identification easy. An example is the identificaton of the four-nodes as four-nodes rather than a pair of three-nodes with a small edge in between them.

7.5   Appendix: Details of the fitting procedures

This appendix contains details of how the lattice parameters and angles were determined, for the references given in Tab. 7.1.

(a) Determination of the lattice parameters a, b and c

The error estimate for a and c is obtained by the following analysis: Points of maximal distance function (the four nodes) were divided, by visual and unambiguous inspection, into planes (the $c = 0, 1/2, and 1$ planes parallel to the a-b plane) and into separate lines (along a and b). Then pairs of nearest lattice points along a (or b) were identified and a distribution of the average edge length computed; if a simple point-point Euclidean distance or distance along a fitted a (or b) vector is used makes no difference to the significant digits. The errors indicated are the standard deviation $\sqrt{\langle l^2 \rangle - \langle l \rangle^2}$ of those distributions. The lattice vector c had to be determined in a different way, as data was only available for the lower half of the unit cell (but a complete monoclinic unit cell). c was obtained by fitting planes to the three planes of maxima, and determining the distances between these fitted planes. Then using the direction $\vec{c}$ (see next footnote), $c/2$ could be determined from the distance between the two extremal planes by dividing the normal plane-plane distance by $\vec{N} \cdot \vec{c}$ (assuming both are normalised). The error is the mean standard deviation of the distribution of vertical deviation of the sample points around the fitted planes divided by the same number.

(b) Euclidean coordinates of lattice directions

Euclidean coordinates are indicated here only as a reference for a reader with access to the dataset itself. They are in units of the voxel size. For a and b, straight lines are fitted to the data points representing the maxima of the EDM. The coordinates of a (and b) are the average of the fit parameters over all those lines and the errors indicated the standard deviation. The vector c was obtained by assuming that the four-node of the origin is aligned in c direction with the three node t_b^2 of the second graph. The corresponding edges in the dataset emanating from maxima of the bottom layer were statistically analysed to give the direction of c and the errors as standard deviation. The length was deducted from the distance between the three planes containing maxima. Only edges emanating from that plane are analysed, as edges in the other layers seem subject to the macroscopic bent of the sample.

(c) Normal direction to the ab plane

z is the normal of the ab plane. It was obtained by fitting planes $\vec{n}_i \cdot \vec{x} = d_i$ to the three maximal planes $i = 1, 2, 3$. The average of these normals is $z = \langle n_i \rangle$. The three normal vectors differ from the average by less than 1.0^o. A second fit fit fixed normal z, $\vec{z} \cdot \vec{x} = d_i$ yields the distances between the planes. The error is the standard deviation of vertical deviations of the data points from these planes.

Crystallographic angles

Angles between coordinate axes are the angles between the directions indicated above. The error for α was computed by identifying all triplets of data points corresponding to four-nodes that form the angle α and computing the average angle (reproducing α) and the standard deviation as the error. For the other edges, the c direction was assumed to be given as the edge connecting the 4-node at the origin to the 3-node t_b^2 of the second graph, and only occurrences of that edge emanating from the bottom layer were considered (because of the macroscopic bent). Then the error in the angles is the standard deviation of the distribution of angles between these edges and the respective second axis plus an extra 3° for the error of the c direction and an extra 1° for the errors in z, a and b direction, respectively. This is a crude estimate for the error, yet only a bigger dataset without the macroscopic bent will help to make the estimates narrower. An estimate for the error of ρ is not given, as the projection of c onto the ab plane is very small, and a reliable computation of ρ and its error not possible.

(e) Determination of coordinates of experimental data points

The experimental coordinates were determined by treating the maxima (4-nodes) of the bottom plane as origins and identifying the corresponding Euclidean point coordinates (x, y, z) with respect to those origins. Solution of the equation $x_a \mathbf{a} + x_b \mathbf{b} + x_c \mathbf{c} = (x, y, z)$ yields the crystallographic coordinates (x_a, x_b, x_c). The given coordinates are the averages of these crystallographic coordinates over all maxima in the bottom plane, and the errors are their standard deviation. The uncertainty in the lattice directions is not taken into account, neither are systematic deviations due to the macroscopic bent of the sample.

Conclusion and outlook

This thesis has demonstrated that the medial surface construction is a valuable concept and tool for the investigation of spatial structure in labyrinthine geometries. We have introduced conceptually robust measures for extrinsic structure characteristics, such as the packing homogeneity and local channel diameter, that are complimentary to and distinct from previous measures. Because the medial surface is a skeletal representation of a labyrinth that is geometrically complete, the medial surface is also a robust intermediate stage for line graph algorithms. The reduction of the medial surface to a line graph has been described and analysed in detail. Furthermore, using the medial surface in combination with computer visualisation we have been able to extract shape and symmetry characteristics of complex, previously intractable 3D data sets (from electron tomography of co-polymer network phases).

Much of this thesis has focused on analysis of infinite periodic minimal surfaces, and continuous one-parameter families of such surfaces. For the first time, we have explicitly shown that the Gyroid is the most packing-homogeneous of the cubic Primitive, Diamond and Gyroid surfaces and their tetragonal and rhombohedral distortions. This result has obvious implications for the occurence of these structures in liquid-crystalline self-assembly processes, and a more detailed applied analysis of these repercussions is now possible. For example, semi-quantitative estimates for the energy cost of the Diamond to Gyroid transition through the tG and tD families could be derived from established models for the chain packing energy, under a few assumptions.

The methods presented in this thesis are not restricted to this class of structures. Analyses of other hyperbolic structure models (such as derived from rod-packings, multi-continuous space partitions and non-minimal labyrinths geometries given as Fourier series) could provide relevant comparisons for the results presented here.

An interesting extension of the methodology of this thesis is the analysis of reduced parallel surfaces in terms of their Minkowski integrals. Reduced parallel surfaces are

that portion of the parallel surface at distance r to an interface for which the parallel distance r is less or equal to the point-wise medial surface distance function. As shown by Mecke *et al.* such analysis produces relevant quantitative indicators of morphology. Furthermore, they also provide the starting point for a variety of physical models, such as for capillary condensation inside a porous medium: condensation is supposed to occur in layers of constant thickness r on the interface between the solid and void/vapour phase.

From a computational perspective, it is now of paramount importance to improve and further automate the medial surface computation, in particular of tomographic data sets. This will involve improved smoothing procedures, possibly with a feed-back loop involving medial surface as well as curvature computations. Judging from our experience with the electron tomography data set, this should be a feasible project worth doing.

It will be a combination of understanding the medial surface of a larger group of model labyrinth structures with analysis of medial surfaces of experimental data sets that will determine the usefulness of this appealing geometric construction.

Description of color scheme used in illustrations

A convenient way to indicate distance function values in computer-visualisations of the MS consists in the following schemes that are used throughout this thesis: Two related but slightly different ways of using a color scheme to indicate the distance function on a surface S are used throughout this thesis. Both use the function hue(x) for $x \in [0, 1)$ which produces the colors purple, pink, red, orange, yellow, cyan, blue (in that order) as x increases from 0 to 1. First, as for example in Fig. 5.7, the distance function on the surface maybe rescaled so that the maximum value gives $x = 1$ and the minimum value $x = 0$. The disadvantage of this scheme is the poor resolution, as small variations may not be visible. The second scheme overcomes that problem: the distance function is now rescaled so that the minimum again corresponds to $x = 0$, but the maximum to some large integer n, for example n=30 in Fig. 3.6. With varying distance function values the surface color iterates through the above color sequence n times, generating iso-distance lines. Critical points are (visually) easy to detect: minima (maxima) are enclosed by a ring of iso-distance (or contour) lines of increasing (decreasing) distance/color. Saddle points correspond to separatrices.

Bibliography

1. ALVAREZ, L., LIONS, P., AND MOREL, J. Image selective smoothing and edge-detection by nonlinear diffusion 2. *SIAM J. Numer. Anal. 29* (1992), 845–866.

2. AMENTA, N., AND BERN, M. W. Surface reconstruction by Voronoi filtering. In *Symposium on Computational Geometry* (1998), pp. 39–48.

3. AMENTA, N., CHOI, S., AND KOLLURI, R. The power crust, unions of balls, and the medial axis transform. *Computational Geometry: Theory and Applications 19*, 2-3 (2001), 127–153.

4. AMENTA, N., CHOI, S., AND ROTE, G. Incremental constructions con BRIO. In *SoCG'03, June 8–10, 2003, San Diego, California, USA* (2003), pp. 211–219.

5. ANDERSON, D., GRUNER, S., AND LEIBLER, S. Geometrical aspects of the frustration in the cubic phases of lyotropic liquid crystals. *Proc. Natl. Acad. Sci. USA 85* (1988), 5364–5368.

6. ARGYROS, A., MANOS, S., COX, G., DWARTE, D., AND LARGE, M. Electron tomography and computer visualisation of a 3-dimensional "photonic" crystal in a butterfly wing-scale. *Micron 33*, 5 (2002), 483–487.

7. ARNS, C., KNACKSTEDT, M., AND MECKE, K. Characterisation of irregular spatial structures by parallel sets and integral geometric measures. *Colloids and Surfaces A 241*, 1–3 (2004), 351–372.

8. ATTALI, D., BOISSONNAT, J., AND LIEUTIER, A. Complexity of the Delaunay triangulation of points on surfaces: The smooth case. In *SoCG'03, June 8–10, 2003, San Diego, California, USA* (2003), pp. 201–210.

9. ATTALI, D., AND MONTANVERT, A. Computing and simplifying 2d and 3d continuous skeletons. *Computer Vision and Image Understanding 67*, 3 (1997), 261–273.

10. AURENHAMMER, F. Voronoi diagrams – a survey of a fundamental geometric data structure. *Computing Surveys 23* (1991), 345–406.

11. BADER, R. *Atoms in Molecules: a Quantum Theory*, 1st ed. No. 22 in The International series of monographs on chemistry. Oxford University Press, New York, 1990.

12. BAILEY, T., CORDELL, M., EPPS, T., AND BATES, F. A noncubic triply periodic network morphology in poly(isoprene-b-styrene-b-ethylene oxide) triblock copolymers. *Macromolecules 35* (2002), 7007–7017.

13. BAKKE, S., AND ØREN, P. 3-d pore-scale modelling of sandstones and flow simulations in the pore network. *Society of Petroleum Engineers Journal 2* (1997), 136–149.

14. BAROIS, P., HYDE, S., NINHAM, B., AND DOWLING, T. Observation of two phases within the cubic phase region of a ternary surfactant. *Langmuir 6* (1989), 1136–1140.

15. BAROIS, P., HYDE, S., NINHAM, B., AND DOWLING, T. Observation of two phases within the cubic phase region of a ternary surfactant solution. *Langmuir 6* (1990), 1136–1140.

16. BATES, F., AND FREDRICKSON, G. Block copolymers – designer soft material. *Physics Today* (February 1999), 32–38.

17. BENEDICTO, A., AND O'BRIEN, D. Bicontinuous cubic morphologies in block copolymers and amphiphile/water systems: Mathematical description through the minimal surface. *Macromolecules 30* (1997), 3395–3402.

18. BLUM, H. Biological shape and visual science (Part I). *J. Theor. Biol. 38* (1973), 205–287.

19. BLUM, H., AND NAGEL, R. Shape description using weighted symmetric axis features. *Pattern Recognition 10* (1978), 167–180.

20. BOGAEVSKI, I. Metamorphoses of singularities of minimum functions and bifurcations of shockwaves of the Burgers equation with vanishing viscosity. *Math. J. 1*, 4 (1990), 807–823.

21. BOISSONNAT, J., AND CAZALS, F. Natural coordinates of points on a surface. In *Proceedings of the 16th Annual ACM Symposium on Computational Geometry* (2000), pp. 223–232.

22. BORGEFORS, G., NYSTRÖM, I., AND DI BAJA, G. Computing skeletons in three dimensions. *Pattern Recognition 32* (1999), 1225–1236.

23. BRAKKE, K. The surface evolver. *Experimental Mathematics 1*, 2 (1992), 141–165.

24. BRUINSMA, R. Elasticity and excitations of minimal crystals. *J. Phys. II France 2* (1992), 425–451.

25. CANHAM, P. The minimum energy of bending as a possible explanation of bi-concave shape of human red blood cel. *J. Theor. Biol. 26*, 61 (1970).

26. CASELLES, V., KIMMEL, R., AND SAPIRO, G. Geodesic active contours. *Int. J.Comput. Vis. 22* (1997), 61–79.

27. CHARVOLIN, J., AND HENDRIKX, Y. Amphiphilic molecules in lyotropic liquid crystals and micellar phases. In *Nuclear Magnetic Resonance of Liquid Crystals*, J. Emsley, Ed. Reidel Publish.Co. ,Dordrecht, 1985, pp. 449–471.

28. CHARVOLIN, J., AND SADOC, J. Structures built by amphiphiles and frustrated fluid films. In *Colloque de Physique C7-1990* (1990), Supplément au Journal de Physique, pp. 83–96.

29. CHOI, H., CHOI, S., AND MOON, H. Mathematical theory of the medial axis transform. *Pacific Journal of Mathematics 181*, 1 (1997), 57–88.

30. CHOI, S., AND LEE, S. Stability analysis of the medial axis transform. In *Proc. 15th International Conference on Pattern Recognition (Barcelona, Spain)* (2000), vol. 3, pp. 139–142.

31. CHOI, S., AND SEIDEL, H. Hyperbolic Hausdorff distance for medial axis transform. MPI-I-2000-4-003, Research Report Max-Planck-Institut für Informatik, September 2000.

32. CLARKSON, K. L., MEHLHORN, K., AND SEIDEL, R. Four results on randomized incremental constructions. *Computational Geometry: Theory and Applications 3*, 4 (1993), 185–212.

33. CLERC, M. A New Symmetry for the Packing of Amphiphilic Direct Micelles. *Journal de Physique II 6* (July 1996), 961–968.

34. CUISENAIRE, O., AND MACQ, B. Fast euclidean distance transformation by propagation using multiple neighborhoods. *Computer Vision and Image Understanding 76*, 2 (1999), 163–172.

35. CULVER, T., KEYSER, J., AND MANOCHA, D. Accurate computation of the medial axis of a polyhedron. Tech. Rep. TR98-038, UNC, 1999.

36. CVIJOVIĆ, D., AND KLINOWSKI, J. The T and CLP families of triply periodic minimal surfaces. Part 1. derivation of parametric equations. *J. Phys. I France 2* (1992), 137–147.

37. CVIJOVIĆ, D., AND KLINOWSKI, J. The o-CLP family of triply periodic minimal surfaces. *Journal de Physique (Paris) I 3* (1993), 909–924.

38. CVIJOVIĆ, D., AND KLINOWSKI, J. The computation of the triply periodic I-WP minimal surface. *Chemical Physics Letters 226*, 1–2 (1994), 93–99.

39. DANIELSSON, P. Euclidean distance mapping. *Computer Graphics and Image Processing 14* (1980), 227–248.

40. DAVIS, P., AND RABINOWITZ, P. *Methods of Numerical Integration*. Academic Press, New York, San Francisco, London, 1975.

41. DE FABRITIIS, G., AND COVENEY, P. Dynamical geometry for multiscale dissipative particle dynamics. *Computer Physics Communications 153*, 18 (2003), 209–226.

42. DEY, T. K., AND ZHAO, W. Approximate medial axis as a voronoi subcomplex. In *Proceedings of the seventh ACM symposium on Solid modeling and applications* (2002), ACM Press, pp. 356–366.

43. DIDONNA, B., AND KAMIEN, R. Smectic phases with cubic symmetry: The splay analog of the blue phase. *Phys. Rev. Lett. 89*, 21 (2002), 215504–215508.

44. DIDONNA, B., AND KAMIEN, R. Smectic phases with cubic symmetry: Layered systems with high intrinsic curvature. *Physical Review E 68* (2003), 041703–041714.

45. DIERKES, U., HILDEBRANDT, S., KÜSTER, A., AND WOHLRAB, O. *Minimal Surface I*, vol. 295 of *Grundlehren der mathematischen Wissenschaften*. Springer-Verlag, Berlin, 1992.

46. DIRICHLET, G. Über die Reduktion der positiven quadratischen Formen mit drei unbestimmten ganzen Zahlen. *Journal für die reine und angewandte Mathematik 40* (1850), 209–227.

47. DO CARMO, AND MANFREDO, P. *Differentialgeometrie von Kurven und Flächen*, 3rd ed. Friedr. Vieweg & Sohn Verlagsgesellscchaft, 1993.

48. DO CARMO, M. *Differential Geometry of Curves and Surfaces*. Prentice Hall, Inc. Englewood Cliffs, New Jersey, 1976.

49. DOBKIN, D. Computational geometry and computer graphics. *Proceedings of the IEEE 80*, 9 (1989), 1400–1411.

50. DUESING, P., TEMPLER, R., AND SEDDON, J. Quantifying packing frustration energy in inverse lyotropic mesophases. *Langmuir 13* (1997), 351–359.

51. EDELSBRUNNER, H., AND SHAH, N. Incremental topological flipping works for regular triangulations. *Algorithmica 15* (1996), 223–241.

52. EGERTON, R. *Electron Energy-Loss Spectroscopy in the Electron Microscope*. Plenum, New York, 1996.

53. ENNEPER, A. Analytisch-geometrische Untersuchungen. *Z. Math. u. Phys. 9* (1864), 96–125.

54. EPPS, T., COCHRAN, E., BAILEY, T., WALETZKO, R., HARDY, C., AND BATES, F. Ordered network phases in linear poly(isoprene-b-styrene-b-ethylene oxide) triblock copolymers. *Macromolecules 37* (2004), 8325–8341.

55. ERICKSON, J. Nice point sets can have nasty Delaunay triangulations. In *17th Annual ACM Symposium on Computational Geometry* (2001), pp. 96–105.

56. EVANS, D., AND WENNERSTRÖM, H. *The Colloidal Domain - Where Physics, Chemistry, Biology and Technology Meet*. Wiley-VCH, 1999.

57. FISCHER, W., AND KOCH, E. On 3-periodic minimal surfaces. *Zeitschrift für Kristallographie 179* (1987), 31–52.

58. FISCHER, W., AND KOCH, E. Genera of minimal balance surfaces. *Acta Cryst. A45* (1989), 726–732.

59. FISCHER, W., AND KOCH, E. New surface patches for minimal balance surfaces. I. branched catenoids. *Acta Cryst. A45* (1989), 166–169.

60. FISCHER, W., AND KOCH, E. New surface patches for minimal balance surfaces. III. infinite strips. *Acta Cryst. A45* (1989), 485–490.

61. FOGDEN, A. *J. Phys. I France 2* (1992), 233–239.

62. FOGDEN, A. Parametrization of triply periodic minimal surfaces. III. general algorithm and specific examples for the irregular class. *Acta Cryst. A49* (1993), 409–421.

63. FOGDEN, A., HAEBERLEIN, M., AND LIDIN, S. Generalizations of the gyroid surface. *J. Phys. I France 3* (1993), 2371–2385.

64. FOGDEN, A., AND HYDE, S. Parametrization of triply periodic minimal surfaces. I. mathematical basis of the construction algorithm for the regular class. *Acta Cryst. A48* (1992), 442–451.

65. FOGDEN, A., AND HYDE, S. Parametrization of triply periodic minimal surfaces. II. regular class solutions. *Acta Cryst. A48* (1992), 575–591.

66. FOGDEN, A., AND HYDE, S. Continuous transformations of cubic minimal surfaces. *Eur. Phys. J. B 7* (1999), 91–104.

67. FOGDEN, A., HYDE, S., AND LUNDBERG, G. Bending energy of surfactant films. *J. Chem. Soc. Faraday Trans 87*, 7 (1991), 949–955.

68. FOL-LEYMARIE, F. *Three-Dimensional Shape Representation via Shock Flows*. PhD thesis, Brown University, 2002.

69. FONTELL, K. X-ray diffraction by liquid crystals – amphiphilic systems. In *Liquid crystals and plastic crystals*, G. Gray, Ed., vol. 2. Ellis Horwood (Chichester), 1974, pp. 80–109.

70. FONTELL, K. Cubic phases in surfactant and surfactant-like lipid systems. *Colloid Polym. Sci. 268* (1990), 264–285.

71. FORTUNE, S.

72. FRANK, J. *Electron Tomography*. Plenum, New York, 1992.

73. FRANK, J. *Three-dimensional Electron Microscopy of Macromolecular Assemblies*. Academic Press, San Diego, 1996.

74. FURUKAWA, H., SHIMIZU, M., SUZUKI, Y., AND NISHIOKA, H. System for three-dimensional reconstruction of tem images based on computerized tomography method. *JEOL News 36* (2001), 12–.

75. GAGVANI, N., AND SILVER, D. Parameter controlled skeletonization of three dimensional objects. Tech. rep., Computer Aids For Industrial Productivity TR, 1997.

76. GAUNT, W., AND GAUNT, P. *Three Dimensional Reconstruction in Biology*. Pitman Medical, Kent, 1978.

77. GIBLIN, P., AND KIMIA, B. On the local form and transitions of symmetry sets, medial axes, and shocks. In *Proc. Int. Conf. Computer Vision* (1999), pp. 385–391.

78. GIBLIN, P., AND KIMIA, B. A formal classification of 3d medial axis points and their local geometry. *IEEE Transactions on Pattern Analysis and Machine Intelligence 26*, 2 (2004), 238–251.

79. GOLDAK, J., YU, X., KNIGHT, A., AND DONG, L. Constructing discrete medial axis of 3-d objects. *Int. J. Computational Geometry and its Applications 1* (1991), 327–339.

80. GOLIN, M., AND NA, H. On the average complexity of 3d-Voronoi diagrams of random points on convex polytopes. In *Proceedings of the 12th Canadian Conference on Computational Geometry* (2000), pp. 127–135.

81. GOMES, J., AND FAUGERAS, O. Reconciling distance functions and level sets. *Journal of Visual Communication and Image Representation 11* (2000), 209–223.

82. GOODMAN, J., AND O'ROURKE, J., Eds. *Discrete and Computational Geometry*. CRC Press, Boca Raton, New York, 1997.

83. GRAY, A. *Modern Differential Geometry of Curves and Surfaces with Mathematica*. CRC Press, 1998.

84. GROSSE-BRAUKMANN, K. On Gyroid interfaces. *Journal of Colloid and Interface Science 187* (1997), 418–428.

85. HAHN, T., Ed. *International Tables For Crystallography*, third and revised ed. Kluwer Academic Publishers, Dordrecht, 1992.

86. HASEGAWA, H., TANAKA, H., YAMASAKI, K., AND HASHIMOTO, T. Bicontinuous microdomain morphology of block copolymers. 1. tetrapod-network structure of polystyrene-polyisoprene diblock polymers. *Macromolecules 20* (1987), 1651–1662.

87. HELFRICH, W. Elastic properties of lipid bilayers: theory and possible experiments. *Z. Naturforsch. 28c* (1973), 693–703.

88. HELFRICH, W., AND RENNSCHUH, H. Landau theory of the lamellar-to-cubic phase transition. In *Colloque de Physique C7-1990* (1990), Supplément au Journal de Physique, pp. 189–195.

89. HERMAN, T. *Image Reconstruction from Projections: The Fundamentals of Computerized Tomography*. Academic Press, New York, 1980.

90. HILBERT, D. Über Flächen von konstanter Gausscher Krümmung. *Transactions of the A.M.S. 2* (1901), 87–99.

91. HOFFMAN, D. Some basic facts, old and new, about triply periodic embedded minimal surfaces. In *Colloque de Physique C7-1990* (1990), Supplément au Journal de Physique, pp. 197–208.

92. HOPF, H. *Differential Geometry in the Large*, 2nd ed., vol. 1000 of *Lecture Notes in Mathematics*. Springer-Verlag, 1989.

93. HSIEH, J. *Computed Tomography: Principles, Design, Artifacts, and Recent Advances*. SPIE Press monograph, 2003.

94. HYDE, S. The topology and geometry of infinite periodic surfaces. *Zeitschrift für Kristallographie 187* (1989), 165–185.

95. HYDE, S. Curvature and the global structure of interfaces in surfactant-water systems. In *Colloque de Physique C7-1990* (1990), Supplément au Journal de Physique, pp. 209–228.

96. HYDE, S. Topological transformations mediated by bilayer punctures: from sponge phases to bicontinuous monolayers and reversed sponges. *Colloids and Surfaces, A: Physicochemical and Engineering Aspects 129–130* (1997), 207–225.

97. HYDE, S. Identification of lyotropic crystalline mesophases. In *handbook of Applied Surface and Colloid Chemistry*, K. Holmberg, Ed. John Wiley & Sons, Ltd, 2001, pp. 850–882.

98. HYDE, S., AND ANDERSSON, S. A systematic net description of saddle polyhedra and periodic minimal surfaces. *Zeitschrift für Kristallographie 168* (1984), 221–254.

99. HYDE, S., ANDERSSON, S., LARSSON, K., BLUM, Z., LANDH, T., LIDIN, S., AND NINHAM, B. *The Language of Shape*, 1st ed. Elsevier Science B. V., Amsterdam, 1997.

100. HYDE, S., AND FOGDEN, A. Hexagonal mesophases: honeycomb, froth, mesh or sponge? *Prog. Colloid. Polym. Sci 108* (1998), 139–152.

101. HYDE, S., FOGDEN, A., AND NINHAM, B. Self-assembly of linear block copolymers. relative stability of hyperbolic phases. *Macromolecules 126* (1993), 6782–6788.

102. HYDE, S., AND SCHRÖDER, G. Novel surfactant mesostructural topologies: between lamellae and columnar (hexagonal) forms. *Curr. Opin. Colloid Interface Sci. 8* (2003), 5–14.

103. ISRAELACHVILI, J., MITCHELL, D., AND NINHAM, B. Theory of self-assembly of hydrocarbon amphiphiles into micelles and bilayers. *J. Chem. Soc. Faraday Trans. 2 72* (1976), 1525–1568.

104. JERAULD, G., AND SALTER, S. The effect of pore-structure on hysteresis in relative permeability and capillary pressure: pore-level modeling. *Transport in Porous Media 5*, 2 (1990), 103–151.

105. JINNA, H., KOGA, T., NISHIKAWA, Y., HASHIMOTO, T., AND HYDE, S. Curvature determination of spinodal interface in a condensed matter system. *Phys. Rev. Lett. 78*, 11 (1997), 2248–2251.

106. JINNAI, H., NISHIKAWA, Y., SPONTAK, R., SMITH, S., AGARD, D., AND HASHIMOTO, T. Direct measurment of interfacial curvature distributions in bicontinuous copolymer morphology. *Phys. Rev. Lett. 84* (2000), 518–522.

107. JOE, B. Constuction of three-dimensional Delaunay triangulations using local transformations. *Computer Aided Geometric Design 10*, 4 (1989), 123–142.

108. JOE, B. Three-dimensional triangulations from local transformations. *SIAM Journal on Scientific and Statistical Computing 10*, 4 (1989), 718–741.

109. KAK, A., AND SLANEY, M. *Principles of Computerized Tomographic Imaging*. IEEE Press, 1988.

110. KARCHER, H. Embedded minimal surfaces derived from Scherk's examples. *Manuscripta Math. 62* (1988), 83–114.

111. KARCHER, H. The triply periodic minimal surfaces of A. Schoen and their constant mean curvature companions. *Man. Math. 64* (1989), 291–357.

112. KARCHER, H. Construction of higher genus embedded minimal surfaces. In *Geometry and topology of submanifolds, III (Leeds, 1990)*. World Sci. Publishing, River Edge, NJ, 1991, pp. 174–191.

113. KARCHER, H., AND POLTHIER, K. Construction of triply periodic minimal surfaces. *Philos. Trans. Roy. Soc. London Ser. A 354*, 1715 (1996), 2077–2104.

114. KASS, M., WITKIN, A., AND TERZOPOULOS, D. Snakes – active contour models. *Int. J. Comput. Vis. 1* (1987), 321–331.

115. KIMIA, B., TANNENBAUM, A., AND ZUCKER, S. Shapes, shocks, and deformations, I: The components of shape and the reaction-diffusion space. *ICJV 15*, 3 (1995), 189–224.

116. KIRK, G., GRUNER, S., AND STEIN, D. A thermodynamic model of the lamellar to inverse hexagonal phase transition of lipid membrance-water systems. *Biochemistry 23* (1984), 1093–1102.

117. KLEMAN, M., AND LAVRENTOVICH, O. *Soft Matter Physics: an Introduction.* Springer-Verlag, 2003.

118. KNACKSTEDT, M., SHEPPARD, A., AND SAHIMI, M. Pore network modelling of two-phase flow in porous rock: the effect of correlated heterogeneity. *Adv. Water Res. 24* (2001), 257–277.

119. KOCH, E., AND FISCHER, W. On 3-periodic minimal surfaces with non-cubic symmetry. *Zeitschrift für Kristallographie 183* (1988), 129–152.

120. KOCH, E., AND FISCHER, W. New surface patches for minimal balance surfaces. II. Multiple catenoids. *Acta Cryst. A45* (1989), 169–174.

121. KOCH, E., AND FISCHER, W. New surface patches for minimal balance surfaces. IV. Catenoids with spout-like attachments. *Acta Cryst. A45* (1989), 558–563.

122. LANDAU, L., AND LIFSHITZ, E. *Theory of Elasticity*, 3rd ed. Pergamon, Oxford, 1986.

123. LARSON, R. *The Structure and Rheology of Complex Fluids.* Oxford University Press, New York, 1999.

124. LARSSON, K. Two cubic phases in monoolein-water system. *Nature 304* (1983), 664.

125. LARSSON, K. Cubic lipid-water phases: structures and biomembranes aspects. *J. Phys. Chem. 93* (1989), 7304–7314.

126. LARSSON, M., LARSSON, K., ANDERSSON, S., KAKHAR, J., NYLANDER, T., NINHAM, B., AND WOLLMER, P. The alveolar surface structure: Transformation from a liposome-like dispersion into a tetragonal clp bilayer phase. *J. Dispersion Sci. Techn. 20* (1999), 1–12.

127. LARSSON, M., TERASAKI, O., AND LARSSON, K. A solid state transition in the tetragonal lipid bilayer structure at the lung alveolar surface. *Solid State Sciences 5* (2003), 109–114.

128. LAURER, J., HAJDUK, D., FUNG, J., SEDAT, J., SMITH, S., GRUNER, S., AGARD, D., AND SPONTAK, R. Microstructural analysis of a cubic bicontinuous morphology in a neat sis triblock copolymer. *Macromolecules 30* (1997), 3938–3941.

129. LAWSON, C. Generation of a triangular grid with applications to contour plotting. Memo 9, Jet Propulsion Laboratory, Pasadena, California, 1972.

130. LEE, T., KASHYAP, R., AND CHU, C. Building skeleton models via 3-d medial surface/axis thinning algorithms. *CVGIP: Graphical Models and Image Processing 56*, 6 (1994), 462–478.

131. LEONI, S. *Applications of Periodic Surfaces for the Study of Crystal Structures, First Order Phase Transitions, Force Ordering, and Systematic Generation of Novel Structure Models.* PhD thesis, Swiss Federal Institute of Technology, Zürich, 1998.

132. LEONI, S., AND NESPER, R. Elucidation of simple pathways for reconstructive phase transitions using periodic equi-surfaces (pes) descriptors. The silica phase system. i. Quartz-tridymite. *Acta Crystallographica Section A A56* (2000), 383–393.

133. LIDIN, S. Ring-like minimal surfaces. *J. Phys. France 49* (1988), 421–427.

134. LIDIN, S., AND HYDE, S. A construction algorithm for minimal surfaces. *J. Physique 48* (1987), 1585–1590.

135. LIDIN, S., HYDE, S., AND NINHAM, B. Exact construction of periodic minimal surfaces: the I-WP surface and its isometries. *J. Phys. France 51* (1990), 801–813.

136. LIDIN, S., AND LARSSON, S. Bonnet transformation of infinite periodic minimal surfaces with hexagonal symmetry. *J. Chem. Soc. Faraday Trans. 86*, 5 (1990), 769–775.

137. LORENSEN, W., AND CLINE, H. Marching cubes: A high resolution 3d surface construction algorithm. In *Computer Graphics (Proceedings of SIGGRAPH '87)* (1987), vol. 21 (4), pp. 163–169.

138. LUCHNIKOV, V., MEDVEDEV, N., OGER, L., AND TROADEC, J. Voronoi-Delaunay analysis of voids in systems of nonspherical particles. *Physical Review E 59*, 6 (1999), 7205–7212.

139. LUZZATI, V., DELACROIX, H., GULIK, A., GULIK-KRZYWICKI, T., MARIANI, P., AND VARGAS, R. The cubic phases of lipid systems. physico-chemical properties and biological implications. In *Current Topics in Membranes*, R. Epand, Ed., vol. 44. Academic Press, 1997, pp. 3–24.

140. LUZZATI, V., AND SPEGT, P. Polymorphism of lipids. *Nature 215* (1967), 701–704.

141. LUZZATI, V., TARDIEU, A., GULIK-KRZYWICKI, T., RIVAS, E., AND REISS-HUSSON, F. Structure of the cubic phases in lipid-water systems. *Nature (London) 220* (1968), 485–488.

142. LUZZATI, V., VARGAS, R., MARIANI, P., GULIK, A., AND DELACROIX, H. Cubic phases of lipid-containing systems. *J. Mol. Biol. 229* (1993), 540–551.

143. MA, C. On topology preservation in 3d thinning. *CVGIP: Image Understanding 59*, 3 (1994), 328–339.

144. MA, C., AND SONKA, M. A fully parallel 3D thinning algorithm and its applications. *Computer Vision and Image Understanding 64*, 3 (1996), 420–433.

145. MAGERLE, R. Nanotomography. *Phys. Rev. Lett. 85* (2000), 2749–2752.

146. MALLADI, R., SETHIAN, J., AND VEMURI, B. Shape modeling with front propagation – a level set approach. *IEEE Trans. Pattern Anal. Mach. Intell. 17* (1995), 158–175.

147. MARTÍN-MORENO, L., GARCÍA-VIDAL, F., AND SOMOZA, A. Self-assembled triply periodic minimal surfaces as molds for photonic band gap materials. *Phys. Rev. Lett. 83*, 1 (1999), 73–75.

148. MAXWELL, J. On hills and dales. *Philosophical Magazine 2* (1870), 233–240.

149. MAZÓN, M., AND RECIO, T. Voronoi diagrams on orbifolds. *Computational Geometry: Theory and Applications 8* (1997), 219–230.

150. MCNULTY, I., HADDAD, W., TREBES, J., AND ANDERSON, E. Soft x-ray scanning microtomography with submicrometer resolution. *Rev. Sci. Instr. 66* (1995), 1431–1433.

151. MECKE, K. Morphological characterization of patterns in reaction-diffusion systems. *Physical Review E 53*, 5 (1996), 4794–4800.

152. MECKE, K. Additivity, convexity, and beyond: Applications of Minkowski functionals in statistical physics. In *Statistical Physics and Spatial Statistics – The Art of Analyzing and Modeling Spatial Structures and Patterns* (2000), K. Mecke and D. Stoyan, Eds., vol. 554 of *Lecture Notes in Physics*, Springer Verlag, pp. 111–184.

153. MEDVEDEV, N. Application of Voronoi-Delaunay method to the structural description of void space in polydisperse systems. *Dokl. Akad. Nauk. 337* (1994), 767.

154. MUECKE, E. A robust implementation for 3d Delaunay triangulations. *International Journal of Computational Geometry And Applications 8*, 2 (1998), 255–276.

155. MUNKRES, J. *Topology: A First Course*. Englewood Cliffs, NJ : Prentice-Hall, 1975.

156. NACKMAN, L. R. Curvature relations in three-dimensional symmetric axes. *Computer Graphics and Image Processing 20* (1982), 43–57.

157. NEOVIUS, E. *Bestimmung zweier speziellen periodischen Minimalflächen, auf welchen unendlich viele gerade Linien und unendlich viele ebene geodätische Linien liegen.* J.C. Frenckell & Sohn, Helsingfors, 1883.

158. NIBLACK, C., GIBBONS, P., AND CAPSON, D. Generating skeletons and centerlines from the distance function. *Graphical Models and Image Processing 54*, 5 (1992), 420–437.

159. NISSEN, H. Crystal orientation and plate structure in echinoid skeletal units. *Science 166* (1969), 1150–1152.

160. NITSCHE, J. *Vorlesungen über Minimalflächen*. Springer-Verlag, Berlin, 1975.

161. OGUEY, C., AND SADOC, J.-F. Crystallographic aspects of the Bonnet transformation for periodic minimal surfaces (and crystals of films). *J. Phys. I France 3* (1993), 839–854.

162. OKABE, A., BOOTS, B., SUGIHARA, K., CHIU, S., AND OKABE, M. *Spatial Tesselations: Concepts and Applications of Voronoi Diagrams*, 2nd ed. John Wiley and Sons, 2000.

163. O'KEEFFE, M., AND HYDE, B. *Crystal Structures, I. Patterns and Symmetry*. Mineralogical Society of America Washington, USA, 1996.

164. OLLA, M., SEMMLER, M., MONDUZZI, M., AND HYDE, S. From monolayers to bilayers: Mesostructural evolution in ddab/water/tetradecane microemulsions. *J. Phys. Chem. B 108* (2004), 12833–12841.

165. PALIOURAS, J., AND MEADOWS, D. *Complex Variables for Scientists and Engineers*, 2nd ed. Collier Macmillan Canada, 1991.

166. PERONA, P., AND MALIK, J. Scale-space and edge-detection using anisotropic diffusion. *IEEE Trans. Pattern Anal. Mach. Intell. 12* (1990), 629–639.

167. PETROV, A., AND BIVAS, . Elastic and flexoelectic aspects of out-of-plane fluctuations in biological and model membranes. *Prog. Surf. Sci. 16* (1984), 389–2511.

168. PISANI, M., BERNSTORFF, S., FERRERO, C., AND MARIANI, P. Pressure induced cubic-to-cubic phase transition in monoolein hydrated systems. *J. Phys. Chem. B 105* (2001), 3109–3119.

169. PITTS, J., AND RUBINSTEIN, J. Application of minimax to minimal surface and the topology of 3-manifolds. In *Proc. Centre Math. Anal. Austral. Nat. Univ.* (1987), vol. 12, pp. 137–170.

170. PRATT, W. *Digital Image Processing*, 2nd ed. Wiley, New York, 1991.

171. RAGNEMALM, I. *The Euclidean Distance Transform*. Linköping studies in science and technology - dissertations - no.304, Linköping University, Dept. of Electrical Engineering, Linköping, Sweden, 1993. 276 pages.

172. RAJAN, V. Optimality of the Delaunay triangulation in $\mathbb{R}^d$. In *Proceedings of the 7th Annual Symposium on Computational Geometry* (1991), pp. 357–363.

173. REMY, E., AND THIEL, E. Medial axis for Chamfer distances: computing look-up tables and neighbourhoods in 2d or 3d. *Pattern Recognition Letters 23* (2002), 649–661.

174. RIEMANN, B. *Gesammelte mathematische Werke*, (1. auflage) ed. B.G. Teubner, Leipzig, 1876.

175. RIVIER, N. Geometry and fluctuations of surfaces. In *Colloque de Physique C7-1990* (1990), Supplément au Journal de Physique, pp. 309–317.

176. SADOC, J., AND CHARVOLIN, J. Periodic systems of frustrated fluid films and bicontinuous cubic structures in liquid crystals. *J. Phys. France 48* (1987), 1559–1569.

177. SADOC, J., AND CHARVOLIN, J. Infinite periodic minimal surfaces and their crystallography in the hyperbolic plane. *Acta Cryst. A45* (1989), 10–20.

178. SAFRAN, S. Curvature elasticity of thin films. *Advances in Physics 48* (1999), 395–448.

179. SAITO, T., AND TORIWAKI, J. New algorithms for euclidean distance transformation of an n-dimensional digitized picture with applications. *Pattern Recognition 27*, 11 (1994), 1551–1565.

180. SAKELLARIOU, A., SAWKINS, T. J., SENDEN, T. J., AND LIMAYE, A. X-ray tomography for mesoscale physics applications. *Physica A 339* (2004), 152–158.

181. SANTALÓ, L. *Integral Geometry and Geometric Probability*. Addison-Wesley, 1976.

182. SATURNI, L., RUSTICHELLI, F., DI GREGORIO, G., CORDONE, L., AND MARIANI, P. Sugar-induced stabilization of the monoolein $Pn3m$ bicontinuous cubic phase during dehydration. *Physical Review E* (2001), 040202(R).

183. SCHOEN, A. Infinite periodic minimal surfaces without self-intersections. Tech. rep., NASA, 1970.

184. SCHRÖDER, G., RAMSDEN, S., CHRISTY, A., AND HYDE, S. Medial surfaces of hyperbolic structures. *Eur. Phys. J. B 35* (2003), 551–564.

185. SCHWARZ, H. *Gesammelte Mathematische Abhandlungen. 2 Bände.* Springer, Berlin, 1890.

186. SCHWARZ, U., AND GOMPPER, G. Systematic approach to bicontinuous cubic phases in ternary amphiphilic systems. *Physical Review E 59*, 5 (1999), 5528–5541.

187. SCHWARZ, U., AND GOMPPER, G. Stability of inverse bicontinuous cubic phases in lipid-water mixtures. *Phys. Rev. Lett. 85*, 7 (2000), 1472–1475.

188. SCHWARZ, U., AND GOMPPER, G. Bending frustration of lipid-water mesophases based on cubic minimal surfaces. *Langmuir 17* (2001), 2084–2096.

189. SCRIVEN, L. Equilibrium bicontinuous structure. *Nature 263* (1976), 123–125.

190. SEDDON, J., AND TEMPLER, R. Polymorphism of lipid-water systems. In *Structure and dynamics of membranes – from cells to vesicles*, R. Lipowsky and E. Sackmann, Eds., vol. 1A of *Handbook of biological physics*. Elsevier, Amsterdam, 1995, pp. 97–160.

191. SETHIAN, J., Ed. *Level Set Methods and Fast Marching Methods*, 2nd ed. Cambridge Monographs on Applied and Computational Mathematics. Cambridge University Press, 1999.

192. SHAKED, D., AND BRUCKSTEIN, A. Pruning medial axes. *Computer Vision and Image Understanding 69*, 2 (1998), 156–169.

193. SHEEHY, D., ARMSTRONG, C., AND ROBINSON, D. Shape description by medial surface construction. *IEEE Transactions on Visualization and Computer Graphics 2*, 1 (1996), 61–72.

194. SHEPPARD, A., SOK, R., AND AVERDUNK, H. Techniques for image enhancement and segmentation of tomographic images of porous materials. *Physica A 339* (2004), 145–151.

195. SHERBROOKE, E., PATRIKALAKIS, N. M., AND WOLTER, F.-E. Differential and topological properties of medial axis transforms. *Graphical Models and Image Processing 58*, 6 (1996), 574–592.

196. SHEWCHUK, J. Adaptive precision floating-point arithmetic and fast robust geometric predicates. *Discrete and Computational Geometry 18* (1997), 305–363.

197. SHEWCHUK, J. Lecture notes on geometric robustness. 2002.

198. SILIN, D., JIN, G., AND PATZEK, T. Robust determination of the pore space morphology in sedimentary rocks. *SPE* (2003), 84296.

199. SJÖSTRAND, F. Ultrastructure of retinal rod synapses of the guinea pig eye as revealed by 3-dimensional reconstructions from serial sections. *J. Ultrastructure Research 2* (1958), 122–170.

200. SOK, R., KNACKSTEDT, M., SHEPPARD, A., PINCZEWSKI, W., LINDQUIST, W., VENKATARANGAN, A., AND PATERSON, L. Direct and stochastic generation of network models from tomographic images; effect of topology on residual saturations. *Transport in Porous Media 46* (2002), 345–372.

201. SPANIER, E. *Algebraic topology*. McGraw-Hill, 1966.

202. SPIVAK, M. *Comprehensive Introduction to Differential Geometry*, vol. 3. Wilmington, DE, Publish or Perish Press, 1979.

203. SPIVAK, M. *Comprehensive Introduction to Differential Geometry*, vol. 1–4. Wilmington, DE, Publish or Perish Press, 1979.

204. SPONTAK, R., WILLIAMS, M., AND AGARD, D. Three-dimensional study of cylindrical morphology in a styrene-butadiene-styrene block copoloymer. *Polymer 29* (1988), 387–395.

205. SQUIRES, A., TEMPLER, R., CES, O., GABKE, A., WOENCKHAUS, J., SEDDON, J., AND WINTER, R. Kinetics of lyotropic phase transitions involving the inverse bicontinuous cubic phases. *Langmuir 16* (2000), 3578–3582.

206. STESSMANN, B. Periodische Minimalflächen. *Math.Z. 38* (1934), 417–442.

207. SVENSON, S. Self-assembly and self-organization: Important processes, but can we predict them? *Journal of Dispersion Science and Technology 25*, 2 (2004), 101–118.

208. TEMPLER, R., SEDDON, J., WARRENDER, N., SYRYKH, A., HUANG, Z., WINTER, R., AND ERBES, J. Inverse bicontinuous cubic phases in 2:1 fatty

acid/phosphatidylcholine mixtures. The effects of chain length, hydration, and temperature. *J. Phys. Chem. 102* (1998), 7251–7261.

209. THOMAS, E., ANDERSON, D., HENKEE, C., AND HOFFMAN, D. Periodic area-minimizing surfaces in block copolymers. *Nature 334* (August 1988), 598–601.

210. THOMPSON, D. *On Growth and Form*, 2nd ed. Cambridge University Press, 1942.

211. VINCENT, L., AND SOILLE, P. Watersheds in digital spaces – an efficient algorithm based on immersion simulations. *IEEE Trans. Pattern Anal. Mach. Intell. 13* (1991), 583–598.

212. VON SCHNERING, H., AND NESPER, R. How nature adapts chemical structures to curved surfaces. *Angew. Chem. Int. Ed. Engl. 26* (1987), 1059–1080.

213. VON SCHNERING, H., AND NESPER, R. Nodal surfaces of Fourier series: fundamental invariants of structured matter. *Z. Phys. B – Condensed Matter 83* (1991), 407–412.

214. VORONOÏ, G. Nouvelles applications des paramètres continus à la théorie des formes quadratiques. Premier Mémoire: sur quelques propriétés des formes quadratiques positives parfaites. *Journal für die reine und angewandte Mathematik 133* (1907), 97–178.

215. WEIERSTRASS, K. *Mathematische Werke*. Mayer & Müller, 1903.

216. WHITE, W., AND WILTZIUS, P. Real space measurement of structure in phase separating binary fluid mixtures. *Phys. Rev. Lett. 75* (1995), 3012–3015.

217. WOHLGEMUTH, M., YUFA, N., HOFFMAN, J., AND THOMAS, E. Triply periodic bicontinuous cubic microdomain morphologies by symmetry. *Macromolecules 34* (2001), 6083–6089.

218. WOLFRAM, S. *The Mathematica Book*, 3rd ed. Wolfram Media/Cambridge University Press, 1996.

219. WOLTER, F.-E. Cut locus and medial axis in global shape interrogation and representation. MIT design laboratory memorandum 92-2, MIT, 1992.

220. YAO, F. Computational geometry. In *Handbook of Theoretical Computer Science, Volume A: Algorithms in Complexity,* R. Earnshaw and B. Wyvill, Eds. Elsevier Science Publishers, Amsterdam, 1990, pp. 345–490.

221. YE, Q. The signed Euclidean distance transform and its applications. In *Proceedings of the* 9th *International Conference on Pattern Recognition* (Rome, Italy, November 1988), vol. 1, IEEE Computer Society Press, pp. 495–499.

222. ZHOU, Y., KAUFMAN, A., AND TOGA, A. Three-dimensional skeleton and centerline generation based on an approximate minimum distance field. *The Visual Computer 14* (1998), 303–314.

223. ZHOU, Y., AND TOGA, A. Efficient skeletonization of volumetric objects. *IEEE Transactions on Visualization and Computer Graphics 5*, 3 (1999), 196–209.